Green Energy and Technology

Hui Lin Ong
Siti Jamilah Hanim Mohd Yusof
Khairul Farihan Kasim
Ahmad Anas Nagoor Gunny
Rahimah Othman *Editors*

Proceedings of the 3rd International Conference on Biomass Utilization and Sustainable Energy; ICoBiomasSE 2023; 4–5 September; Kuala Lumpur, Malaysia

Advancing Circular Economy Towards Academic-Industrial Sustainability

Springer

Green Energy and Technology

Climate change, environmental impact and the limited natural resources urge scientific research and novel technical solutions. The monograph series Green Energy and Technology serves as a publishing platform for scientific and technological approaches to "green"—i.e. environmentally friendly and sustainable—technologies. While a focus lies on energy and power supply, it also covers "green" solutions in industrial engineering and engineering design. Green Energy and Technology addresses researchers, advanced students, technical consultants as well as decision makers in industries and politics. Hence, the level of presentation spans from instructional to highly technical.

Indexed in Scopus.

Indexed in Ei Compendex.

Hui Lin Ong · Siti Jamilah Hanim Mohd Yusof ·
Khairul Farihan Kasim ·
Ahmad Anas Nagoor Gunny · Rahimah Othman
Editors

Proceedings of the 3rd International Conference on Biomass Utilization and Sustainable Energy; ICoBiomasSE 2023; 4–5 September; Kuala Lumpur, Malaysia

Advancing Circular Economy Towards Academic-Industrial Sustainability

Springer

Editors
Hui Lin Ong
Faculty of Chemical Engineering
& Technology
Universiti Malaysia Perlis
Arau, Perlis, Malaysia

Khairul Farihan Kasim
Faculty of Chemical Engineering
& Technology
Universiti Malaysia Perlis
Arau, Perlis, Malaysia

Rahimah Othman
Faculty of Chemical Engineering
& Technology
Universiti Malaysia Perlis
Arau, Perlis, Malaysia

Siti Jamilah Hanim Mohd Yusof
Faculty of Chemical Engineering
& Technology
Universiti Malaysia Perlis
Arau, Perlis, Malaysia

Ahmad Anas Nagoor Gunny
Faculty of Chemical Engineering
& Technology
Universiti Malaysia Perlis
Arau, Perlis, Malaysia

ISSN 1865-3529 ISSN 1865-3537 (electronic)
Green Energy and Technology
ISBN 978-981-99-9357-4 ISBN 978-981-99-9164-8 (eBook)
https://doi.org/10.1007/978-981-99-9164-8

Organization

Technical Chairs

Hui Lin Ong, Universiti Malaysia Perlis, Malaysia
Siti Jamilah Hanim Mohd Yusof, Universiti Malaysia Perlis, Malaysia
Khairul Farihan Kasim, Universiti Malaysia Perlis, Malaysia
Ahmad Anas Nagoor Gunny, Universiti Malaysia Perlis, Malaysia
Rahimah Othman, Universiti Malaysia Perlis, Malaysia

Technical Reviewers

Ahmad Anas Nagoor Gunny, Universiti Malaysia Perlis, Malaysia
Ain Nihla Kamarudzaman, Universiti Malaysia Perlis, Malaysia
Akmal Hadi Ma'Radzi, Universiti Malaysia Perlis, Malaysia
Azalina Mohamed Nasir, Universiti Malaysia Perlis, Malaysia
Boon Beng Lee, Universiti Malaysia Perlis, Malaysia
Hafizah Mohd Johar, Universiti Malaysia Perlis, Malaysia
Hairul Nazirah Abdul Halim, Universiti Malaysia Perlis, Malaysia
Hui Lin Ong, Universiti Malaysia Perlis, Malaysia
Khairul Farihan Kasim, Universiti Malaysia Perlis, Malaysia
Kunasundari Balakrishnan, Universiti Malaysia Perlis, Malaysia
Liza Patacsil, University of the Philippines Los Banos, Philippines
Maha Al-Rajabi, Universiti Malaysia Perlis, Malaysia
Masitah Hasan, Universiti Malaysia Perlis, Malaysia
Mohd Asraf Mohd Zainudin, Universiti Malaysia Perlis, Malaysia
Mohd Faidz Mohamad Shahimin, Universiti Malaysia Perlis, Malaysia
Muhammad Faiq Abdullah, Universiti Malaysia Perlis, Malaysia
Noor Hasyierah Mohd Salleh, Universiti Malaysia Perlis, Malaysia
Noormaizatul Akmar Ishak, Universiti Malaysia Perlis, Malaysia

Nor Ashikin Ahmad, Universiti Malaysia Perlis, Malaysia
Nor Hidawati Elias, Universiti Malaysia Perlis, Malaysia
Nurhadijah Zainalabidin, Universiti Malaysia Perlis, Malaysia
Rahimah Othman, Universiti Malaysia Perlis, Malaysia
Ras Izzati Ismail, Universiti Malaysia Perlis, Malaysia
Rozaini Abdullah, Universiti Malaysia Perlis, Malaysia
Safa Senan Mahmod, Universiti Malaysia Perlis, Malaysia
Shing Fhan Khor, Universiti Malaysia Perlis, Malaysia
Siti Jamilah Hanim Mohd Yusof, Universiti Malaysia Perlis, Malaysia
Siti Nazrah Zailani, Universiti Malaysia Perlis, Malaysia
Syed Nuzul Fadzli Syed Adam, Universiti Malaysia Perlis, Malaysia
Tengku Nuraiti Tengku Izhar, Universiti Malaysia Perlis, Malaysia
Tengku Roslina Tuan Yusof, Universiti Malaysia Perlis, Malaysia
Tiang Tow Leong, Universiti Malaysia Perlis, Malaysia
Umi Fazara Md Ali, Universiti Malaysia Perlis, Malaysia
Wooi Chin Leong, Universiti Malaysia Perlis, Malaysia
Zafifah Zamrud, Universiti Malaysia Perlis, Malaysia
Zulkarnain Mohamed Idris, Universiti Malaysia Perlis, Malaysia

Preface

The 3rd International Conference on Biomass Utilization and Sustainable Energy (ICoBiomasSE 2023) in conjunction with Global Trends in Engineering, Science and Technology Congress 2023 (GTEST 2023) was organized from 4 to 5 September 2023 at World Trade Centre (WTC) Kuala Lumpur, Malaysia.

This year, "Advancing Circular Economy Towards Academic-Industrial Sustainability", was selected as the conference theme which intended to provide a platform for deliberating current findings in a wide variety of topics that include, but not limited to:

- Sustainable Biomass Resources for Decarbonising the Economy;
- Biomass Conversion Technology for Bioenergy;
- Biomass Conversion to Intermediates and Products;
- Bioenergy Integration.

The ICoBiomasSE 2023 marks the third conference that has been organized by the Centre of Excellence for Biomass Utilization (CoEBU), Universiti Malaysia Perlis (UniMAP). This conference is organized in collaboration with the Taiwan–Thailand–Malaysia Innovation Centre for Clean Water and Sustainable Energy (WISE), UniMAP, and TIIAME National Research University, Uzbekistan, who are serving as co-organizers. The two-day hybrid format conference (combining online and physical) has gathered 28 presenters with a total of 18 papers accepted following a rigorous peer-review process to ensure the relevance of the research to the conference's theme.

The editors would like to express sincere appreciation to all participants for their valuable contributions to ICoBiomasSE 2023. Moreover, the editors extend their gratitude to the keynote speakers, reviewers, and committee members for their outstanding commitment and dedication in making the conference a success.

The ICoBiomasSE 2023 committee members extend their kudos to Springer for their technical assistance.

Arau, Perlis, Malaysia

Hui Lin Ong
Siti Jamilah Hanim Mohd Yusof
Khairul Farihan Kasim
Ahmad Anas Nagoor Gunny
Rahimah Othman

Contents

Sustainable Biomass Resources for Decarbonising the Economy

The Perceptive Classification of the Wastes for Recycling and Composting for Sustainable Waste Management

Nattapon Leeabai, Methawee Nukunudompanich, and Chinnathan Areeprasert

Abstract The problem with municipal solid waste (MSW) in Thailand necessitates the well-planned MSW management is important. The perceptive classification of waste is the effective tool to design MSW management and waste separation campaign. It was found that the perceptive classification of the waste was significantly graded in order to the characteristics of the waste. The certain numbers of the wastes were high perceptive classification to the target category. Thus, the perceptual classification of these wastes did not prevent their separation into the designated waste bin. On the other hand, careful attention was required to increase the perception classification of aluminum foil as recyclable waste. The perceptive classification of recyclable waste on aluminum foil was too low, and it was around 37.66%. Misclassification may result from a misunderstanding of the waste type. In addition, some wastes were hardly segregated to a specific category, and there were depending on the implementation process in the MSW management system. For example, the perceptive classification of tissue paper as compostable wastes was low. To design the composting process including the input of tissue paper, the campaign to improve the perceptive classification on tissue papers was recommended. In contrast, the

N. Leeabai
Department of Environmental Engineering, Faculty of Engineering, Kasetsart University, 50 Ngam Wong Wan Road, Lat Yao, Chatuchak, Bangkok 10900, Thailand
e-mail: fengnpl@ku.ac.th

M. Nukunudompanich
Department of Industrial Engineering, Faculty of Engineering, King Mongkut's Institute of Technology Ladkrabang, 1 Soi Chalong Krung Road, 1 Lat Krabang, Bangkok 10520, Thailand
e-mail: Methawee.nu@kmitl.ac.th

C. Areeprasert (✉)
Department of Mechanical Engineering, Faculty of Engineering, Kasetsart University, 50 Ngam Wong Wan Road, Lat Yao, Chatuchak, Bangkok 10900, Thailand
e-mail: fengcta@ku.ac.th

H. L. Ong et al. (eds.), *Proceedings of the 3rd International Conference on Biomass Utilization and Sustainable Energy; ICoBiomasSE 2023; 4–5 September; Kuala Lumpur, Malaysia*, Green Energy and Technology,
https://doi.org/10.1007/978-981-99-9164-8_1

implementation of composting without the input of tissue paper did not need the campaign to modify the perceptive classification on tissue papers. Therefore, the significant findings of this study will be the designing tools to enable the effective and sustainability MSW management.

Keywords Solid waste management · Perceptive classification · Waste separation behavior

1 Introduction

According to the Pollution Control Department of Thailand [1], Thailand generated 24.98 million tons of municipal solid waste (MSW) in 2021. Although there was a decrease of 1% compared to the previous year, the MSW generation rate of Thailand was still considered a high value. The population of Thailand was approximately 66.2 million people in 2022 [2]. Therefore, the particular waste generation rate in Thailand was 1.03 kg/person/day, which is higher than the global average of 0.74 kg/person/day [3]. In addition, the proportion of MSW recycling was 32% of total MSW in 2021, which decreased by 27% compared to MSW recycling in 2019. Contradictory to improper treatment and disposal, the proportion of improper treatment and disposal of MSW was increased by 41% in comparison with the year 2019. Thus, MSW management in Thailand needs improvement. To enhance MSW management, waste separation at source is an effective campaign [4, 5]. In particular, the quality of recycling production is better than the recycled products from commingled wastes [6]. Since the waste separation at source is depended on waste separation behaviors [7, 8], the perceptive classification of wastes is the key to design an efficient source separation.

Perceptive classification of wastes is one of the influenced factors toward waste disposal behavior [9]. It was noted that misunderstandings in waste classification lead to non-essential costs in waste disposal. According to the previous study, misunderstandings in waste classification directly affected waste separation execution [10]. For example, slowly biodegradable wastes could be found in the compostable waste bin because the perceptive classification of those wastes was categorized as compostable waste. In this example, the waste management system needed to be expanded with an additional separation process performed by a waste sorting facility. Well-planned waste management using perceptive classification as an improvement tool will eliminate non-essential costs. For example, the campaign provides information on misunderstanding waste to enable effective waste separation because the informational tool is efficient to improve waste separation behavior [11]. Therefore, designing waste collection systems at source separation requires a thorough understanding of the perceptive classification of wastes.

Generally, the visual prompts for waste separation are located alongside with source separation. However, there is limited research on waste type perception. The design of the visual prompt should be enhanced to indicate the target waste with low

perceptive classification. This study conducted a survey to collect data on trash bin selection for certain waste types. The comparison of perceptive classification of food waste, bone/shell waste, plastic, and other recyclable waste will provide significant findings to improve waste separation at the source.

2 Materials and Methods

2.1 Survey Questionnaires

Online surveying took place between October 21, 2021, and November 2, 2021. Google Form was the online tools used for data collection. There were 397 Thai respondents from Thailand, including 138 males, 251 females, and 8 others. The age of respondents was categorized by the generation, consisting of baby boomer, Generation X, Generation Y, and Generation Z. There were 78, 127, 98, and 94 respondents in each generation, respectively. When asked to select the appropriate bins for the waste, respondents were given three options: a compostable waste bin (green), a recyclable waste bin (yellow), and a general waste bin (blue), as shown in Fig. 1. It should be noted that the colors of trash bin were representative of the common bin colors used in Thailand for source separation. There were 12 questions, including the number of 40 wastes. Thus, the percentage of bin selection of the tested waste represented the perceptive classification of the waste.

2.2 Waste Categorization

A total of 40 wastes are categorized into 19 different waste types. These waste type includes aluminum foil, banana leaf containers, beverage waste, biodegradable plastic, bone, cans, food scrap, fruit peel, glass bottles, paper containers, plastic bags, plastic containers, plastic fork/spoon, shell, Styrofoam, tissue paper, vegetable scrap, wooden chopsticks, and wooden skewers, respectively (see Fig. 2).

2.3 Data Comparison

The collected data were averaged to find out the mean values in each waste type. The dataset was separated into four groups of age generation because pro-environmental behaviors were influenced by a person's life span [12, 13]. The mean values were compared to justify the perceptive classification of those wastes. Respondents may dispose of their waste in the target bin if they classify it with high perception.

Fig. 1 The example of questionnaires

2.4 Statistical Analysis

The results were analyzed using statistical methods. The Welch's t-test or one-way ANOVA was used to identify the difference in findings at a significant level of 5%. The null hypothesis of these statistical methods is that there are no differences among datasets. To reject the null hypothesis, the *p*-value of the tested data must be less than 0.05. The results of null hypothesis rejection are described as "significantly different" or "significant difference". In addition, the pairwise comparison of the Tukey–Kramer procedure for one-way ANOVA was used to analyze significant differences between mean values in each pair. The null hypothesis of this statistical method is that there is no difference between datasets. To reject the null hypothesis, the absolute difference of mean values must be greater than the critical range (Tukey's HSD). The rejection of a null hypothesis is described as "significantly different" or "significant difference".

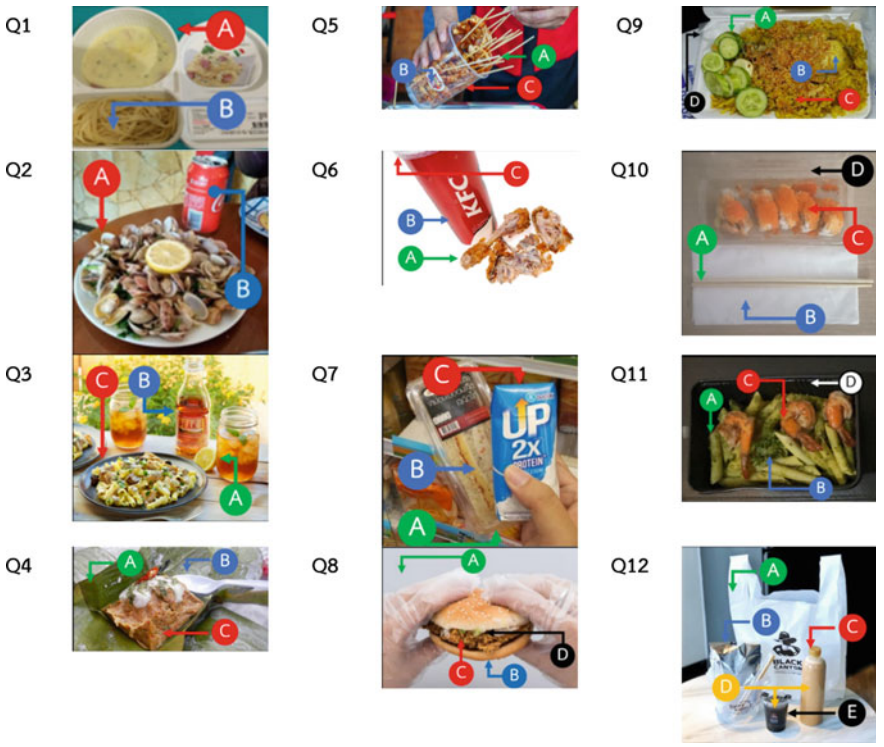

Fig. 2 Wastes for perceptive classification analysis

3 Results and Discussion

3.1 Overview Results

The results of perceptive classification of all waste types were shown in Fig. 3. The ranking of perceptive classification in each category was shown in Table 1. The results showed that the perceptive classification of recyclable wastes and that of compostable wastes were clearly contrasted. Recyclable wastes were high perceptive classification of recyclable waste such as cans, glass bottles, and recyclable plastic wastes. On the other hand, there were low perceptive classification of compostable waste. In contradictory, the rapid biodegradable wastes were high perceptive classification of compostable waste such as food scraps, vegetable scraps, and fruit peels. On the other hand, there were low perceptive classification of recyclable waste. The wooden-based slowly biodegradable wastes contained the highest perceptive classification of general wastes. In addition, there were some recyclable wastes with a high perceptive classification of general wastes such as aluminum foil.

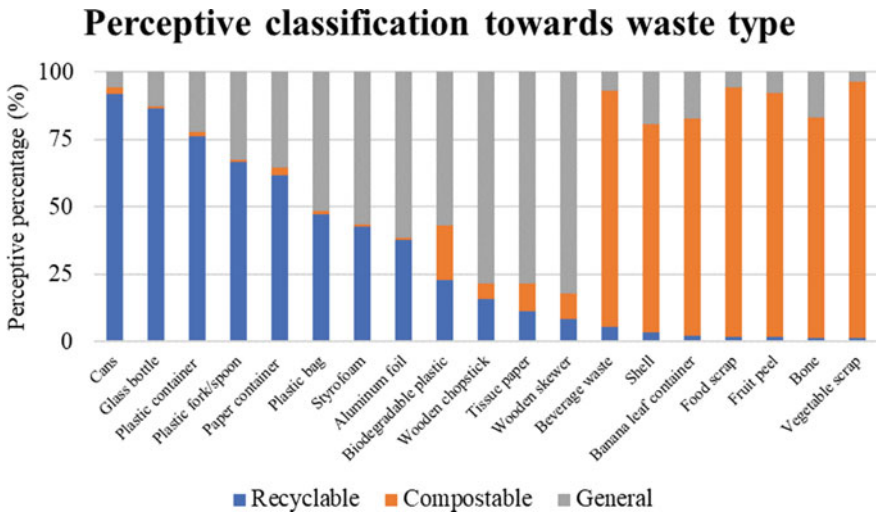

Fig. 3 Perceptive classification of wastes

3.2 Perceptive Classification Toward Recyclable Wastes

According to the results, the ANOVA test suggested that the significant differences among the values of recyclable perceptive classification were found ($p = 2.37 \times 10^{-37}$). All paired data points of perceptive classification toward recyclable wastes were tested by the post-hoc analysis using the pairwise comparison of Tukey–Kramer procedure. The statistical test suggested that, after excluding some cases, there was a significant difference in the perceptive classification of recycle waste between the rankings. The perceptive classification of recyclable waste on cans showed the highest value among all wastes, and it was about 91.72%, followed by 86.78% on glass bottles and 76.40% on plastic containers. It could be concluded that cans, glass bottles, and plastic containers were easily found in the recyclable waste bin. On the other hand, the biodegradable wastes including wooden chopsticks, tissue papers, wooden skewers, beverage waste, shells, banana leaf containers, food scrap, fruit peel, bone, and vegetable scrap were significantly less than 20% of the perceptive classification of recyclable waste. Therefore, there was not necessary to induce the persons to segregate those wastes out of a recyclable waste bin. However, some wastes, including biodegradable plastics, paper cups, plastic bags, Styrofoam, and plastic forks and spoons, were misclassified by the respondents. The perceptive classification of recyclable wastes on these wastes ranged from 22.77 to 66.61%. It should be carefully noted that in order to guarantee the success of waste separation at the source, education and information about these wastes are required.

Table 1 Ranking of perceptive classification score in each category

Rank	Recyclable waste	Perceptive score (%)	Compost-able waste	Perceptive score (%)	General waste	Perceptive score (%)
1	Cans	91.72	Vegetable scrap	95.05	Wooden skewer	81.97
2	Glass bottle	86.48	Food scrap	92.73	Wooden chopstick	78.44
3	Plastic container	76.40	Fruit peel	90.81	Tissue paper	78.23
4	Plastic fork/ spoon	66.61	Beverage waste	87.62	Aluminum foil	61.24
5	Paper container	61.57	Bone	81.85	Biodegradable plastic	56.89
6	Plastic bag	47.16	Banana leaf container	80.84	Styrofoam	56.38
7	Styrofoam	42.59	Shell	77.58	Plastic bag	51.28
8	Aluminum foil	37.66	Biodegradable plastic	20.35	Paper container	35.56
9	Biodegradable plastic	22.77	Tissue paper	10.35	Plastic fork/ spoon	32.43
10	Wooden chopstick	15.97	Wooden skewer	9.53	Plastic container	22.06
11	Tissue paper	11.42	Wooden chopstick	5.59	Shell	19.11
12	Wooden skewer	8.50	Paper container	2.87	Banana leaf container	16.97
13	Beverage waste	5.50	Cans	2.55	Bone	16.72
14	Shell	3.30	Plastic bag	1.57	Glass bottle	12.81
15	Banana leaf container	2.19	Plastic container	1.54	Fruit peel	7.57
16	Food scrap	1.77	Aluminum foil	1.10	Beverage waste	6.88
17	Fruit peel	1.62	Styrofoam	1.03	Cans	5.73
18	Bone	1.42	Plastic fork/ spoon	0.96	Food scrap	5.50
19	Vegetable scrap	1.28	Glass bottle	0.71	Vegetable scrap	3.68

3.3 Perceptive Classification Toward Compostable Wastes

The ANOVA test suggested that the significant differences among the values of compostable perceptive classification were found ($p = 4.03 \times 10^{-56}$). The statistical test suggested that the perceptive classification of compostable waste was

significantly different between the rankings excluding the group among rank 12–19. In contradictory to the perceptive classification of recyclable waste, the rapidly biodegradable wastes were significantly high percentages of the perceptive classification of compostable wastes, and the values were greater than 80%. However, there are carefully noted that come slowly biodegradable wastes were also high perceptive classification of compostable waste such as bone and shell, there were 81.85 and 77.58%, respectively. It could be considered in the process of waste treatment and disposal of these waste types since these wastes are difficult to decompose in a short duration [14]. On the other hand, the non-compostable wastes were significantly lower than the perceptive classification of compostable wastes; the values were less than 20%. As a result, action on these wastes may not be required.

3.4 Perceptive Classification Toward General Wastes

The general waste perceptive classification values showed significant differences in the ANOVA test ($p = 4.68 \times 10^{-30}$). The statistical analysis, which excluded some cases, suggested that the perceptive classification of general waste was significantly different between the rankings. The wooden skewers had the highest perceptive classification value among general waste of around 81.96%, followed by wooden chopsticks and tissue papers with the perceptive classification value of 78.44 and 78.23%, respectively. In the case of tissue paper, it was also recommended to add in the composting process [15]. To design the composting process with tissue papers as an input, it is crucial to increase the perception of tissue papers as compostable waste. In addition, aluminum foil contained 61.24% of the perceptive classification of general waste. According to the previous study, the recycling of aluminum foil greatly reduced the environmental impact compared to landfilling [16]. The action to increase of perceptive classification of recyclable waste for aluminum foil was carefully noted.

4 Conclusion

This study found a significant correlation between the perceptive classification of the waste and characteristics of the waste. The aluminum cans, glass bottles, and plastic containers were high perception as recyclable waste. Thus, the perceptive classification of these wastes was not hampered the separation of these wastes into the recyclable waste bin. As well as the case of compostable waste, the perceptive classification of compostable waste on rapidly biodegradable wastes showed very high values. Contrary to expected results, waste separation at the source was ineffective [10, 17]. Other factors such as inconvenient waste separation, attitudes toward waste separation, subject norms, and perceived behavioral controls may also contribute to improper waste disposal. The campaigns to increase the other influential factors by

the authorization were recommended to enhance the waste separation efficiency of these wastes. On the other hand, careful attention was required to alter the perception classification of aluminum foil as recyclable trash. The perceptive classification of recyclable waste on aluminum foil was too low, and it was about 37.66%. The incorrect categorization of waste can result in improper sorting. Lastly, the significant findings of this study can be used to develop MSW management systems. Some wastes were hardly segregated to a specific category; segregation largely depended on the implementation process in the MSW management stream. For example, the tissue paper was classified as a low perceptive classification of compostable wastes. To design the composting process that incorporates tissue paper, the campaign to improve the perceptive classification on tissue papers was recommended. Conversely, the implementation of composting without the input of tissue paper did not require the campaign to alter the perceptive classification on tissue papers. Therefore, the findings of this study will serve as design tools for sustainable and effective MSW management.

Acknowledgements This research was supported by the Kasetsart University Research Development Institute (KURDI, FF(KU)25.64) and the Faculty of Engineering, Kasetsart University.

References

1. Pollution Control Department, Ministry of Natural Resources and Environment, Thailand (2022) Thailand State of Pollution Report 2021 (In Thai). https://www.pcd.go.th/pcd_news/12628. Last accessed 20 Sept 2023
2. BORA, the Bureau of Registration Administration (BORA), the Department of Provincial Administration, Thailand (2022) Notification of total population in Thailand on 31 December 2021 (In Thai). https://www.bora.dopa.go.th. Last accessed 20 Sept 2023
3. Kaza S, Yao L, Bhada-Tata P, Van Woerden F (2018) What a waste 2.0: a global snapshot of solid waste management to 2050. The World Bank Group, Washington D.C.
4. Sukholthaman P, Sharp A (2016) A system dynamics model to evaluate effects of source separation of municipal solid waste management: A case of Bangkok, Thailand. Waste Manage 52:50–61
5. Gundupalli SP, Hait S, Thakur A (2017) A review on automated sorting of source-separated municipal solid waste for recycling. Waste Manage 60:56–74
6. Moh Y (2017) Solid waste management transformation and future challenges of source separation and recycling practice in Malaysia. Resour Conserv Recycl 116:1–14
7. Oztekin C, Teksöz G, Pamuk S, Sahin E, Kilic DS (2017) Gender perspective on the factors predicting recycling behavior: Implications from the theory of planned behavior. Waste Manage 62:290–302
8. Stoeva K, Alriksson S (2017) Influence of recycling programmes on waste separation behaviour. Waste Manage 68:732–741
9. Lee M, Choi H, Koo Y (2017) Inconvenience cost of waste disposal behavior in South Korea. Ecol Econ 140:58–65
10. Leeabai N, Areeprasert C, Siripaiboon C, Khaobang C, Congsomjit D, Takahashi F (2022) The effects of compost bin design on design preference, waste collection performance, and waste segregation behaviors for public participation. Waste Manage 143:35–45

11. Matiiuk Y, Liobikienė G (2021) The impact of informational, social, convenience and financial tools on waste sorting behavior: Assumptions and reflections of the real situation. J Environ Manage 297:113323
12. Ahlfeldt GM, Maennig W, Mueller SQ (2021) The generation gap in direct democracy: age vs. cohort effects. Eur J Polit Econ 102120
13. Karunasena GG, Ananda J, Pearson D (2021) Generational differences in food management skills and their impact on food waste in households. Resour Conserv Recycl 175:105890
14. Stanford K, Hao X, Xu S, McAllister T, Larney F, Leonard J (2009) Effects of age of cattle, turning technology and compost environment on disappearance of bone from mortality compost. Biores Technol 100:4417–4422
15. Karagiannidis A, Theodoseli M, Malamakis A, Bilitewski B, Reichenbach J, Nguyen T, Parayno P (2010) Decentralized aerobic composting of urban solid wastes: some lessons learned from ASIAN-EU cooperative research. Glob Nest J 12(4):343–351
16. Xie M, Bai W, Bai L, Sun X, Lu Q, Yan D, Qiao Q (2016) Life cycle assessment of the recycling of Al-PE (a laminated foil made from polyethylene and aluminum foil) composite packaging waste. J Clean Prod 112:4430–4434
17. Leeabai N, Areeprasert C, Khaobang C, Viriyapanitchakij N, Bussa B, Dilinazi D, Takahashi F (2021) The effects of color preference and noticeability of trash bins on waste collection performance and waste-sorting behaviors. Waste Manage 121:153–163

Delaying the Ripening of Banana Fruit and Increased Storage Shelf-Life Using Hydrophobic Deep Eutectic Oil (Menthol–Thymol)-In-Water Nanoemulsion Coating

M. J. Gidado, Ahmad Anas Nagoor Gunny, R. Sri Alamelu Sankari, Subash C. B. Gopinath, Chalermchai Wongs-Aree, Hafiza Shukor, and Roshita Ibrahim

Abstract Hydrophobic deep eutectic oil (menthol-thymol)-in-water nanoemulsion was developed to preserve the quality of banana fruit and extend their storage shelf life. Storage preservation of bananas presents several challenges due to their high respiration rate, ethylene production, and susceptibility to various physiological and

M. J. Gidado · A. A. N. Gunny (✉) · S. C. B. Gopinath · H. Shukor · R. Ibrahim
Faculty of Chemical Engineering & Technology, Universiti Malaysia Perlis, Kompleks Pusat Pengajian Jejawi 3, Kawasan Perindustrian Jejawi, 02600, 08544 Arau, Perlis, Malaysia
e-mail: ahmadanas@unimap.edu.my

M. J. Gidado
e-mail: Gidadomjay@gmail.com

S. C. B. Gopinath
e-mail: subash@unimap.edu.my

H. Shukor
e-mail: hafizashukor@unimap.edu.my

R. Ibrahim
e-mail: roshita@unimap.edu.my

A. A. N. Gunny · H. Shukor · R. Ibrahim
Center of Excellence for Biomass Utilisation, Universiti Malaysia Perlis, Kompleks Pusat, Pengajian Jejawi 3, Kawasan Perindustrian Jejawi, 02600 Arau, Perlis, Malaysia

R. Sri Alamelu Sankari
Faculty of Food and Technology, Karpagam Academy of Higher Education, Pollachi Main Road, Eachanari Post, Coimbatore 641021, India

S. C. B. Gopinath
Institute of Nano Electronic Engineering, & Micro System Technology, CoEUniversiti Malaysia Perlis, 01000 Kangar, Perlis, Malaysia

C. Wongs-Aree
School of Bioresources and Technology, King Monkut's University of Technology Thonburi, Bangkok, Thailand

H. L. Ong et al. (eds.), *Proceedings of the 3rd International Conference on Biomass Utilization and Sustainable Energy; ICoBiomasSE 2023; 4–5 September; Kuala Lumpur, Malaysia*, Green Energy and Technology,
https://doi.org/10.1007/978-981-99-9164-8_2

biochemical changes. The storage shelf life of bananas is relatively short compared to other fruits due to the combination of rapid ripening and sensitivity to ethylene and temperature. In this study, the effectiveness of HyDEN treatment was assessed on changes in banana fruit's physiological parameters such as firmness, weight loss, total soluble solids, titratable acidity, and colour for 14 days storage time [25 °C ± 1 °C, 67% relative humidity (RH)]. HyDEN treatment preserved the physicochemical characteristics of banana fruit and was effective in delaying the ripening process. The storage shelf life of banana fruit treated with HyDEN increased for 14 days compared to control that ripened and physically damaged after 8 days of storage. This study provided a new delivery system for applying HyDEN as an edible coating to fruit after harvest preservation.

Keywords Postharvest · Edible coating · Banana · Shelf life · Ripening

1 Introduction

Bananas are widely consumed fruit with over 100 million tons of bananas are harvested and marketed worldwide [1]. Bananas have a relatively short storage life compared to other fruits. They produce high amount of ethylene that accelerates their ripening process. The short storage life of banana fruit is challenging worldwide most especially in a place where refrigerated storage systems are not available [2]. Several storage systems such as control atmosphere storage, low temperature storage, surface coating, and use of I-MCP were deployed to delay ripening process in fruit [3–6]. However, the use of these storage systems was limited in most cases due to high capital cost, improper ripening, and chilling injury that can affect the quality of bananas during storage [1].

Bananas have a climacteric pattern of ripening that undergoes a swift and sudden change in texture, colour, and flavour. This rapid ripening affects the storage quality, shelf life, and marketability. Bananas have high water content and are highly susceptible to water loss during storage which can significantly impact their quality, appearance, and shelf life [7]. Water loss from bananas occurs primarily through transpiration, a natural process in which water evaporates from the fruit's surface. Bananas have a high respiration rate which can significantly impact their storage life and quality during storage. High respiration rates lead to the conversion of starches into sugars resulting in a softer texture which can result in a loss of firmness and turgidity. Ethylene promotes the breakdown of cell wall components such as pectin which contributes to the softening of the bananas. As bananas produce more ethylene, their texture can change from firm to soft and mushy. Colour is one of the most important

Postharvest Technology Innovation Centre, Ministry of Higher Education, Science, Research and Innovation, Bangkok 10400, Thailand

C. Wongs-Aree
e-mail: chalermchai.won@kmutt.ac.th

characteristics of banana ripening and consumers acceptance. Mature green bananas are harvested and distributed to retailers before they start to ripen. Bananas lost their marketability to consumers within 1–3 days after turning yellow [5]. Therefore, a search for treatment methods is in demand to increase the shelf life of bananas to reduce losses within the supply chain.

Several postharvest control methods such as films and coatings made from hydrophilicity materials exhibit poor water vapour barriers. The uses of various packaging materials are limited due to their safety, poor water barrier property, and may contain harmful substances that can contaminate the food [8]. However, edible coating materials such as lipids, polysaccharides, and proteins have been used to conserve fruit quality and extend their shelf life at the storage time [9]. Unfortunately, these coating materials have setbacks in their water vapour barrier, undesirable flavours, sensitivity to environmental conditions, and possible contamination with other compounds that limit their uses [10, 11]. The use of 1-MCP has been reported to be effective in delaying the ethylene production in bananas [12]. However, it has been reported that banana treated with 1-MCP can affect the colour after ripening and may inhibit the aroma and production of total volatile compounds in banana fruit [12, 13].

Currently, most of the effective commercial treatments and products used to extend the shelf life of banana significantly affect their peel colour, flavour, and aroma profile [1]. Therefore, hydrophobic deep eutectic solvents nanoemulsions (HyDEN) were introduced in this research as potential edible coating treatments due to their high hydrophobic, antioxidant, and antimicrobial properties in order to preserve the quality of banana fruit and extend their storage shelf life. In this study, HyDEN based on menthol and thymol was prepared by ultrasonic treatment of hydrophobic deep eutectic solvent (HDES) with Tween 80 as a surfactant using standardised solutions. HyDEN as a novel treatment was used to preserve the quality of banana fruit and extend their storage shelf life to minimise banana postharvest losses. The aim of this research was to develop a sustainable and less expensive treatment with an excellent water vapour barrier in banana fruit postharvest preservation without affecting their physicochemical characteristics. No research was performed from the literature using HDES nanoemulsion as an edible coating in postharvest technology of fruits. This study provided a new delivery system for applying HyDEN as an edible coating in fruits postharvest preservation.

2 Materials and Methods

2.1 Materials

Menthol (purity > 99%), thymol (purity > 99%), and Tween 80 were purchased from Take It Global Sdn. Bhd. Malaysia. Mature green banana fruit of the same index with average weights (25 ± 18 g) and free from ethylene, disease, or injury were purchased

from Local Farmer Gerai Buah Buahan Segar (GBBS) Jejawi, Perlis, Malaysia, which comply with the Federal Agricultural Marketing Authority, Malaysia (FAMA) standards.

2.2 Design of Experiment

Experiments were carried out using a completely randomised design (CRD), with three replications of each treatment (one fruit per replication). A total of 42 banana fruit (the same maturity index) were assembled and divided into two groups. From the groups, a single banana fruit was used as one replicate, and three replications for each treatment were used for experiment on each day. Two treatments: HyDEN (HDES of menthol–thymol (1:1) and Tween 80 as surfactant using standardised solution) and control (treated with distilled water) were used for the experiments. HyDEN treatment was prepared using method described by Zeng et al. [14]. First, HDES was prepared by the combination of menthol and thymol at 1:1 molar concentration. Solid components of menthol and thymol were weighed and mixed in mini glass bottles, and then, the solid mixture was magnetically stirred and heated at 60^0C until clear homogeneous liquid is formed. Then, HyDEN was prepared by mixing HDES (menthol–thymol 1:1) and Tween 80 (as surfactant) in an aqueous solution using standardised solutions: 10 wt% HDES, 5 wt% Tween 80, and 85 wt% aqueous phase (10 mM sodium phosphate, pH 7.0). The solution was subjected into a digital ultrasonic cleaner (Model: PS-40 A, China) with a 240 W heating power processor for 15 min to stabilise and reduce the droplets size of the HyDEN emulsion. Dipping method was used in application of HyDEN coating on banana fruit. Fruit samples were dipped inside the coating solution for a few seconds, and then, the samples were lifted out and allowed any excess to drip off. After that, the fruit samples were allowed to dry at room temperature [25 °C ± 1.06 °C, 67% relative humidity (RH)] for 14 days. Selected quality parameters (weight loss, firmness, total soluble solids, titratable acidity, and colour) were assessed every 2 day intervals starting from first day.

2.3 Physicochemical Analysis of Banana Fruit

Weight Loss and Firmness. Weight loss of banana fruit was determined by measuring the weight of each banana fruit before and during the storage at 2-day intervals for 14 days and expressed as a percentage of the initial weight. The firmness of banana samples was measured using a texture analyser (TA XT Plus, Stable Micro Systems, Godalming, Surrey, UK). Three banana fruit from both treatment groups were taken randomly and analysed before and during the storage at 2-day intervals

for 14 days. The probe used was 2 mm (P/2), and the continuous speed was 3 mm/s. The measurements were taken at different areas of the banana fruit.

Total Soluble Solids (TSS) and Titratable Acidity (TA). TSS concentration of the pulp was determined using a mini refractometer (S/No.AB210420, 6678FF6AA4, Japan). Banana pulp was squeezed, a drop of the pulp was placed on the refractometer at the sample stage, and the readings were displayed as %Brix. 10 g of banana pulp were homogenised with 20 mL of distilled water and transferred into a conical flask. 2–3 drops of phenolphthalein were added into the solution and titrated with sodium hydroxide until the endpoint was reached. Total acidity was expressed as the percentage of % malic acid.

Colour Measurement. The peel colour of banana fruit was determined using a geometry reflectance meter (Lovibond, 403,035: TR 520 4 mm & 8 mm Sphere). The peel colour was measured in three regions: equatorial, stem, and centre of the fruit. The colour reading was displayed in the form of L^*, a^*, and b^*. The colour index of the samples was calculated using the following Eq. (1):

$$\text{Colour index (CI)} = \frac{1000 \times \text{a*}}{\text{L* x b*}} \tag{1}$$

2.4 Statistical Analysis

Minitab 17 Statistical Software was used to perform statistical analysis. ANOVA was used to determine the difference between the banana fruit samples, and P values < 5 were considered to be significant.

3 Results and Discussion

3.1 Physicochemical Analysis of Banana Fruit

Weight Loss. Weight loss is often associated with a decrease in the moisture content of the fruit. This can lead to changes in texture, loss in turgidity, and firmness. As bananas lose water, they become softer and more prone to bruising, physical damage, and unappealing appearance. As shown in Fig. 1a, weight loss started from second day of storage with a difference between coated fruit (1.5%) and control (2.8%). The percentage weight loss reduced from both the coated and uncoated banana fruit throughout the storage. The control fruit showed significant increase in weight loss of 5.3% at day 8 which was two times higher than the coated fruit with 2.5% after day 8, and control fruit was no longer assessed further due to physical damage and

loss of marketability. Coated fruit observed a slower ripening process and reduced weight loss and hence were further assessed until 14 days. Coated fruit displayed very low percentage of weight loss indicating that HyDEN coating was effective in reducing the permeability of the fruit's surface to water vapour due to the coating hydrophobic property. Hydrophobic coatings repel water and create a barrier that limit the movement of water vapour through the fruit skin by reducing the rate of moisture loss and slow ripening process. By reducing the moisture loss and delaying the ripening process, HyDEN coating can contribute to an extended shelf life of bananas allowing them to remain in a more desirable condition for a longer period. Thakur et al. [1] observed similar result in weight loss on banana fruits using starch edible surface coating. Similar reduction in weight loss was observed on banana fruit using shellac (60%) and gelatin (40%) composite coating [16].

Firmness. Firmness loss in bananas is often accompanied by a softer texture and is an inevitable process during ripening. As bananas ripen, they undergo physiological changes as a result of dehydration and breakdown of cell wall components such as pectin, hemicellulose, and cellulose that leads to a loss of cell structure and firmness [6]. As presented in Fig. 1b, the firmness in both coated and control banana fruit reduced continuously during the ripening at the storage time. At day 0, the firmness of coated banana fruit was 52.8 and control fruit at 53.2 which indicates the firm nature and compact tissue of the banana fruit before the storage. The coated fruit showed highest firmness retention compared to control fruit during the storage time and the control fruit were damaged after day 8 and can no longer assess further due to over ripening that shortened their shelf life. The significant reduction of firmness in control fruit is often associated with an increase in respiration rate, ethylene production, and dehydration during the ripening process. The coated fruit displayed highest firmness retention of 38.1% at day 2, 31.3% at day 4, 28.1% at day 6, 24.2% at day 8, and 17.5% at day 10. There was no significant difference of firmness in coated fruit beyond 10 days of storage. This indicates that HyDEN coating is effective in retaining the physiological changes in banana fruit and often associated with the rate of dehydration and ripening during the storage. This finding is supported by Thakur et al. [1] obtained similar results on banana fruit coated with starch edible surface coating.

Total Soluble Solids (TSS). The change in TSS content in banana fruit is an important indicator of the fruit's ripening process and overall quality. When bananas are harvested, the TSS content is relatively low, and the starch content is higher than the sugar content. As bananas ripen, the starches are converted into sugars, and this enzymatic conversion results in an increase in TSS content. As shown in Fig. 1c, the TSS content increased in both coated and control fruit during the storage time. The significance difference in TSS content between the coated and control fruit was between 0 and 8 days. The maximum TSS content in coated fruit was 17.6% Bx on day 14, while the maximum in control fruit was 17.4% Bx at day 8. The control fruit undergoes fast ripening and increased in ethylene production that accelerated the enzymatic conversion of starches to sugars that contributed to greater accumulation of TSS in control fruit. While in coated fruit, low accumulation of TSS was observed

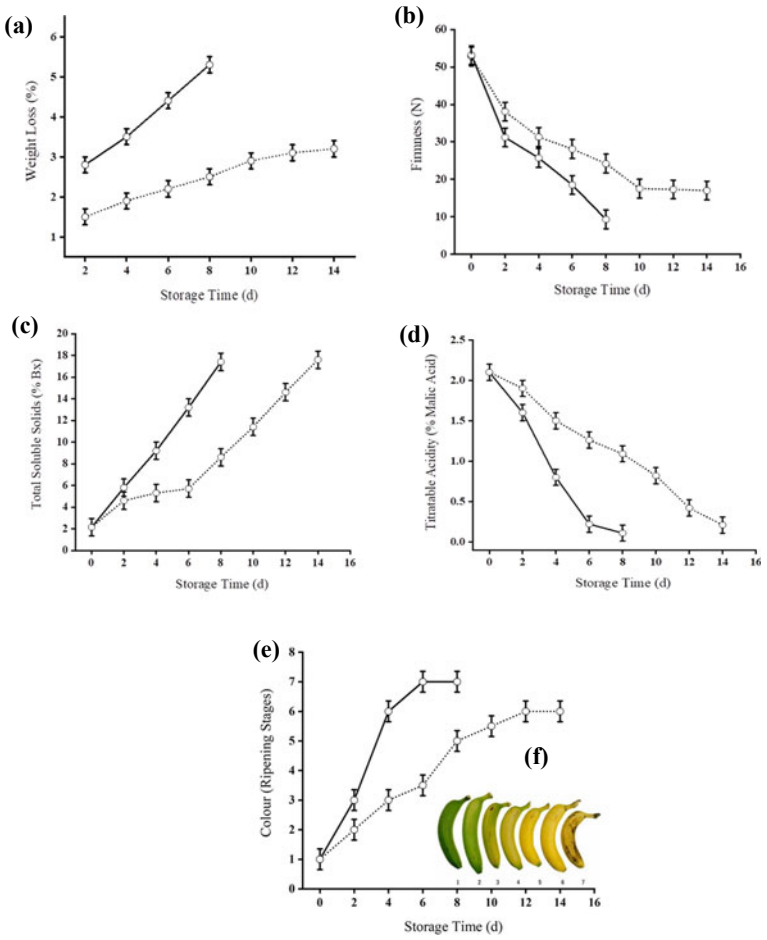

Fig. 1 Effect of coated and uncoated banana fruit on the contents of **a** weight loss, **b** firmness, **c** total soluble solids, **d** titratable acidity, and **e** colour. The values are presented as mean ± SE with error bars at $p < 0.05$. The dotted and solid lines in the graphs represent HyDEN treatment and control samples, respectively. **f** Standard ripening chart for banana fruit [15]

due to the coating antioxidant property that slowed down the rate of ethylene production and respiration which are the key factors in the ripening process. By delaying the onset of ripening, the conversion of starches into sugar was also delayed leading to more controlled change in TSS content. Similar results were obtained in slower increase in TSS on banana fruit coated with biopolymer coating [16, 17].

Titratable Acidity (TA). Titratable acidity refers to the concentration of acidic compounds primarily organic acids present in a fruit. The level of titratable acidity is an important quality parameter that contributes to the overall taste and flavour balance of banana fruit. As bananas ripen, there is often a decrease in titratable acidity. This

is because many of the organic acids present in the fruit are metabolised or broken down as the fruit undergoes ripening. Malic acid is one of the major organic acids in banana fruit [18]. As presented in Fig. 1d, the percentage of TA in both coated and control fruit reduced across the storage time. Control fruit showed significant decrease in TA compared to coated fruit. The percentage of TA in both coated and control fruit on day 0 was recorded at 2.1% and started declining after day 2 until day 8 at 0.11% for control fruit and day 14 at 0.21% for coated fruit. Control banana fruit was not assessed further after day 8 due to fast ripening that accelerated the metabolic conversion of organic acids into sugars that lead to decay and physical damage. Coated banana fruit observed slow decrease in TA across the storage time due to slow ripening process and low ethylene production that may accelerate the sugar accumulation. Similar results were obtained on banana fruit using starch edible coating [1].

Colour. The change in colour intensity from green to yellow in banana fruit is a natural and expected process that is closely associated with the fruit ripening and biochemical changes. The colour change in banana is primarily due to the breakdown of pigments and the synthesis of new compounds as the fruit undergoes physiological and biochemical transformations. In this study, the skin colour of both coated and uncoated banana fruit transformed from green to yellow, and the change in colour intensity was influenced by the rate of ripening and ethylene production in the fruit. Coated banana fruit observed gradual change in colour across the storage time due to slow ripening process that significantly affected the enzymatic activity responsible for chlorophyll degradation. This indicates that HyDEN coating is effective in delaying the ripening and biochemical changes in banana fruit due to its high antioxidant property. As seen in Fig. 1e, the standard chart of visual colour change and ripening stages in banana fruit was used to study the change in colour intensity across the storage time [19].

4 Conclusion

Banana fruit undergoes a series of complex physiological and biochemical changes that transform its taste, texture, colour, and overall quality during the ripening at the storage. These changes are influenced by various factors such as moisture loss, enzymatic activities, ethylene production, and metabolic processes. Bananas have a climacteric pattern of ripening that undergoes a swift and sudden change in texture, colour, and flavour. This rapid ripening affects the storage quality, shelf life, and marketability. In this study, hydrophobic deep eutectic oil (menthol–thymol)-in-water nanoemulsion coating was developed as a novel coating to slow down the ripening of banana and prolong their storage shelf life by preserving their physiological characteristics during storage. Banana fruit coated with HyDEN retained weight loss, reduced firmness, slowed down the ripening process, and reduced the enzymatic activities responsible for biochemical conversion of starches and change

in colour intensity after 14 days storage time. These results showed that HyDEN coating effectively preserved the physiological characteristics and delays the ripening in banana fruit at ambient storage conditions. HyDEN coating is cheaper and effective in preserving banana fruit without any undesirable changes in fruit quality that make it to be more superior to other treatment methods such as 1-MCP and refrigerated storage systems. This novel treatment has the capacity to significantly reduce the banana postharvest losses most especially in the developing countries.

Acknowledgements Authors thank the Ministry of Education for funding the research under the Fundamental Research Grant Scheme FRGS/1/2023/STG02/UNIMAP/02/4. Authors thank the Research Management Centre, Universiti Malaysia Perlis for their financial contribution to this research.

References

1. Thakur R, Pristijono P, Bowyer M, Singh SP, Scarlett CJ, Stathopoulos CE, Vuong QV (2018) A starch edible surface coating delays banana fruit ripening. LWT—Food Sci Technol. https://doi.org/10.1016/j.lwt.2018.10.055
2. Peroni-Okita FHG, Cardoso MB, Agopian RGD, Louro RP, Nascimento JRO, Purgatto E, Cordenunsi BR (2013) The cold storage of green bananas affects the starch degradation during ripening at higher temperature. Carbohyd Polym 96:137–147. https://doi.org/10.1016/j.carbpol.2013.03.050
3. Jiang Y, Joyce DC, Macnish AJ (1999) Extension of the shelf life of banana fruit by 1-methylcyclopropene in combination with polyethylene bags. Postharvest Biol Technol 16:187–193. https://doi.org/10.1016/S0925-5214(99)00009-5
4. Pongprasert N, Srilaong V (2014) A novel technique using 1-MCP microbubbles for delaying postharvest ripening of banana fruit. Postharvest Biol Technol 95:42–45. https://doi.org/10.1016/j.postharvbio.2014.04.003
5. Ahmed ZFR, Palta JP (2016) Postharvest dip treatment with a natural lysophospholipid plus soy lecithin extended the shelf life of banana fruit. Postharvest Biol Technol 113:58–65. https://doi.org/10.1016/j.postharvbio.2015.10.016
6. Deng Z, Jung J, Simonsen J, Zhao Y (2017) Cellulose nanomaterials emulsion coatings for controlling physiological activity, modifying surface morphology, and enhancing storability of postharvest bananas (Musa acuminate). Food Chem 232:359–368. https://doi.org/10.1016/j.foodchem.2017.04.028
7. Embuscado ME, Huber KC (2009) Edible films and coatings for food applications. Springer. https://doi.org/10.1007/978-0-387-92824-1
8. Amirullah NA, Samsudin MH, Norrahim MNF, Ilyas RA, Nurazzi NM, Jenol MA, Hawanis HSN, Gunny AAN (2022) Regulation for food packaging materials. Phys Sci Rev. https://doi.org/10.1515/psr-2022-0033
9. Jose A, Pareek S, Radhakrishnan EK (2020) Advances in edible coating materials. In: Advances in agri-food biotechnology. Springer, Singapore. https://doi.org/10.1007/978-981-15-2874-3_15
10. Iniguez-Moreno M, Ragazzo-Sanchez JA, Calderon-Santoyo M (2021) An extensive review of natural polymers used as coatings for postharvest shelf-life extension: trends and Challenges. Polymers 13:3271. https://doi.org/10.3390/polym13193271
11. Silva A, Chamorro V, Palou L, Miguel A, Maria BPG (2011) Antimicrobial edible films and coatings for fresh and minimally processed fruits and vegetables: a review. Crit Rev Food Sci Nutr 51:872–900. https://doi.org/10.1080/10408398.2010.485705

12. Zhu X, Shen L, Fu D, Si Z, Wu B, Chen W, Li X (2015) Effects of the combination treatment of 1-MCP and ethylene on the ripening of harvested banana fruit. Postharvest Biol Technol 107:23–32. https://doi.org/10.1016/j.postharvbio.2015.04.010
13. Harris DR, Seberry JA, Wills RBH, Spohr LJ (2000) Effect of fruit maturity on efficiency of 1-methylcyclopropene to delay the ripening of bananas. Postharvest Biol Technol 20:303–308. https://doi.org/10.1016/S0925-5214(00)00150-2
14. Zeng C, Liu Y, Ding Z, Xia H, Guo S (2021) Physicochemical properties and antibacterial activity of hydrophobic deep eutectic solvent-in-water nanoemulsion. J Mol Liq 338:116950. https://doi.org/10.1016/j.molliq.2021.116950
15. Wills R, Golding J (2016) Postharvest: an introduction to the physiology and handling of fruit and vegetables, 6th edn. UNSW Press. ISBN 13:9781786391483
16. Soradech S, Nunthanid J, Limmatvapirat S, Luangtana-anan M (2017) Utilization of shellac and gelatin composite film for coating to extend the shelf life of banana. Food Control 73:1310–1317. https://doi.org/10.1016/j.foodcont.2016.10.059
17. Al-Qurashi AD, Awad MA, Mohamed SA, Elsayed MI (2017) Postharvest chitosan, trans-resveratrol and glycine betaine dipping affect quality, antioxidant compounds, free radical scavenging capacity and enzymes activities of 'Sukkari' bananas during shelf life. Sci Hortic 219:173–181. https://doi.org/10.1016/j.scienta.2017.02.046
18. Turner DW, Fortescue JA (2012) Bananas (Musa spp.) crop post-harvest: science and technology. Wiley-Blackwell, pp 24–42. https://doi.org/10.1002/971444354652.ch3
19. Nannyonga S, Bakalis S, Andrews J, Mugampoza E, Gkatzionis K (2016) Mathematical modelling of color, texture kinetics and sensory attributes characterisation of ripening bananas for waste critical point determination. J Food Eng 190:205–210. https://doi.org/10.1016/j.jfoodeng.2016.06.006

Biomass Conversion Technology for Bioenergy

Characterization and Bioenergy Potential Analysis of Queen Pineapple Waste for Solid Fuel Production via Torrefaction in Camarines Norte, Bicol Region

Gelyn L. Bongabong, Isaac Jerome C. Dela Cruz, and Bryan G. Alamani

Abstract Global demand for biofuels is predicted to upsurge in the future to unravel the scarcity of fossil fuel source and its environmental impact. Lignocellulosic biomass (LCB), derived from agricultural and industrial wastes, is a promising feedstock for biofuel production because of its advantages such as wide availability, economical, and no issue of food competition. Thus, it provides a significant contribution to meeting the biofuel demand. This study investigates the characteristics and the bioenergy potential of queen pineapple waste (QPW) from the processing facility in Camarines Norte, Philippines, for biofuel production. The physical and chemical characteristics of untreated QPW were determined via proximate and ultimate analyses, respectively. The structure of the QPW (lignin, hemicellulose, and cellulose) was determined through compositional analysis. QP waste was pre-dried at 150 °C for 5 h to lower its moisture content down to $\leq$ 10%. The pre-dried samples were ground and sifted to reduce the particle size. The torrefaction method was employed to produce biochar in a minimal oxidative atmospheric condition using a muffle furnace with temperature levels and reaction time as variables. Lastly, the bioenergy potential test of raw, pre-dried, and torrefied samples was carried out using a bomb calorimeter. The results revealed that the torrefaction technique increased the higher heating value of raw-dry biomass by 13–68%, depending on the reaction severity.

G. L. Bongabong (✉)
Energy Engineering Program, College of Engineering, University of the Philippines Diliman, 1101 Quezon City, Metro Manila, Philippines
e-mail: glbongabong@up.edu.ph; gelynbongabong@cnsc.edu.ph

Department of Agricultural and Biosystems Engineering, College of Agricultural and Natural Resources, Camarines Norte State College, 4600 Camarines Norte, Philippines

I. J. C. Dela Cruz · B. G. Alamani
Department of Chemical Engineering, College of Engineering, University of the Philippines Diliman, 1101 Quezon City, Philippines
e-mail: icdelacruz1@up.edu.ph

B. G. Alamani
e-mail: bgalamani@up.edu.ph

H. L. Ong et al. (eds.), *Proceedings of the 3rd International Conference on Biomass Utilization and Sustainable Energy; ICoBiomasSE 2023; 4–5 September; Kuala Lumpur, Malaysia*, Green Energy and Technology,
https://doi.org/10.1007/978-981-99-9164-8_3

Keywords Lignocelullosic biomass · Bioenergy · Biofuel · Torrefaction · And Heating Value

1 Introduction

In recent years, the energy sector has been expanding its focus on lignocellulosic biomass (LCB) materials for biofuel production because of the alarming global impact of fossil-based fuels and their dwindling sources. Fossil fuels (coal, gas, and oil) have significantly contributed to global carbon dioxide emissions of approximately 36.8 billion tonnes in 2022 of which the Philippines was responsible for around 124.26 million tonnes of CO_2 emissions [1]. Conversely, the combustion of biofuels emits much lower net greenhouse gas (GHG) than petroleum-based fuels. As established in recent works, biofuels are classified into four generations [2]. First-generation biofuels namely biodiesel (fats and vegetable oil) and bioethanol (starch and sugars). These are commonly extracted from edible crops which risen the issue on food competition. On the other hand, the second-generation biofuels are made from a diverse range of feedstock, and non-edible materials refer to as lignocellulosic biomass [3]. Both third- and fourth-generation biofuels utilize algae as feedstock but employ different methodology. The third-gen technologies process algal biomass to produce biofuels, while fourth-generation employ algal-to-biofuel conversion through metabolic method from oxygenated photosynthetic microbes [4].

Lignocellulosic biomass is a promising economical and most abundant feedstock for biofuel production. Potential sources of LCB are agricultural residues, food scraps, municipal solid waste, and industrial waste [5, 6]. The physical properties of LCB include proximity (i.e., moisture, volatile combustible matter, ash, and fixed carbon), grindability, particle size, hygroscopicity, density, and energy content. Whereas the chemical properties is called ultimate characteristics such as elemental components (i.e., C, H, O, N, and S) [7]. The main structural components of LCB materials are lignin (10–25%), cellulose (35–50%), and hemicellulose (20–35%). The residual fraction of LCB is called extractives such as proteins, oils, and ash [8, 9]. A significant source of lignocellulosic biomass is agricultural waste or residue which is considered to be carbon neutral. It is cheap, readily available, renewable, and relatively unexplored [10]. Agricultural residues such corn cob and stover, rice hull and straw, bagasse, cotton stalk, soybean hull, coconut husk, etc., can be utilized for biofuel (solid, liquid, or gas) production [11]. These large amount of wastes generated from the agricultural sector have significant effects on humans, animals, and environment. Therefore, converting agricultural waste into biofuels is one of the sustainable waste management strategies to ensure sanitation, resource recovery, and maintenance of carbon balance in the environment. Recent studies have shown several processes and biotechnologies for biomass conversion into biofuel through biological, physical, chemical, and thermal conversion methods. Biochemical or thermochemical techniques remain to be the sustainable methods for converting agricultural wastes into biofuels [12–14].

Torrefaction, also known as mild pyrolysis or high-temperature drying, is a promising thermochemical conversion technique to produce biofuel (solid fuel or biochar) from LCB. The goal of torrefaction is to improve the fuel properties of biomass such that it can be co-combusted with coal or utilized as a standalone fuel by being pelletized and stored with little to no microbial degradation [15]. By gradually heating biomass at relatively low temperatures (200–300 °C) in a low-oxygen atmosphere, devolatilization and degradation reactions take place, leading to torrefaction. Under such conditions, significant chemical and physical changes produce a more homogenous, hydrophobic, and energy-dense solid fuel source. Torrefaction therefore provides benefits for production of solid fuel with low moisture content, hydrophobicity, greater reactive capacity, better homogeneity, and higher calorific value [16].

Queen pineapple (*Ananas comosus* L. Merr), also known as the "Formosa"—the sweetest variety, is mainly grown in Camarines Norte. According to the Office of the Provincial Agriculturists, the QP production volume was approximately 5694.21 metric tons, with an area planted of 1551.02 hectares in 2020. The production is dominated by the municipality of Labo, with the largest volume and an area planted of 3147.40 metric tons and 751.17 hectares, respectively [17]. Queen pineapple waste (QPW), like wastes of other pineapple varieties, is classified as LCB and therefore has potential for solid fuel production. Waste from other pineapple variety contains 14.22% dry matter, 81.90% organic matter, 8.10% ash, 0.56% nitrogen, 3.50% crude protein, 3.49% crude fat, and 4481.2 cal/g gross energy [18]. As the demand for pineapple fruit and processed products grows, so does the amount of pineapple produced from the processing stage, resulting in a significant amount of waste. During pineapple processing, about > 80% of the pineapple parts, including the crown, peel, and core, end up as waste [19]. Approximately 30% of freshly harvested queen pineapple in Camarines Norte is processed to make value-added goods including concentrated juice ('Queench' juice) and dried pineapple rings. Labo Progressive Multi-Purpose Cooperative (LPMPC) is among the province's main producers of queen pineapple juice and dried fruits. Based on the estimation of LPMPC, nearly 60–80% of the fruit during processing results in the peel, core, crown, etc., which are not utilized and are generally discharged as wastes [20].

Valorization of biomass, a novel value-adding technique used to resolve waste management challenges, involves different waste-to-energy conversion processes [21, 22]. However, previous studies used starch-rich and higher-value lignocellulosic materials under fermentation and anaerobic digestion processes. Recent studies on lignocellulosic biomass pyrolysis only include biochar yield assessment. There are very limited studies on mild pyrolysis or torrefaction of low-value LCBs (e.g., pineapple waste in the country). This study investigates the potential of low-value lignocellulosic materials such as queen pineapple waste for biofuel production through torrefaction. The solid biofuel (biochar) produced from these processes could be used in many applications in the QP processing facility, such as gasifier stoves and biomass furnaces for drying.

2 Materials and Methods

2.1 Feedstock Preparation and Characterization

Queen pineapple waste (QPW), including peels, cores, leaves, and crowns (generally discarded parts), was used as biomass feedstock and was collected from the QP processing center in Labo, Camarines Norte known as LPMPC. Five hundred (500) grams of raw biomass were weighed and oven-dried at 150 °C for 5 h to lower the moisture content down to $\leq$ 10%, which is the desirable MC_{db} for torrefaction [23]. The moisture analyzer (MA) at CNSC-CANR Labo Campus was used in moisture content determination of the dried samples. Five grams of dried samples were placed in the MA with standard settings (105 °C). The moisture analysis was done in triplicate. The oven-dried samples were then ground and sifted using a food processor and sieve no. 20 (850 μm particle size), respectively.

Compositional Analysis. The compositional or structural analysis was performed at the Biotech Lab in UPLB, Laguna. The standards used for moisture free extractives and acid soluble/insoluble lignin determination were NREL/TP-510–42,619, 2008 [24] and NREL/TP-510–42,618, 2012 [25], respectively. The TAPPI 203 standard was employed to determine the α-cellulose and hemicellulose of the dried sample (extractive and moisture free basis) [26]. Holocellulose is the summation of α-cellulose and hemicellulose biomass components.

Physicochemical Analysis. Physicochemical characteristics of the raw biomass were determined by a proximate analysis and an ultimate analysis conducted at the Standard Testing Division of PH-DOST-ITDI following ASTM D5373 [27] and ASTM D4239 [28] standards, respectively. The physical components of the untreated QPW (moisture, volatile combustible matter, ash, and fixed carbon content) were determined through proximate analysis. The mean proximate composition was determined by plotting the values of the VM, ash, and fixed carbon via R-studio 4.2.0 version. Ultimate (elemental) analysis was performed to determine the predied sample's chemical constituents (carbon, hydrogen, oxygen, nitrogen, and sulfur) [29]. These ultimate characteristics (C, H, and O) were used to estimate the calorific value of the QPW, expressed as its gross or higher heating value given by Eq. (1) below [30]:

$$\mathrm{HHV}\left(\frac{\mathrm{MJ}}{\mathrm{kg}}\right) = \left[\begin{array}{l}(33.5 \times \%\mathrm{C}) + \sim (142.3 \times \%\mathrm{H}) \\ -(15.4 \times \%\mathrm{O}) - \sim (14.5 \times \%\mathrm{N})\end{array}\right] \times 10^{-2} \quad (1)$$

where HHV represents the higher heating value, and C, H, O, N are the carbon, hydrogen, oxygen, and nitrogen, respectively, expressed in MJ/kg.

2.2 Torrefaction Experiment

The laboratory scale torrefaction with minimal oxidative atmospheric medium [31] was done using a muffle furnace with different temperature levels from light to severe (light T = 200 °C, medium T = 250 °C, and severe T = 300 °C) for varying reaction time of 15 and 45 min. Five (5) grams of pre-dried samples were placed in a 30-mL crucible then in a muffle furnace with set reaction temperature and time. The torrefied samples (TS) were labeled as TS-temperature-reaction time (e.g., TS-200–15). This experimental procedure was done in triplicate. Mass yield for torrefied solid was calculated using Eq. (2):

$$M_y(\%) = \frac{M_{\mathrm{TS}}}{M_{\mathrm{RD}}} \times 100 \tag{2}$$

where M_y is the mass yield in percent, M_{TS} and is the torrefied solid mass in grams, and M_{RD} is the mass of raw-dry biomass in grams.

2.3 Bioenergy Potential Test

Bioenergy potential test (BPT) was performed to determine the energy content (calorific/heating value) of the torrefied/biochar samples (approximately 0.5 g) using a bomb calorimeter (PARR 6200) at the CEAL, Chemical Engineering Department, UP Diliman. Energy yield was calculated given Eq. (3):

$$E_y(\%) = \frac{M_{\mathrm{TS}} \times \mathrm{HHV}_{\mathrm{TS}}}{\mathrm{M}_{\mathrm{RD}} \times \mathrm{HHV}_{\mathrm{RD}}} \times 100 \tag{3}$$

where E_y is the energy yield in percent, and $\mathrm{HHV}_{\mathrm{TS}}$ and $\mathrm{HHV}_{\mathrm{RD}}$ are the heating values of torrefied solid and raw-dry QPW in MJ/kg, respectively. Whereas the energy density/densification ratio, *EDR,* was calculated using Eq. (4):

$$\mathrm{EDR} = \frac{\mathrm{HHV}_{\mathrm{TS}}}{\mathrm{HHV}_{\mathrm{RD}}} \tag{4}$$

3 Results and Discussion

3.1 QP Waste as LCB and Its Characteristics

Generally, the structure of LCB is suitable for solid biofuel (biochar) production via thermochemical conversion methods: carbonization; torrefaction; pyrolysis; gasification; and direct combustion. Among the LCB's components, the cellulose has the simplest and most ordered structure. The temperature level influenced the cellulose primary and secondary conversion process [32]. Hemicellulose's transformation mechanism is quite similar to that of cellulose; however, due to the five-carbon sugar structure, Furan derivatives tend to be the major products. With its high degree of activity, the conversion process can occur rapidly at low temperatures [33]. Lignin is the most complex and has the highest thermal stability among the three LCB components. Its conversion process is influenced by various factors such as reaction temperature and time, lignin source (type of feedstock), and pretreatment method [34].

A compositional analysis was done to determine the major lignocellulosic components of queen pineapple waste which is depicted in Table 1. QPW is composed of 29.87% extractives, 7.04% acid insoluble lignin, 4.55% acid soluble lignin, 18.6% α-cellulose, and 19.34% hemicellulose. The total lignin content of 11.59% was calculated as the summation of the acid soluble lignin and acid insoluble lignin. Most of the agricultural residues have a large fraction of cellulose which is a significant structural characteristic of a biomass for advanced biofuel production as shown in Fig. 1 [35–41]. In this study, it can be seen that the lignin content of QP waste was relatively low, and the cellulose and hemicellulose contents were considerably high, implicating that QPW structure is comparable with that of the other agricultural wastes.

The physicochemical characteristics of QP waste are presented in Table 2. The moisture content (MC), volatile combustible matter (VCM or VM), ash content, and fixed carbon (FC, by difference) of raw QP waste (as received untreated) were measured through proximate analysis. The MC_{db} is the quantity of water per unit mass of the dry QPW sample. The conventional oven drying method for moisture determination to constant weight at 105 °C was employed for less than 4 h to prevent loss of VM due to decomposition of the biomass sample [42]. Whereas the VM is

Table 1 Lignocellulosic components of queen pineapple waste

Composition	wt. %
Extractives	29.87
Acid insoluble lignin, AIL	7.04
Acid soluble lignin, ASL	4.55
Holocellulose	37.93
α-cellulose	18.60
Hemicellulose	19.34

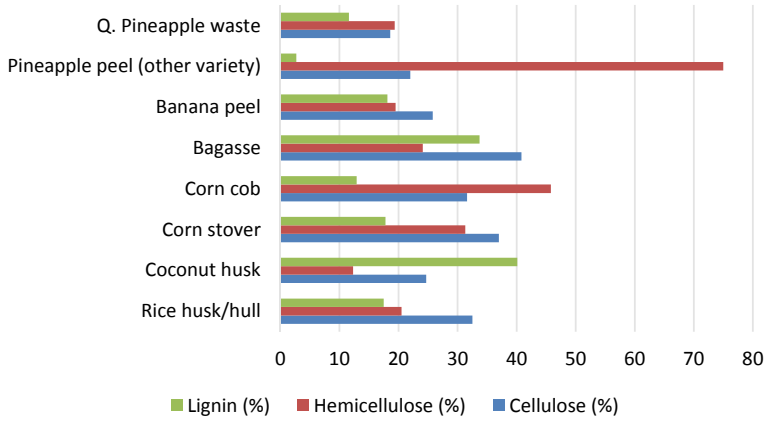

Fig. 1 Comparison of lignocellulosic composition of the different agricultural waste

Table 2 Physicochemical characteristics of QPW

Physicochemical components	wt. %
Proximate Analysis	
Moisture	84.3
Volatile combustible matter	83.4
Total solid [a]	15.7
Ash	3.2
Fixed carbon [b]	13.4
Ultimate Analysis	
Carbon	40.6
Hydrogen	6.12
Nitrogen	1.19
Oxygen [c]	52.09
Sulfur	0.204

[a] Difference of total wt.% and moisture content (untreated), [b] Difference of total wt.%, ash, and volatile matter, [c] by difference (100% less sum of %C, %H, and %N)

the weight percentage of the biomass that was released after being heated for 7 min at 925 °C. During this heating phase, the sample burns off solid material as char while decomposing into gases [43]. QPW has a high moisture content of 84.3% and volatile matter of 83.4%. The total solid of 15.7% was determined by subtracting the MC (%) of the samples to 100%.

The ash yield (dry basis) was quantified at 600 °C for QPW. It is one of the most investigated characteristics of biomass, yet it is also one of the least understood. The complexity of this parameter is the source of challenges because ash is formed during the combustion of biomass from natural and technogenic, organic, inorganic,

and fluid components [44]. For this study, the ash yield of 3.2% is considerably low which is a good characteristic of a solid fuel for combustion. Fixed carbon of 13.4% was calculated by subtracting the wt% of VM and ash to the total wt%. of the biomass sample. The mean proximate composition is depicted in Fig. 2, a triangular plot showing the mean value of VM, FC, and ash as the three key physical characteristics of a solid fuel. The proximity of QP waste was closely related to the proximities of the different solid fuel types as proposed by Vassilev et al. [44], indicating that QPW is a good alternative fuel source.

The chemical (elemental) composition of the dried QP waste with 10% MC was determined by the ultimate analysis as presented in Table 2. The oxygen content of about 52.09% was estimated by the difference of %C, %H, and %N from 100%. QPW has a considerable amount of carbon (40.6%) with small fractions of hydrogen and nitrogen contents of 6.12% and 1.19%, respectively. Only 0.204% sulfur was present in the QPW biomass sample. The C, H, O, and N elements were emphasized as these determine the fuel efficacy by estimating the gross heating value or HHV of the sample (presented in the next page) using Eq. (1).

The C, H, and O elements from the ultimate analysis were used to plot the H:C (0.15) and O:C (1.28) atomic ratios of dried QP waste in Van Krevelen diagram as illustrated in Fig. 3. This relationship shows that the lower the H:C and O:C molar ratios, the higher is the energy content of the material. Moreover, the material with a

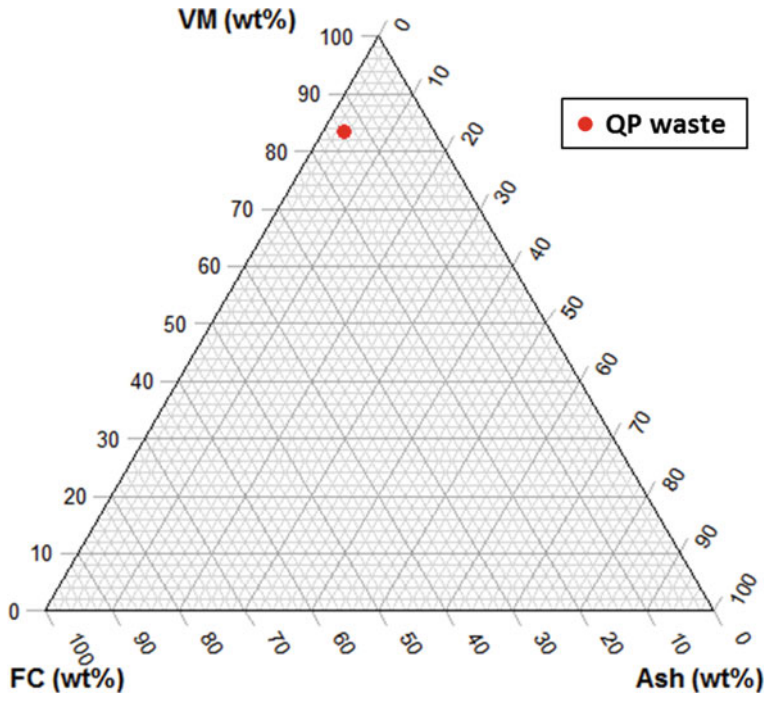

Fig. 2 Mean proximate composition of untreated QP waste

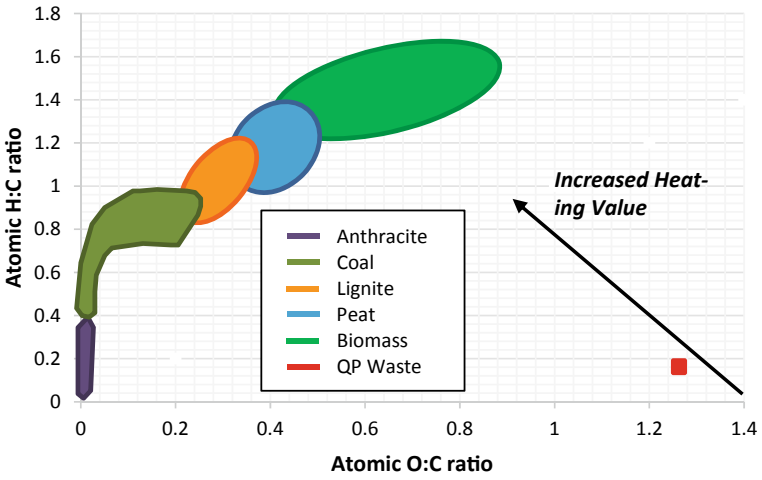

Fig. 3 Van Krevelen graph with H:C and O:C ratios of dried QPW, adapted and redrawn from [45]

low O:C ratio has a greater energy density and HHV. This is due to higher chemical energy of C–C bonds than C-O bonds [34]. These findings revealed that the H/C ratio of dried QPW was relatively low and comparable with that of the anthracite, coal, lignite, and peat. However, the O/C ratio of dried QPW was high as compared to the other solid fuel types since the sample was simply pre-dried at 150 °C for 5 h, indicating that it has higher MC than torrefied sample. In general, a fuel that has minimal H/C and O/C ratios is an ideal fuel since it creates less water vapor, has minimal energy loss, and emits small amount of smoke during incineration [45, 46]. These findings suggest that the QPW is a noble alternative biomass feedstock for an environmentally friendly biofuel production based on its ultimate properties.

3.2 Bioenergy Potential Analysis

Calorific Value of QPW. The energy potential of a biomass sample can be expressed as its calorific value (CV), or heating value (HV), released when completely burnt in air. CV/HV is commonly expressed in terms of energy content per unit mass of solid (cal/g, KJ/kg, or MJ/kg), which can be stated in two ways: gross CV or higher heating value (HHV) and net CV or lower heating value (LHV) [43]. For this study, the CVs of the TS were obtained using the PARR 6200 bomb calorimeter, expressed as gross heating value or higher heating value as presented in Table 3. The HHV's in cal/g of the raw-dry and torrefied samples were converted to MJ/kg using engineering toolbox [47]. Only the HHV of the raw-dry QPW sample was estimated given the C, H, N, and O values substituting to Eq. (1). The estimated HHV (14.12 MJ/kg) of the dried QPW, at 10% moisture content, is comparable

Table 3 Heating value of raw-dry sample and torrefied samples at different torrefaction conditions

Samples	Estimated HHV (MJ/kg)	CV/HHV (cal/g)	Converted HHV (MJ/kg)
Raw-Dry	14.12	3562.82	14.92
TS-200–15	–	4121.26	17.25
TS-200–45	–	4401.76	18.43
TS-250–15	–	4035.73	16.90
TS-250–45	–	5669.77	23.74
TS-300–15	–	5614.91	23.51
TS-300–45	–	6012.12	25.17

to the HHV (3562.82 cal/g or 14.92 MJ/kg) determined by the bomb calorimetric test (BCT). As observed, the torrefaction severity (temperature and reaction period) has significantly influenced the HHV of the biochar product. The most severe torrefaction condition (300 °C Temp and 45 min RT) led to highest HHV of the biochar. As the reaction temperature and time increased, the energy content of the solid fuel increased. Moreover, the torrefaction process employed (i.e., minimal oxidative atmospheric medium, without purging of oxygen with nitrogen gas) improved the heating value of the material, which proved that torrefaction of QPW has high potential for solid biofuel production with no additional operation cost.

Calculation of mass yield, energy yield, and energy density ratio. In this study, calculation of the mass yields (*My*), energy yields (*Ey*), and energy densification/density ratios (*EDR*) of the raw-dry sample and torrefied solids for bioenergy potential analysis were substantially performed after the torrefaction experiment and bomb calorimetric test. These were significant parameters in measuring the torrefaction severity. *My* is the weight percentage of the solid recovered after the torrefaction phase as expressed in Eq. (2). *Ey* is the percentage of energy gained after torrefaction as shown in Eq. (3). *EDR* is the ratio of the HHV of the TS-to-HHV of the pre-dried QPW as in Eq. (4).

Depicted in Fig. 4 are the trends of the *My*, *Ey*, and *EDR* of pre-dried and torrefied samples under different torrefaction conditions. As the torrefaction temperature increased from 200 °C to 300 °C with prolonged reaction time from 15 to 45 min, the *My* reduced from maximum of 96% (T = 200 °C; RT = 15 min) to minimum of 59% (T = 300 °C; RT = 45 min). These findings could be related to moisture loss under severe torrefaction conditions and thermal degradation of certain low-molecular-weight volatile compounds in the biomass such as cellulose and hemicellulose. The trend of the energy yields of the torrefied samples followed the trend of the mass yields, but these were higher than *My*, particularly the energy yields of the torrefied solids at 200 °C. The maximum and minimum energy yields of 114% and 99%, respectively, were observed during the torrefaction at 300 °C for 15 min and 45 min, respectively. As seen in the graph (Fig. 4), the highest EDR of 1.69 was observed at the most severe torrefaction condition (T = 300 °C; RT = 45 min), which implicates that the torrefaction severity improved the HHV of QPW-derived biochar.

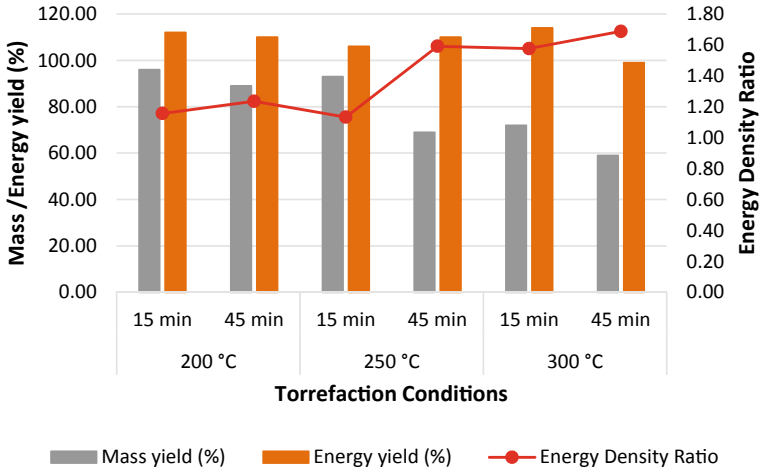

Fig. 4 Computed mass yields, energy yields, and energy density ratio under different torrefaction conditions

4 Conclusions

This study investigates the bioenergy potential of queen pineapple waste in Camarines Norte through characterization and torrefaction. The structural (lignocellulose), physical (proximate), and chemical (ultimate) characteristics of the biomass suggest that QPW is a good alternative source for second-generation biofuel production. It was observed that the torrefaction in a minimal oxidative medium improved the heating value of the biochar which entails no additional cost for an inert atmospheric condition. It was also observed that the torrefaction temperature and reaction time influenced the major production parameters: heating value; mass yield; energy yield; and energy density ratio. The HHV and EDR of the torrefied solid were maximum at the most severe torrefaction condition (i.e., at 300 °C Temp for 45 min RT). On the other hand, the *My* and *Ey* were significantly affected by this severity. Thus, the results revealed that there is a high bioenergy potential from queen pineapple waste for solid fuel production, which can further be used for heating application and electricity generation. Moreover, these findings recommend for future investigation of the optimization of the torrefaction process which includes biomass pretreatment to determine which method would maximize the yields. Nevertheless, this work provides baseline data for future study focusing on the exploitation of alternative sources by utilization of waste materials as biomass feedstock for bioenergy generation while resolving the issues on waste management in agro-industrial sector and food competition in biofuel industry.

Acknowledgements The authors acknowledge the Dept. of Science and Technology (DOST) of the Philippines, for providing research grants through the Engineering Research and Development for Technology (ERDT) scholarship program that supports the implementation of this research

project. The authors also acknowledge the Dept. of Chem. Eng'g-Bioprocess Engineering Laboratory (DChE-BPEL) of UP Diliman, and the Camarines Norte State College—College of Agriculture and Natural Resources for providing support in the form of laboratory supplies and equipment utilization during the conduct of this work.

References

1. IEA Homepage. https://www.iea.org/reports/co2-emissions-in-2022. Last Accessed 08 Feb 2023
2. Sikarwar VS, Zhao M, Fennell PS, Shah N, Anthony EJ (2017) Progress in biofuel production from gasification. Progress in Energy and Combust Sci 61:189–248
3. Lee RA, Lavoie JM (2013) From first- to third-generation biofuels: challenges of producing a commodity from a biomass of increasing complexity. Animal Front 3(2):6–11
4. Lü J, Sheahan C, Fu P (2011) Metabolic engineering of algae for fourth generation biofuels production. Energy and Environ Sci 4(7):2451–2466
5. Merklein K, Fong SS, Deng Y (2016) Biomass utilization. In: Biotechnology for biofuel production and optimization, pp 291–324
6. Gutiérrez-Antonio C, Romero-Izquierdo AG, Gómez-Castro FI, Hernández S (2021) Production processes from lignocellulosic feedstock. In: Production processes of renewable aviation fuel, Elsevier, pp 129–169
7. da Silva SB, Arantes MDC, de Andrade JKB, Andrade CR, Carneiro AdeCO, Protásio TdeP (2020) Influence of physical and chemical compositions on the properties and energy use of lignocellulosic biomass pellets in Brazil. Renew Energy 147:1870–1879
8. Limayem A, Ricke SC (2012) Lignocellulosic biomass for bioethanol production: current perspectives, potential issues and future prospects. Progress in Energy and Combust Sci 38(4):449–467
9. Saravanan A, Yaashikaa PR, Kumar PS, Thamarai P, Deivayanai VC, Rangasamy G (2023) A comprehensive review on techno-economic analysis of biomass valorization and conversional technologies of lignocellulosic residues. Indus Crops and Prod 200:116822
10. Zhang J, Rentizelas A, Zhang X, Li J (2022) Sustainable production of lignocellulosic bioethanol towards zero waste biorefinery. Sustain Energy Technol Assessments 53:102627
11. Jayakumar M, Gindaba GT, Gebeyehu KB, Periyasamy S, Jabesa A, Baskar G, BeJohn BI, Pugazhendhi A (2023) Bioethanol production from agricultural residues as lignocellulosic biomass feedstock's waste valorization approach: a comprehensive review. Sci Total Environ 879:163158
12. Mujtaba M, Fraceto LF, Fazeli M, Mukherjee S, Savassa SM, de Medeiros GA, Pereira AES, Mancini SD, Lipponen J, Vilaplana F (2023) Lignocellulosic biomass from agricultural waste to the circular economy: a review with focus on biofuels, biocomposites and bioplastics. J Cleaner Prod 402:136815
13. Pasinszki T, Krebsz M (2021) Agricultural waste valorization for sustainable biofuel production. INC
14. Awogbemi O, Von Kallon DV (2022) Valorization of agricultural wastes for biofuel applications. Heliyon 8(10):e11117
15. Gent S, Twedt M, Gerometta C, Almberg E (2017) Introduction to thermochemical conversion processes. In: Theoretical and applied aspects of biomass torrefaction, pp 1–16
16. Queiroz LS, da Costa CE, de Souza LK (2023) Biomass conversion by torrefaction process. Elsevier Ltd.
17. Office of the Provincial Agriculturist (2020) Queen pineapple production in camarines norte. Department of Agriculture RFO V

18. Adrizal Heryandi Y, Amizar R, Mahata ME (2017) Evaluation of pineapple [Ananas comosus (L.) Merr] waste fermented using different local microorganism solutions as poultry feed. Pakistan J Nutrit 16(2):84–89
19. Aili Hamzah AF, Hamzah MH, Che Man H, Jamali NS, Siajam SI, Ismail MH (2021) Recent updates on the conversion of pineapple waste (Ananas comosus) to value-added products. Future Perspect Challenges Agronomy 1(1):1–27
20. Labo Progressive Multi-Purpose Cooperative: Processing of Queen Pineapple Fruit (2022) Labo, Camarines Norte
21. Gemar G, Soler IP, Sánchez-Teba EM (2021) Waste management: valorisation is the way. Foods 10(10)
22. Capanoglu E, Nemli E, Tomas-Barberan F (2022) Novel approaches in the valorization of agricultural wastes and their applications. J Agricul Food Chem 70(23):6787–6804
23. Thengane SK, Kung KS, Gomez-Barea A, Ghoniem AF (2022) Advances in biomass torrefaction: Parameters, models, reactors, applications, deployment, and market. Progress in Energy and Combust Sci 93:101040
24. Sluiter A, Ruiz R, Scarlata C, Sluiter J, Templeton D (2008) Determination of extractives in biomass: laboratory analytical procedure (LAP). National Renewable Energy Laboratory Technical Report, NREL/TP-510–42619, pp 1–9
25. Sluiter A Ruiz R, Scarlata C, Sluiter J, Templeton D (2012) Determination of structural carbohydrates and lignin in biomass: laboratory analytical procedure (LAP). National Renewable Energy Laboratory Technical Report, NREL/TP-510–42618, pp 1–9
26. TAPPI 203 (2022) Alpha-, beta- and gamma-cellulose in pulp. TAPPI Standards, Test Method T 203 cm-22
27. ASTM D5373–21 (2021) Standard test methods for determination of carbon, hydrogen and nitrogen in analysis samples of coal and carbon in analysis samples of coal and coke. ASTM Standards, ASTM D5373
28. ASTM D4239–18e1 (2018) Standard test method for sulfur in the analysis sample of coal and coke using high-temperature tube furnace combustion. ASTM Standards, ASTM D4239
29. Singh YD, Mahanta P, Bora U (2017) Comprehensive characterization of lignocellulosic biomass through proximate, ultimate and compositional analysis for bioenergy production. Renew Energy 103:490–500
30. Demirbas A (2016) Calculation of higher heating values of fatty acids. Energy Sour Part A: Recovery, Utilization and Environ Effects 38(18):2693–2697
31. Riaz S, Oluwoye I, Al-Abdeli YM (2022) Oxidative torrefaction of densified woody biomass: Performance, combustion kinetics and thermodynamics. Renew Energy 199:908–918
32. Qin F, Zhang C, Zeng G, Huang D, Tan X, Duan A (2022) Lignocellulosic biomass carbonization for biochar production and characterization of biochar reactivity. Renew Sustain Energy Rev 157:112056
33. Liu C, Wang H, Karim AM, Sun J, Wang Y (2014) Catalytic fast pyrolysis of lignocellulosic biomass. Chem Soc Rev 43(22):7594–7623
34. Collard FX, Blin J (2014) A review on pyrolysis of biomass constituents: mechanisms and composition of the products obtained from the conversion of cellulose, hemicelluloses and lignin. Renew Sustain Energy Rev 38:594–608
35. Abbas A, Ansumali S (2010) Global potential of rice husk as a renewable feedstock for ethanol biofuel production. Bioenergy Res 3(4):328–334. https://doi.org/10.1007/s12155-010-9088-0
36. Cabral MMS, Abud AKdeS, Silva CEdeF, Almeida RMRG (2016) Bioethanol production from coconut husk fiber. Ciência Rural 46(10):1872–1877
37. Saha BC, Yoshida T, Cotta MA, Sonomoto K (2013) Hydrothermal pretreatment and enzymatic saccharification of corn stover for efficient ethanol production. Indus Crops and Prod 44:367–372
38. Selvakumar P, Adane AA, Zelalem T, Hunegnaw BM, Karthik V, Kavitha S, Jayakumar M, Karmegam N, Govarthanan M, Kim W (2022) Optimization of binary acids pretreatment of corncob biomass for enhanced recovery of cellulose to produce bioethanol. Fuel 321:124060

39. Philippini RR, Martiniano SE, Chandel AK, de Carvalho W, da Silva SS (2019) Pretreatment of sugarcane bagasse from cane hybrids: effects on chemical composition and 2G sugars recovery. Waste Biomass Valorization 10:1561–1570
40. Palacios S, Ruiz HA, Ramos-Gonzalez R, Martínez J, Segura E, Aguilar M, … Ilyina A (2017) Comparison of physicochemical pretreatments of banana peels for bioethanol production. Food Sci Biotechnol 26:993–1001
41. Choonut A, Saejong M, Sangkharak K (2014) The production of ethanol and hydrogen from pineapple peel by Saccharomyces cerevisiae and Enterobacter aerogenes. Energy Proc 52:242–249
42. García R, Pizarro C, Lavín AG, Bueno JL (2013) Biomass proximate analysis using thermogravimetry. Bioresour Technol 139:1–4
43. McKendry P (2002) Energy production from biomass (part 1): overview of biomass. Bioresour Technol 83(1):37–46
44. Vassilev SV, Baxter D, Andersen LK, Vassileva CG (2010) An overview of the chemical composition of biomass. Fuel 89(5):913–933
45. Raza SS, Janajreh I, Ahmed R, AlKatheeri A (2015) Numerical simulation of char particle gasification. J Energy Power Eng 9(8):679–686
46. Liu Z, Quek A, Hoekman SK, Balasubramanian R (2013) Production of solid biochar fuel from waste biomass by hydrothermal carbonization. Fuel 103:943–949
47. The Engineering ToolBox Homepage (2023). https://www.engineeringtoolbox.com/energy-conversion-factors-d_1606.html. Last Accessed 21 June 2023

Thermogravimetric Analysis and Kinetics Study of MSW and Wood Pellet Co-Gasification Using Flue Gas as a Medium

Panawit Sitthichirachat, Chootrakul Siripaiboon, Prysathryd Sarabhorn, Chanoknunt Khaobang, Haryo Wibowo, and Chinnathan Areeprasert

Abstract This study investigates thermogravimetric analysis (TGA) and kinetics study (KS) of the co-gasification of municipal solid waste (MSW) and wood pellets (WP) using flue gas as the gasification medium. Our novel decoupling gasifier design facilitates a gasification process utilizing flue gas as the reaction medium. Therefore, studying the thermal decomposition characteristics of MSW and WP during this unique gasification process is crucial. Thermal decomposition exhibited two stages based on mass loss and the rate of mass loss. The maximum mass loss rate occurred during the first stage for all samples at temperatures of 286.5/318 (two peaks), 286.5, and 293.4 ℃ for 0WP100MSW, 10WP90MSW, and 20WP80MSW, respectively. The addition of WP to MSW significantly increased the DTG maximum value and eliminated the second decomposition peak of MSW. KS illustrates that the E value decreased from 19.70 to 3.35 kJ/mol under air and 64.05 to 2.12 kJ/mol under flue gas with the addition of 20%wt wood pellets.

Keywords Gasification · Municipal solid waste · Wood pellet · Thermogravimetric analysis · Kinetics study

P. Sitthichirachat · C. Siripaiboon · P. Sarabhorn · C. Khaobang · H. Wibowo · C. Areeprasert (✉)
Department of Mechanical Engineering, Faculty of Engineering, Kasetsart University, 50 Ngam Wong Wan Road, Lat Yao, Chatuchak, Bangkok 10900, Thailand
e-mail: fengcta@ku.ac.th

P. Sitthichirachat
e-mail: panawit.s@ku.th

C. Khaobang
e-mail: chanoknunt.kh@ku.th

C. Siripaiboon
Department of Industrial Technology, School of Science and Technology, Sukhothai Thammathirat Open University, Nonthaburi 11120, Thailand

H. L. Ong et al. (eds.), *Proceedings of the 3rd International Conference on Biomass Utilization and Sustainable Energy; ICoBiomasSE 2023; 4–5 September; Kuala Lumpur, Malaysia*, Green Energy and Technology,
https://doi.org/10.1007/978-981-99-9164-8_4

1 Introduction

The thermochemical conversion process has been recognized as an effective method of transforming solid waste into valuable products [1]. It is typically done by heating the feedstock in an oxygen-deprived environment to convert it into gas, ash, and tar. It is a very enticing approach to be considered for the treatment of waste such as municipal solid waste (MSW) [2]. A multitude of research has been done in this field to improve the conversion efficiency of these processes. Phatavee et al. [3] investigated the fuel properties and thermal decomposition of hydrothermally treated MSW (HTT-MSW) during combustion, utilizing a hydrothermal process combined with thermogravimetric analysis (TGA). Their findings revealed that HTT-MSW exhibited a higher activation energy than raw MSW, suggesting enhanced combustion characteristics. Areeprasert et al. [4] explored the impact of hydrothermal treatment (HTT) on the co-firing of paper sludge (PS) with coal, analyzing thermal degradation through TGA. The study demonstrated that the treated paper sludge significantly reduced emissions by approximately 26–31%, indicating its potential as an environmentally friendly fuel source. Ayyadurai et al. [5] conducted an experiment on gasifying heterogeneous feedstock with MSW using a downdraft gasifier. Their work improved efficiency in hot gas generation and a remarkable reduction in thermal energy consumption, highlighting the significance of optimizing gasification processes for enhanced performance.

Gasification is particularly effective in producing valuable synthesis gas or syngas from MSW. Syngas holds great potential for various applications, including heat generation, power generation, and chemical synthesis [6]. One of the novel designs in gasification technology is decoupling gasification, which is often defined as gasification process that physically separates combustion and gasification zones [7, 8]. The heating of the gasification zone is done by using flue gas from the separated combustion chamber. Therefore, the reacting medium of the decoupling gasification is the flue gas. This is expected to improve the performance of the gasifier.

Another approach in improving gasification performance, especially for MSW, is by mixing it with biomass such as wood pellets (WP). Since this is also a novel approach, there is a significant gap and a lack of comprehensive research on the kinetics of MSW and WP/MSW gasification. This paper addresses this research gap by conducting a comprehensive thermogravimetric analysis (TGA) on both MSW and WP/MSW during the gasification process. Flue gas was employed as the medium to study kinetic parameters and gained insights into the thermal degradation of MSW and WP/MSW during gasification. By investigating the gasification behavior of MSW and WP/MSW, this study aims to contribute to understanding thermal decomposition of the feedstock under flue gas, a medium representing the fixed-bed decoupling gasification process. The obtained kinetic parameters and thermal degradation characteristics are expected to provide more insight into the body of knowledge on this new gasifier configuration.

2 Methodology

2.1 Raw Materials

In this study, MSW was collected and sorted to remove harmful and non-combustible elements. The sorted MSW samples were categorized into four types: Type 1 (paper and cardboard), Type 2 (mixed plastics), Type 3 (rubber and textile), and Type 4 (wood waste), representing 45%, 33%, 12.7%, and 9.3% of the total MSW mass, respectively. WP produced from sawdust was selected as the co-firing material to enhance the decoupling gasification efficiency of the sorted MSW. MSW and WP were then mixed in three mass ratios: 0%WP: 100%MSW, 10%WP: 90%MSW, and 20%WP: 80%MSW. To facilitate the experiments, MSW samples were cut into tiny pieces approximately 0.5–1 cm in length, while WP was pulverized to achieve a finer particle size. These materials and methods were implemented to evaluate the impact of WP on the gasification process of MSW, ensuring the accuracy and consistency of the experimental analysis.

2.2 Material Characterizations

The heating value was assessed by the bomb calorific technique (bomb calorimeter, LECO-AC-500, USA) under the ASTM D5865 standard. The proximate analysis was executed by a Thermogravimetric analyzer (LECO-TGA801, USA) under the ASTM D7582 standard. Meanwhile, an element analyzer (CHNS/O Analyzer, LECO-Model 628 series, USA) carried out the ultimate analysis under ASTM D3176 standard. The material properties are given in Table 1.

2.3 Kinetic Study

A thermogravimetric analyzer (LECO-TGA801, USA) was utilized to examine the thermal behavior of the prepared materials during gasification. The TGA analysis was conducted at a temperature of 900 °C with a heating rate of 10 °C/min under flue gas conditions. In this study, mass loss (TG) and the rate of mass loss (DTG) were determined, and the kinetics study was performed based on non-isothermal thermogravimetric data. The kinetics parameters, including the apparent activation energy (E) and the pre-exponential factor (A), were obtained through data calculations from the TGA analysis. The thermal decomposition of MSW and WP/MSW during the combustion process could be represented by the following Eq. (1):

$$d\alpha/dT = k(T)f(\alpha) \tag{1}$$

Table 1 Properties of the feedstock

Item	100%MSW	10%WP + 90%MSW	20%WP + 80%MSW
Proximate analysis			
Moisture	5.2%	3.2%	3.2%
Volatile matter	73.7%	77.1%	78.7%
Fixed carbon	14%	13.1%	13.9%
Ash	7.1%	6.6%	4.2%
Ultimate analysis			
Carbon	42.3	45.8	42.5
Hydrogen	6.2	7.4	5.8
Nitrogen	0.2	0.3	0.5
Oxygen[a]	44.2	39.9	47
Heating value			
HHV (MJ/kg)	18.6	20.1	22.2

[a] Oxygen is calculated by difference (100–(C + H + N + Ash))

Where $k(T)$ is representing temperature-dependent rate constant, α is the extent of the conversion of the sample at t time, $f(\alpha)$ is a function of conversion, as defined by Eq. (2).

$$\alpha = (m_i - m_t)/(m_i - m_f) \tag{2}$$

where m_i is the initial mass of the sample, m_t is the mass of the sample at time t, and m_f is the final mass of the sample. The temperature-dependent rate constant $k(T)$ is conventionally expressed through the Arrhenius equation, Eq. (3).

$$k(T) = A\exp(-E/RT) \tag{3}$$

where A is the pre-exponential factor, E is the apparent activation energy, and R is the universal gas constant (8.314 $J/\text{mol}\cdot K$). A mathematical term for constant heating rate β is described as Eq. (4).

$$\beta = dT/dt \tag{4}$$

Then, (3) and (4) were substituted to (1), methodized in general form, and integrated: which gives Eq. (5).

$$g(\alpha) = \int_0^{\alpha} d\alpha/f(\alpha) = (A/\beta)\int_{T_0}^{T} \exp(-E/RT)dT = (AE/\beta R)p(x) \tag{5}$$

where $g(\alpha)$ is defined as an integral of the reaction model [3]. To estimate the kinetic parameters, the temperature integral term in (5) was calculated by the coats Redfern approximation [9], applying natural logarithms and rearranging yields Eq. (6).

$$\ln(g(\alpha)/T^2) = \ln(AR/\beta E)(1 - 2RT/E) - (E/RT) \tag{6}$$

Since (RT/E) << 1, the term (1-2RT/E) was approximately equal to unity (1-2RT/E $\approx$ 1). Thus,

$$\ln(g(\alpha)/T^2) = \ln(AR/\beta E) - (E/R)(1/T) \tag{7}$$

Plotting, $(\ln g(\alpha)/T^2)$ versus $(1/T)$ will carry out a straight line that slope equals to −E/R. Therefore, the E and the A can be acquired by slope and the intercept, respectively.

3 Results and Discussion

3.1 Thermogravimetric Analysis

The TG profiles of all samples using air as the medium (Fig. 1a) exhibited similar characteristics. Decomposition of a significant portion of the samples occurred during the initial combustion period (260–310 °C) and a subsequent period (400–800 °C). When flue gas was used as the medium (Fig. 1c), slight differences in the decomposition characteristics were observed. The first-period temperature range decreased slightly to (220–300 °C), particularly noticeable in the F-20%WP80%MSW sample. This could have been due to combustible elements. The second period of decomposition occurred between 340 and 790 °C.

From the TG profile data, it can be deduced that transitioning the medium from air to flue gas resulted in a subtle modification of the combustion mechanism. This observation aligns with prior research by Kwon et al., which demonstrated that CO_2 improved gasification performance by enhancing volatile chemicals cracking during thermal degradation [10]. This is supported by the lower E value of gasification under flue gas compared to air in the temperature range of 350–460 °C.

Additionally, the introduction of WP accelerated the combustion rate of MSW compared to raw MSW. Previous studies have explored various catalysts to improve biomass gasification efficiency [11, 12]. Research by Soomro et al. demonstrated that adding dolomite, alkaline metal, nickel, or olivine reduced tar generation and increased gas production [13]. However, these catalysts often have a short active life, high cost, and potential regeneration difficulty. Based on our findings, the use

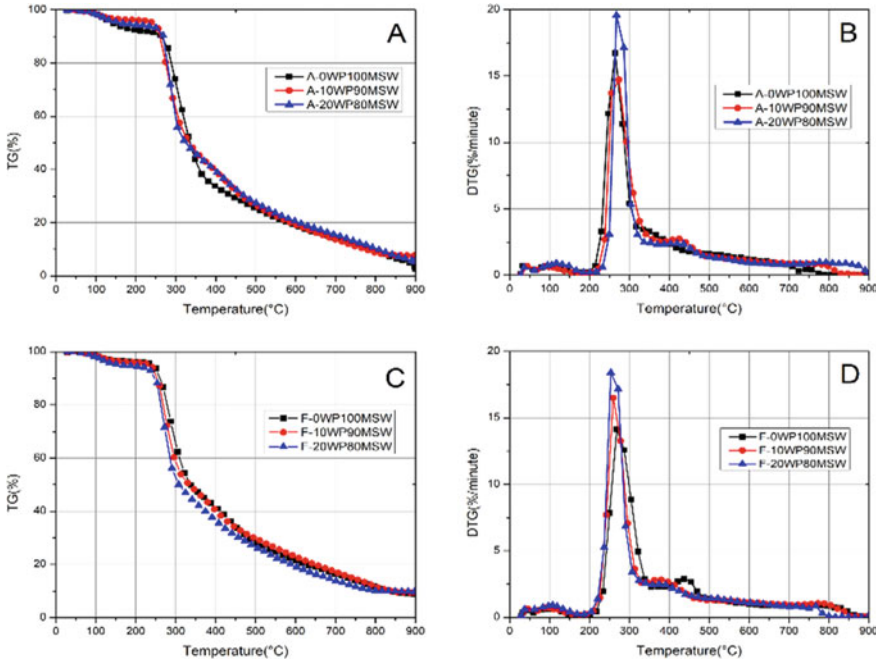

Fig. 1 Mass loss (TG) and the rate of mass loss (DTG) profiles. **(a)** TG of air as medium. **(b)** DTG of air as medium. **(c)** TG of flue gas as a medium. **(d)** DTG of flue gas as a medium

of WP as additives showed promise for improving the performance of the gasification process. However, its potential drawback of increased tar generation during gasification should also be considered.

The TGA profiles of mixed samples using air as the medium (see Fig. 1b) displayed a major peak (220–350 ºC) and a minor peak (400–480 ºC). In pure MSW, the major peak occurred within the range of (210–320 °C), with the minor peak appearing the range of (330–480 ºC). The DTG rates for the major peak were 20%, 16%, and 14.1% for A-20WP80MSW, A-0WP100MSW, and A-10WP90MSW, respectively. The corresponding DTG values for the minor peak were 2.2%, 2.5%, and 3%, respectively.

When flue gas was used as the medium (Fig. 1d), the DTG results showed changes. The temperature profiles exhibited a similar trend, with the major peak appearing within the range of (220–340 ºC), and the minor peak from (330–450 ºC). The DTG rates for the major peak decreased to 18.1% for F-20WP80MSW, increased to 16% for F-10WP90MSW, and decreased to 14% for F-0WP100MSW. The DTG values for the minor peak were 2%, 2.5%, and 2.6% for the respective samples.

3.2 Kinetic Parameters

Kinetic parameters were determined using the first-order reaction model, and the obtained parameter results are summarized in Table 2. The temperature range for the analysis was divided into two major decomposition regions, and corresponding minor decomposition peaks were identified. In the first temperature range, where air was used as the medium, temperatures between 210 and 380 ºC were selected. For A-0WP100MSW, the activation energy (E) was found to be 32.85 kJ/mol. However, with the addition of WP, the E values for the WP/MSW samples, namely A-10WP90MSW and A-20WP80MSW, slightly increased to 48.74 and 58.19 kJ/mol, respectively.

When considering the first temperature range with flue gas as the medium, the selected temperature range was between 245 and 355 ºC. For F-0WP100MSW, the E was notably higher at 60.34 kJ/mol compared to A-0WP100MSW. With the addition of WP, the E values for the mixed samples, F-10WP90MSW and F-20WP80MSW, increased slightly to 63.11 and 64.25 kJ/mol, respectively. In the second temperature range, which was within the range of 350 to 460 ºC, the E value for F-0WP100MSW was noticeably lower than A-0WP100MSW. It indicated that at lower temperatures, the addition of WP caused the conversion of feedstock to require more energy than feedstock without WP. However, at higher temperatures (range 2), adding WP lowered the E value significantly. It indicated that WP caused the system to require less energy to achieve conversion. This relation between E and energy required for conversion was reported by Sarabhorn et al. [7]. This result suggests that MSW started to combust at a lower temperature than WP, which could be the result of components with relatively low ignition temperature such as plastics in MSW [14, 15]. However, when the system reached higher temperatures at range 2 and WP also spontaneously

Table 2 Kinetic parameters results

First order (O1)	Range 1 (R1)				Range 2 (R2)			
Sample	T(ºC)	R^2	E (kJ/mol)	A (min^{-1})	T(ºC)	R^2	E (kJ/mol)	A (min^{-1})
A-0%WP100MSW	220–320	0.9518	58.12	8.29E + 05	390–510	0.977	19.70	2.52E-01
A-10%WP90%MSW	210–385	0.9309	48.74	4.82E + 04	395–485	0.978	4.61	8.02E-01
A-20%WP80%MSW	220–340	0.9380	58.19	5.04E + 05	440–490	0.986	3.35	4.56E-01
F-0%WP100MSW	245–355	0.968	60.34	1.23E + 06	350–400	0.981	6.30	1.22E + 00
F-10%WP90%MSW	210–300	0.9512	63.11	1.87E + 06	360–460	0.994	4.51	7.64E-01
F-20%WP80%MSW	220–310	0.9689	64.05	6.67E + 05	355–400	0.998	2.12	2.69E-01

combusted, its presence appeared to assist in the spontaneousness of the feedstock conversion, as shown by the much lower E values. This provides evidence that the addition of WP could assist in converting MSW, but only at temperatures above 350 ºC. This was probably caused by the degradation of cellulose, which is the main component of WP, at around this temperature [16].

The same phenomenon was also observed when the atmosphere was replaced with flue gas, supporting the notion that it was driven more by the feedstock than the atmosphere. However, it was noticed that the E values under flue gas were higher than under air. This was in line with the finding in the study by Sarabhorn et al. [7], which explained that WP required more energy to thermally decompose under flue gas than under air. This might be because of the higher oxygen content in the air compared to flue gas, promoting more degradation of cellulose through oxidation [17].

4 Conclusion

In summary, the TGA analysis identified two stages of thermal decomposition based on the mass loss and rate of mass loss. The maximum mass loss occurred at approximately 286/318 ºC (two peaks) under air and 260/310 ºC (two peaks) under flue gas conditions. When WP was mixed with MSW, the DTG value significantly improved, indicating a higher rate of mass loss during thermal decomposition. Moreover, the second decomposition peak of MSW was eliminated; therefore enhancing the mixed material's thermal behavior.

Kinetic study found that adding WP to MSW increased the E value at a temperature lower than 350 ºC. When the temperature reaches over 350 ºC, the WP combusted, enhancing the combustion and conversion rate as indicated by the E value decrease from 19.70 to 3.35 kJ/mol under air and 64.05 to 2.12 kJ/mol under flue gas with the addition of 20%wt wood pellets. It was also observed that the E values for gasification under flue gas atmosphere were higher than under air, indicating that the thermal degradation of material required a higher amount of energy under flue gas.

Acknowledgements P. Sitthichirachat received a scholarship from the Faculty of Engineering, Kasetsart University, the Department of Mechanical Engineering, Faculty of Engineering, Kasetsart University, and the Graduate School of Kasetsart University.

References

1. Siwal SS, Zhang Q, Devi N, Saini AK, Saini V, Pareek V, Gaidukovs S, Thakur VK (2021) Recovery processes of sustainable energy using different biomass and wastes. Renew Sustain Energy Rev 150:111483
2. Nandhini R, Berslin D, Sivaprakash B, Rajamohan N, Vo D-VN (2022) Thermochemical conversion of municipal solid waste into energy and hydrogen: a review. Environ Chem Lett 20(3):1645–1669

3. Phasee P, Areeprasert C (2017) Thermal decomposition behavior during combustion of hydrothermally treated MSW by thermogravimetric analysis. Energy Proc 138:616–621
4. Areeprasert C, Chanyavanich P, Ma D, Shen Y, Yoshikawa K (2017) Effect of hydrothermal treatment on co-combustion of paper sludge with coal: thermal behavior, NO emissions, and slagging/fouling tendency. Biofuels 8(2):187–196
5. Saravanakumar A, Chen W-H, Arunachalam KD, Park Y-K, Ong HC (2022) Pilot-scale study on downdraft gasification of municipal solid waste with mass and energy balance analysis. Fuel 315:23287
6. Seo YC, Alam MT, Yang WS (2018) Gasification of municipal solid waste. Gasification for low-grade feedstock, IntechOpen, London, UK
7. Sarabhorn P, Sitthichirachat P, Siripaiboon C, Khaobang C, Palay P, Thapsamut T, Wibowo H, Areeprasert C, Scala F (2023) Investigation of wood pellet gasification in a novel pilot-scale fixed-bed decoupling gasifier. Fuel 352:129025
8. Khaobang C, Sarabhorn P, Siripaiboon C, Scala F, Areeprasert C (2022) Pilot-scale combined pyrolysis and decoupling biomass gasification for energy and metal recovery from discarded printed circuit board and waste cable. Energy 245:123268
9. Coats AW, Redfern J (1964) Kinetic parameters from thermogravimetric data. Nature 201(4914):68–69
10. Kwon EE, Jeon YJ, Yi H (2012) New candidate for biofuel feedstock beyond terrestrial biomass for thermo-chemical process (pyrolysis/gasification) enhanced by carbon dioxide (CO_2). Biores Technol 123:673–677
11. Abu El-Rub Z, Bramer EA, Brem G (2004) Review of catalysts for tar elimination in biomass gasification processes. Ind Eng Chem Res 43(22):6911–6919
12. Anis S, Zainal Z (2011) Tar reduction in biomass producer gas via mechanical, catalytic and thermal methods: a review. Renew Sustain Energy Rev 15(5):2355–2377
13. Soomro A, Chen S, Ma S, Xiang W (2018) Catalytic activities of nickel, dolomite, and olivine for tar removal and H2-enriched gas production in biomass gasification process. Energy and Environ 29(6):839–867
14. Thomson H, Drysdale D (1987) Flammability of plastics I: ignition temperatures. Fire Mater 11(4):163–172
15. Grotkjær T, Dam-Johansen K, Jensen AD, Glarborg P (2003) An experimental study of biomass ignition☆. Fuel 82(7):825–833
16. Benítez-Guerrero M, López-Beceiro J, Sánchez-Jiménez PE, Pascual-Cosp J (2014) Comparison of thermal behavior of natural and hot-washed sisal fibers based on their main components: cellulose, xylan and lignin. In: TG-FTIR analysis of volatile products. Thermochimica Acta, vol 581. pp 70–86
17. Parascanu M, Sandoval-Salas F, Soreanu G, Valverde JL, Sanchez-Silva L (2017) Valorization of Mexican biomasses through pyrolysis, combustion and gasification processes. Renew Sustain Energy Rev 71:509–522

Assessment of Fuel Feed Ratio and Emissions for Coal and Biomass Co-Firing in the Circulating Fluidized Bed Boiler

Danny M. Urian, Reylina G. Tayactac, Jaime P. Honra, Edward B.O. Ang, and Ricky D. Umali

Abstract Global warming and reduced reliance on fossil fuels for electricity generation have prompted many nations to pursue sustainable energy alternatives. Singapore's future carbon tax pricing will subsequently increase in coming years; from 2019 to 2023, the initial carbon pricing scheme is set at S$5/t$CO_2$e and scheduled to increase by S$25/t$CO_2$e in 2024. The CFB boiler in Tembusu Multi-Utilities Complex consumed coal fuel in co-firing with biomass, contributing to higher carbon emission than biomass fuel. The study aims to reduce coal consumption by increasing the feed flow of palm kernel shells and woodchips fuel by improving the fuel feed ratio in coal-biomass co-firing use in the CFB boiler. The study highly safeguards the boiler's safe operating limits and reliability; the as-built and design specifications of the boiler are identified and reviewed before the adjustment test. The study assessed the effects of fuel feed ratio adjustment on the boiler's critical parameters, and no significant impact was observed. The revised 59:41 fuel feed ratio is obtained, compared to the original 80:20 design ratio. The emissions have shown promising results in reducing the following pollutants: SO_2 by 65.33%, NO_x by 5.59%, Mercury by 19.98%, CO by 36.74%, and opacity by 3.83%, while CO_2, dust, and excess %O_2 were maintained. The fly ash and bed ash physical properties are also improved and beneficial for both fly ash collectors and bed ash recycling life. The boiler efficiency

D. M. Urian (✉) · R. G. Tayactac · J. P. Honra · E. B.O. Ang · R. D. Umali
School of Mechanical, Manufacturing, and Energy Engineering, Mapúa University, 658 Muralla Street, 1002 Intramuros, Manila, Philippines
e-mail: dmurian@mymail.mapua.edu.ph

R. G. Tayactac
e-mail: rgtayactac@mapua.edu.ph

J. P. Honra
e-mail: jphonra@mapua.edu.ph

E. B.O. Ang
e-mail: eboang@mapua.edu.ph

R. D. Umali
e-mail: rdumali@mapua.edu.ph

H. L. Ong et al. (eds.), *Proceedings of the 3rd International Conference on Biomass Utilization and Sustainable Energy; ICoBiomasSE 2023; 4–5 September; Kuala Lumpur, Malaysia*, Green Energy and Technology,
https://doi.org/10.1007/978-981-99-9164-8_5

increased by + 0.79% as the revised mixed fuel specific heat input and other heat credits increased.

Keywords CFB boiler · Coal-biomass · Co-Firing · Emissions · Fuel feed ratio

1 Introduction

The imperative to address global warming and reduce reliance on fossil fuels for electricity generation has prompted many nations to pursue sustainable energy alternatives. Co-firing biomass with coal is a cost-effective and straightforward method for generating electricity using biomass, particularly given the current high demand for low-carbon energy and the rising cost of natural gas. A typical fuel feed ratio of 5% on an energy basis would equate to approximately 40 Gigawatt of global power share, resulting in an emission reduction of approximately 300 metric tons of CO_2/year [3].

Technically, co-firing more than 20% of biomass is feasible; depending on the power plant design and co-firing capabilities, more than 50% of the coal could also be co-fired [2]. Biomass is carbon neutral because the energy it absorbs almost equals the CO_2 emitted when burned.

Singapore introduced the first carbon pricing scheme in the region in January 2019; implementing a carbon tax provides a comprehensive pricing indication that incentivizes enterprises to decrease their emissions while granting them the freedom to act by economic rationality [4]. Up to this date, the initial pricing is set at S$5/$tCO_2e$ and scheduled to increase by S$25/$tCO_2e$ in 2024. The carbon tax will be increased until it reaches its target of $50 to $80/$tCO_2e$ in 2030 [4].

Taking the unique design and advantages of CFB boilers, many related studies cited in the literature show successful results and advancements in coal fuel reduction to lessen carbon emissions. The substitution of 5% RDF pellets on 100% coal-fired CFB boiler has no effect on boiler fluidization, and no agglomeration is observed [5]. Raising the biomass share leads to a more homogeneous temperature distribution along the axis within the dense zone, with increased heat release occurring in the upper portion of the boiler's bottom furnace [10].

Singapore's future carbon emission tax pricing will subsequently increase in years to come; the CFB boiler located in Tembusu Multi-Utilities Complex consumption of coal fuel in co-firing with biomass contributes higher carbon emission than biomass fuel and to mitigate the upcoming increase of carbon emission tax in 2024, this study needs to know if the CFB boiler can deviate from the 80:20 design fuel feed ratio (80% coal and 20% biomass) by reducing the design coal fuel feed flow share and increasing the biomass fuel feed flow without compromising its safe operating limits.

The research aims to improve the fuel feed ratio to reduce coal consumption by increasing the feed flow of palm kernel shells and woodchips fuel in coal-biomass co-firing use in CFB boilers. The quantitative research approach is intended to examine the coal-biomass co-firing in a CFB boiler to adjust or deviate beyond the design fuel

feed ratio without jeopardizing the boiler's safe operating limits. Additionally, the author evaluates the effect of the revised fuel feed ratio using observation of collected data. The CFB boiler unit #1 in Tembusu Multi-Utilities Complex, situated in Jurong Island, Singapore, is chosen as the location of this research study.

The study used woodchips, palm kernel shells, and coal as co-firing fuel and used fuel analysis from laboratory reports to determine the properties of the mixed fuel. The cogeneration plant exports electricity and process steam as the main product to nearby customers; due to low steam demand, the fuel feed ratio adjustment test is limited to 50–55% Boiler Maximum Continuous Rating (BMCR). The boiler's safe operating and efficiency limits primarily bound the study and specifically if the flue gas emissions are significantly affected and exceed the NEA[1] allowable limits.

The results may be implemented in CFB boiler unit #2 as the test results are within the boiler's operating limits and with no significant effect on the boiler's efficiency and performance. The results may provide additional reference to the CFB boiler operators and efficiency engineers on the corresponding impact of fuel feed ratio adjustment on the boiler parameters, emissions, and ash physical properties using the fuel mix mentioned. This study may also provide valuable information on the different contributing heat input credits and heat losses that may affect the overall boiler efficiency and performance.

2 Methodology

2.1 Review of As-Built, Design Specification, and Current Data of the Co-Firing CFB Boiler

The research begins with gathering the CFB boiler as-built and design specification and reviewing the 50% BMCR coal firing at 80:20 co-firing fuel feed ratio to compare the parameters that must be closely monitored. The test will be aborted if any parameter(s) significantly deviates from its normal operating condition. The boiler parameter limits are collected, organized, and serve as a reference data sheet before conducting the test.

The review and parameters gathered are from the three (3) systems comprising the CFB boiler: the Steam and Feedwater System [7], as given in Tables 1 and 2; Combustion Air and Flue Gas System [8] in Tables 3, 4, 5 and 6 and the Biomass Feeding System [9] in Tables 8. A separate table for Continuous Emission Monitoring System (CEMS) parameters is collected, including the allowable emissions limits set by NEA [6], as given in Table 7.

[1] The National Environment Agency of Singapore.

Table 1 Steam and water system parameters (1/2)

BMCR ratio	Units	Feed water inlet	DeSH spray	ECO inlet	ECO outlet	Steam drum outlet	1SH inlet
50% 80% coal 20% BM	t/h	227.3	13.6	213.6	213.6	211.4	211.4
	MPa	17.0	14.6	11.2	11.0	11.0	10.9
	°C	178.0	178.0	178.0	267.0	319.0	331.0
Design	t/h						
	MPa	21	21	14.4	14.4	14	14
	°C	210	210	340	340	338	390

Table 2 Steam and water system parameters (2/2)

BMCR ratio	Units	1SH outlet	2SH inlet	2SH outlet	3SH inlet	3SH outlet	4SH inlet	4SH outlet	Main steam
50% 80% coal 20% BM	t/h	211.4	218.2	218.2	223.3	223.3	225.0	225.0	225.0
	MPa	10.9	10.8	10.8	10.7	10.6	10.6	10.5	10.5
	°C	382.0	362.0	396.0	380.0	434.0	427.0	480.0	480.0
Design	t/h								
	MPa	14	14	14	14	14	14	14	12.1
	°C	472	472	474	474	496	496	530	521

Table 3 Combustion air system parameters (1/2)

BMCR ratio	Units	Air flow	PAF outlet	1SAH outlet	1GAH outlet	Wind box	Fuel feed	SAF outlet	2SAH outlet
50% 80% coal 20% BM	Nm^3/h	229.24	161.64			126.08	34.19	53.85	
	kPa		19.1	18.6	16.5	10	6	9	8.7
	°C		42	70	200	200	200	42	70
Design	Nm^3/h	488	320					153.5	
	kPa		25.2	25.2	25.2	25.2	25.2	16.3	16.3
	°C		80	80	230	230	230	20	80

Table 4 Combustion air system parameters (2/2)

BMCR ratio	Units	2m	4m	6m	Start-up burner	HPB outlet	Wind box	Wall seals	Intrex seals
50% 80% coal 20% BM	Nm^3/h	11.8	11.8	11.8	18.46	13.25	3.52	2.19	0.754
	kPa	8	3	3	2.5	60	15	60	60
	°C	200	200	200	200	83	83	83	83
Design	Nm^3/h					14.4	0	3.2	10.05
	kPa	16.3	16.3	16.3	16.3	69	69	69	69
	°C	230	230	230	230	95	95	95	95

Table 5 Flue gas system parameters (1/2)

BMCR ratio	Units	Average FBP	Furnace draft	Furnace right	Furnace left	Furnace exit
50% 80% coal 20% BM	Nm^3/h					
	kPa	5.6	−0.09			
	°C	910		750	750	745
Design	Nm^3/h					
	kPa	−3.5 ~ 7	−3.5 ~ 7			
	°C	1150		1150	1150	1150

Table 6 Flue gas system parameters (2/2)

BMCR ratio	Units	2SH inlet	1SH inlet	ECO inlet	GAH inlet	GAH exit	BF ΔP	IDF inlet
50% 80% coal 20% BM	Nm^3/h							
	kPa	−0.4	−0.4	−0.4	−0.4	−0.6	−1.33	−1.5
	°C	613	546	422	218	138		138
Design	Nm^3/h							
	kPa	−6.0	−6.0	−6.0	−6.0	−7.0	−7.0	−8.5
	°C	1150	1150	535	275	185		180

Table 7 Continuous emission monitoring system (CEMS) parameters

BMCR ratio	Units	$\%O_2$	PM	NO_x	SO_2	CO	Hg	CO_2	Opacity
50% 80% coal 20% BM	mg/Nm^3		1.0	160	59.76	25			
	$\mu g/Nm^3$						0.10		
	%	5.67						15	7.9
Allowable emission limits	mg/Nm^3		< 100	< 700	< 500	< 625			
	$\mu g/Nm^3$						3		
	%	7[2]						25[2]	< 20[2]

Table 8 Biomass feeding system—BMSR and biomass feed flow function curve

BMSR rotation speed (%SC)	Biomass feed flow (t/h)
10	2.599
60	15.592
70	18.191
80	20.790

[2] Excess $\%O_2$, CO_2, and Opacity are not subject to legal limits by NEA.

2.2 Co-Firing Fuel Feed Ratio Adjustment Test

Fuel Feed Ratio Adjustment Test and Emission Monitoring. After reviewing the as-built and design specification and current data of the CFB boiler, the target fuel feed ratio is expected to reach the maximum set biomass feed flow of 20.79 t/h, as given in Table 8. Based on the Biomass Main Screw Reclaimer (BMSR) and biomass feed flow function curve during the review, it was also determined that the maximum rated feed flow of the BMSR is 40 t/h [9]. Even though it is rated in 100% palm kernel shells (PKS) feeding, based on records, there are no issues or underlying problems in fuel feed flow when mixed with woodchips (WC). Established steps or guidelines are set to execute the fuel feed ratio adjustment test safely. A guideline for adjustment tests includes the preparation, execution of the adjustment, monitoring, and post-briefing after the test is established.

3 Result and Discussions

3.1 Fuel Feed Ratio Adjustment Test Evaluation

The fuel feed ratio adjustment test was conducted in CFB boiler unit #1, which lasted 5 h. The test data are collected in Yokogawa Exaquantum data historian and plotted within 60 Periods, and a five (5) minute time interval is set between each period. The adjustment test was permitted at a 50% BMCR minimum stable load up to 55% BMCR.

Coal-Biomass Co-Firing Fuel Feed Ratio Adjustment Result. The BMSR speed is set to 10% speed control (SC) at 2.60 t/h before the fuel feed ratio adjustment test with the corresponding equivalent of ≈7.0 t/h of coal in each coal weigh feeder (CWF A ~ F), as shown in Fig. 1. The coal-biomass co-firing fuel feed ratio is 94:6 (94% coal and 6% biomass). A further adjustment was made until it reached the base design co-firing of 80:20 at 50% BMCR; the boiler condition was held for 1 h for stabilization. The coal and biomass feed flow was recorded at 31.13 t/h and 8.99 t/h, respectively. The target fuel feed ratio is expected to reach the maximum biomass feed flow of 20.79 t/h based on the BMSR and biomass feed flow function curve, as given in Table 8.

In Fig. 2, further adjustments increased the coal and biomass feed flow rates to 25.90 t/h and 18.19 t/h, respectively. Following the measurement and evaluation of the boiler parameters during the adjustment test, a new fuel feed ratio of 59:41 (59% coal and 41% biomass) is obtained, as shown in Fig. 3.

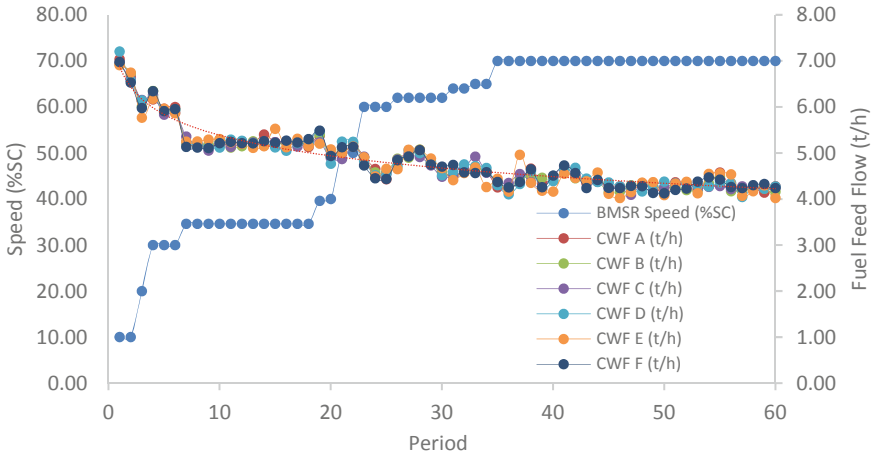

Fig. 1 Coal weigh feeders feed flow versus biomass screw reclaimer speed

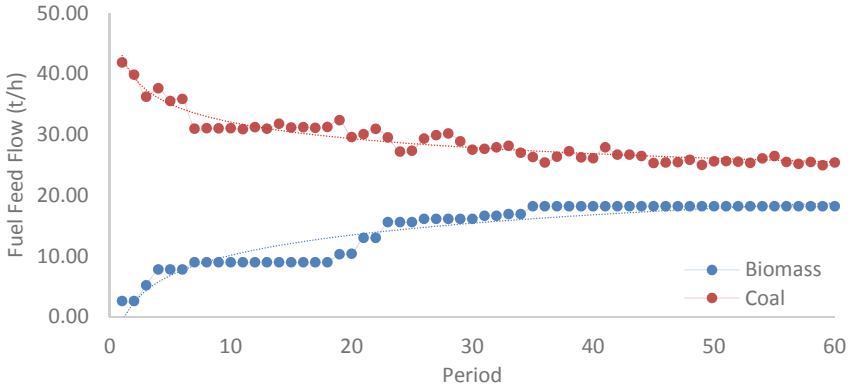

Fig. 2 Coal and biomass feed flow test profile

3.2 Boiler Parameters, Emissions, and Ash Evaluation

Boiler Parameters Evaluation. The high-pressure blower delivered a stable air flow of 1429.95 Nm^3/h, 56.04 kPa at Period 35 to 60 when the fuel feed ratio is at 59:41 additional air to wind box in excess from the return leg and wall seal's airflow stable flow of 3148.31 Nm^3/h, 3221.42 Nm^3/h, 695.35 Nm^3/h, 713.34 Nm^3/h, 741.92 Nm^3/h, and 741.27 Nm^3/h, indicating that the bed material in Integrated Heat Exchanger (INTREX) for 3rd and 4th superheaters flows as normal as it returns to the bottom furnace. Constant airflow also indicates no excessive carry-over and accumulation of bed material at the return leg.

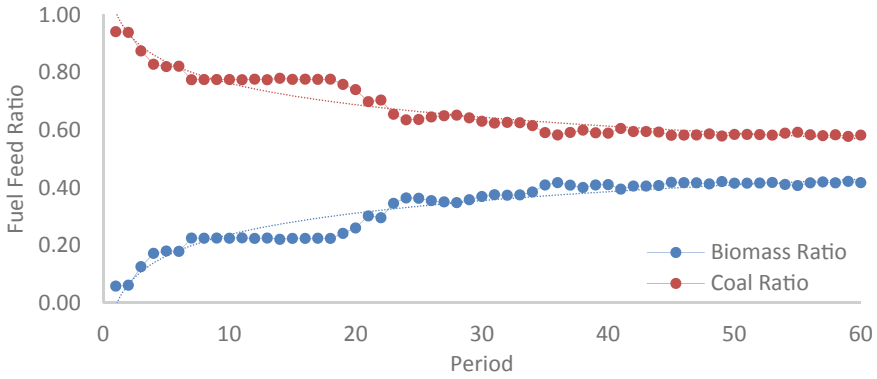

Fig. 3 Coal and biomass co-firing fuel feed ratio

The staged combustion airflow at 2 m, 4 m and 6 m elevation is stable at 11.29 kNm^3/h, 10.69 kNm^3/h, and 11.26 kNm^3/h, respectively, indicating that the combustion air requirement during the adjustment test is sufficient and has no variation. Burner air flow is constant at 18.45 kNm^3/h to provide air sealing to the Start-up Burners (SUBs) to prevent the burner tip from overheating due to the high temperature (900 °C) in the bottom furnace. The fuel-feeding air flow is also constant at 35.0 kNm^3/h to provide air sealing to all fuel feeders' entry points in the furnace to contain any backfire.

There were no significant changes in boiler load, and it was maintained at 50% BMCR; this shows sufficient air for combustion (air-rich condition). Hence, the wind box at 154.85 kNm^3/h and total airflow at 225.39 kNm^3/h remained stable during the adjustment test; the total fuel demand is also the same throughout, and the co-firing fuel feed ratio varies.

The average furnace bottom pressure stability at 5.95 kPa indicates that the accumulation of heavy particles does not restrain the fluidization of bed material. The furnace draft pressure was maintained at −0.085 kPa close to the setpoint of 0.10 kPa and in the mean range from the Master Fuel Trip (MFT) value of ± 3.50 kPa, while the 2SH and 1SH inlet flue gas pressure is at −0.329 kPa and −0.389 kPa, respectively. The GAH and economizer inlet flue gas was maintained at −0.473 kPa and −0.395 kPa, respectively. The bag filter differential pressure and outlet pressure (IDF inlet flue gas pressure) were stable at 0.575 kPa and −1.356 kPa, far from the bag filter HH pressure MFT setpoint of −7.00 kPa; this shows no significant change in fly ash generated from combustion that the flue gas carries and exit all through the bag filter system.

The furnace exit flue gas temperature exceeds its typical working value on 50%BMCR (80:20) of 754.75 °C and continues to rise. When the biomass feed flows at 16.63 t/h, the average bottom temperature rises steadily to 910.33 °C in Period 33. Gradually, when the biomass feed flow was increased to 18.19 t/h, the temperature reached 911.16 °C in Period 36 and peaked at 913.03 °C in Period 38.

The temperatures for the 2SH, 1SH, and economizer incoming flue gas were recorded at 593.59 °C, 517.15 °C, and 403.77 °C, respectively, with a rising trend. The GAH continues to increase gradually from the lowest to the highest, measured at 141.99 °C to 143.26 °C, respectively, with an average temperature of 142.73 °C. The flue stack flue gas temperature average is at 137.27 °C with an increase of + 1.33 °C. A low limit target temperature of 135 °C is set to prevent the acid point temperature of 120 °C ~ 124 °C from being reached.

There are no significant changes in feedwater temperatures; the economizer outlet temperature is 273.49 °C, even though it reached the normal operating condition at 50%BMCR at an 80:20 ratio, the maximum temperature recorded is 284 °C at 100% BMCR, and the design temperature of the tubes is 340 °C. The steam drum saturated temperature is 319.32 °C. The degree of superheat of 89.07 (1st SH), 128.53 (2nd SH), 155.20 (3rd SH), and 178.24 (4th SH) as the steam enters and leaves each superheater until it reaches the fourth (final) superheater are within the design values.

Continuous Emission Monitoring System Evaluation. Emissions are monitored during the fuel feed ratio adjustment test via visual inspection of the flue gas stack and CEMS at the DCS. The test results are gathered and analyzed to help determine the effect of the revised fuel feed ratio on the CFB boiler.

As shown in Fig. 4, the design fuel feed ratio of 80:20 was set and stabilized, and an average of 0.853 mg/Nm^3 of particulate matter (Dust) was recorded. In Periods 35 to 60, the actual adjustment test was conducted, and an average of 0.856 mg/Nm^3 of was achieved. An increase of 0.0028 mg/Nm^3, given that there has been no discernible change in the data collected thus far and that it is much below the permissible limit of 100 mg/Nm^3. The Mercury (Hg) was reduced by 0.198 μg/Nm^3 and dropped from 0.991 to 0.793 μg/Nm^3. This result is due to decreased coal fuel ratio, which contains 59.52 μg/kg of Mercury (Hg). One observation also was that the traces of metals such as Fe, Al, Cu, and Pb composition in woodchips is relatively low, less than 0.01 to 0.02% compared to coal, where the Fe_2O_3 accounts for 12.59%.

In Fig. 5, based on the CFB boiler operating at the design fuel feed ratio, the SO_2 recorded an average of 58.39 mg/Nm^3, but at the adjusted ratio, the SO_2 drops to 20.24 mg/Nm^3 on the collected data, a 38.15 mg/Nm^3 decrease; this is due to a reduction in the coal fuel ratio, which contains 0.09% sulfur, whereas PKS and woodchips fuel is lesser at 0.03% and 0.04% on an as-received basis (AR), respectively. The nitrogen oxides (NO_x) decreased by 9.15 mg/Nm^3, from 163.77 to 154.62 mg/Nm^3. This result is due to a decrease in the coal fuel ratio, which contains 0.98% nitrogen, even though woodchips contain 1.33%, whereas PKS fuel is relatively low at 0.33% on an as-received basis (AR).

In Fig. 6, the carbon monoxide (CO) was reduced by 6.61 mg/Nm^3, dropping from 17.99 to 11.38 mg/Nm^3; this result is due to a decrease in the coal fuel ratio, which contains 48.30% carbon, whereas PKS and woodchips fuel is lesser at 44.6% and 32.40% on an as-received basis (AR), respectively. The CO_2 slightly increased by 0.079%vol from 14.036%vol to 14.115%vol.

The increase considerably maintains and might be due to fluctuation of excess $\%O_2$. The opacity slightly decreased by 0.39%vol from 10.18%vol to 9.79%vol. During the actual adjustment test, a visual inspection was conducted on the flue

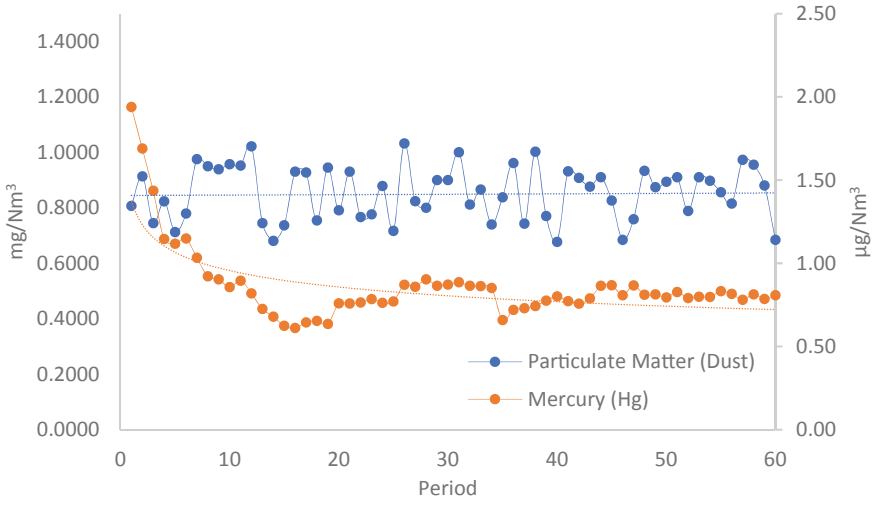

Fig. 4 Particulate matter (Dust)

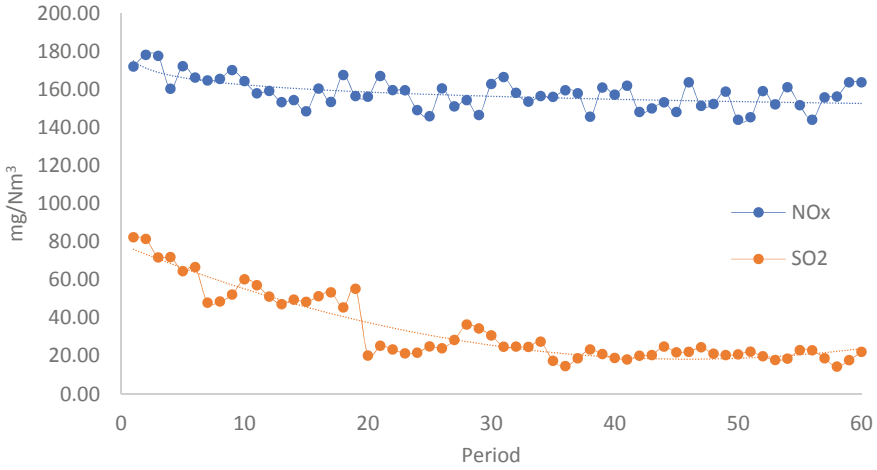

Fig. 5 Sulfur dioxide (SO_2) and nitrogen oxides (NO_x)

gas stack, and no visible smoke was observed during the entire test. The excess oxygen fell slightly by 0.114%O_2 from 5.76%O_2 to 5.66%O_2. Fine-tuning the %O_2 trim control may reduce the amount of incomplete combustion products like carbon monoxide and soot, resulting in lower carbon dioxide emissions. The slight increase in dust and CO_2 transmitter-based reading found no significant effect on implementing the revised fuel feed ratio. The CO_2, dust, and excess %O_2 were fairly maintained, considering the minimal deviations from the collected data.

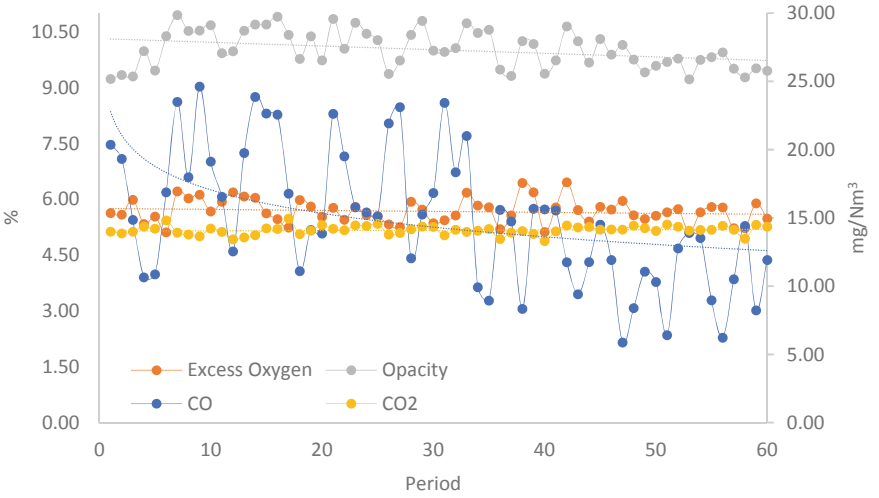

Fig. 6 Carbon monoxide (CO), carbon dioxide (CO_2), opacity, and excess oxygen ($\%O_2$)

Evaluation of Fly Ash and Bed (Bottom) Ash Generated. The physical appearance of fly ash, particularly its color, also can indicate its underlying properties. A study proves a connection between iron oxide content and the physical color of fly ash [11]. It was observed in Fig. 7 that the 59:41 coal-biomass ratio had lesser Fe_2O_3 content than the 80:20 ratio. Since after the adjustment test, the fly ash sample was light brownish than the 80:20 ratio fly ash sample. In the latest ash analysis, the amount of Fe_2O_3 in the coal is 12.59% compared to biomass (woodchips), with a relatively low presence of iron oxide at 0.02%. In addition, the ash collectors accept the fly ash sample taken.

As shown in Fig. 7, the sample of bed ash taken after the adjustment test observed lesser unburned carbon compared to the 80:20 coal-biomass ratio, where a significant amount of unburned carbon and other granule materials are present where in coal's solid by-products are typical after being burned. The result is beneficial for the recycling life of the bed ash to reduce the amount of heavy particles like the unburned carbon and granule materials trapped in the furnace bed that may block the passage through the bed ash chutes that connect to bed ash coolers (BACs). Accumulating heavy particles in the furnace will result in high furnace bed pressure, thus will affect the fluidization and needing more airflow from the wind box to maintain the operating condition in the furnace.

Evaluation of FBT and GAH Temperature Increase. Due to the incremental increase in the furnace and flue gas temperature during the adjustment and evaluation, it was decided to halt the adjustment and maintain the last adjusted fuel feed ratio of 59:41 while monitoring the parameters and stabilizing the boiler until the necessary data are collected. Further assessment has been made; the furnace exit flue gas and average furnace bottom temperatures saturate and stabilize over time. The average operating temperature on the furnace exit is 881°C at 100%BMCR—80:20 fuel feed

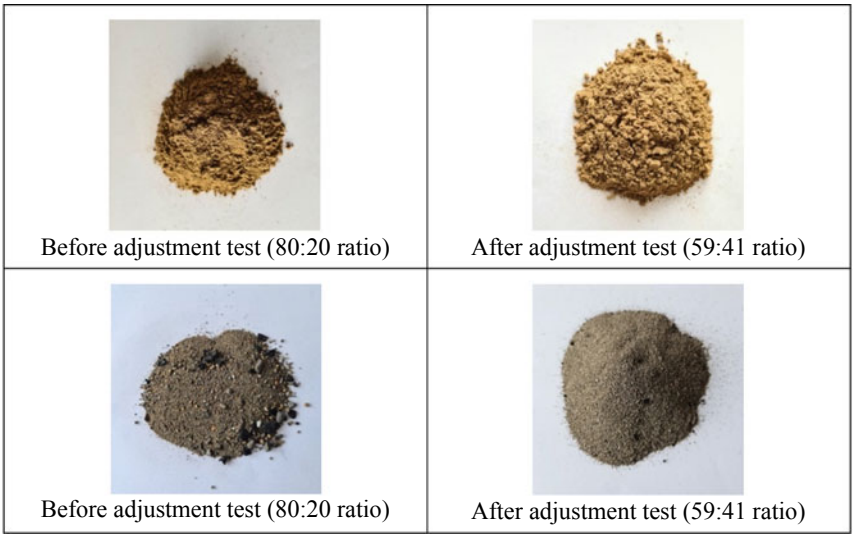

Fig. 7 Comparison of fly ash and bed ash before and after the adjustment test

ratio, and the average furnace bottom temperature is 900 °C. The airflow to the wind box is 234.16 kNm^3/h compared to 50%BMCR (regardless of fuel feed ratio); the airflow is ≈50% lesser at 126 kNm^3/h. The heating value of the mixed fuel, as given in Table 9, is higher than the given calorific setpoint (Coal = 16.80 MJ/kg and Biomass mixed = 14.50 MJ/kg) for the computation of the required fuel feed flow. These conditions will translate to heat retention in the furnace bed due to less fluidization with higher heat value carried by the new mixed fuel.

Hence, the furnace temperature will increase momentarily and saturate once the air and fuel demand controls adjust accordingly to maintain the air-rich condition of the CFB boiler. Matching the calorific setpoint with the new fuel-mixed heating value will be beneficial to maintain the average FBT across the furnace bed.

3.3 Assessment of the Fuel Consumption, Revised Fuel Feed Ratio, and Boiler Efficiency

Mixed Fuel Properties. Table 9 gives the revised fuel feed ratio and new mixed fuel properties based on the co-firing ratio weight basis calculated. These new mixed fuel properties are used to determine the supplementary calculations for the boiler efficiency.

The fuel mixture during the adjustment test is 80% coal, 4% PKS, and 16% woodchips from Period 7 to 18 (1 h), and the fuel feed ratio is at a design setting of 80:20. The average feed flow is 31.13 t/h of coal and 8.99 t/h of biomass, respectively.

Table 9 Summary of ultimate analysis for each fuel type and mixed fuel properties (AR basis)

Item		Units	3 types of fuel			Mixed fuel	Reference (Design)
			Coal	PKS	WC		
Co-firing ratio (wt. basis)		%-wt	58.74	8.25	33.01		
Total moisture		%	30.94	17.94	31.06	29.907	33.07
HHV		MJ/kg	17.93	16.75	17.64	17.736	17.42
LHV		MJ/kg	16.40	14.99	15.63	16.027	15.78
Ultimate analysis	C	%	48.30	42.40	32.40	42.565	42.85
	H	%	5.02	5.21	5.96	5.346	3.69
	N	%	0.98	0.33	1.33	1.042	0.80
	O	%	10.87	31.62	25.20	17.312	17.80
	Total S	%	0.0900	0.0300	0.040	0.069	0.13
	Total Cl	%	0.0040	0.0961	0.010	0.014	0.00166
	Ash	%	3.80	2.37	4.00	3.75	1.67
	Total moisture	%	30.94	17.94	31.06	29.91	33.07
	(Total)	%	100.0	100.0	100.0	100.00	100.00

On the other hand, as mentioned in Figs. 2 and 3, the adjusted fuel feed ratio of 59:41 shows that the average fuel feed flow for coal and biomass is 25.90 t/h and 18.19 t/h, respectively. Table 10 gives the summary of the coal and biomass for 1-h consumption.

Boiler Efficiency Calculation by Heat Loss Method. The heat loss method under ASME PTC 4.1 [1] evaluates the CFB boiler efficiency. This method involves calculating the energy input (H_f), including the credits (B), and less all the closure losses (L), as shown and presented in Eq. (1).

$$\text{boiler efficiency} = 100 - \frac{L}{H_f + B} \times 100\% \tag{1}$$

Table 10 Summary of the coal and biomass for 1-h consumption

Fuel feed ratio	Total coal consumed	Total biomass consumed		Total fuel reduction/ gain			Percentage fuel reduction/ gain		
		PKS	WC	Coal	PKS	WC	Coal	PKS	WC
	Tons	Tons	Tons	Tons	Tons	Tons	%	%	%
80:20	31.13	1.798	7.192						
59:41	25.90	3.638	14.552	−5.23	+ 1.86	+ 7.43	−16.80	+ 103.34	+ 103.34

Table 11 Boiler efficiency calculation summary

Heat losses	Symbol	Units	Value
Unburned carbon	Lubc	%	0.07788
Dry flue gas	Lg	%	3.00358
Moisture in fuel	Lmf	%	4.35994
Moisture from burning of hydrogen	Lh	%	6.98258
Moisture in the air	Lma	%	0.11163
Moisture in the limestone[3]	Llim	%	0.00
Formation of CO	Lco	%	0.0000442
Ash	Lash	%	0.23764
SO_2 removal[3]	LSO_2	%	0.00
$CaCO_3$ calcination[3]	$LCaCO_3$	%	0.00
$MgCO_3$ calcination[3]	$LMgCO_3$	%	0.00
Surface radiation and convection	Lrad	%	0.370
Hot water injection[3]	Lhw	%	0.00
Total heat loss	Ltot	%	15.143
Boiler efficiency	ηB	%	**84.857**

Table 12 Boiler efficiency with correction factors

Correction factors	Symbol	Units	Value
Efficiency correction for ambient temperature	ECT	%	−0.2499
Efficiency correction for total moisture in the fuel	ECM	%	−0.0418
Efficiency correction for HHV	ECH	%	−0.4354
Total efficiency correction	EC	%	−0.727
Boiler efficiency before correction	ηB	%	84.857
Boiler efficiency after correction	ηB_corr	%	**84.13**

Boiler Efficiency Calculation Summary. The boiler efficiency and heat losses given in Table 11 are determined by the supplementary calculations, data collected during the adjustment test, the specific heat input, credits, and detailed computation of each heat loss. Table 12 gives boiler efficiency with a correction factors based on the correction curves given by the manufacturer during the commissioning stage and performance test of the CFB boiler [6].

The resulting boiler efficiency did not breach the set limit of $\geq$ 81.5%, and the efficiency improved by + 0.79% compared to the 83.34% performance guarantee tests report in 2013 [6]. The performance guarantee test is at 100%BMCR at 80:20 fuel feed ratio (100% PKS of 20% biomass share), while the test study conducted

[3] There are no hot water and limestone injections in the CFB boiler as it was designed to fire with low Sulfur sub-bituminous coal. Hence, losses on hot water injection, moisture in the limestone, SO_2 removal, and $CaCO_3$ and $MgCO_3$ calcination are zero [6].

is at 50%BMCR with a revised fuel feed ratio of 59:41 (59% coal, 8.2% PKS, and 32.8% WC).

Identified specific wet air and dry flue gas that contribute to overall heat loss is contingent upon several factors, including moisture in the air and fuel, humidity, and fan outlet and GAH outlet temperature. The initial pair of factors are determined to correlate with the quantity of air present in the boiler to achieve complete combustion. The excess air ratio, calculated using a 50%BMCR at a fuel feed ratio of 59:41, is established to be 1.38. The hydrogen content of the mixed fuel is high at $H = 5.346$; this is a critical factor in heat loss, together with the high exit flue gas temperature. The heat loss resulting from radiation and convection is attributed to the energy content of steam (enthalpy), in addition to other factors, e.g., heat energy carried by the feedwater, wherein in this study, is lower because the boiler is only running at 50%BMCR with rated ≈225 t/h steam flow resulting to heat loss of 0.370% while at 100%BMCR is at 450 t/h, resulting to heat loss of 0.224%, in this boiler, loading difference alone the heat loss will be 0.146%.

Overall, the important factor why the boiler efficiency is higher even only running at 50%BMCR is the specific heat input of the 59:41 mixed fuel and other heat credits equating to 17.965 MJ/kg.

4 Conclusion

After measuring and evaluating the boiler parameters during the adjustment test, the revised fuel feed ratio of 59:41 (59% coal, 8.2% PKS, and 32.8% WC) is obtained. The biomass shares doubled, accounting for 59:41 compared to the original design ratio of 80:20. The adjustment test has shown promising results in emission reduction of SO_2 by 65.33%, NO_x by 5.59%, Mercury by 19.98%, CO by 36.74%, and opacity by 3.83%. Fine-tuning the $\%O_2$ trim control may reduce the amount of incomplete combustion by-products, like carbon monoxide and soot, to lower carbon dioxide emissions. The slight increase in dust and CO_2 transmitter-based reading found no significant effect on implementing the revised fuel feed ratio. The main factor in calculating the carbon emission and its tax is the amount of fuel consumed. Consumption of coal contributes a higher carbon tax than biomass fuel, as biomass is categorized as a renewable energy source and carbon neutral. Bed ash sample taken after the adjustment observed lesser unburned carbon compared to the 80:20 coal-biomass ratio; the result is beneficial for the recycling life of the bed ash. The fly ash sample taken shows improvement in physical properties. The amount of Fe_2O_3 in coal is 12.59% compared to biomass (woodchips), which accounts for 0.02% of the mixed fuel based on the ash analysis.

The boiler parameters, emissions assessment, ash physical properties evaluation, and the revised fuel feed ratio have no significant impact on boiler performance. Hence, the new fuel feed ratio can be implemented at CFB boiler unit #2, and further test at 100%BMCR is recommended. The heat loss due to surface radiation and convection and other heat losses will be expected to be reduced.

Acknowledgements The author is sincerely grateful to the TMUC Cogeneration Department for making this study possible and for helping to finish this research.

References

1. American Society of Mechanical Engineers (1985) PTC 4.1 performance test code: steam generating units
2. IRENA Homepage. https://www.irena.org/publications/2013/Jan/Biomass-co-firing. Last Accessed 26 Apr 2022
3. Koppejan J, Baxter L (2022) Global operational status on co-firing biomass and waste with coal experience with different co-firing concepts and fuels, IAE Bioenergy Homepage. https://www.ieabioenergy.com/wp-content/uploads/2013/10/ExCo55-P1a-Global-Operational-Status-of-Co-firing-Biomass-and-Waste-with-Coal.pdf. Last Accessed 26 Apr 2022
4. National Climate Change Secretariat Homepage. https://www.nccs.gov.sg/singapores-climate-action/carbon-tax. Last Accessed 20 Apr 2022
5. Soleh M, Hidayat Y, Abidin Z (2019) Co-firing RDF in CFB boiler power plant. In: International conference on technologies and policies in electric power and energy, Yogyakarta, Indonesia, pp 1–6
6. Sumitomo Heavy Industries Ltd. (2013) Performance guarantee tests report, doc no. TB-13–5-B023-RC
7. Sumitomo Heavy Industries Ltd. (2013) Process flow diagram (1/3) feedwater/main steam, dwg no. 1310-R2
8. Sumitomo Heavy Industries Ltd. (2013) Process flow diagram (2/3) combustion air/flue gas, dwg no. 1311-R2
9. Sumitomo Heavy Industries Ltd. (2013) Process flow diagram (3/3) material handling, dwg no. 1312-R2
10. Sun P, Hui S, Gao Z, Zhou Q, Tan H, Zhao Q, Xu T (2013) Experimental investigation on the combustion and heat transfer characteristics of wide size biomass co-firing in 0.2 MW circulating fluidized bed. Appl Therm Eng 52(2):284–292
11. Wattimena OK, Antoni Hardjito D (2017) A review on the effect of fly ash characteristics and their variations on the synthesis of fly ash based geopolymer, In: AIP conference proceedings, East Java, Indonesia

Harnessing Solar Energy for Pyrolysis of Empty Fruit Bunch: A Fresnel Lens Approach in Malaysia

Alia Syafiqah Abdul Hamed, Nurul Iffah Farhah Mohd Yusof, Muhammad Syarifuddin Yahya, Nurul Adilah Abdul Latiff, and Nur Farizan Munajat

Abstract Malaysia's palm oil industry generates a significant amount of biomass waste, particularly empty fruit bunches (EFB). The conventional heating methods used in pyrolysis for converting EFB into value-added products are carbon-positive and decrease energy efficiency. Therefore, this study aims to explore the feasibility of solar pyrolysis using a Fresnel lens in Malaysia. The performance of the Fresnel lens-based solar pyrolysis reactor was evaluated, focusing on its thermal characteristics and biochar yield. The results indicated that, in the absence of EFB, the highest temperature within the reactor at the Fresnel lens' focal point was 618 °C and the maximum solar irradiance value was 987 W/m^2. When EFB was introduced, the temperature inside the reactor was maintained at around 500 °C. Biochar yields reached 40–45% for residence times of 20–30 min. These findings demonstrate the potential of concentrated solar energy for converting EFB into renewable energy and endorse the suitability of the Fresnel lens in harnessing solar energy for the pyrolysis process in Malaysia.

A. S. A. Hamed · N. I. F. M. Yusof · M. S. Yahya · N. A. A. Latiff
Faculty of Ocean Engineering Technology, Universiti Malaysia Terengganu, 21030 Kuala Nerus, Terengganu, Malaysia
e-mail: p5334@pps.umt.edu.my

N. I. F. M. Yusof
e-mail: p5147@pps.umt.edu.my

M. S. Yahya
e-mail: syarif_yahya@umt.edu.my

N. A. A. Latiff
e-mail: nurul_adilah@umt.edu.my

N. F. Munajat (✉)
Renewable Energy and Power Research Interest Group (REPRIG), Eastern Corridor Renewable Energy Special Interest Group (SIG), Faculty of Ocean Engineering Technology, Universiti Malaysia Terengganu, 21030 Kuala Nerus, Terengganu, Malaysia
e-mail: nurfarizan@umt.edu.my

H. L. Ong et al. (eds.), *Proceedings of the 3rd International Conference on Biomass Utilization and Sustainable Energy; ICoBiomasSE 2023; 4–5 September; Kuala Lumpur, Malaysia*, Green Energy and Technology,
https://doi.org/10.1007/978-981-99-9164-8_6

Keywords Solar pyrolysis · Fresnel lens · Oil palm · Solar energy · Renewable energy

1 Introduction

The Malaysian oil palm industry performed well in 2022, with total crude and processed palm oil increasing from 1,614,594 to 2,196,574 million metric tonnes and total exports increased by about 1.8% compared to the year 2021 [1].

As one of the major producers and exporters of palm oil globally, Malaysia has a sizable amount of oil palm planted, which was estimated at 5.67 million hectares in 2022. This positive development demonstrates that Malaysia has produced a lot of significant potential biomass over the years throughout the industrial process, especially in renewable energy production [2–6].

Pyrolysis is one of the most efficient renewable energy technologies due to its high conversion efficiency, significant economic potential, and environmental friendliness. Conventional pyrolysis relies on conventional heating methods, such as the direct combustion of fossil fuels or electricity, to generate the required heat for the pyrolysis process. Many research studies have been conducted on the use of biomass, primarily empty fruit bunches (EFB), in different types of pyrolysis reactors, including microwave [7–11], fluidized [12–14], fixed bed [15–17], etc. and pyrolysis category including slow, fast, microwave, catalytic, etc. This technique was proven to successfully transform EFB as lignocellulosic biomass into the desired renewable energy products such as biochar, liquid fuels, and biogas. However, by making the entire process carbon-positive and reducing the amount of feedstock available for pyrolysis, this conventional heating technique also decreases energy efficiency [18–20].

Solar concentrating technology is an alternative method to provide the energy required to power the pyrolysis process, particularly for Malaysia, which has an abundance of biomass resources and solar energy. Wheat straw, scrap tires, chicken litter, willow wood, pine sawdust, and Jatropha seeds are among the feedstocks that have been employed in the solar pyrolysis process [21]. Various types of solar concentrators, including parabolic trough, parabolic dish, heliostats, and Fresnel lens, have been tested to concentrate solar energy for the pyrolysis process [20, 21]. Of these, Fresnel lenses have advantages due to attributes cost-effectiveness, compact size, ease of tracking, and uniform light output [22]. They offer high sunlight concentration, flexibility in capturing varied incident angles, and are modular, enabling scalable installations. However, it can be challenging to develop an effective solar heating system because sunlight strikes the earth's surface in an uneven flux, is relatively diluted in form, and is intermittent [18]. Consequently, the implementation of solar pyrolysis demands a comprehensive assessment of local solar resources to establish its feasibility.

While many solar pyrolysis studies have used artificial sun sources or complex solar furnaces studies using natural sunlight are limited. The unpredictability of

sunlight can result in uneven heating. In particular, literature on solar pyrolysis of EFB is notably lacking. In this preliminary study, the feasibility of harnessing solar energy for pyrolyzing EFB in Malaysia is examined. A Fresnel lens is used to concentrate solar energy. The analysis aims to examine the relationship between solar irradiance, pyrolysis temperature, and product yield. The findings give a preliminary understanding of the potential to harness Malaysia's rich solar energy and biomass waste resources for renewable energy and sustainable waste management.

2 Material and Methodology

The study was conducted at Universiti Malaysia Terengganu (coordinates 5.4145, 103.0861) using empty fruit bunch (EFB) feedstock collected from TDM Sungai Tong Palm Oil Mill, Terengganu. Prior to the experiment, the EFB were dried, ground, and sieved to obtain particles of less than 3 mm in size, with each trial using a 1.0 g sample. The experimental setup, as depicted in Fig. 1, comprised a glass tube as the pyrolysis reactor and a Fresnel lens as the solar concentrator. The lens had dimensions of 30 by 40 cm, a focal length of 30 cm, and a 1 cm focus spot. The reactor was positioned under the Fresnel lens' focus spot during the experiment, with argon gas purged continuously into the reactor at a rate of 10 ml/min. Solar irradiance and ambient temperature at the site were measured using a Seaward 200R irradiance meter, while a Type K thermocouple located at the focal point within the reactor monitored the internal temperature. Data on solar irradiance and air temperature were also procured from the Solcast website for comparison. Experiments were conducted both with and without feedstock to observe differences in conditions. When feedstock was included, the EFB sample was subjected to pyrolysis within the reactor for 20 and 30 min. The solid biochar yield, obtained post-pyrolysis, was weighed, and its percentage was calculated using Eq. (1).

$$\text{Biochar Yield}\,(wt\%) = \frac{\text{mass of char}}{\text{mass of feedstock}} \times 100\% \tag{1}$$

3 Result and Discussion

3.1 Zero Load Conditions

The zero-load condition experiment was conducted on June 19, 2023, from 10:00 am to 4 pm, aimed to comprehend the relationship between solar irradiance, ambient temperature, and reactor internal temperature. Figures 2 and 3, respectively, display

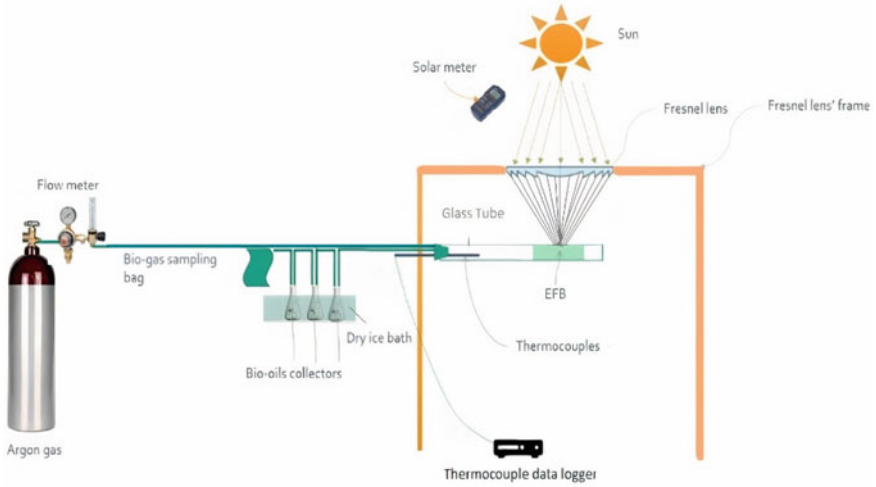

Fig. 1 Experimental setup diagram

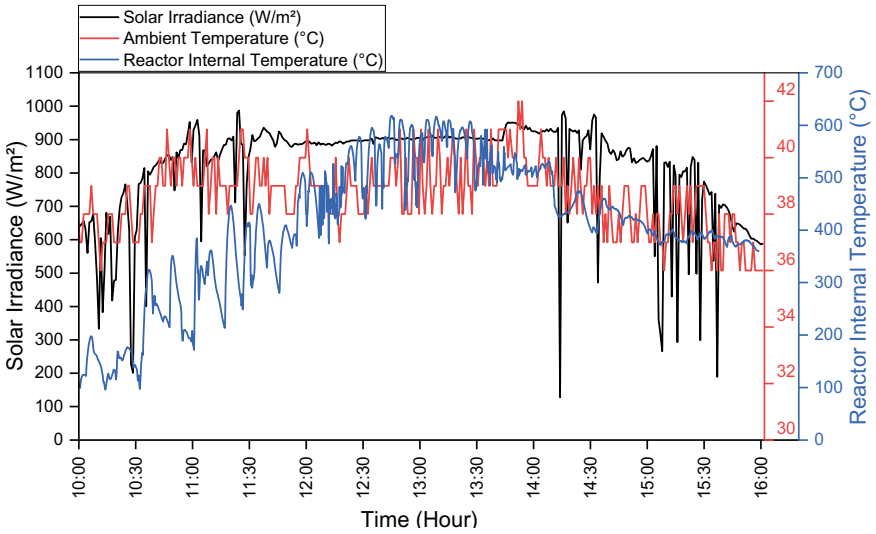

Fig. 2 Solar irradiance, ambient temperature, and reactor internal temperature on June 19, 2023

these parameters measured during the experiment and the corresponding solar irradiance and air temperature data obtained from Solcast [23].

Solar irradiance, a crucial factor for solar energy applications, showed significant variations during the experimental period, ranging from 116 to 987 W/m^2 (Fig. 2). A significant correlation was discerned between the solar irradiance patterns recorded

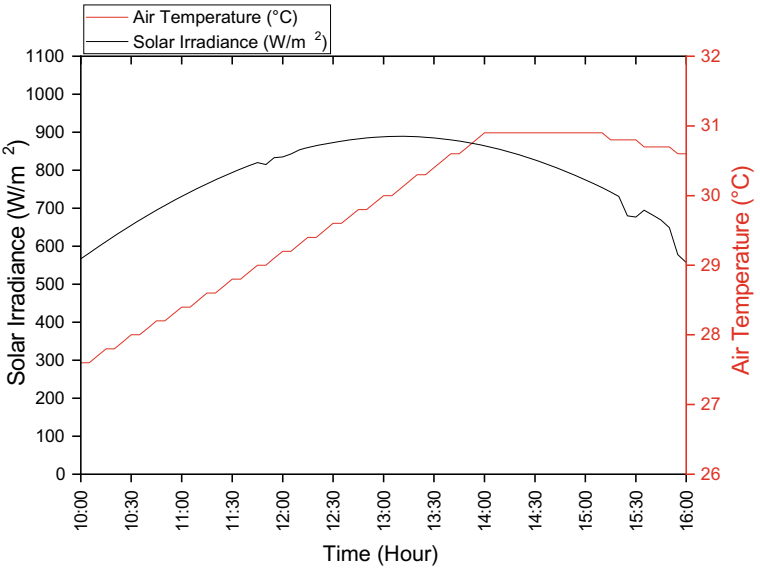

Fig. 3 Solar irradiance and air temperature from Solcast for June 19, 2023

via the solar meter and the data retrieved from Solcast (Fig. 3), highlighting the consistency of the measurements. During the experiment's peak hours, between 12 and 2 pm, the average solar irradiance measured was 905 W/m^2, while the highest recorded peak reached 987 W/m^2. These values are consistent with the typical average solar irradiance observed in tropical countries like Malaysia. For instance, the highest average solar irradiance intensity previously reported for Terengganu, a state in Malaysia, was 1139 W/m^2 [24]. Such conditions are particularly conducive for solar pyrolysis applications. A study by Hijazi et al. [25] lends support to this perspective, wherein they executed solar pyrolysis at a solar irradiance range of 950–1050 W/m^2 and reached a temperature of 550 to 570 °C using a Fresnel lens. These results highlight the feasibility of utilizing this method under real-world conditions in Malaysia and similar climatic zones.

The ambient temperature recorded by the solar meter rose from 30 °C at the experiment's start to a peak of 41 °C and then fluctuated mostly between 38 and 40 °C toward the end of the experiment. A consistent pattern between the ambient temperature and solar irradiance readings was observed, suggesting a direct relationship between these parameters. This direct relationship is expected as solar irradiance which is a primary driver of ambient temperature, though it can be influenced by factors such as cloud cover, humidity, wind speed, and the angle of sun rays. However, the ambient temperature readings were moderately higher than the air temperature data obtained from Solcast. The Solcast data show a steady rise from 25 °C to around 31 °C between 10:00 am and 2 pm, remaining constant until around 3 pm before starting to decrease. This discrepancy might be attributed to differences

in measurement methodologies (e.g., direct sunlight vs shaded air temperature) or location-specific factors such as microclimate conditions.

The internal temperature of the pyrolysis reactor exhibited a range between 162 and 618 °C throughout the experimental period. Pyrolysis reactions generally require elevated temperatures, often within the range of 400 to 900 °C [18]. The reactor was at an average temperature of 533 °C during peak hours (12 pm to 2 pm). The maximum temperature recorded during this study was 618 °C, which fits within the pyrolysis reaction range, illustrating that solar energy, when concentrated via a Fresnel lens, can effectively initiate and sustain pyrolysis reactions. The results indicate the feasibility of harnessing solar energy via a Fresnel lens for the pyrolysis process in Malaysia, thus highlighting the capacity of this renewable energy source for driving pyrolysis reactions under local conditions.

3.2 Solar Pyrolysis of EFB

Temperature characteristics. Figure 4 depicts the solar irradiance and air temperature as reported by Solcast for June 27, 2023, during the period of the experimental trials. Meanwhile, Fig. 5a, b shows the onsite solar irradiance and the internal temperature of the reactor during the solar pyrolysis of EFB at residence times of 20 and 30 min, respectively. These experiments were conducted between 12 and 2 pm, a period identified as optimal from findings illustrated in Fig. 3.

According to Solcast data (Fig. 4), the solar irradiance during the experimental period varied between 800 and 900 W/m^2, and the air temperature was around 31 °C. Despite the solar irradiance data from Solcast, the solar meter at the experimental site recorded a relatively consistent irradiance of approximately 900 ± 20 W/m^2 (Fig. 5).

Throughout the pyrolysis process of EFB, for both 20 and 30 min residence times, the reactor internal temperature range maintained a stable range between 450 and 550 °C. The desired temperature was reached within approximately 5 min from the start of each experiment, demonstrating the efficacy of the Fresnel lens in concentrating solar energy and thus ensuring rapid heating ramp-up. The reactor internal temperature aligns with findings from previous solar pyrolysis studies by Hijazi et al. [25] and Marcus et al. [26], which obtained temperature ranges of 550 to 570 °C and 600 ± 40 °C, respectively. Meanwhile, the observed heating ramp pattern is congruent with the pattern reported during solar pyrolysis by [26].

The maximum temperature recorded during the pyrolysis process in Fig. 5 (550 °C) differed from the peak value recorded under zero-load conditions in Fig. 3 (618 °C). This divergence can be attributed not only to the different solar irradiance levels on the respective days, with 921 and 987 W/m^2 reported, but also to the presence of the feedstock in the reactor. It is widely recognized that higher solar irradiance corresponds to higher reactor temperatures. Furthermore, during the pyrolysis process, the feedstock absorbs some of the heat energy for the thermal decomposition, which can result in a lower reactor temperature compared to the zero-load

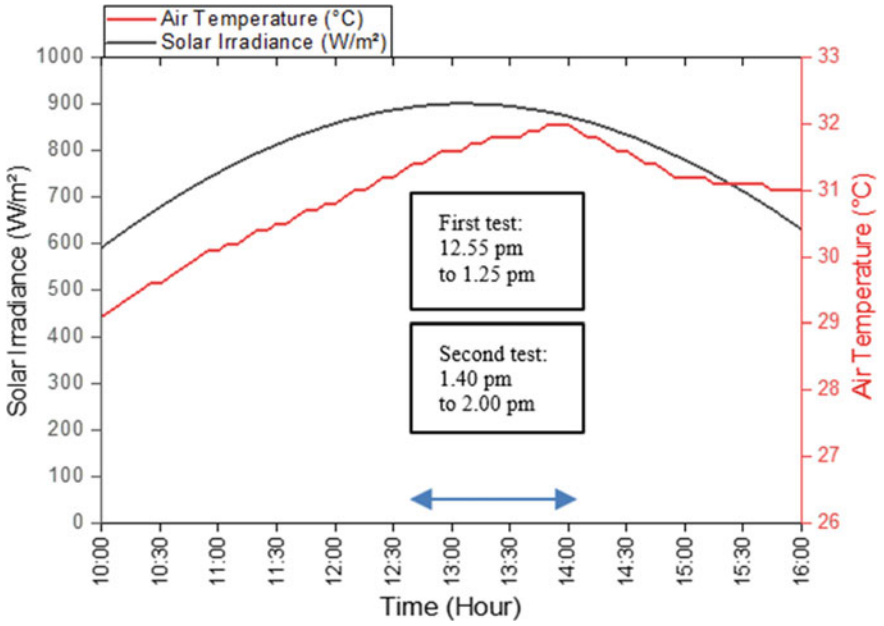

Fig. 4 Solar irradiance and air temperature from Solcast for June 27, 2023

condition. Therefore, both the variation in solar irradiance and the presence of the feedstock could have contributed to the observed differences in reactor temperatures.

Biochar yield analysis. Figure 6 shows biochar yield obtained at the different residence times: 20 and 30 min. As the residence time increased, the biochar yield decreased from 45 to 40%. The trend of biochar yield time is consistent with the results reported by Qureshi et al. [27, 28] and Sohaib et al. [28]where lesser biochar yield was achieved as the pyrolysis time increased. Biochar range in this research is similar to the range reported by [29], pyrolysis under 550 °C and no catalyst used, the biochar yield was 40~%. Besides, Mohamed et al. [30] reported that by using the conventional method of heating with a sample size of 5 g of EFB, a pyrolysis time of 6 to 12 min, and a pyrolysis temperature of 442.15 °C, the fixed bed reactor can produce biochar at a yield of between 24 and 30%. Inconsistency in solar irradiance and reactor operating temperature may result in non-uniform heating and a high percentage of biochar output in solar pyrolysis, as compared to conventional methods. To mitigate these inconsistencies, future studies could provide more consistent heating profiles by using solar tracking technologies. Besides, the low heating rate in Fig. 5a, b which is 1.66 °C/s, also giving effect to the biochar yield. This result is aligned with research reported by De Souza et al. [31], which explores the effect of heating rates on solar pyrolysis of Luffa Cylindrica biomass. The author stated that in order to maximize solid yields, the thermal degradation of biomass at a relatively low heating rate provides enough time for the repolymerization process.

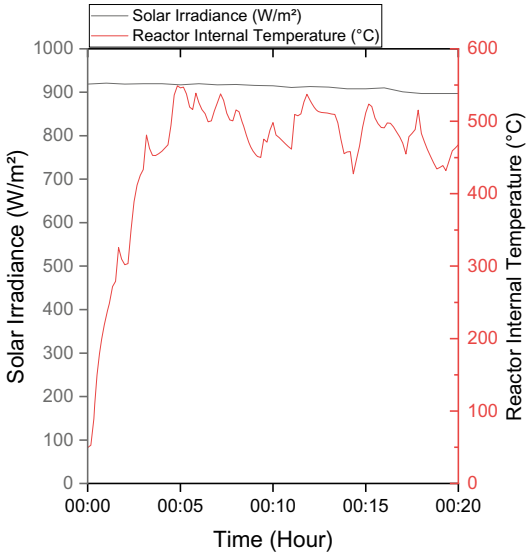

(a)

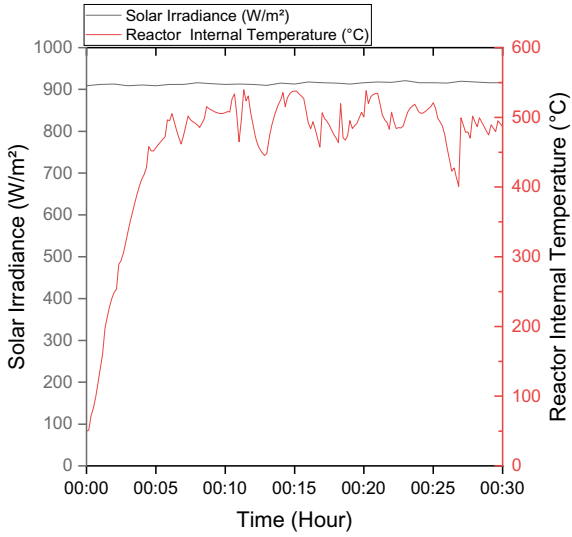

(b)

Fig. 5 Solar irradiance and pyrolysis temperature profile for residence time **a** 20 min **b** 30 min

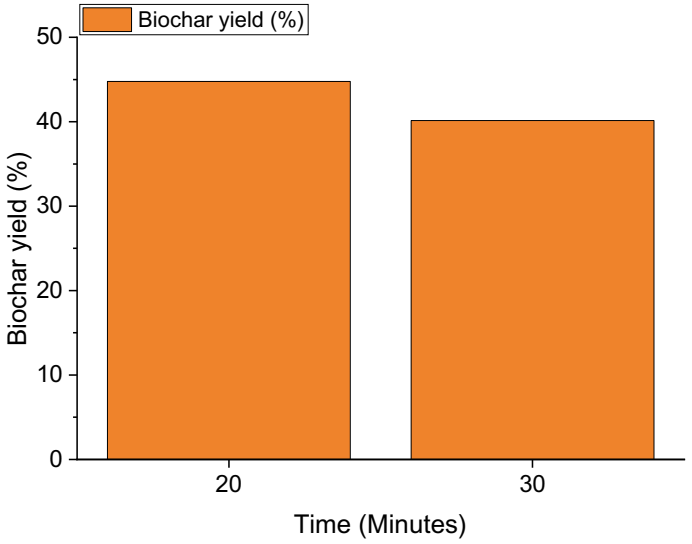

Fig. 6 Biochar yield and residence time

4 Conclusion

In this preliminary study, the feasibility of converting empty fruit bunches (EFB) into biochar via solar pyrolysis using a Fresnel lens was explored. Under zero-load conditions, there was a consistent correlation between solar irradiance, ambient temperature, and the reactor's internal temperature. During the solar pyrolysis tests, the Fresnel lens effectively concentrated solar energy, keeping the reactor's temperature around 500 °C, ideal for pyrolysis. Furthermore, with residence times between 20 and 30 min, the biochar yields of 40–45% exhibited comparable yields to that of conventional heating approaches. The results highlight the feasibility of solar pyrolysis in Malaysia, thereby suggesting its potential to significantly contribute to sustainable waste management practices and the utilization of renewable energy. In the future, strategies to enhance system performance and overall efficiency need to be included to address the intermittent nature of solar energy.

Acknowledgements This research was funded by a grant Fundamental Research Grant Scheme from the Ministry of Higher Education of Malaysia (FRGS Grant Number: FRGS/1/2021/TK0/UMT/02/2).

Author Contribution **Alia Syafiqah Abdul Hamed:** Conceptualization, Writing-Original draft preparation, Methodology, Data curation. **Nurul Iffah Farhah Mohd Yusof:** Resources, Investigation. **Muhammad Syarifuddin Yahya:** Validation, Writing-Reviewing, and Editing. **Nurul Adilah Abdul Latiff:** Writing-Reviewing and Editing **Nur Farizan Munajat:** Supervision, Data Curation, Writing-Reviewing and Editing, Funding acquisition.

References

1. Kadir APG (2022). Overview of the Malaysian oil palm industry 2022. Retrieved from https://bepi.mpob.gov.my/images/overview/Overview2022.pdf. Accessed on 30 July 2023
2. Su G, Mohd Zulkifli NW, Ong HC, Ibrahim S, Bu Q, Zhu R (2022) Pyrolysis of oil palm wastes for bioenergy in Malaysia: a review. Renew Sustain Energy Rev 164
3. Onoja E, Chandren S, Abdul Razak FI, Mahat NA, Wahab RA (2019) Oil palm (Elaeis guineensis) biomass in Malaysia: the present and future prospects. Waste Biomass Valoriz 10:2099–2117
4. Zamri MFMA, Milano J, Shamsuddin AH, Roslan MEM, Salleh SF, Rahman AA, Bahru R, Fattah IMR, Mahlia TMI (2022) An overview of palm oil biomass for power generation sector decarbonization in Malaysia: progress, challenges, and prospects. Wiley Interdiscip Rev Energy Environ 11
5. Loh SK (2017) The potential of the Malaysian oil palm biomass as a renewable energy source. Energy Convers Manag 141:285–298
6. Umar MS, Jennings P, Urmee T (2014) Renewable energy from oil palm biomass in Malaysia: the feed- in tariff policy framework. Biomass Bioenergy Sci Direct Biomass Bioenergy 2:37–46
7. Omar R, Idris A, Yunus R, Khalid K, Aida Isma MI (2011) Characterization of empty fruit bunch for microwave-assisted pyrolysis. Fuel 90:1536–1544
8. Salema AA, Ani FN (2012) Pyrolysis of oil palm empty fruit bunch biomass pellets using multimode microwave irradiation. Biores Technol 125:102–107
9. Salema AA, Yeow YK, Ishaque K, Ani FN, Afzal MT, Hassan A (2013) Dielectric properties and microwave heating of oil palm biomass and biochar. Ind Crops Prod 50:366–374
10. Hossain MA, Jewaratnam J, Ganesan P, Sahu JN, Ramesh S, Poh SC (2016) Microwave pyrolysis of oil palm fiber (OPF) for hydrogen production: parametric investigation. Energy Convers Manag 115:232–243
11. Liew RK, Nam WL, Chong MY, Phang XY, Su MH, Yek PNY, Ma NL, Cheng CK, Chong CT, Lam SS (2018) Oil palm waste: an abundant and promising feedstock for microwave pyrolysis conversion into good quality biochar with potential multi-applications. Process Saf Environ Prot 115:57–69
12. Sulaiman F, Abdullah N (2011) Optimum conditions for maximising pyrolysis liquids of oil palm empty fruit bunches. Energy 36:2352–2359
13. Jeong JY, Lee U, Do Chang WS, Jeong SH (2016) Production of bio-oil rich in acetic acid and phenol from fast pyrolysis of palm residues using a fluidized bed reactor: influence of activated carbons. Bioresour Technol 219, 357–364
14. Sukiran MA, Loh SK, Bakar NA (2018) Conversion of pre-treated oil palm empty fruit bunches into bio-oil and bio-char via fast pyrolysis. J Oil Palm Res 30:121–129
15. Abnisa F, Arami-Niya A, Wan Daud WMA, Sahu JN, Noor IM (2013) Utilization of oil palm tree residues to produce bio-oil and bio-char via pyrolysis. Energy Convers Manag 76:1073–1082
16. Chow LW, Tio SA, Teoh JY, Lim CG, Chong YY, Thangalazhy-Gopakumar S (2018) Sludge as a relinquishing catalyst in co-pyrolysis with palm empty fruit bunch fiber. J Anal Appl Pyrolysis 132:56–64
17. Ferreira MFP, Oliveira BFH, Pinheiro WBS, Correa NF, França LF, Ribeiro NFP (2020) Generation of biofuels by slow pyrolysis of palm empty fruit bunches: Optimization of process variables and characterization of physical-chemical products. Biomass Bioenergy 140:105707
18. Ndukwu MC, Horsfall IT, Ubouh EA, Orji FN, Ekop IE, Ezejiofor NR (2021) Review of solar-biomass pyrolysis systems: focus on the configuration of thermal-solar systems and reactor orientation. J King Saud Univ Eng Sci 33:413–423
19. Rahman MA, Parvej AM, Aziz MA (2021) Concentrating technologies with reactor integration and effect of process variables on solar assisted pyrolysis: a critical review. Therm Sci Eng Progr 25:100957
20. Zeng K, Gauthier D, Soria J, Mazza G, Flamant G (2017) Solar pyrolysis of carbonaceous feedstocks: a review. Sol Energy 156:73–92

21. Parthasarathy P, Al-Ansari T, Mackey HR, Sheeba Narayanan K, McKay G (2022) A review on prominent animal and municipal wastes as potential feedstocks for solar pyrolysis for biochar production. Fuel 316:123378
22. Xie WT, Dai YJ, Wang RZ, Sumathy K (2011) Concentrated solar energy applications using Fresnel lenses: a review. Renew Sustain Energy Rev 15:2588–2606
23. Solcast: Solcast API Toolkit. Retrieved from https://toolkit.solcast.com.au/historical. Accessed on 15 July 2023
24. Muzathik AM (2013) Potential of global solar radiation in Terengganu Malaysia. Int J Energy Eng (IJEE) 3:130–136
25. Hijazi A, Boyadjian C, Ahmad MN, Zeaiter J (2018) Solar pyrolysis of waste rubber tires using photoactive catalysts. Waste Manage 77:10–21
26. Martins MPB, Hori CE, Barrozo MAS, Vieira LGM (2022) Solar pyrolysis of spirulina platensis assisted by Fresnel lens using hydrocalumite-type precursors. Energies (Basel). 15
27. Qureshi KM, Kay Lup AN, Khan S, Abnisa F, Wan Daud WMA (2021) Optimization of palm shell pyrolysis parameters in helical screw fluidized bed reactor: effect of particle size, pyrolysis time and vapor residence time. Clean Eng Technol 4
28. Sohaib Q, Habib M, Fawad Ali Shah S, Habib U, Ullah S (2017) Fast pyrolysis of locally available green waste at different residence time and temperatures. Energy Sour Part A: Recov Utiliz Environ Effects 39:1639–1646
29. Zeaiter J, Ahmad MN, Rooney D, Samneh B, Shammas E (2015) Design of an automated solar concentrator for the pyrolysis of scrap rubber. Energy Convers Manag 101:118–125
30. Mohamed AR, Hamzah Z, Daud MZM, Zakaria Z (2013) The effects of holding time and the sweeping nitrogen gas flowrates on the pyrolysis of EFB using a fixed bed reactor. Procedia Eng 53:185–191
31. De Souza PHC, Rocha SDF, de Rezende DB (2022) Luffa cylindrica slow pyrolysis and solar pyrolysis: impact of temperature and heating rate on biochar properties and iodine adsorption performance. Waste Biomass Valorizat

The Effect of Carbonization on the Quality Characteristics of Empty Fruit Bunch Briquettes and Biomass Producer Gas

Munira Mohamed Nazari, Mohamad Yusof Idroas, and Muhamad Azman Miskam

Abstract Developing a briquette made from empty fruit bunch (EFB) fibers and using it as a source to produce biomass gas is one of the potential ways to solve the waste management issue of palm oil EFB in the palm oil industry. At the same time, it will also contribute to diversifying the alternative renewable energy sources in Malaysia as encouraged by the government through sustainable development goals (SDG) plans. However, briquetting raw EFB fibers is challenging due to the properties that contain lignin and cellulose content and lower combustion characteristics produced by the briquette. Therefore, thermochemical pretreatment of EFB through the carbonization process could remove this limitation. This study aims to evaluate the quality characteristics of carbonized EFB briquette and its effects on the quality of the biomass producer gas (BPG) produced. Experiments were conducted by carbonizing the raw EFB fibers with a temperature and heating time range of 350–400 °C and 40–60 min, blended with tapioca starch as a binder, and densified into a briquette. Briquettes were then combusted in the downdraft gasifier to produce the BPG. From the analysis of the carbonized EFB briquettes, results indicate the high heating value (HHV) ranged from 21.39 to 23.62 MJ/kg, and fixed carbon and ash content varied from 50.89 to 56.94% and 7.49 to 10.93%, respectively. This study also discussed the relationship of the HHV with fixed carbon and ash content in producing BPG. Overall, carbonization treatments reduce the generation of tar, and the quality of BPG increases when the carbonized EFB briquettes are gasified.

M. M. Nazari (✉)
Centre of Excellence for Biomass Utilization, Universiti Malaysia Perlis, 02100 Arau, Perlis, Malaysia
e-mail: muniranazari@unimap.edu.my

M. M. Nazari · M. Y. Idroas · M. A. Miskam
School of Mechanical Engineering, Universiti Sains Malaysia, 14300 Nibong Tebal, Pulau Pinang, Malaysia
e-mail: meyusof@usm.my

M. A. Miskam
e-mail: azman@usm.my

H. L. Ong et al. (eds.), *Proceedings of the 3rd International Conference on Biomass Utilization and Sustainable Energy; ICoBiomasSE 2023; 4–5 September; Kuala Lumpur, Malaysia*, Green Energy and Technology,
https://doi.org/10.1007/978-981-99-9164-8_7

Keywords Carbonization · Briquette · Empty fruit bunch · Biomass producer gas

1 Introduction

The palm oil industry is Malaysia's second largest agricultural industry; in 2021, the total oil palm planted area was recorded at 5.74 million hectares [1]. However, this also leads to this industry as the primary biomass source in Malaysia, and the supply is abundant. Due to the enormous amounts of biomass generated, Malaysia has the potential to utilize biomass and biogas as a source of renewable energy and biomass, mainly empty fruit bunch (EFB) fibers, which is a promising alternative source of raw materials. At the same time, it will also contribute to diversifying the alternative renewable energy sources in Malaysia as encouraged by the government through sustainable development goals (SDG) plans.

Converting EFB fibers into briquette, also known as solid fuel, offers excellent potential as an alternative to renewable energy [2]. However, briquetting raw EFB fibers is challenging due to the properties that contain lignin and cellulose content and lower combustion characteristics produced by the briquette. Therefore, thermochemical pretreatment of EFB fibers through carbonization could remove this limitation. This pretreatment was selected as it offered the production of high-value fuels and environmentally friendly waste disposal [3]. Besides that, pretreatment on biomass is needed to increase the energy content and grind ability [4].

There are many studies using thermochemical pretreatment that have been conducted. However, most of these used the method as a biomass pretreatment step in biogas production. Few studies have considered the benefits of the resulting solid. So, the focus of this study is to emphasize upgrading solid material into solid fuel. In this work, carbonized EFB fibers were used to produce the briquettes, and then the briquettes were combusted to produce biomass producer gas (BPG).

The main objective of this study is to investigate the effect of carbonization treatment at different residence times, which are 40, 50 and 60 min, on the quality characteristics of the EFB briquettes and BPG. The excellent quality of the briquettes is described as having feasible sizes used for transportation purposes, higher density and energy content [5]. A good quality briquette also needs low moisture and ash content to receive a uniform and complete combustion process [6]. Based on the results of the briquette quality, generating a good quality BPG is possible, which can then be used as dual fuel with diesel in the combustion chamber.

2 Materials and Methods

2.1 Materials

The collected raw EFB fibers from Taclico Company Sdn Bhd, Kulim, Kedah, were used in this work. Before the raw EFB fibers were chipped into smaller pieces, the raw materials needed to dry under the sun for 3–5 days. For the briquetting process, an organic binder, tapioca starch, is selected as a binding agent.

2.2 Apparatus and Experimental Procedure

This research was done at the Bio-energy Laboratory at the School of Mechanical Engineering, Universiti Sains Malaysia. The first process starts with carbonization treatment on the dried EFB fibers. The EFB fibers were carbonized at the temperature range of 350–400 °C using a rotary carbonizer, as shown in Fig. 1(i) which are equipped with a thermocouple and temperature controller. In this process, 1 kg of fibers was loaded into the machine, and with a controlled speed of 30 rpm, the rotary carbonized was heated into the targeted temperature. After that, the fibers were held for a further 40, 50 and 60 min, respectively, based on the treatment time before the machine was cooled to the ambient temperature. The result of the carbonization treatment on the fibers is shown in Fig. 1(ii). From this process, there is about 300 g of carbonized EFB were produced.

Next, the briquette was produced by manually densified the carbonized fibers mixed with starch solution (tapioca flour/water) in a ratio of 100:110/20. Figure 2 shows the briquette produced using cylindrical mold of 3 × 3 cm. Briquettes were then kept in the tight container to reduce moisture absorption from surrounding humidity.

After briquettes were analyzed, the experiment is continued to produce BPG through gasification process set up as shown in Fig. 3. In this experiment, about 5

(i) (ii)

Fig. 1 (i) Rotary carbonizer. (ii) Carbonized EFB fibers

Fig. 2 Carbonized EFB briquettes

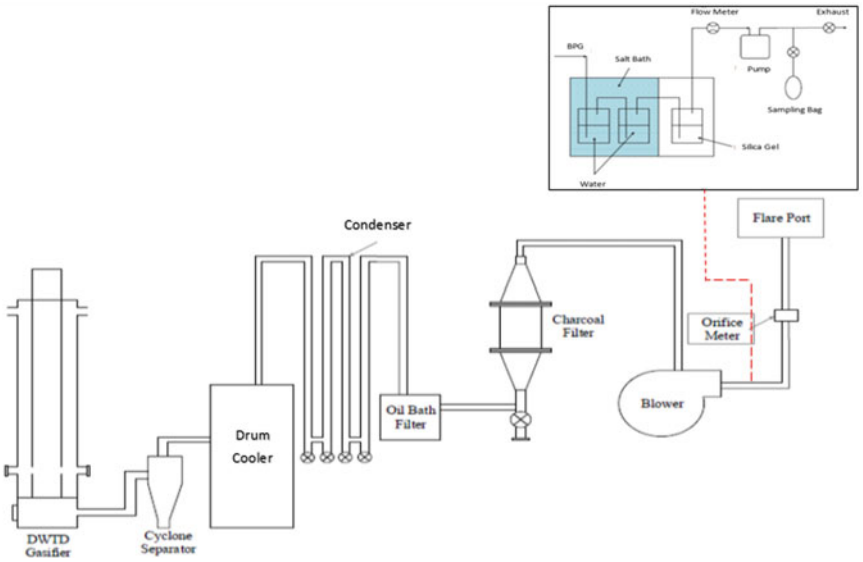

Fig. 3 Schematic diagram of the gasification process set up

kg feed/h of the optimum carbonized EFB briquettes were combust in the downdraft gasifier. The BPG flowed out from the gasifier through the outlet port and went through cooling system before it was filtered by the oil bath and charcoal filters. To assess the gas component, the BPG was collected using a gas sampling bag.

2.3 Analysis

The analysis of this study is divided into two parts: analysis of the briquette and analysis of the biomass producer gas. To determine the quality of the briquette, physical, proximate, ultimate and high heating value (HHV) analysis were conducted. All the analysis was replicated three (3) times, and their mean values were taken. The physical analysis which is to determine the maximum compressive load of the briquette was measured using a universal testing machine (5969–50kN Electro-Mechanical UTM). Proximate analysis was carried out to determine the amount of fixed carbon (FC), volatile matter (VM), ash content (AC) and moisture content (MC). The analysis was done by using a Thermogravimetric Analyzer (TGA) Pyris 1 (Perkin Elmer, USA) according to ASTM standards. For ultimate analysis using an Elemental Analyzer Agilent module 4890, the analysis was done to determine the composition of carbon, hydrogen, nitrogen and sulfur contents. Lastly, the HHV was measured using a Nenken 1013-B bomb calorimeter.

This study performs extended analysis on the gas components of the biomass producer gas produced using Agilent module 4890 gas chromatography (GC). Through this analysis, the quality of the producer gas is determined from the percentage of the gas components such as carbon monoxide (CO), carbon dioxide (CO_2), hydrogen (H_2), oxygen (O_2), nitrogen (N_2) and methane (CH_4).

3 Results and Discussions

3.1 Physicochemical Properties

The effects of carbonization treatment on the quality characteristics of the carbonized EFB briquettes were assessed through physicochemical properties analysis which are including physical, proximate, ultimate and high heating value analysis. In order to see the effect of the carbonization process, the results are compared to raw EFB briquette except for physical analysis.

Physical Analysis. Table 1 gives that the maximum compressive load of the carbonized EFB briquette produced from different carbonization time found to be in the range of 380–515 N. The lowest was found 380 N in carbonized EFB briquette produced from 40 min carbonization treatment, while the maximum was found 515 N in carbonized EFB briquette produced from 60 min carbonization treatment.

From the results in Table 1, carbonized time influences the physical strength of the briquette. This is because carbonization improves raw materials grind ability and reduces EFB fibers' size. Thus, it will produce a higher density briquette material. When the carbonized time is higher and more prolonged, depolymerization and devolatilization occur, where the lignin of the raw material is softened and causes

Table 1 Effect of carbonization treatment on the maximum compressive load of the carbonized EFB briquette

Carbonization treatment	Carbonized time (min)	Maximum compressive load (N)
T1	40	380
T2	50	431
T3	60	515

the material to be more suitable for briquetting. Softened lignin of the raw materials helps in the compaction of the briquette [7].

Proximate Analysis. The results on the effect of carbonization treatment on the fixed carbon, volatile matter, ash content and moisture content of the carbonized EFB briquettes produced from different carbonization time are given in Table 2. It was observed that the carbonization treatment changes the proximate properties compared to the briquette produced from raw EFB and thus enhances the quality of the EFB briquettes made through the high value of fixed carbon and low moisture content.

From the results in Table 2, the fixed carbon for briquettes with carbonization treatment was found to be 50.891–56.938%. As reported by Du et al. [8], high fixed carbon content is important for the gasification process because it will substantially contribute to thermal energy release when burned. So that, fixed carbon content in briquette properties becomes the critical parameter in determining the quality of biomass producer gas produced. Even though the carbonized briquette might be difficult to ignite due to the low volatile matter but it will have less smoke.

Besides that, carbonization treatments also produced a low moisture content of EFB briquette compared to raw EFB briquette. In this study, moisture content was found to decrease with carbonized time increased from 40 to 60 min, which are 8.268, 7.143 and 5.715%, respectively. Low moisture content is required because a higher moisture content value will affect the HHV of the briquettes [9].

On the other hand, carbonization treatments were observed to increase the ash content which is in the range of 7.493–10.927% compared to raw EFB briquette which is only 6.43%. This shows that the carbonized EFB briquettes are not fully combusted due to increased residue after the oxidation reaction.

Table 2 Effect of carbonization treatment on the fixed carbon, volatile matter, ash content and moisture content of the briquette

Component (wt.%)	Treatment			
	Raw	T1 (40 min)	T2 (50 min)	T3 (60 min)
Fixed carbon	13.05	50.891	54.438	56.938
Volatile matter	80.21	32.126	29.741	26.42
Ash content	6.43	7.493	8.742	10.927
Moisture content	15.8	8.268	7.143	5.715

Ultimate Analysis and High Heating Value. The results of carbonization treatment on the carbon, hydrogen, nitrogen, oxygen and sulfur are listed in Table 3. The result of the HHV is also listed in the same table as it is correlated with the ultimate composition of the solid. It was observed that the carbonization treatment improved the EFB briquettes properties and energy densities compared to the raw EFB briquette. Carbonized EFB briquette with T2 treatment which is briquette produced from carbonized time 50 min appears as the best quality briquette in this study as it produced the highest HHV of 23.62 MJ/kg.

From the results in Table 3, carbonization treatment increased the carbon content and decreased the EFB briquettes' oxygen content. High carbon and low oxygen compositions indicate that energy densities of the EFB briquette will increase as these two compositions are the main contributors to the heat energy release of biomass material. This is proven as the HHV results of carbonized EFB briquettes with T2 treatment which are the composition of carbon (62.03%) and oxygen (33.281%) had the highest value compared to others. Table 3 also lists the composition of nitrogen and sulfur produced from the briquettes which will develop the formation of harmful emissions and forming ash. However, the sulfur and nitrogen content produced are below 1%, indicating minimal release of sulfur and nitrogen oxides into the atmosphere. Therefore, limiting the pollution effect from the briquette's combustion process [10].

The HHV results of the carbonized EFB briquettes in this study were also comparable with other previous briquette produced such as briquette prepared from torrefied rice husk and banana residue briquette as reported by Nazari et al. [11], which is 18.87 MJ/kg, torrefied rice husk (19.4 MJ/kg) and torrefied cotton stalk (16.9 MJ/kg) [12]. Furthermore, it also meets the HHV minimum requirement of about 17.5 MJ/kg for making commercial briquette as stated by DIN 51,731.

Furthermore, the HHV of the carbonized EFB briquette also affected the quality of BPG produced. Besides that, the low sulfur release from the carbonized EFB briquettes showed that carbonization treatment reduces tar's generation and thus increases the quality of BPG when the carbonized EFB briquettes are gasified.

Table 3 Effect of carbonization treatment on the carbon, hydrogen, nitrogen, oxygen, sulfur and HHV of the briquette

Properties		Treatment			
		Raw	T1 (40 min)	T2 (50 min)	T3 (60 min)
Ultimate analysis (%)	C	54.1	60.270	62.031	59.337
	H	5.85	4.035	3.9531	3.7169
	N	0.58	0.6353	0.6720	0.6002
	O (diff)	36.5	34.9869	33.2810	36.2576
	S	0.09	0.0728	0.0629	0.0591
HHV (MJ/kg)		17.66	21.39	23.62	22.46

3.2 Combustion Analysis

Figure 4 presented the derivative thermogravimetric (DTG) curves of raw and carbonized EFB briquette (T2). Only T2 was used for comparison with the raw briquette as T2 presented the higher HHV for the carbonization treatment. The curves showed the temperature range in the DTG curve can be divided into three zones which are 1st zone (<200 °C), 2nd zone (200–400 °C) and 3rd zone (400–800 °C). The 1st zone indicates the drying performance of the samples, the 2nd zone suggests the composition of most of the volatile materials and the 3rd zone indicates the complete combustion of fixed carbon content.

From the curves shown in Fig. 4, the combustion behavior of the carbonized EFB briquette showed improvement compared to the raw EFB briquette even though the results showed the drying performance in the 1st zone was similar for the raw and carbonized. It was observed that the T2 curve shifted to the right, showing that the degradation process of the T2 briquette was faster than the raw EFB briquette. A small DTG hump was also found to occur at around 150°C, indicating moisture removal for both samples. This shows that the fine fibers of EFB allow faster and more efficient evaporation [13].

In the 2nd zone, this zone indicates the decomposition stage, where most of the volatile material of the briquette is decomposed. The decomposition of hemicellulose and cellulose during the combustion process caused the chemical bond in EFB began to break and the lightest volatile compounds were released. It is clear that the higher peak at about 340 °C occurred in the DTG curves in Fig. 4 corresponds to the releasing and combustion of volatile matter from the carbonized EFB briquette at 50 min of carbonization treatment. Briquette with low decomposition of volatile matter should not be recommended as it may led to serious fouling and slagging problems in the combustion boiler [14].

For the 3rd zone, curves indicated complete combustion of fixed carbon content and the remaining material was considered as ash. At this stage, complete combustion

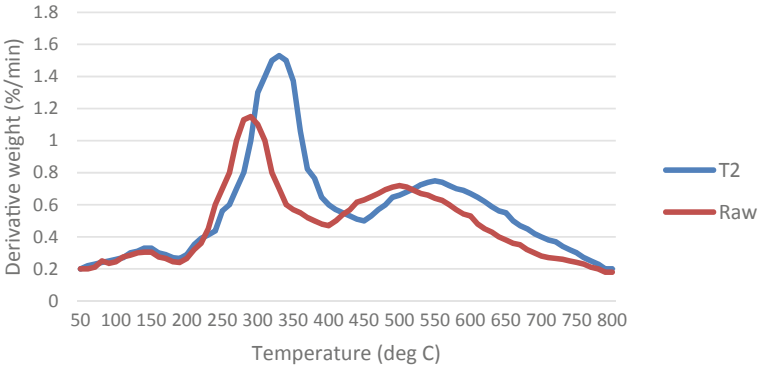

Fig. 4 DTG profile raw EFB briquette and T2 carbonized EFB briquette

Table 4 BPG components and LHV

Parameter		T2 carbonized EFB briquette
BPG composition (%)	Hydrogen	2.59
	Oxygen	28.68
	Nitrogen	36.56
	Carbon monoxide	2.86
	Methane	3.26
	Carbon dioxide	26.05
LHV (MJ/Nm^3)		1.89

of fixed carbon content corresponds to char oxidation and lignin decomposition [15]. From Fig. 4, the curves show the decomposition of lignin of T2 carbonized EFB briquette occurred at 450 °C, while raw EFB briquette decomposed early at 400 °C.

3.3 Gasification

Based on the analysis done using gas chromatography, results of the BPG compositions and the other parameters such as air flow rate, equivalent ratio, consumption rate and low heating value of the T2 carbonized EFB briquette are listed in Table 4. These parameters are generally used to determine the quality of the BPG. BPG consists of combustible gas which is CO, H_2 and CH_4 and non-combustible gas which are CO_2, O_2 and N_2. However, the LHV of producer gas was determined only based on the composition of the combustible gas.

From Table 4, it was calculated that the amount of LHV of this study BPG produced is only 1.89 MJ/Nm^3. LHV of BPG is influenced by the biomass characteristic of moisture content as high moisture content will decrease the LHV and residence time in the gasifier as higher residence time contributes to the production of CO and CH_4. Even though the value of the LHV of this BPG gets a minimum value, it shows the possibility of this BPG as another alternative renewable energy source. This BPG can be injected together with the diesel to combust the engine.

4 Conclusion

This study analysis thus verified that carbonization treatments had improved the physicochemical properties and energy density of the EFB briquettes compared with the raw EFB as briquette material. Besides that, the carbonized EFB briquette's quality is also influenced by the increment of carbonized time. In this study, the selection of T2 carbonized EFB briquette as the optimum carbonized time is decided as this briquette produced at 50 min of carbonization treatment has moderate properties

and the highest HHV. The findings of this study show that the carbonization treatment influences quality characteristics of the EFB briquettes and biomass producer gas, and the following conclusions can be drawn from this study:

i. For EFB briquette quality control, the physicochemical parameters such as compressive strength, fixed carbon, ash content and high heating value were found to be the best indicators of carbonization treatment applied.
ii. The physicochemical characteristics of the carbonized EFB briquettes assessed in this study showed the welcome development to produce high-quality biomass producer gas, especially based on the HHV produced by the briquette.
iii. Overall, the results obtained provide an essential reference for converting carbonized EFB briquettes into useful BPG for combustion engine application can be established.

References

1. MPOB (2022) Report on the overview of the Malaysian oil palm industry 2021
2. Biomass-SP (2011) EU-Malaysia biomass sustainable production initiative newsletter. 2
3. Mahendra R, Monoj KM (2022) Opportunities and challenges: chapter 13—biomass gasification: a step forward cleaner fuel and chemicals. Biofuel Bioenergy 253–276
4. Norfadhilah H, Tokimatsu K, Yoshikawa K (2019) Solid fuel from oil palm residues and municipal solid waste by hydrothermal treatment for electrical power generation in Malaysia: a review. Sustainability 11:1060
5. Aizuddin AR, Fauziah S, Nurhayati A (2014) The physical, chemical and combustion characteristics of EFB fuel briquettes. In: AIP conference proceedings, pp 1657
6. Oladeji J (2012) Comparative study of briquetting of few selected agro-residue commonly found in Nigeria. Pacific J Sci Technol 13(2):80–86
7. Tumuluru JS, Sokhansanj S, Wright CT, Hess JR, Boardman RD (2011) A review on classification and com-position, co-firing issues and pretreatment methods. Am Soc Agricult Biologic Eng (ASABE)
8. Du SW, Chen WH, Lucas JA (2014) Pretreatment of biomass by torrefaction and carbonization for coal blend used in pulverized coal injection. Bioresour Technol 161
9. Wang C, Wang F, Yang Q, Liang R (2009) Thermogravimetric studies of the behavior of wheat straw with added coal during combustion. Biomass Energy 33:50–56
10. Joseph OA, Francis K, Stephen JM (2012) Physico-chemical characteristics and market potential of sawdust charcoal briquette. Int J Energy Environ Eng 3:1–6
11. Nazari MM, Chin PS, Atan NA (2019) Combustion performance of biomass composite briquette from rice husk and banana residue. Int J Adv Sci Eng Inform Technol 9(2):455–460
12. Nam H, Capareda S (2015) Experiment investigation of torrefaction of two agricultural wastes of different composition using RSM (response surface methodology). Energy 91:507–516
13. Keat HY, Shafie SA, Al-attab KA, Zainal ZA (2018) Upgrading agricultural wastes using three different carbonization methods: thermal, hydrothermal and vapothermal. Biores Technol 265:365–371
14. Blasing M, Muller M (2013) Investigating of the effect of alkali metal sorbents on the release and capture of trace elements during combustion of straw. Combust Flame 160:3015–3020
15. Lapuerta M, Hernandez JJ, Rodriguez J (2004) Kinetics of devolatilization of forestry wastes from thermogravimetric analysis. Biomass Bioenerg 27:385–391

Biomass Conversion to Intermediates and Products

Physicochemical and Phytochemical Properties of MD2 Pineapple

Siti Mariam A. Rani, Lee Boon Beng, Nor Hidawati Elias, Mohd Khairul Ya'kub, Jantana Suntudprom, and Khairul Farihan Kasim

Abstract MD2 pineapple is one of the most popular pineapples because of its sweetness. The sweetness of the MD2 pineapple varies depending on the geographical location and cultivation technique, fruit parts, and maturity at harvest. This study focuses on the effect of maturity at harvest and the fruit parts used on the physicochemical and phytochemical properties of the MD2 pineapple. The pineapples were harvested at three different maturity stages, i.e. mature-green, ripe (50% yellow peel), and over ripe (100% yellow peel). Then, each pineapple was cut horizontally to obtain three different parts of the pineapple, namely the top, middle, and bottom and the juice was extracted from each part. The volume recovery percentage, total soluble solids (TSS), and pH were found to increase for each part from mature-green to overripe except for titratable acidity (TA) which decreases. Total phenolic content (TPC) and total flavonoid content (TFC) were found to increase from mature-green to ripe but decrease from ripe to over ripe fruit. The proteolytic activity increases,

S. M. A. Rani · L. B. Beng · N. H. Elias · K. F. Kasim (✉)
Faculty of Chemical Engineering & Technology, Universiti Malaysia Perlis, 02600 Arau, Perlis, Malaysia
e-mail: khairulfarihan@unimap.edu.my

S. M. A. Rani
e-mail: mariamrani@studentmail.unimap.edu.my

L. B. Beng
e-mail: bblee@unimap.edu.my

N. H. Elias
e-mail: norhidawati@ukm.edu.my

L. B. Beng · N. H. Elias · K. F. Kasim
Centre of Excellence for Biomass Utilization, Universiti Malaysia Perlis, 02600 Arau, Perlis, Malaysia

M. K. Ya'kub
Smart KJ Food Industries (Asia), Plt. Bandar Amanjaya, 08000 Sungai Petani, Kedah, Malaysia

J. Suntudprom
Faculty of Engineering and Technology, Department of Postharvest and Processing Engineering, Rajamangala University of Technology Isan, Nakhorn Ratchasima 30000, Thailand

H. L. Ong et al. (eds.), *Proceedings of the 3rd International Conference on Biomass Utilization and Sustainable Energy; ICoBiomasSE 2023; 4–5 September; Kuala Lumpur, Malaysia*, Green Energy and Technology,
https://doi.org/10.1007/978-981-99-9164-8_8

while vitamin C content decreases with fruit maturity. The total protein was found to be not significantly affected by fruit maturity. TSS, pH, and proteolytic activity show an increasing trend from the top to the bottom of the pineapple, while TA and vitamin C content show the opposite trend. The middle and bottom parts of the pineapple were found to have the highest proteolytic activity.

Keywords MD2 pineapple · Physicochemical · Phytochemical · Maturity at harvest · Horizontally cut

1 Introduction

The pineapple (*Ananas comosus*) of the Bromeliaceae family is a popular fruit that is widely consumed as a juice. A new hybrid, MD2, is one of the more popular varieties, and it is nicknamed 'Extra Sweet' or 'Golden Ripe' because of its thinner, golden-yellow peel, and flesh colour. The flesh has low fibre and acidity content, higher vitamin C content, and is noticeably sweeter than other varieties [1].

The physicochemical properties of pineapple include its pH value, titratable acidity (TA), and total soluble solids (TSS). TSS represent dissolved constituents in fruit juice mainly sugar components like fructose, glucose, and sucrose and these are measured in units of Brix. Sucrose is the primary sugar in pineapple juice, and it is the key contributor to the overall flavour [2]. Another property that influences flavour is TA, and it is a measure of the organic acid content in the pineapple. Notably, citric acid is one of the main organic acids present in pineapple fruit. TA is negatively correlated to pH, and pineapples typically have a pH of around 4.1 ± 0.0 [3].

Pineapples also contain various phytochemical components like vitamins and secondary phytochemical metabolites. Bromelain, phenolic compounds, flavonoids, and vitamin C are important bioactive molecules that give the nutritional value of a food product [4]. Bromelain is a complex of proteolytic enzymes that is uniquely present in pineapple fruits. The activity of these enzymes is measured as proteolytic activity [5]. Pineapple is also an important source of polyphenolic compounds and these compounds are commonly measured as equivalents of gallic acid [6]. The total phenolic content (TPC) of pineapple juice typically ranges from 33.3 to 78.9 mg/100 mL GAE [7–9]. Pineapple juice that contain 24.3–54.63 mg/100 mL vitamin C is known to be beneficial to human health.

The chemical composition in pineapple juice varies depending on the variety, growing climate and conditions, and post-harvest handling [1]. Therefore, determining the appropriate harvest time is crucial to ensure the maximum quantity and quality of the chemical and bioactive content in the fruit. According to post-harvest physiologists, fruits undergo three life stages: maturation, ripening, and senescence. Because this research focuses on the juice of the pineapple, pineapples at the ripening stage are used as they are better suited for juicing.

Literature detailing the examination of pineapple juice properties obtained from different parts of the fruit is still limited. Hence, the present work aims to discuss

the physicochemical and phytochemical properties of MD2 pineapple juice obtained from fruits at different maturity at harvest (mature-green, ripe, and over ripe) and parts of the fruit i.e. three cross sections (top, middle and bottom).

2 Materials and Methods

2.1 Chemicals and Reagents

Sodium hydroxide, di-sodium-hydrogen phosphate-12-hydrate, sodium dihydrogen phosphate 2-hydrate, gallic acid, sodium nitrate, aluminium chloride, metaphosphoric acid, ascorbic acid, and 2,6-dichlorophenol-indophenol were purchased from HmbG Chemicals, Germany. Citric acid, sodium carbonate, phenolphthalein, Bradford reagent, casein, and ethylene diamine tetraacetic acid (EDTA) were acquired from R&M, Malaysia. Bovine serum albumin was obtained from Nacalai Tesque, Japan, and trichloroacetic acid was obtained from Chemiz, Malaysia. Tyrosine was bought from Merck, Germany, while Folin-Ciocalteu's phenol reagent and sodium carbonate were purchased from Sigma-Aldrich, USA.

2.2 Sample Preparation

The MD2 pineapples were donated by Smart KJ Agro (Asia), Bukit Tangga, Kedah. The pineapples were collected at three different maturity stages; mature-green, ripe (50% yellow peel), and over ripe (100% yellow peel). The maturity index of pineapple studied was 3, 5 and 7, respectively, according to the Malaysian Federal Agricultural Marketing Authority (FAMA) [10]. After the crown, the pineapples were manually peeled with a kitchen knife and cut transversely into three parts; the top, middle, and bottom. Each part was processed using a slow juicer (BioChef Synergy BCSYN, Australia) to obtain the juice. Finally, the pineapple juice was filtered using a 40-mesh filter cloth to remove the pulp. The pineapple juice samples were kept in a freezer (Acson R134a, Malaysia) at −20 °C until further analysis.

2.3 Physicochemical Properties of MD2 Pineapple Juice

Juice volume. The pineapple juice yield was calculated as juice volume recovered over weight of pineapple part used and was expressed as a percentage.

Total soluble solids (TSS). The TSS value was determined in terms of degree Brix (°Brix) using a handheld refractometer (Atago PAL-1, Japan).

Titratable acidity (TA). The TA determination was carried out by titrating the diluted pineapple juice samples (1 mL juice with 5 mL distilled water) with 0.1 M NaOH. Phenolphthalein was added as an indicator. The titrated amount of NaOH was converted to g of citric acid per 100 mL of juice, as described in the work of Adulvitayakorn et al. [11].

pH value. The pH of the juice was measured at room temperature using a handheld pH metre (Hanna Instruments pHep H198107, Malaysia).

2.4 Phytochemical Properties of MD2 Pineapple Juice

Bradford Assay (Protein content). The protein content in the pineapple juice samples was determined using bovine serum albumin (BSA) as a standard curve and expressed in terms of BSA equivalent (mg of BSA/100 mL of juice) [9].

Proteolytic activity. The proteolytic activity of the juice was measured according to the method described in Banerjee et al. [12] which used tyrosine as a standard curve. 1 unit of protease activity was defined as 1 mg of tyrosine released per mL per minute of the sample when casein is hydrolysed for 10 min at 37 °C and pH 7.0.

Total phenolic content (TPC) and Total flavonoid content (TFC). The TPC of the pineapple juice was determined using the Folin-Ciocalteu's phenol reagent method [12] while TFC was determined using the aluminimiun trichloride method described in Adulvitayakorn et al. [11].

2,6-dichlorophenol-indophenol (DCPIP) visual titration method (Vitamin C). The amount of vitamin C expressed in mg/100 mL ascorbic acid was determined according to the method described in Hassan and Joshi [13].

2.5 Statistical Analysis

All measurements were carried out in triplicate and reported as a mean with standard deviation. One-way Analysis of Variance (ANOVA) was carried out using Minitab version 17 software (Minitab Inc., USA) to compare between mean values of the data. Tukey's post-hoc test determines the individual significance differences between samples.

3 Results and Discussion

3.1 Effect of Maturity at Harvest on Physicochemical Properties of the MD2 Pineapple Juice

Figure 1 shows the effect of fruit maturity on the physicochemical properties of MD2 pineapple juice. Most physicochemical properties of the pineapple juice (TSS, TA, and pH) are affected by fruit maturity except for percentage of juice recovered. The average percentage of juice recovery is 72%, TSS is 11.4° Brix, and TA is 0.61 g/100 mL citric acid equivalent. The pH is measured to be in the range of 3.7–4.2. The high TSS and low TA values in MD2 pineapple indicates that the pineapple juice is less sour and more palatable [16].

The results of TSS, TA, and pH in this research are comparable to those reported for Moris cultivar and MD2 from Ghana [8, 14]. The mature-green pineapple has the highest acidity. The acid concentration was found to reduce with fruit maturity due

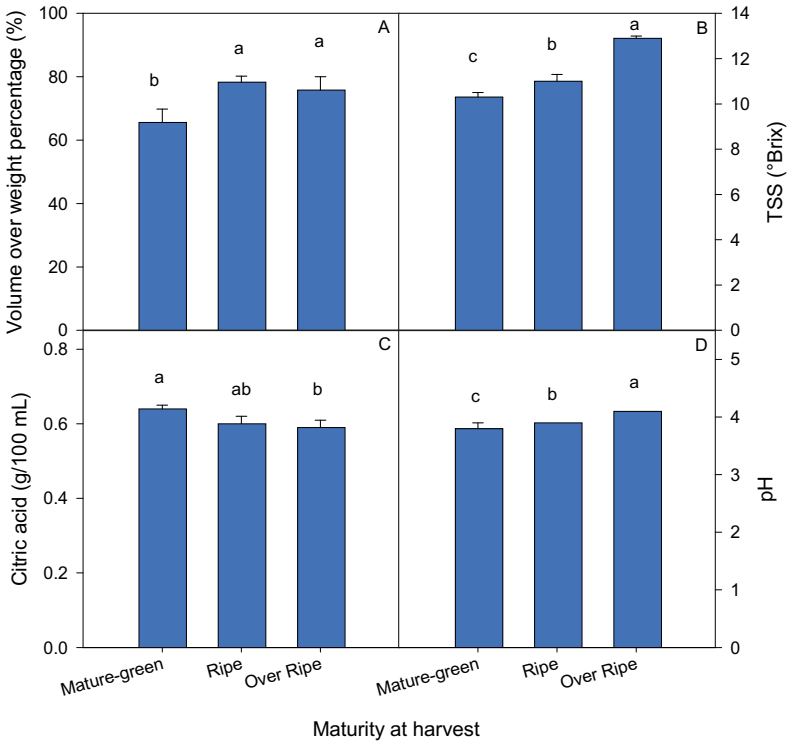

Fig. 1 Effect of MD2 pineapple maturity on physicochemical properties of the juice. **a** Volume recovered, **b** TSS, **c** TA and **d** pH. Data is represented as a mean ± SD ($n = 3$)

to the use of organic acids in the respiration process which converts it into sugar. This also results in an increase of the concentration of TSS. The decrease in TA causes the increase in pH during the ripening stage.

3.2 *Effect of Maturity at Harvest on Phytochemical Properties of the MD2 Pineapple Juice*

Figure 2 shows the effect of pineapple maturity on the phytochemical properties of the juice. There was no significant difference ($p > 0.05$) in the protein content of juice from MD2 pineapple harvested at different maturities. The mean protein content, TPC, and TFC are 81.1 mg of BSA, 76.1 mg GAE, and 66.5 mg/100 mL QE, respectively. The protein content only decreased by 1.8% from mature-green to over ripe, making the difference insignificant. The TPC value obtained is comparable to that reported in the finding by Du et al. [15] (72.57 mg GAE/100 g) for MD2 pineapple planted in China. The TPC value increased 11% from mature-green to ripe but decreased by 3% to over ripe with significant difference ($p < 0.05$). The trend continues for TFC and it is always just below the TPC as TFC also contributes to the TPC value [16].

The content of other phytochemicals in MD2 pineapple juice that are significantly affected ($p < 0.05$) by fruit maturity is vitamin C and proteolytic activity (Fig. 2d, e). Vitamin C content is noted to decrease with fruit ripening. The vitamin C content, measured as ascorbic acid, are 64.3, 55.9, and 33.7 mg per 100 mL for mature-green, ripe, and over ripe, respectively, and the values are again statistically different. The vitamin C content is found to be reduced after the ripening stage because the ascorbic acid had been converted into 2–3-dioxy-L-gluconic acid by the ascorbic acid dehydrogenase enzyme [17]. However, the proteolytic activity of MD2 pineapple juice from mature-green fruit was found to be the lowest (0.16) followed by ripe (0.22) and finally over ripe (0.25 CDU/mL). In conclusion, proteolytic activity increases with fruit maturity, since the enzyme becomes more active with fruit ripening [18].

3.3 *Effect of Pineapple Cross-Sectional on Physicochemical Properties of the MD2 Pineapple Juice*

The effect of different MD2 pineapple part (top, middle, and bottom part) on the physicochemical properties of the juice is shown in Fig. 3. For all maturity indexes, the middle part of the fruit always resulted in the highest percentage of juice yield (70.3, 82.7, and 75.1% for mature-green, ripe, and over ripe, respectively). However, the differences are negligible as they are statistically insignificant ($p > 0.05$). This tells that different cross section of pineapples effectively result in the same percentage of juice yield.

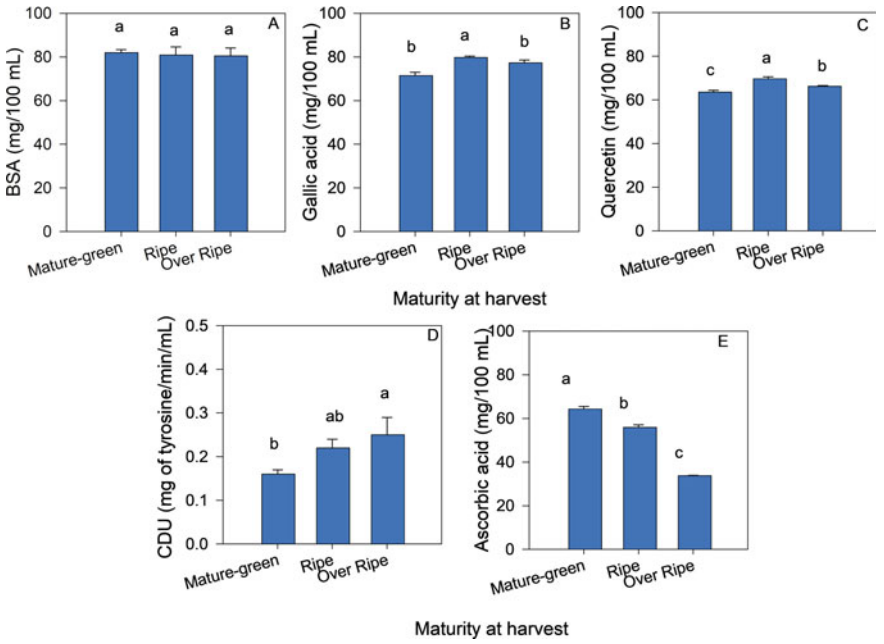

Fig. 2 Effect of MD2 pineapple maturity indexes on phytochemical properties of the juice. **a** Protein content, **b** TPC, **c** TFC, **d** proteolytic activity and **e** vitamin C. Data is represented as the mean ± SD ($n = 3$)

However, juice obtained from different cross sectionals of the MD2 pineapple have statistically different ($p < 0.05$) TSS, TA, and pH. The TSS value (10.4–12.3°Brix) and pH (3.7–4.2) increased, while TA decreased (0.7–0.6 g/100 mL citric acid) from the top to the bottom part of the pineapple. A plausible explanation for these findings is that the pineapple reaches maturity from the bottom-up and therefore the TSS value of bottom part is the highest because starch is converted to monosaccharides during ripening, thus increasing the TSS value [19]. For the same reason, the bottom part has the lowest TA value because TA decreases as maturity level increases [20]. As the MD2 pineapple fruit ripens from the bottom part (12–100% yellow), TA reduces by 15.4% from top to bottom due to the decrease in acidity. This is because as the fruit matures, the amount of sugars in the juice increases [21]. The pH also increases with maturity and it increases slightly from top to bottom. The bottom part is expected to be more palatable because it has a higher sugar content (higher TSS) and a lower acidity (low TA) [22].

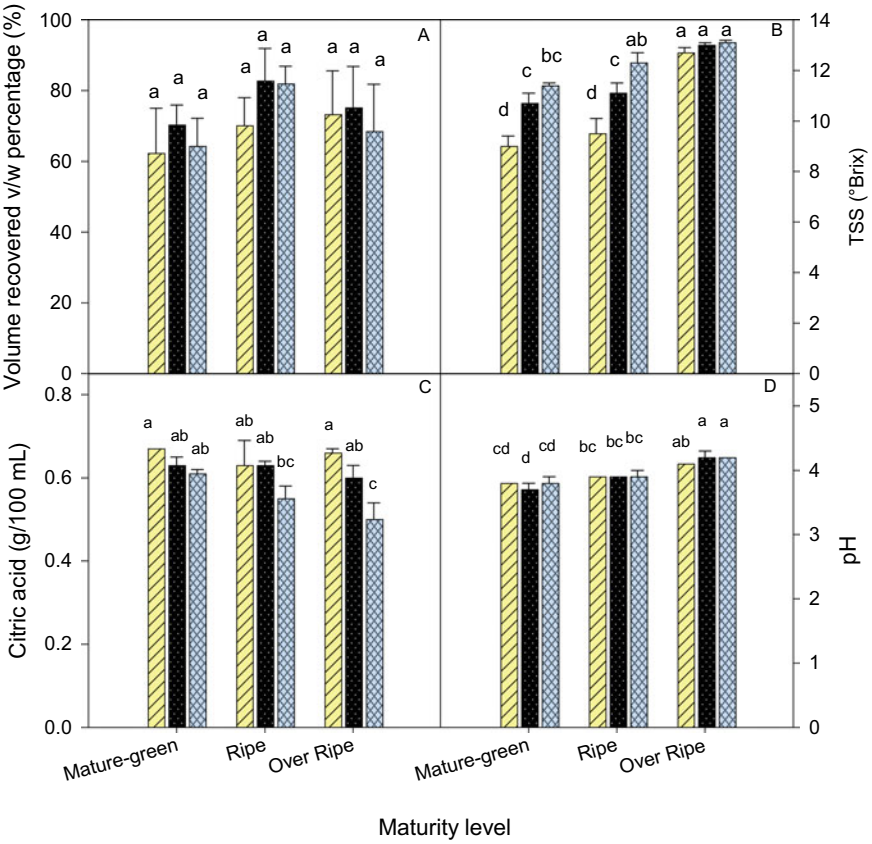

Fig. 3 Physicochemical properties of pineapple juice based on fruit parts. **a** Volume recovered, **b** TSS, **c** TA and **d** pH for the top ( ), middle ( ) and bottom ( ) parts of the pineapple. The data is presented as a mean ± SD ($n = 3$)

3.4 *Effect of Pineapple Cross-Sectional on Phytochemical Properties of the MD2 Pineapple Juice*

Figure 4 shows the concentration of the phytochemical properties in the juice obtained from different cross sections of the MD2 pineapple. Similar to the fruit maturity analysis in Sect. 3.2, protein content also shows the same trend from the top to the bottom of the pineapple ($p > 0.05$). The protein content, TPC, and TFC in MD2 pineapple juice obtained from different parts of the fruit ranged from 77.6 to 86.5 mg/100 mL BSA, 67.8 to 83.3 mg/100 mL GAE, and 61.2 to 74.3 mg of QE, respectively.

The difference in proteolytic activity and vitamin C concentration of the juice obtained from each different cross section of the pineapple is significant ($p < 0.05$), drawing parallels to the result of the fruit maturity analyses discussed in Sect. 3.2. The middle and bottom sections have higher proteolytic activity compared to the

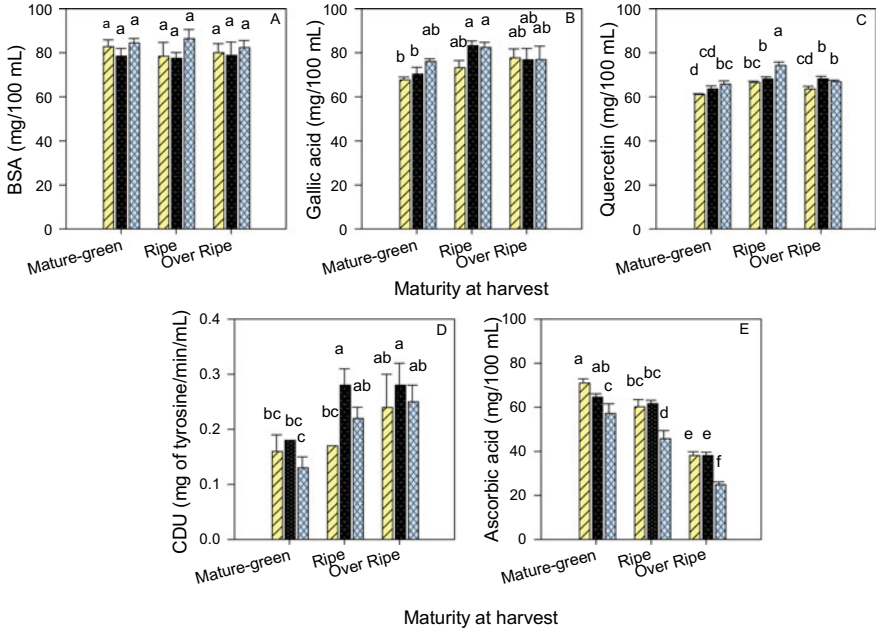

Fig. 4 Phytochemical properties of pineapple juice as a function of maturity level. **a** Protein content, **b** TPC, **c** TFC, **d** proteolytic activity, and **e** vitamin C for the top ( ), middle ( ) and bottom ( ) parts of the pineapple. Data is presented as a mean ± SD ($n = 3$)

top, except in the mature-green fruit (Fig. 4d), and it is again due to the pineapple fruit maturing from the bottom-up. The parts which mature first will have the higher proteolytic activity. As expected, the bottom part of the fruit regardless of maturity index have the lowest concentration of vitamin C (Fig. 4e) and the overall results show that vitamin C content decreases from the top to the bottom of the pineapple. This also corresponds to the observed reduction in TA reduction, since vitamin C is acidic [17].

4 Conclusion

Considerable variation was observed in the physicochemical and phytochemical properties of the juice of MD2 pineapples harvested at different maturity levels and from different cross sections. The percentage of juice yield and protein content did not show any significant differences between all fruit maturity levels (mature-green, ripe, and over ripe) and cross sections (top, middle, and bottom). TSS, pH, TPC, TFC, and proteolytic activity increased significantly from mature-green to over ripe, while TA and vitamin C decreased. The ripened fruits are healthier because they have higher TPC, TFC, and proteolytic activity and are also more palatable as they have

higher TSS and lower TA. However, the ripened fruits also have lower vitamin C content compared to mature-green pineapples. The bottom part of the fruit matures first followed by the middle and then the top, and the physicochemical and phytochemical properties of the different fruit cross sections are comparable to those of the fruit different maturity levels. Consumer acceptance and preference of MD2 pineapples will vary due to the variations in physiochemical and phytochemical properties. Significantly, this study creates an opportunity for food processors to manipulate the harvest time and use suitable parts of the MD2 pineapple fruit to improve their product and make it more palatable to consumers.

Acknowledgements The authors would like to thank Universiti Malaysia Perlis (UniMAP) for providing the facilities, technical support and financial support (University–Private Matching Fund (UniPRIMA) (9001-00637 and 9002-00114) for this work.

References

1. Ali M, Hashim N, Abd Aziz S, Lasekan O (2020) Pineapple (Ananas comosus): a comprehensive review of nutritional values, volatile compounds, health benefits, and potential food products. Food Res Int 137:109675
2. Wu W, Xiao G, Yu Y, Xu Y, Wu J, Peng J, Li L (2021) Effects of high pressure and thermal processing on quality properties and volatile compounds of pineapple fruit juice. Food Control 130
3. Adda C, Latifou AB, Ahyi V (2023) Microbiological and physicochemical evaluation of pineapple fruit and its juice for compliance with export requirements. Asian Food Sci J 22:11–19
4. Shourove JH, Zzaman W, Chowdhury RS, Hoque MM (2020) Effect of thermal treatment on physicochemical stability and antioxidant properties of locally available underutilized star fruit juice. Asian Food Sci J
5. Varilla C, Marcone M, Paiva L, Baptista J (2021) Bromelain, a group of pineapple proteolytic complex enzymes (Ananas comosus) and their possible therapeutic and clinical effects: a summary. Foods 10. https://doi.org/10.3390/foods10102249
6. Islam Z, Tabassum S, Harun-ur-Rashid M, Vegarud GE, Alam MS, Islam MA (2021) Development of probiotic beverage using whey and pineapple (Ananas comosus) juice: sensory and physico-chemical properties and probiotic survivability during in-vitro gastrointestinal digestion. J Agric Food Res 4:100144
7. Saikia S, Mahnot NK, Mahanta CL (2016) A comparative study on the effect of conventional thermal pasteurisation, microwave and ultrasound treatments on the antioxidant activity of five fruit juices. Food Sci Technol Int 22:288–301
8. Difonzo G, Vollmer K, Caponio F, Pasqualone A, Carle R, Steingass CB (2019) Characterisation and classification of pineapple (Ananas comosus [L.] Merr.) juice from pulp and peel. Food Control 96, 260–270
9. Arampath P, Dekker M (2021) Thermal effect, diffusion, and leaching of health-promoting phytochemicals in commercial canning process of mango (Mangifera indica l.) and pineapple (Ananas comosus l.). Foods 10
10. FAMA webpage. Retrieved from https://www.fama.gov.my/documents/20143/0/Nanas.pdf/e228dc38-c796-ca4f-5d31-502d34f78540. Accessed on 9 Sept 2023
11. Adulvitayakorn S, Azhari SH, Hasan H (2020) The effects of conventional thermal, microwave heating, and thermosonication treatments on the quality of sugarcane juice. J Food Process Preserv 44:1–8

12. Banerjee S, Arora A, Vijayaraghavan R, Patti AF (2020) Extraction and crosslinking of bromelain aggregates for improved stability and reusability from pineapple processing waste. Int J Biol Macromol 158:318–326
13. Hassan MM, Joshi N (2020) Hydrothermal effects on physicochemical, sensory attributes, vitamin C, and antioxidant activity of frozen immature Dolichos lablab. Heliyon. 6:e03136
14. Rashima R, Azhar ME, Maizura M (2021) Influence of post-harvest physiology on sensory perception, physical properties, and chemical compositions of Moris pineapples (Ananas comosus L.). J Food Sci 86, 4159–4171
15. Du L, Sun G, Zhang X, Liu Y, Prinyawiwatkul W, Xu Z, Shen Y (2016) Comparisons and correlations of phenolic profiles and anti-oxidant activities of seventeen varieties of pineapple. Food Sci Biotechnol 25:445–451
16. Albuquerque TG, Nunes MA, Bessada SMF, Costa HS, Oliveira MBPP (2020) Biologically active and health promoting food components of nuts, oilseeds, fruits, vegetables, cereals, and legumes. Elsevier Inc.
17. Moldoveanu SC (2019) Pyrolysis of various derivatives of carboxylic acids. In: Pyrolysis of organic molecules. Elsevier, pp 635–696
18. Maulana I, Prabowo Soewondo BR, Prayitno R, Amelya W (2022) The effects of sugar, blanching, and pasteurization on the antioxidant properties of pineapple juice. KnE Life Sci 48–57
19. Ali M, Hashim N, Abd Aziz S, Lasekan O (2022) Quality prediction of different pineapple (Ananas comosus) varieties during storage using infrared thermal imaging technique. Food Control 138:108988
20. Rashima R, Maizura M, Wan Nur Hafzan WM, Hazzeman H (2019) Physicochemical properties and sensory acceptability of pineapples of different varieties and stages of maturity. Food Res 3, 491–500
21. Ding P, Syazwani S (2016) Physicochemical quality, antioxidant compounds and activity of MD-2 pineapple fruit at five ripening stages. Int Food Res J 23:549–555
22. Kumara BAMS, Hettige KDT (2020) Ripening stage affects the quality of fresh and dehydrated pineapples (*Ananas comosus* (L.) Merr.) *cv.* Mauritius in Sri Lanka. Sustain. Food Prod 8, 29–37

Formation of Bioresorbable PCL-Loaded *Moringa Oleifera* L./Natural Clay Functional Particles by Solvent Displacement Method for Pharmaceutical Applications

Monisha Devi, Rahimah Othman, Mohd Irfan Hatim Mohd Dzahir, and Siti Pauliena Mohd Bohari

Abstract Bioresorbable functional particles offer unique advantages based on different synthetic strategies, with the activated moiety may achieve various targeted drug delivery to minimize side effects. Thus, in this study, a highly MO-loaded adsorptive smart-assembled natural clay (montmorillonite, MMT) dispersion onto poly (ε-caprolactone) nanoparticles matrix (hereafter known as MO-loaded MMT/PCL NPs) is formed by solvent displacement method. MMT is selected due to its great drug loading ability due to high specific surface area and grants mucoadhesive properties with *tortuous pathway* needed for drug delivery across the gastrointestinal barrier. The MO-loaded MMT/PCL NPs are synthesized by self-solvation interaction between the organic phase that composed of dissolved 1 g L^{-1} PCL, 2–20 wt % of MMT, and 0.6–3.0 g L^{-1} of MO in acetone and the aqueous phase consisted of

M. Devi · R. Othman (✉) · M. I. H. M. Dzahir
Faculty of Chemical Engineering & Technology, Universiti Malaysia Perlis, 02600 Arau, Perlis, Malaysia
e-mail: rahimah@unimap.edu.my

M. Devi
e-mail: monishadevi@studentmail.unimap.edu.my

M. I. H. M. Dzahir
e-mail: irfan@unimap.edu.my

R. Othman
Centre of Excellence for Biomass Utilization (CoEBU), Universiti Malaysia Perlis (UniMAP), 02600 Arau, Perlis, Malaysia

S. P. M. Bohari
Department of Bioscience, Faculty of Science, Universiti Teknologi Malaysia, 81310 Johor Bahru, Malaysia

Cosmetic and Fragrance Laboratory, Institute of Bioproduct Development, Universiti Teknologi Malaysia, 81310 Johor Bahru, Malaysia

S. P. M. Bohari
e-mail: pauliena@utm.my

H. L. Ong et al. (eds.), *Proceedings of the 3rd International Conference on Biomass Utilization and Sustainable Energy; ICoBiomasSE 2023; 4–5 September; Kuala Lumpur, Malaysia*, Green Energy and Technology,
https://doi.org/10.1007/978-981-99-9164-8_9

0.2 wt% poly (vinyl alcohol) surfactant solution. The injection rate of organic phase was fixed at 5 mL min^{-1} with volume ratio aqueous phase to organic phase (V_{aq}/V_{or}) between 3–10, and 600–1200 rpm of stirring speed. The inclusion of MMT in polymer was found to improve the entrapment of hydrophilic MO, hence hindering untimely drug leakage. Particle size decreased with increasing the stirring rate and the aqueous-to-organic volumetric ratio as well as the concentration MMT, thus resulting in drug encapsulation efficiency and drug loading up to 30–50 and 5–10%, respectively. The encapsulation of MMT and MO in the NPs was confirmed by X-ray diffraction (XRD) and Fourier transform infrared (FTIR) spectroscopy.

Keywords Functional particles · *Moringa oleifera L.* · Bioresorbable

1 Introduction

In recent years, bioresorbable functional nanoparticles (NPs) have garnered significant attention and interest within the field of pharmaceutical applications. These NPs, composed of biodegradable polymers, have exhibited remarkable potential in revolutionizing drug delivery systems. Moreover, their ability to degrade over time and be metabolized by the body further contributes to their appeal as a safe and biocompatible option. With their unique properties and versatile design, bioresorbable functional polymeric NPs hold great promise in improving the efficacy and safety profiles of various pharmaceutical treatments, paving the way for a new era in personalized medicine. By encapsulating therapeutic agents within their polymeric matrix, they offer a range of advantages over conventional delivery methods, including enhanced drug stability, controlled release kinetics, targeted tissue localization, and reduced systemic toxicity [1].

Various types of polymers play a part in the synthesis of bioresorbable functional polymeric nanoparticles (NPs). The commonly utilized synthetic aliphatic polyesters include poly(ε-caprolactone) (PCL), polylactic acid (PLA), poly lactic-co-glycolic acid (PLGA), and polyanhydrides, which are widely employed in the fabrication of polymeric NPs [2]. Among these polymers, PCL has emerged as an exceptional candidate for drug transportation due to its controlled and sustainable release properties, biocompatibility, non-toxicity, and suitability for various soluble drugs [2]. To prepare polymeric NPs, the solvent displacement method can be employed, which requires minimal energy and time. Considerable attention has been given to enhancing polymeric NPs through the incorporation of nanoclays, aiming to introduce additional features for improved drug delivery.

Montmorillonite (MMT) is a type of naturally occurring clay with medical applications, belonging to the smectite group [2]. MMT possesses noteworthy properties such as intercalation, swelling, ion exchange, and exceptional absorption capabilities [3]. Its high specific surface area enables MMT to exhibit a high capacity for loading drugs, while also providing the necessary mucoadhesive properties for drug delivery

across the gastrointestinal barrier [3]. The crystal lattice imperfections and the substitution of Al^{3+} with Mg^{2+} result in a net negative charge, facilitating the adsorption of alkali and alkaline earth metal cations within the interlayer space [2]. These cations can be exchanged with cationic forms of therapeutic molecules and drugs. Incorporating MMT into polymeric nanoparticles can actively protect against disturbances that may occur during the passage of anticancer drugs through the gastrointestinal tract [4]. Additionally, strong adhesive capacity of MMT can aid in the NPs ability to cross the gastrointestinal barrier effectively [3].

Moringa oleifera (MO) is a widely recognized as the plant with high nutrition and has been extensively utilized in traditional medicine. It has earned the nickname "the miracle tree" due to its remarkable array of pharmacological properties [4]. MO plants are predominantly cultivated in Asia, Africa, and various other regions around the globe [5]. Previous reports have highlighted the abundance of bioactive components in MO leaves, including benzyl isothiocyanate, niazinin B, benzylamine, and astragalin [6]. These components contribute to the plant's pharmacological activities, such as anti-obesity and anti-diabetic effects, thanks to the substantial presence of flavonoids, phenolics, glucosides, and glucosinates [7].

Considering the above-mentioned views, this study is aimed to create drug delivery systems using MO-loaded MMT/PCL nanoparticles through the solvent displacement method. MMT and PCL possess favorable characteristics such as high drug loading capacity, excellent biocompatibility, and controlled release properties, making them ideal carriers for drug delivery. MO is a widely recognized plant with a wide array of bioactive compounds, making it an attractive candidate for medicinal purposes.

2 Materials and Methods

2.1 Materials

Acetone (Ace, with a purity of at least 99.98%) and poly(ε-caprolactone) (PCL, $M_w = 14{,}000$ g mol^{-1} with a glass transition temperature of 60 °C) were procured from Sigma-Aldrich. Additional chemicals, including acetone, sodium chloride, and montmorillonite (MMT), were obtained from R&M Chemicals, Malaysia. In the Soxhlet extraction process, distilled water served as the aqueous phase. The leaves of the *Moringa oleifera* (MO) plant were harvested from wild shrub regions in Perlis, with selection criteria based on uniform size (approximately 15–20 × 10 mm) and coloration. The organic phase consisted of a homogeneous solution comprising 1 g/L (1000 ppm) of the polymer mixed with specified proportions of MO and MMT in Ace.

2.2 Preparation of MO Powder

The process began by collecting MO leaves, which were still attached to their stems. To remove any sorts of dirt or impurities, the detached leaves were meticulously cleaned using tap water. After this cleansing step, the leaves were immersed in a 0.9% sodium chloride solution for 20 min. They were then rinsed again with tap water to ensure the complete removal of any residual traces of the sodium chloride solution. To facilitate thorough drying, the rinsed leaves were left to air-dry naturally for four days at room temperature. Once they were completely dry, these leaves underwent a blending process using a suitable blender or grinder. The resulting powder was carefully sieved to achieve a fine consistency, with particles approximately 250 μm in size. To preserve the quality of the powdered MO, it was securely stored in an airtight, opaque container to protect it from potential degradation caused by exposure to light, moisture, and air, all of which could have a detrimental impact on its quality over time.

2.3 MO Extraction

The MO powder extraction process utilized Soxhlet extraction. About 5 g of MO powder were measured and placed in thimble. Concurrently, 167 mL of distilled water was measured and added to a beaker. To create a solution, a mixture of aqueous methanol (42 mL) and acetone (126 mL) was prepared in a 1:3 ratio and mixed with the distilled water in the beaker. This mixture was then subjected to reflux using a heating mantle set within the temperature range of 80–90 °C for 240 min. Notably, the heating mantle input was maintained at approximately 150, with the upper limit not exceeding 300. The timing began when the solvent reached its boiling point. Following the reflux, the extracted yield was concentrated using a rotary evaporator for 15 min and subsequently stored in a refrigerator at 5 °C to ensure stability and potency. To obtain the concentrated MO extract in powdered form, a Lanconco FreeZone 4.5 L −50 °C Benchtop Freeze Dryer was utilized at −46 °C for 2 days at the Institute of Sustainable Agrotechnology (INSAT), UniMAP. The resulting freeze-dried MO powder was obtained and promptly placed in a desiccator for later use in the synthesis of MO-loaded MMT/PCL nanoparticles.

2.4 MO-Loaded MMT/PCL NPs Formation by Nanoprecipitation Method

The MO-loaded MMT/PCL nanoparticle synthesis involved a self-solvation interaction between the organic phase and the aqueous phase. Blank PCL were produced with varying organic phase solutions to identify the best formulation of MO-loaded

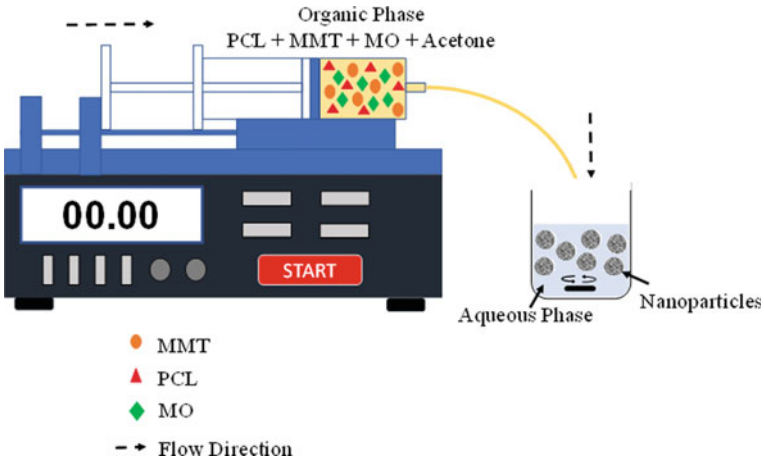

Fig. 1 Experiment setup for MO-loaded MMT/PCL NPs formation

MMT/PCL NPs. The organic phase was comprised of 1 g. L^{-1} PCL, 2–20 wt% MMT, and 0.6–3.0 g. L^{-1} MO dissolved in acetone, while the aqueous is the deionized water. The injection rate of the organic phase remained constant at 5 mL min^{-1}, and the volume ratio of the aqueous phase to the organic phase (V_{aq}/V_{or}) ranged from 1.5 to 10.

The stirring speed was varied between 200 and 1200 rpm. Organic phase was introduced by using a syringe pump, while the aqueous phase was continuously stirred, as depicted in Fig. 1. The experiment continued until a pre-established volumetric ratio of aqueous-to-organic phase (ranging from 1.5 to 10) was reached. When the organic phase was introduced to the aqueous phase, the aqueous solution rapidly became cloudy and turbid. Subsequently, acetone (Ace) evaporated from the nanosuspension at room temperature until the characteristic odor of acetone had completely dissipated. The nanosuspension was then freeze-dried in freeze dryer for 3 days to obtain powdered nanoparticles. The powdered nanoparticles were subjected to XRD analysis to evaluate the particle size of the nanoparticles. Each experiment was conducted at least three times. The study examined four different variables: (i) stirring speed, (ii) volumetric ratios of the aqueous-to-organic phase (V_{aq}/V_{org}), (iii) amount of MMT, and (iv) amount of MO.

2.5 X-ray Diffraction (XRD) Analysis

A Bruker D8 diffractometer was employed for wide-angle X-ray diffraction analysis of MO-loaded MMT/PCL NPs' crystalline structure. The samples underwent exposure to Cu Kα radiation (40 kV, 20 mA) within a 2θ range spanning from 10° to 40°. The measurement parameters included a step size of 0.02°, an acquisition time of 5

s per step, and a scanning speed of 0.5° per minute. These NPs were produced via injection molding in a nitrogen environment at 100 °C and subsequently transferred to a circular mold with dimensions of 20 mm in diameter and 1 mm in thickness at atmospheric temperature.

Using Scherrer's equation from XRD, the particle sizes of the NPs can be obtained, therefore achieving the formulation optimal operational parameters for creating MO-loaded MMT/PCL NPs. Scherrer's equation, developed by Swiss physicist Paul Scherrer in the early twentieth century, allows determining the average size of crystalline particles in a sample by analyzing the diffraction pattern formed when X-rays interact with the crystal lattice. The formula for calculating particle size is represented as follows:

$$D = K\lambda/\beta \cos\theta \quad (1)$$

where

D is the nanocrystalline size.
K is the Scherrer constant,
λ is wavelength of the X-ray beam = 1.5406 Å.
β is the full-width at half-maximum (FWHM) of the peak.
θ is the Bragg angle.

2.6 Characterization of MO-Loaded MMT/PCL NPs

Fourier Transform Infrared Spectroscopy (FTIR). For characterization, Fourier transform infrared spectroscopy (FTIR) was used to determine the presence of several distinctive functional groups present in the MO-loaded MMT/PCL NPs. Total of five samples were subjected to FTIR analysis including pure MMT powder, pure PCL powder, MO leaves extract powder, physical mixture of pure MMT powder, pure PCL powder and MO leaves extract powder, and MO-loaded MMT/PCL NPs. The FTIR spectrometer was subjected to scanning across the wavelength range from 650 to 4000 cm^{-1} [8].

3 Results and Discussion

3.1 Operational Parameters for the Synthesis of MO-Loaded MMT/PCL NPs

The fabrication of MO-loaded MMT/PCL nanoparticles requires a thorough understanding of how various factors like stirring speeds, V_{aq}/V_{org} ratios, amount of MMT, and amount of MO to impact nanoparticle characteristics. Therefore, a systematic investigation of these parameters is crucial to achieve the desired experimental formulations and attain the targeted particle size using the nanoprecipitation method.

3.2 Effects of Stirring Speeds

The choice of stirring speeds directly influences the size and distribution of nanoparticles in the nanoprecipitation method. In this study, different agitation speeds ranging from 200 to 1200 rpm were applied to blank PCL NPs, while keeping a constant injection rate of 5 mL min^{-1} for the organic phase to aqueous phase. The results and the impact of stirring speeds on the particle sizes of NPs are presented in Fig. 2a. The stirring speeds increased from 200 to 1200 rpm, and the particle sizes of the NPs decreased from 880 to 337 nm. This reduction in size is a result of achieving greater homogeneity at higher stirring speeds, ensuring a uniform distribution, and preventing agglomeration [9] also observed a similar trend, where particle sizes decreased from 800 to 300 nm with an increase in stirring speed from 300 to 1200 rpm. The decrease in particle size can be attributed to improved mass transfer, diffusion rate, rapid nucleation, and precipitation, as explained by [9].

3.3 Effects of Aqueous-To-Organic Phase Volume Ratios

The selection of aqueous-to-organic phase volume ratios (V_{aq}/V_{org}) is a critical aspect of the nanoprecipitation design. In this sequences of experiments, blank PCL NPs were created by introducing 5 mL of the organic phase into the aqueous phase. Various (V_{aq}/V_{org}) ratios, namely 1.5, 3.0, 4.5, 7.0, and 10.0, were used.

The resulting particle sizes corresponding to each (V_{aq}/V_{org}) ratio are depicted in Fig. 2b. The particle sizes of NPs decreased from 530 to 247 nm with an increase in V_{aq}/V_{org} ratios from 1.5 to 10.0. The size of NPs formed is influenced by various factors such as stoichiometry, nucleation, and agglomeration. The volumetric ratios determine the availability of reactants for NP formation, and when the ratio aligns with the desired reaction's stoichiometry, it results in controlled and uniform NP sizes [10]. Additionally, varying V_{aq}/V_{org} ratios impact the nucleation rate. Higher ratios of V_{aq}/V_{org} lead to faster nucleation due to increased solvent removal, resulting

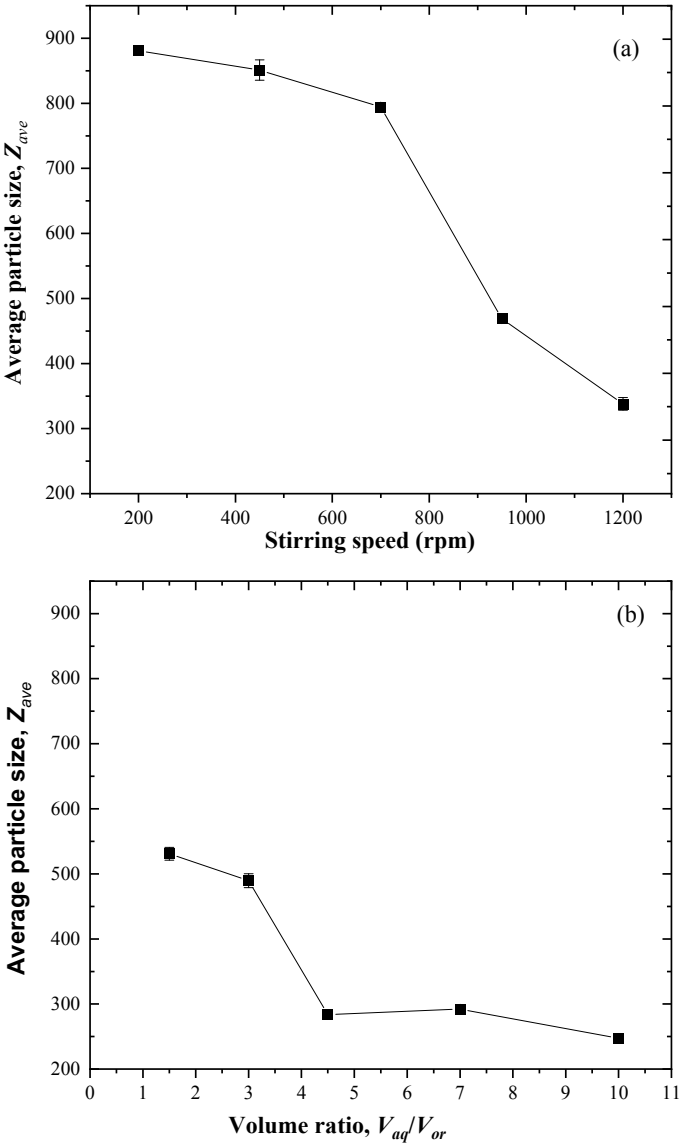

Fig. 2 **a** Influence of stirring speeds, and **b** aqueous-to-organic phase volume ratios (V_{aq}/V_{org}) on the particle sizes of NPs. **c** Effects of the MMT amount, and **d** MO amount on the particle size of NPs

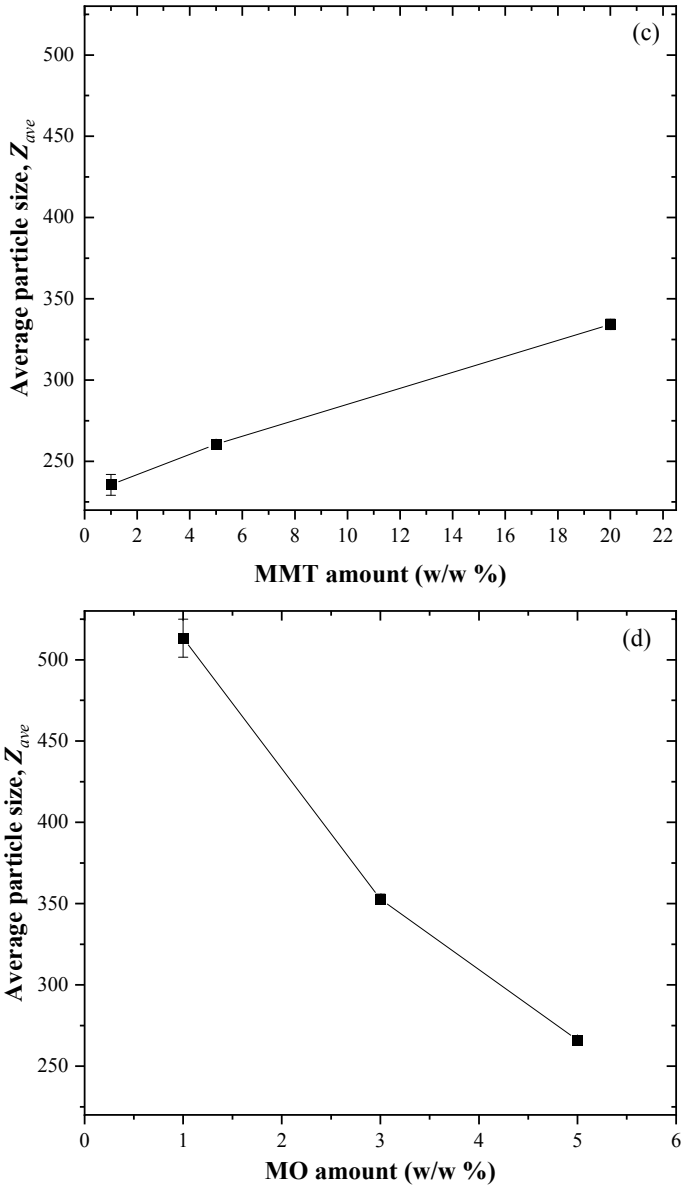

Fig. 2 (continued)

in smaller NPs. Moreover, diluted suspensions at higher V_{aq}/V_{org} ratios experience reduced agglomeration tendencies, leading to smaller and well-dispersed NPs [11].

3.4 Effects of Amount of MMT

The amount of MMT clay is a crucial factor in the nanoprecipitation method for NP formation. MMT is added to improve drug entrapment within the NPs. However, it is essential to carefully consider the MMT quantity during NP formation to avoid any disturbances in the particle size and shape. In the organic phase, MMT was used at concentrations of 2, 5, and 20%, while maintaining the stirring speed and volumetric ratio at 1200 rpm and 10.0, respectively. Figure 2c presents the particle sizes and the influence of MMT amount on NP particle size.

The size of NPs increases from 235 to 334 nm with an elevation in the MMT amount from 2 to 20%. A significant increase in MMT content leads to larger NPs, which may result in particle agglomeration or hinder proper polymer matrix formation, leading to less uniform NPs [10]. Furthermore, excessive MMT incorporation can destabilize the NPs, as the MMT layers may facilitate NP aggregation, reducing stability and homogeneity. Additionally, a higher MMT content can alter NP morphology, causing irregular shapes and larger sizes [12]. This phenomenon was also observed by [11], where increased MMT inclusion caused distortion and deviation from the spherical shape of NPs.

3.5 Effects of Amount of MO

The MO extract powder, also the active ingredient, plays a crucial role in the NPs' formation. It is essential to carefully regulate the quantity of this active ingredient to achieve optimal functionality of the NPs. In this research, NPs were produced using active ingredient quantities of 1, 3, and 5%, while maintaining a constant stirring speed of 1200 rpm and a volumetric ratio of 10.0. Figure 2d illustrates the particle sizes of the NPs and demonstrates the impact of the active ingredient's amount on their size.

The nanoparticle size reduces from 513 to 266 nm with an increase in the active ingredient content from 1 to 5%. This phenomenon is influenced by various factors, including polymer chain length, dilution effect, and aggregation inhibition. The length of the polymer chain, such as PCL, plays a role in determining the nanoparticle size. Higher concentrations of the active ingredient may interact differently with the polymer chains, leading to changes in the overall nanoparticle size. Dilution effects during nanoparticle formation can also impact thermodynamics and result in smaller nanoparticles. Moreover, higher active ingredient concentrations effectively prevent nanoparticle aggregation and growth, leading to smaller and more stable nanoparticles.

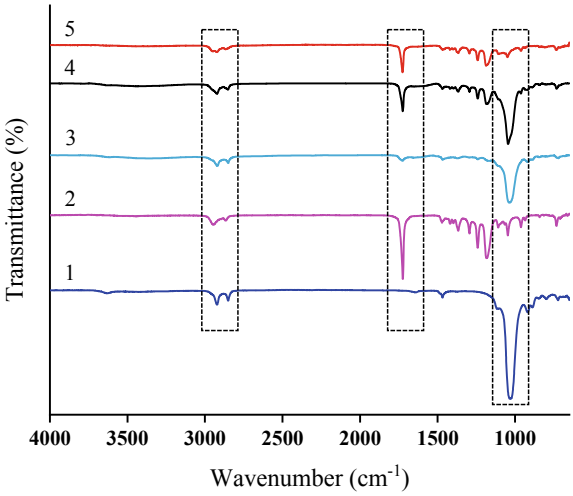

Fig. 3 FTIR spectra of: (1) pure MMT, (2) pure PCL, (3) MO powder, (4) physical mixture of MMT, PCL, and MO powder, (5) MO-loaded MMT/PCL NPs

3.6 Characterization of MO-Loaded MMT/PCL NPs

FTIR analysis was employed to examine the chemical stability of the elements utilized in the nanoprecipitation process to produce MO-loaded MMT/PCL NPs. Figure 3 showcases the spectra of various samples.

In Fig. 3(1), the FTIR spectra exhibit a prominent peak at approximately 1000 cm^{-1}, signifying the stretching vibration of Si–O groups within tetrahedral sheets. As seen in Fig. 3(2), the PCL spectrum displays multiple bands corresponding to the stretching vibrations of aliphatic C–H, O–H, C-O, and N–O bonds, in addition to C–O stretching. The PCL IR spectrum also reveals a doublet in the range of 2921–2851 cm^{-1}, representing asymmetric and symmetric CH_2 stretching. Furthermore, there's a distinct peak at around 1724 cm^{-1}, which corresponds to the carbonyl group's (C–O stretching) presence. Bands spanning from 700 to 1600 cm^{-1} indicate molecular motions and isomerization of ester groups within the polymer, offering insights into its configuration and behavior.

When comparing the composite spectrum to the spectra of MO and pure MMT powder, a significant decrease in transmittance at around 1000 cm^{-1} indicates that MO and MMT are likely encapsulated within the nanoparticles. This reduction is likely due to the absorption of infrared radiation by the confined MO and MMT particles. Furthermore, there is an observable increase in transmittance at approximately 1720 cm^{-1}, which could be attributed to the interaction between MO and PCL within the nanocomposite. This interaction alters the molecular environment around the C–O bond when compared to the individual components, possibly leading to a shift in the absorption frequency or intensity of the C–O stretching peak, resulting in higher transmittance.

4 Conclusions

In this study, MO-loaded MMT/PCL NPs were synthesized by self-solvation interaction between the organic phase composed of dissolved 1 g L^{-1} PCL, 2–20 wt % of MMT, and 1–5 wt % of MO in acetone and the aqueous phase consisted of 0.2 wt% poly (vinyl alcohol) surfactant solution. The injection rate of the organic phase was fixed at 5 mL min^{-1} with a volume ratio of aqueous phase to organic phase (V_{aq}/V_{or}) between 1.5–10, and 200–1200 rpm of stirring speed. The formulations of the synthesized NPs were studied by X-ray diffraction (XRD) analysis and Scherrer's equation. The functional groups in MO-loaded MMT/PCL NPs were confirmed by Fourier transform infrared (FTIR) spectroscopy. The best formulations for the formation of MO-loaded MMT/PCL NPs were obtained at stirring speed of 1200 rpm, aqueous-to-organic phase ratio (V_{aq}/V_{or}) of 10.0, amount of MMT of 2%, and MO amount of 5%. FTIR analysis showed a few peaks around the area of 1000, 2921–2851, and 1742 cm^{-1} attributing to the stretching of Si–O of tetrahedral sheets and to asymmetrical and symmetrical CH_2 stretching and C-O stretching. These results showed that with the inclusion of PCL and MMT into the NPs formation for the encapsulation of MO, small sizes were still able to be maintained. Therefore, these novel MO-loaded MMT/PCL NPs has the potential in drug delivery system for targeted area.

Acknowledgements This work is supported by the Fundamental Research Grant Scheme (FRGS) under the grant number FRGS/1/2021/TK0/UNIMAP/02/11 from the Ministry of Higher Education.

References

1. Kumari A, Yadav SK, Yadav SC (2010) Biodegradable polymeric nanoparticles-based drug delivery systems. Colloids Surf B 75(1):1–18
2. Li Z, Liu K, Sun P, Mei L, Hao T, Tian Y, Chen D (2013) Poly ($_{D}$, $_{L}$-lactide-co-glycolide)/montmorillonite nanoparticles for improved oral delivery of exemestane. J Microencapsul 30(5):432–440
3. Okumu MO, Mbaria JM, Kanja LW, Gakuya DW, Kiama SG, Ochola FO (2016) Phytochemical profile and antioxidant capacity of leaves of Moringa oleifera (Lam) extracted using different solvent systems. J Pharmacogn Phytochem 5(4):302
4. Fitriana WD, Ersam T, Shimizu K, Fatmawati S (2016) Antioxidant activity of Moringa oleifera extracts. Indonesian J Chem 16(3):297–301
5. Wangcharoen W, Gomolmanee S (2011) Antioxidant capacity and total phenolic content of Moringa oleifera grown in Chiang Mai Thailand. Thai J Agricult Sci 44(5):118–124
6. Sreelatha S, Padma PR (2009) Antioxidant activity and total phenolic content of Moringa oleifera leaves in two stages of maturity. Plant Foods Hum Nutr 64(4):303–311
7. Singh AK, Rana HK, Tshabalala T, Kumar R, Gupta A, Ndhlala AR, Pandey AK (2020) Phytochemical, nutraceutical and pharmacological attributes of a functional crop Moringa oleifera Lam: an overview. S Afr J Bot 129:209–220
8. Ansari MJ (2017) Factors affecting preparation and properties of nanoparticles by nanoprecipitation method. Indo Am J Pharmaceutic Sci 4(12):4854–4858

9. Wang N, Fuh JYH, Dheen ST, Senthil Kumar A (2021) Synthesis methods of functionalized nanoparticles: a review. Bio-Design Manufact 4:379–404
10. Sun W, Zeng H, Tang T (2021) Enhanced adsorption of anionic polymer on montmorillonite by divalent cations and the effect of salinity. J Phys Chem A 125(4):1025–1035
11. Othman R, Vladisavljevic GT, Nagy ZK, Holdich RG (2016) Encapsulation and controlled release of rapamycin from polycaprolactone nanoparticles prepared by membrane micromixing combined with antisolvent precipitation. Langmuir 32(41):10685–10693
12. Sinha VR, Bansal K, Kaushik R, Kumria R, Trehan A (2004) Poly-∈-caprolactone microspheres and nanospheres: an overview. Int J Pharm 278(1):1–23

A Pilot-Scale Co-composting Experiment of University Cafeteria's Food Waste and Cow Manure for Sustainable Waste Management

Pisit Klingosum, Nattapon Leeabai, Chanoknunt Khaobang, Kor Taweengern, Haryo Wibowo, and Chinnathan Areeprasert

Abstract This study investigated the co-composting of food waste and cow manure and the resulting compost product properties. Food waste composition and the source of waste were also studied. Food waste composition survey showed that carbohydrate was the main constituent of food waste. The composting experiment was conducted by using an aerobic method at 45–60 °C for 24 h to achieve maximum thermophilic microbe activity. It was found that addition of 30% cow manure produced compost with pH of 6.17, moisture content of 27.4%, as well as having high phosphorus (P) and potassium (K) content at about 1.48% and 2.13%, respectively. Overall, it was found that short composting time could still produce high-quality compost by applying proper heat and environment control to optimize the aerobic digestion process.

Keywords Food waste · University · Cafeteria · Composter · Co-composting

P. Klingosum · C. Khaobang · K. Taweengern · H. Wibowo · C. Areeprasert (✉)
Department of Mechanical Engineering, Faculty of Engineering, Kasetsart University, 50 Ngam Wong Wan Road, Lat Yao, Chatuchak, Bangkok 10900, Thailand
e-mail: fengcta@ku.ac.th

C. Khaobang
e-mail: chanoknunt.kh@ku.th

N. Leeabai
Department of Environmental Engineering, Faculty of Engineering, Kasetsart University, 50 Ngam Wong Wan Road, Lat Yao, Chatuchak, Bangkok 10900, Thailand
e-mail: fengnpl@ku.ac.th

H. L. Ong et al. (eds.), *Proceedings of the 3rd International Conference on Biomass Utilization and Sustainable Energy; ICoBiomasSE 2023; 4–5 September; Kuala Lumpur, Malaysia*, Green Energy and Technology,
https://doi.org/10.1007/978-981-99-9164-8_10

1 Introduction

According to the United Nations Environment Programme (UNEP) report, more than 32% of all food became food waste. This is compounded by its increased generation due to population growth. For example, in 2021, it was reported that Thai households' food waste generation was 79/kg/capita/year and rising [1]. The Pollution Control Department reported that food waste made up 46% of landfilled waste in Bangkok municipality [2]. During the Covid-19 pandemic, there was a significant decrease in food waste generation. In 2019 and 2020, about 3.85 and 3.48 million tons, respectively, were generated [3]. However, with the post-pandemic reopening, these numbers are expected to climb. Therefore, food waste management should be considered an important issue.

Food waste disposal has been done using various methods such as landfilling, incineration, recycling, reuse as animal feed, composting, and others [4]. Composting in particular has garnered attention for its environmentally friendliness. It is defined as an organic digestion process between microorganisms and organic waste to produce biofertilizer which is rich in micronutrients [5]. Composting could be divided into two types based on their aeration conditions, anaerobic and aerobic. Aerobic digestion is relatively simple and produce high-quality biodegradable product for agriculture applications. On the other hand, it has a high consumption of energy. Anaerobic digestion is considered better at preserving energy through the possibility of energy recovery in the form of biogas, but its product quality tends to be harder to control [6]. One natural source of microorganism used for composting is from cattle manure, which contains a variety of microbial communities [7]. During the aerobic composting process, microorganisms use carbon substrate and energy in their metabolism process while producing CO_2 and water [8]. The products from aerobic digestion could be utilized for soil amendment since it contains nutrients such as potassium, sodium, calcium, and magnesium.

Therefore, this work offers an investigation of food waste composition study in university cafeterias, which are a major source of food waste, through the co-composting of food waste with cow manure. Process data was collected and the products from co-composting were analyzed. The information from this study is expected to contribute to the knowledge and serve as an example for food waste composting implementation in the university area.

2 Materials and Methods

2.1 Composting Machine and Experimental Procedure

Aerobic composting of food waste was conducted using a pilot-scale food waste composter with a capacity of 150 kg. The reactor of the composter is made from stainless steel assembled with a mechanical stirrer. Air was continuously supplied

during the composting process and the exhaust air was removed through the ventilation system. The hot air produced by electric heater externally attached to the reactor provided temperature adjustment ability to the reactor. The temperature was controlled to be around 45–60 °C. In each test, the food waste was mixed with cow manure obtained from the local area. The composition of food waste was derived from the survey from one of the Kasetsart University's cafeterias. The ratio of food waste to cow manure was 70:30 by weight, making up 142 kg of feedstock. The composting process lasted 24 h, during which a series of measurements were conducted during the first 24 h to ensure the compost quality. Five repetitions were done to ensure the reliability of the data.

2.2 Compost Product Characterization

The compost properties including pH, electrical conductivity (EC), carbon to nitrogen (C/N) ratio, organic carbon (OC), nitrogen (N), phosphorous (P), potassium (K), calcium (Ca), magnesium (Mg), and moisture contents were measured every hour for the analysis of their evolution during the composting process. The pH value was measured by Hanna HI-981030 pH meter with the capability of measuring pH value between 0.0 and 12.0 pH by mixing sample soil and deionized water by weight per volume with a 1:10 ratio [9]. Soil mineral property characterization followed the standard guide from the Department of Agriculture of Thailand [10]. In terms of EC measurement, 5 g of sample soil was mixed with 50 mL of deionized water, and shaken for 30 min. After that, it was filtered through a filter membrane and the collected liquid was characterized by an EC meter [11]. For moisture analysis, a soil sample was first heated at 105 °C overnight in an oven to get rid of exceeding moisture. Weight measurement before and after drying was conducted, and the difference was taken as the moisture content.

3 Results and Discussion

3.1 Compositions of Food Waste for Composting

The food waste source was collected from the university canteen. According to Fig. 1a, "Single-meal" shops took almost the half of total food shops. "Beverage" shops were second most numerous, making up 22.86%. Other shop types such as "Rice curry" and "Meat-meal" shop made up 8.57%, while "Dessert" shops and "Vegetable and grains" shops accounted for 5.71% of the total shop number.

Based on the menu of each shop, this data was then translated to the amount of compounds expected to be found in the cafeteria's aggregate food waste bin. According to Fig. 1b, food waste composition consisted mostly of carbohydrate.

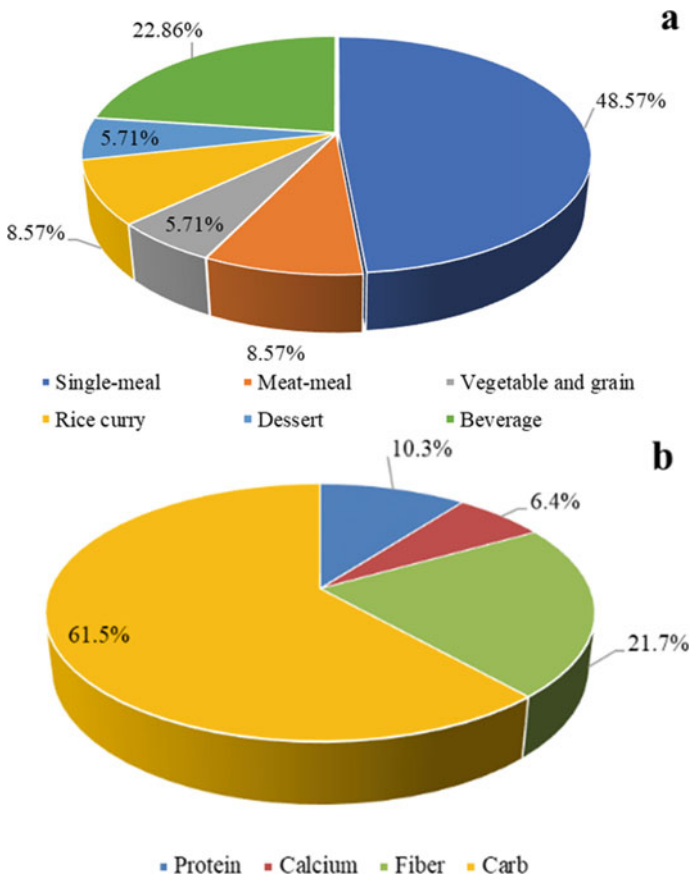

Fig. 1 Types of shop in the cafeteria (**a**) and its food waste composition (**b**)

Moreover, carbohydrate was reported to have a positive effect on mycelium mushroom growth in mushrooms on cellulose [12]. Fiber was found to made up nearly a quarter of the total composition. Protein and calcium made up the final 10.3% and 6.4%, respectively.

3.2 Compost Product Characterization

The physical appearance of the compost solid before and after the process are shown in Fig. 2. It could be seen that after 24 h of composting process, the food waste has been decomposed and became a more uniform and relatively dry compared to the original material.

Fig. 2 Food waste before and after 24 h aerobic composting process

Figure 3 shows the compost temperature hovered around has been controlled along the experiment by 40 °C, which has been reported as a suitable temperature for thermophilic microorganism activity [13]. The observed pH of the product was decreasing at a relatively steady pace until the end of the experiment, where it ended up at approximately 6.1. This value meant that compost product from 30% manure condition was found to meet the pH value standard for compost nutrient requirement [14]. The dried appearance and relatively neutral pH could be the result of the nature of cow manure, which typically has a high pH value and low moisture content [15]; which acted to counter the acidic tendency of compost product from food waste compositing, as well as acting as a bulking agent for the highly moist food waste. Figure 3 shows that at the beginning of experiment, the compost had moisture content of almost 75%, which could hinder microbial growth [16].

From Table 1, the compost made with 30% manure had high amounts of nitrogen (N), phosphorus (P), and potassium (K) at about 1.91%, 1.48%, and 2.13%, respectively. The nutrients composition was very close to the nutrient content requirement for fertilizer, which N, P, and K contents are typically recommended to be about 1.5%, 0.2%, and 1%, respectively [14]. However, the compost had higher EC (9.37) than cow manure which had 6.65%. This could have been the result of the high salt amount from food waste affecting the conservation of nitrogen in compost.

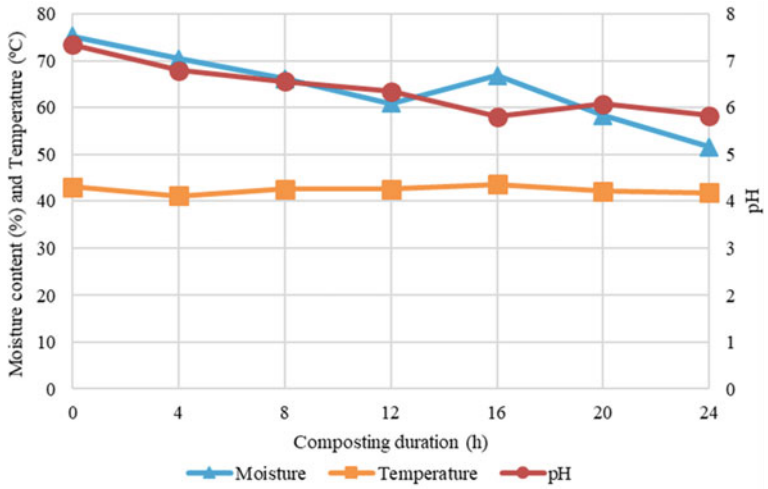

Fig. 3 Evolution of important parameters during composting

Table 1 Composition of compost product and cow manure

Parameters	70% Food waste/30% Cow manure	Cow manure
pH	6.17 ± 0.286	9.27
EC (%)	9.37 ± 0.680	6.65
OC (%)	42.8 ± 1.39	35.14
N (%)	1.91 ± 0.100	1.42
P (%)	1.48 ± 0.300	1.61
K (%)	2.13 ± 0.310	3.99
C/N ratio (%)	22.62 ± 1.770	24.79
Ca (%)	0.96 ± 0.240	1.31
Mg (%)	0.36 ± 0.020	0.58
Moisture (%)	27.4 ± 2.610	8.87

4 Conclusion

This work performed the food waste composition and waste source types survey with the co-composting of food waste and cow manure study. It was found that the compost with 70% food waste and 30% cow manure had the lowest moisture content at 10%, the highest pH at 6.17, and the highest nutrient content with phosphorus (P) and potassium (K) contents at about 1.48% and 2.13%, respectively. Food waste proportion obtained from sampling from one of the cafeterias in Kasetsart University Bangkok campus showed that carbohydrates made up the majority 61.5%. This could be one of the main positive factors since carbohydrate could promote microbial activity through its degradation to sugary substances.

Acknowledgements The research is funded by the Kasetsart University Research Development Institute—FF(KU)25.64. P. Klingosum received a scholarship from the Graduate School of Kasetsart University, the Faculty of Engineering, Kasetsart University, and the Department of Mechanical Engineering, Faculty of Engineering, Kasetsart University, Thailand.

References

1. Quested T, O'connor C, Forbes H (2021) UNEP food waste index report 2021
2. Pollution Control Department: Guidelines for the feasibility study and design municipal solid waste management system for department of local administration. Bangkok. (2012). https://www.pcd.go.th. Accessed 20 Sept 2023
3. Thailand Environment Institute: consumer information for sustainable consumption and production in food supply chain in Bangkok. (2021). https://www.tei.or.th/file/library/English_Report_on_SCP_in_Food_51.pdf. Accessed 20 Sept 2023
4. Kim MH, Song HB, Song Y, Jeong IT, Kim JW (2013) Evaluation of food waste disposal options in terms of global warming and energy recovery: Korea. Int J Energy Environ Eng 4(1)
5. Ayilara MS, Olanrewaju OS, Babalola OO, Odeyemi O (2020) Waste management through composting: challenges and potentials. Sustainability 12(11):4456
6. Novak JT, Banjade S, Murthy SN (2011) Combined anaerobic and aerobic digestion for increased solids reduction and nitrogen removal. Water Res 45(2):618–624
7. Wan J, Wang X, Yang T, Wei Z, Banerjee S, Friman VP, Mei X, Xu Y, Shen Q (2021) Livestock manure type affects microbial community composition and assembly during composting. Front Microbiol 12:621126
8. Song JH, Murphy RJ, Narayan R, Davies GB (2009) Biodegradable and compostable alternatives to conventional plastics. Philos Trans Royal Soc B Biol Sci 364(1526):2127–2139
9. Cools N, De Vos B (2010) Manual on methods and criteria for harmonised sampling, assessment, monitoring and analysis of the effect of air pollution on forests
10. Agricultural Production Sciences Research and Development Division: Guide to Analyzing Organic Fertilizers (2008)
11. Jackson ML (1958) Soluble salt analysis for soils and waters 435
12. Jurak E, Kabel MA, Gruppen H (2014) Carbohydrate composition of compost during composting and mycelium growth of Agaricus bisporus. Carbohydr Polym 101:281–288
13. Brock TD (1975) Effect of water potential on growth and iron oxidation by Thiobacillus ferrooxidans. Appl Microbiol 29(4):495–501
14. Castro H, Gómez M (2010) Fertilidad de suelos y Fertilizantes. Ciencia del Suelo Principios básicos Sociedad Colombiana de la Ciencia del Suelo Bogotá, Colombia 213–303
15. Tutkimuskeskus M (1963) Annales Agriculturae Fenniae. Agricultural Research Centre
16. Richard TL, Hamelers HVM, Veeken A, Silva T (2002) Moisture relationships in composting processes. Compost Sci Utilization 10(4):286–302

Synthesis of Cellulose Beads from Wastepaper via the Microemulsion and Precipitation Method

Kimberly-Wei-Wei Tay, Suk-Fun Chin, and Mohd Effendi bin Wasli

Abstract Synthesis parameters such as cellulose (1–5% w/v) and surfactant (0–6% w/v) concentrations are investigated and optimized on controlling the mean diameter of cellulose beads. Cellulose fibers from printed paper wastes are extracted and used to prepare cellulose beads via a water-in-oil (W/O) microemulsion and precipitation techniques. Different cellulose solutions of concentrations were prepared by dissolving cellulose fibers in NTU solvent (NaOH: thiourea, urea, 8:6.5:8% w/v). Cellulose beads were precipitated out by dilute acetic acid solution. Under FESEM, it was observed that smaller cellulose beads (≤ 1 μm) were formed with and without surfactant, which in this case, Span 80 (Sorbitan monooleate). Spherical beads with porous surfaces were shown when surfactant concentration increased. The smallest mean diameter was 0.166 μm at 1% w/v cellulose concentration without Span 80, while the largest mean diameter of 1.153 μm obtained from 5% w/v cellulose concentration and 6% w/v Span 80 concentration. Hence, small size cellulose beads of high specific surface area, low-cost and environmentally friendly are potentially useful as control release carriers.

Keywords Cellulose beads · Printed paper wastes · Water-in-oil microemulsion · Synthesis parameters

K.-W.-W. Tay · S.-F. Chin (✉) · M. E. Wasli
Faculty of Resource Science and Technology, Universiti Malaysia Sarawak, 94300 Kota Samarahan, Malaysia
e-mail: sukfunchin@gmail.com

M. E. Wasli
e-mail: wmeffendi@unimas.my

H. L. Ong et al. (eds.), *Proceedings of the 3rd International Conference on Biomass Utilization and Sustainable Energy; ICoBiomasSE 2023; 4–5 September; Kuala Lumpur, Malaysia*, Green Energy and Technology,
https://doi.org/10.1007/978-981-99-9164-8_11

1 Introduction

Biopolymers have been explored as sustainable choices with considerable intrinsic benefits of being environmentally friendly, biocompatible, biodegradable and their vast availability, together with the associated affordable output costs [1]. Cellulose-based materials have been emerging in various fields due to its intrinsic advantages of being abundant, renewable, cheap, biodegradable, biocompatible and easy to be modified [2–4]. The presence of intra- and intermolecular hydrogen bond network of cellulose is accountable to its crystallinity, insoluble in water as well as nearly all common organic solvents and three-dimensional (3-D) network structure into microfibrils [5]. Due to the 3-D arrangement, cellulose was found to be a more appropriate material to synthesize porous microspheres as it can form inner channel structures [6].

The preparation of microspheres from printed paper wastes was previously studied [7, 8]. In addition, water-in-oil (W/O) microemulsion method has been explored by several researches in synthesizing polymeric microspheres because of the ease of handling, zero need of high temperature and pressure as well as experts or costly instrument [9, 10]. The synthesis parameters also play significant roles in determining the final particle size formed [7, 11, 12]. Smaller size of cellulose beads was reported within 10–20 μm [13] and even below 6 μm [14]. As smaller particle size is accompanied with a high specific surface area, these cellulose beads produced could potentially be utilized in control release applications.

Herein, we have reported the synthesis of cellulose beads with smaller mean diameter ($\leq$ 1 μm) from printed paper wastes using the W/O microemulsion with Span 80 as the surfactant and precipitation techniques. The mean diameter of cellulose beads could be modulated by varying the concentrations of Span 80 (0–6% w/v) and cellulose (1–5% w/v). Due to their abundance, low-cost and biodegradability, cellulose beads of high specific surface area are potentially valuable as control release carriers.

2 Methodology

2.1 Materials

Printed paper wastes were obtained from the campus of the Faculty of Resource and Science Technology, Universiti Malaysia Sarawak. Hydrochloric acid (HCl), sodium hydroxide (NaOH), urea, thiourea, Span 80 (Sorbitan monooleate), paraffin oil and pure ethanol were purchased from Merck. All chemicals were utilized directly without additional purification. A Water Purifying System (ELGA, Model Ultra Genetic) was required to prepare the deionized water (~ 18.2 MΩ cm, 25 °C) [4].

2.2 Preparation of Samples

Extraction of cellulose fibers. The extraction process was based on a reported method with slight modifications [4]. Printed paper wastes were soaked in water overnight before putting it to grind using a high-speed grinding machine (ZT-4500, ~ 220 V). NaOH (12.0 wt%) treatment was carried out on the slurry for 24 h and afterward with HCl treatment (18.2 wt%) for 2 h at 80 °C to eliminate the hemicellulose, lignin as well as the residual ink. The refined cellulose fibers were washed with deionized water and pure ethanol. Subsequently, oven-drying of the samples was conducted at 60 °C for 24 h.

Preparation of Cellulose Beads. A known quantity of the cellulose fibers was dispersed and sonicated for 30 min in a 100 mL of NTU solvent (NaOH: thiourea: urea, 8: 6.5: 8, % w/v). The solvent was put to cool overnight at – 20 °C in a freezer to obtain a solid frozen mass and then, thawed at normal temperature to attain a clear cellulose solution [4]. A W/O microemulsion technique was employed [4]. Span 80 was the surfactant, while acetic acid was the precipitating agent. Normally, 0.6 g of Span 80 was dissolved in 20 mL of paraffin oil at ambient temperature and agitated for 30 min to achieve a uniform oil phase. Then, 3.5 mL of cellulose solution was added drop by drop into the oil phase in middle of the stirring process at 1000 rpm for 1 h to produce a microemulsion. The beads were solidified by incorporating 10% v/v acetic acid under vigorous agitating. A separating funnel was used to separate the mixture and procure the beads. To eliminate the residuals of NTU solvent and oil phase, the beads were washed with deionized water and pure ethanol twice each. Process parameters such as amount of surfactant (0–6% w/v) and cellulose concentration (1–5% w/v) were adjusted to regulate the mean diameter of beads produced.

Characterization. Before characterization, the beads were dried using supercritical carbon dioxide (Quorum K850). The surface morphology of the samples was observed by Field Emission Scanning Electron Microscope (FESEM) (JOEL-SM 6390 LA) with a voltage of 5–10 kV. The samples were coated with a platinum layer in an Auto Fine Coater (JEOL/ JFC-1600). By observing the FESEM micrographs, the mean diameter of cellulose beads was obtained by randomly measuring 20 beads using ImageJ software.

3 Results and Discussions

3.1 Morphology of Cellulose Beads

Figures 1, 2 and 3 demonstrate the FESEM micrographs of cellulose beads (1–5% w/v) with different Span 80 concentrations (0% w/v, 3% w/v, 6% w/v). Meanwhile, Fig. 4 summarizes the overall effects of cellulose and Span 80 concentrations on the

mean diameter of beads. The morphology of beads when synthesized without Span 80 (Fig. 1) was observed to have smoother and aggregated surfaces than those produced with Span 80 (Figs. 2 and 3). However, spherical beads were mostly produced when Span 80 concentration increased to 6% w/v. The presence of porous structure was clearly seen when more amount of Span 80 was added. Drying using supercritical carbon dioxide helps to maintain the morphology of network and porosity [15]. Beads with porous surfaces were more often desirable with unique properties such as big specific surface area [16] and high loading efficiency [17]. Being abundance, low-cost, biodegradable and non-toxic, the cellulose beads could have potential to be used as control release carriers or drug delivery agents.

3.2 Effect of Surfactant Concentrations

Span 80 is a hydrophobic surfactant or oil-soluble and can form a stable emulsion to produce smaller particle sizes [18]. The function of surfactants helps to hinder the polymeric chain interactions, therefore decreasing the individual mean particle sizes [19]. Surfactant concentration has a profound effect on the mean diameter of cellulose beads. A distinct change in mean diameter of cellulose beads was noted as surfactant and cellulose concentration increased.

Under free Span 80, the mean diameter was increased drastically from 0.166 μm to 0.952 μm as cellulose concentration increased from 1% w/v to 5% w/v. No hindrance between cellulose chains to interact one another. This led to larger agglomerated beads as the mean diameter is completely dependent on the effect of cellulose concentration. Surfactant helps to reduce interfacial tension of oil and water phase in the system of microemulsion [20]. A gradual increase in particle size was observed under 3% w/v Span 80 concentration from 0.380 μm to 0.701 μm for 1% to 5% w/v cellulose concentrations of cellulose beads. Although previous findings showed the optimal surfactant concentration at 3% w/v would provide the smaller size [4, 21], other parameters should also be considered. Factors such as the injection distance, duration of synthesis process as well as surface tension of precipitation liquid have great consequences in particle size, porosity and gel strength of the beads [22].

Surfactant molecules will start to assemble together in a form of aggregates when they reached a specific number in the solution [23]. When the surfactant concentration was more than 3% w/v, the particles will have a complete coverage of the surface area, providing nearly same size of smaller stabilized particles [24]. However, Fig. 4 portrays a notable growth in mean diameter to as high as 1.153 μm for 5% w/v cellulose concentration of cellulose beads when 6.0% w/v Span 80 was incorporated. Other researchers also reached the same conclusions, where increasing surfactant concentrations would result in larger particle size [17, 25]. This was probably caused by depletion flocculation phenomenon from the non-adsorbed micelles [26]. Similarly, a high volume of Span 80 could cause the instability and deformation of microspheres to occur [27].

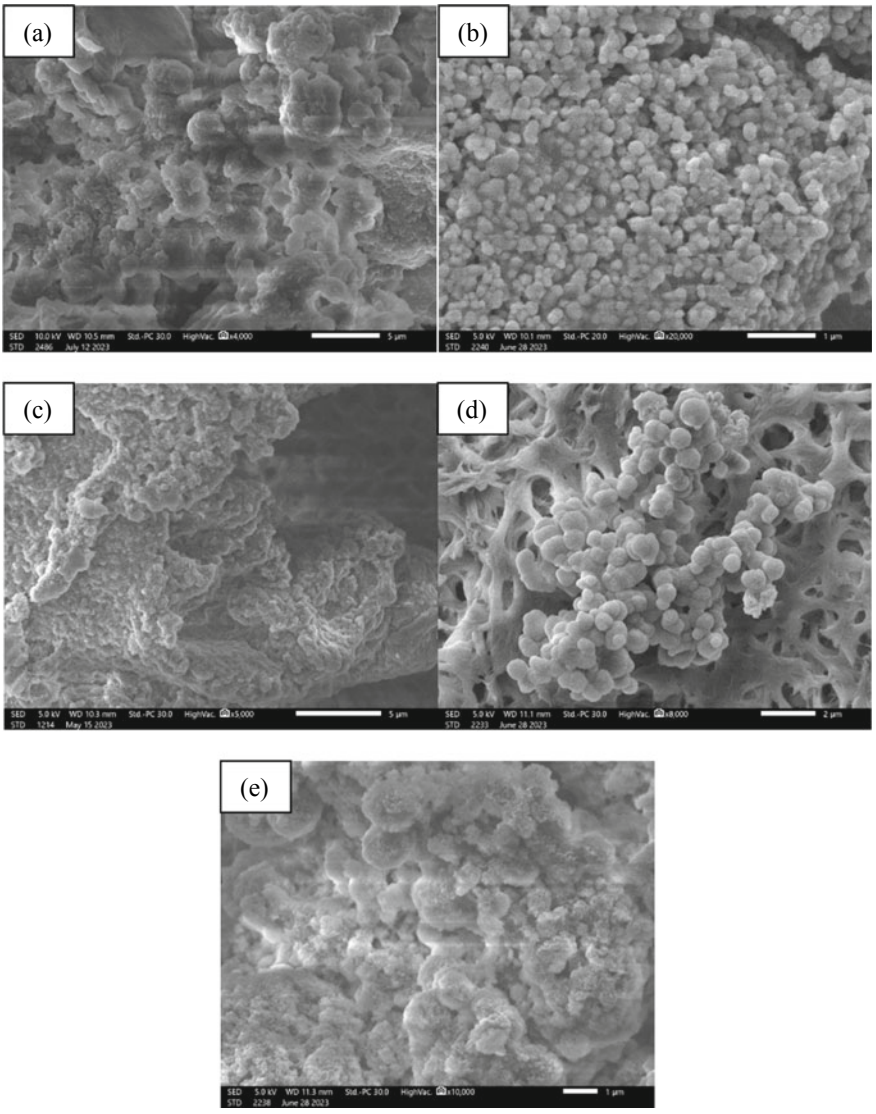

Fig. 1 FESEM micrographs of cellulose beads **a** 1% w/v, **b** 2% w/v, **c** 3% w/v, **d** 4% w/v and **e** 5% w/v of cellulose concentration without Span 80

3.3 Effect of Cellulose Concentrations

Regardless of surfactant concentration, an increment of cellulose concentration was observed to produce larger particle size. To put it briefly, cellulose concentration is directly proportional with mean diameter of beads. Cellulose concentration could be associated with viscosity.

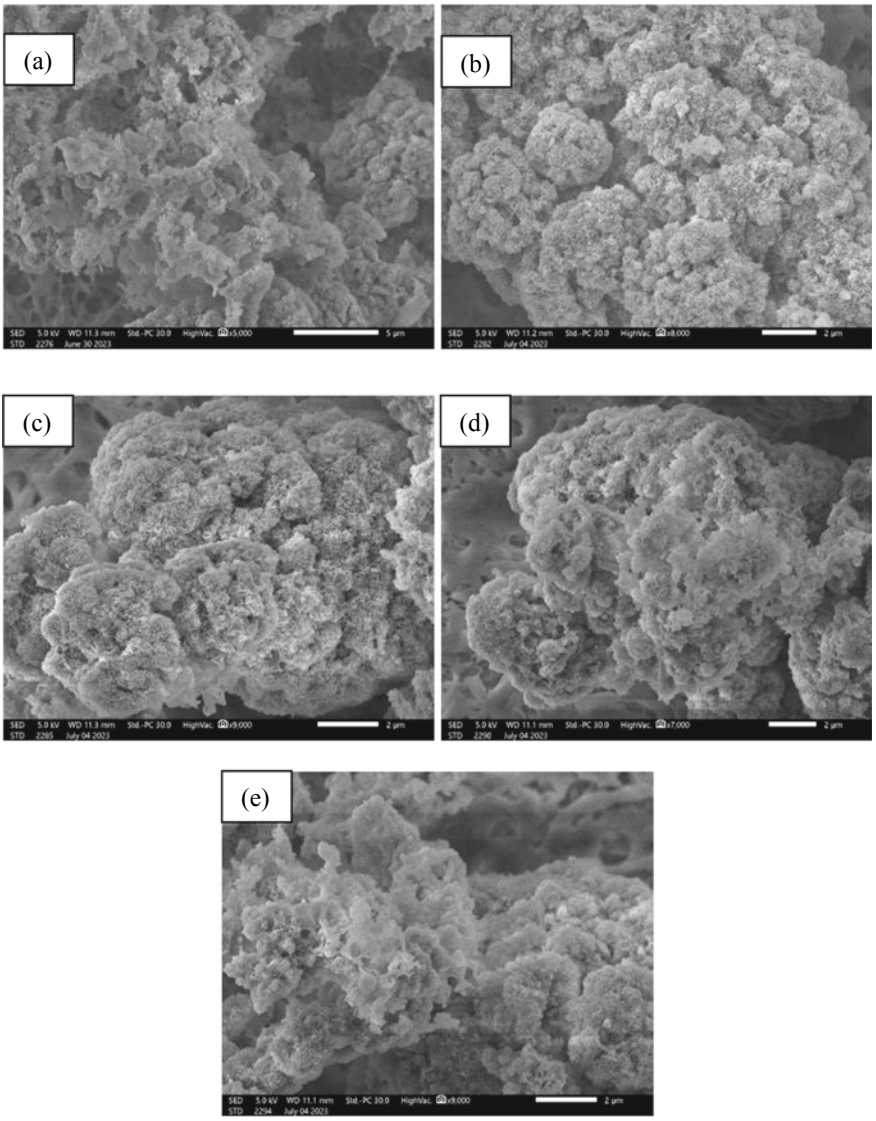

Fig. 2 FESEM micrographs of cellulose beads **a** 1% w/v, **b** 2% w/v, **c** 3% w/v, **d** 4% w/v and **e** 5% w/v of cellulose concentration with 3% w/v Span 80

At a low cellulose concentration, the viscosity was mainly governed by the resistance between fibrils and entanglements in the dispersion which caused the interaction effects to be negligible. But, as concentration increased, the viscosity was predominantly influenced by the aggregates formed in the dispersion which led to the dependent of other factors like the nature of dispersion, concentration, solvent

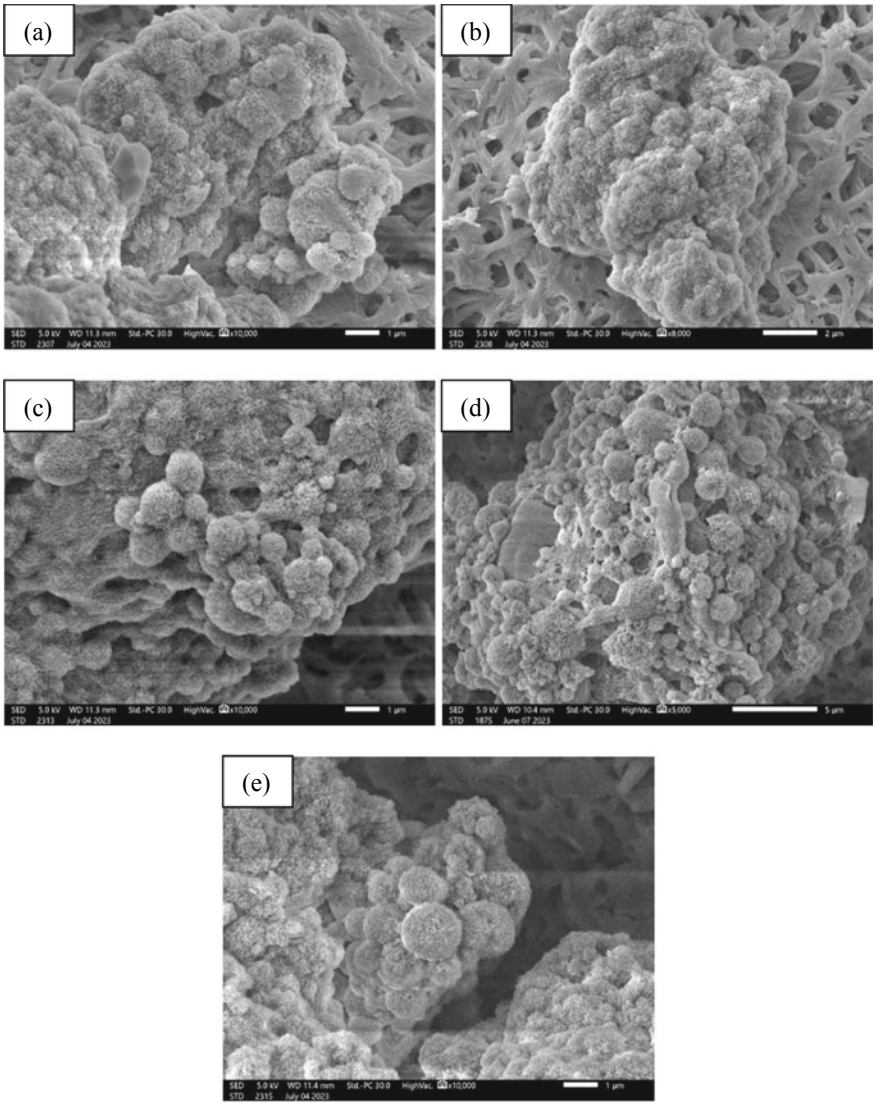

Fig. 3 FESEM micrographs of cellulose beads **a** 1% w/v, **b** 2% w/v, **c** 3% w/v, **d** 4% w/v and **e** 5% w/v of cellulose concentration with 6% w/v Span 80

used, shear rate and size distribution [28]. Li et al. expressed that the formation of aggregates inside the beads could be hindered when very small amount of cellulose concentration was applied [29]. Furthermore, aggregates also increased the true molecular weight of single cellulose chain due to strong intermolecular and

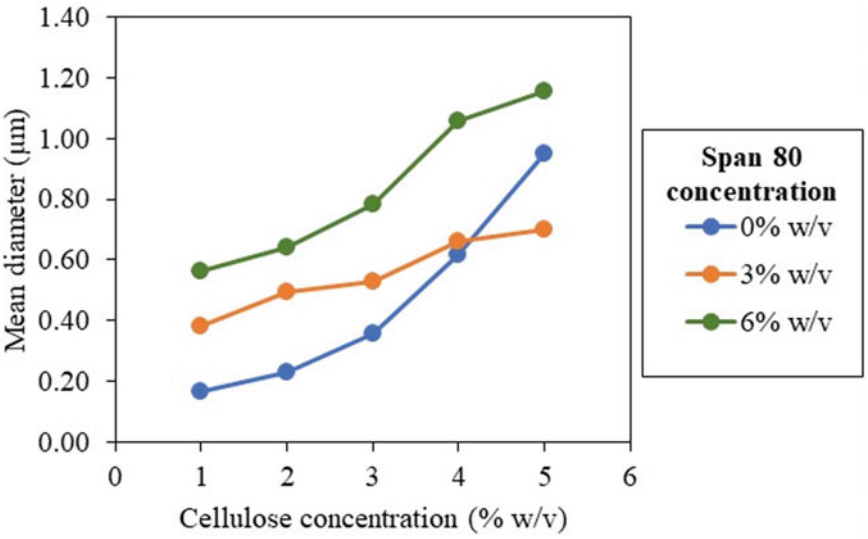

Fig. 4 Effects of Span 80 and cellulose concentrations on mean diameter of cellulose beads

intramolecular hydrogen bonds [30, 31]. Other work also claimed cellulose concentration as the most influential parameter in modulating the size of beads [32]. Furthermore, an increase in capillary attractive force as well as van der Waals would cause the augmentation of particle size [33]. Therefore, larger beads were expected to form as viscosity increased due to significant effects of cellulose chain interaction.

4 Conclusion

Smaller cellulose beads of controllable size ($\leq$ 1 μm) from printed paper wastes were demonstrated to form via a W/O microemulsion and precipitation method with and without surfactant under room temperature. Stirring speed was kept constant at 1000 rpm. Synthesis parameters such as surfactant and cellulose concentrations were observed to affect the mean diameter of cellulose beads significantly. Under free Span 80 condition, the mean diameter increased drastically along with increasing cellulose concentrations. At 3% w/v Span 80, the mean diameter of cellulose beads increased moderately. As Span 80 concentrations reached 6% w/v, the mean diameter of cellulose beads was the largest among others with a slow increment across the cellulose concentrations. Overall, the effects of cellulose and Span 80 concentrations were significant on fabricating cellulose beads. Therefore, small size cellulose beads of high porosity and specific surface area could be potentially envisaged as control release carrier, or drug delivery agent in agricultural and biomedical applications, respectively.

References

1. Baigorria E, Sanchez LM, Primiano RPO, Alvarez VA (2023) Recent trends in eco-friendly materials for agrochemical pollutants removal: polysaccharide-based nanocomposite materials. Springer Nature, Singapore
2. Li H, Kruteva M, Mystek K, Dulle M, Ji W, Pettersson T, Wagberg L (2020) Macro- and microstructural evolution during drying of regenerated cellulose beads. ACS Nano 14(6):6774–6784
3. Qiao L, Li S, Li Y, Liu Y, Du K (2020) Fabrication of superporous cellulose beads via enhanced inner cross-linked linkages for high efficient adsorption of heavy metal ions. J Clean Prod 253:120017
4. Voon LK, Pang SC, Chin SF (2017) Optimizing delivery characteristics of curcumin as a model drug via tailoring mean diameter ranges of cellulose beads. Int J Polym Sci. 2017:1–10
5. Carvalho JPF, Silva ACQ, Silvestre AJD, Freire CSR, Vilela C (2021) Spherical cellulose micro and nanoparticles: a review of recent developments and applications. Nanomaterials 11(10):2744
6. Zhang W, Wang XC, Li XY, Zhang LL, Jiang F (2020) A 3D porous microsphere with multistage structure and component based on bacterial cellulose and collagen for bone tissue engineering. Carbohydr Polym 236:116043
7. Voon LK, Pang SC, Chin SF (2015) Highly porous cellulose beads of controllable sizes derived from regenerated cellulose of printed paper wastes. Mater Lett 164:264–266
8. Yang M, Fang C, Su J, Cheng Y, Zhang Q, Liu M (2022) Synthesis mechanism of carbon microsphere from waste office paper via hydrothermal method. BioResources 17(4):5568–5577
9. Mehebub Rahaman S, Chakraborty M, Mandal T, Kundu S, Dhibar S, Kumar D, Ibrahim SM, Chakravarty M, Saha B (2023) Mechanically tuned lanthanum carbonate nanorods in water-in-oil microemulsion scaffolds. J Mol Liq 372:121204
10. Ruan L, Su M, Qin X, Ruan Q, Lang W, Wu M, Chen Y, Lv Q (2022) Progress in the application of sustained-release drug microspheres in tissue engineering. Mater Today Bio. 16:100394
11. Chin SF, Jimmy FB, Pang SC (2018) Size controlled fabrication of cellulose nanoparticles for drug delivery applications. J Drug Deliv Sci Technol. 43:262–266
12. Voon LK, Pang SC, Chin SF (2017) Porous cellulose beads fabricated from regenerated cellulose as potential drug delivery carriers. J Chem 2017:1–11
13. Wang G, Li F, Li L, Zhao J, Ruan X, Ding W, Cai J, Lu A, Pei Y (2020) In situ synthesis of Ag-Fe3O4 nanoparticles immobilized on pure cellulose microspheres as recyclable and biodegradable catalysts. ACS Omega 5(15):8839–8846
14. Xu F, Cho BU (2022) Preparation of porous regenerated cellulose microstructures via emulsion-coagulation technique. Cellulose 29(3):1527–1542
15. Druel L, Budtova T (2023) Aerogel-like (low density and high surface area) cellulose monoliths and beads obtained without supercritical-or freeze-drying. Cellulose 1–15
16. Cai Y, Chen Y, Hong X, Liu Z, Yuan W (2013) Porous microsphere and its applications. Int J Nanomedicine 8:1111–1120
17. Jo S, Park S, Oh Y, Hong J, Kim HJ, Kim KJ, Oh KK, Lee SH (2019) Development of cellulose hydrogel microspheres for lipase immobilization. Biotechnol Bioprocess Eng 24(1):145–154
18. Pachuau L, Mazumder B (2009) A study on the effects of different surfactants on ethylcellulose microspheres. Int J PharmTech Res. 1(4):966–971
19. Tay SH, Pang SC, Chin SF (2012) A facile approach for controlled synthesis of hydrophilic starch-based nanoparticles from native sago starch. Starch 64(12):984–990
20. Chin SF, Mohd Yazid SNA, Pang SC (2014) Preparation and characterization of starch nanoparticles for controlled release of curcumin. Int J Polym Sci 1–8
21. Alnaief M, Alzaitoun MA, García-González CA, Smirnova I (2011) Preparation of biodegradable nanoporous microspherical aerogel based on alginate. Carbohydr Polym 84(3):1011–1018
22. Lengyel M, Kállai-Szabó N, Antal V, Laki AJ, Antal I (2019) Microparticles, microspheres, and microcapsules for advanced drug delivery. Sci Pharm 87(3):20

23. Song T, Gao F, Guo S, Zhang Y, Li S, You H, Du Y (2021) A review of the role and mechanism of surfactants in the morphology control of metal nanoparticles. Nanoscale 13(7):3895–3910
24. Chin SF, Azman A, Pang SC (2014) Size controlled synthesis of starch nanoparticles by a microemulsion method. J Nanomater 2014
25. Pezeshki A, Ghanbarzadeh B, Mohammadi M, Fathollahi I, Hamishehkar H (2014) Encapsulation of vitamin A palmitate in nanostructured lipid carrier (NLC)-effect of surfactant concentration on the formulation properties. Adv Pharm Bull 4(Suppl 2):563–568
26. Wulff-Pérez M, Torcello-Gómez A, Gálvez-Ruíz MJ, Martín-Rodríguez A (2009) Stability of emulsions for parenteral feeding: preparation and characterization of o/w nanoemulsions with natural oils and Pluronic f68 as surfactant. Food Hydrocoll 23(4):1096–1102
27. Hakim SL, Kusumasari FC, Budianto E (2020) Optimization of biodegradable PLA/PCL microspheres preparation as controlled drug delivery carrier. Mater Today Proc. 22:306–313
28. Albornoz-Palma G, Ching D, Andrade A, Henríquez-Gallegos S, Teixeira Mendonça R, Pereira M (2022) Relationships between size distribution, morphological characteristics, and viscosity of cellulose nanofibril dispersions. Polymers 14(18):3843
29. Li H, Kruteva M, Dulle M, Wang Z, Mystek K, Ji W, Pettersson T, Wagberg L (2022) Understanding the drying behavior of regenerated cellulose gel beads: the effects of concentration and nonsolvents. ACS Nano 16(2):2608–2620
30. Xie K, Tu H, Dou Z, Liu D, Wu K, Liu Y, Chen F, Zhang L, Fu Q (2021) The effect of cellulose molecular weight on internal structure and properties of regenerated cellulose fibers as spun from the alkali/urea aqueous system. Polymer 215:123379
31. Zhou Y, Zhang X, Zhang J, Cheng Y, Wu J, Yu J, Zhang J (2021) Molecular weight characterization of cellulose using ionic liquids. Polym Test 93:106985
32. Druel L, Niemeyer P, Milow B, Budtova T (2018) Rheology of cellulose-[DBNH][CO2Et] solutions and shaping into aerogel beads. Green Chem 20(17):3993–4002
33. Li C, Li Y, Sun P, Yang C (2013) Pickering emulsions stabilized by native starch granules. Colloids Surf 431:142–149

A Comparative Study of the Phytochemicals and Antioxidant Activity of Pruned Harumanis Mango Leaves Using Microwave-Assisted Extraction

Nurfitrah Syahirah Mohd Asri, Farizul Hafiz Kasim, Noor-Soffalina Sofian-Seng, and Khairul Farihan Kasim

Abstract Harumanis mango is one of the best mangoes in the world, and it is only produced in Perlis, Malaysia. Pruning of the Harumanis plant is an important and routine step to maximize both the quantity and quality of the fruits. During pruning season, a lot of leaves and branches are typically discarded. The leaves can however be upcycled into a source of phytochemicals and antioxidants, and this may be used to partially offset the cost of producing the Harumanis. Therefore, in line with zero waste practice, this study examines the phytochemical content and antioxidant activity of young and matured pruned Harumanis leaves. Microwave-assisted extraction (MAE) with water as the solvent was used to extract the phytochemical and antioxidant compounds. The total phenolic compounds (TPC) and total flavonoid compounds (TFC) were then quantified, and 1,1-diphenyl-2-picrylhydrazyl (DPPH) assay was used to determine antioxidant activity. It was found that ground leaves sieved to a

N. S. M. Asri · F. H. Kasim · K. F. Kasim (✉)
Faculty of Chemical Engineering & Technology, Universiti Malaysia Perlis, 02600 Arau, Perlis, Malaysia
e-mail: khairulfarihan@unimap.edu.my

N. S. M. Asri
e-mail: syahirahfitrah@studentmail.unimap.edu.my

F. H. Kasim
e-mail: farizul@unimap.edu.my

F. H. Kasim · K. F. Kasim
Centre of Excellence for Biomass Utilization, Universiti Malaysia Perlis (UniMAP), 02600 Arau, Perlis, Malaysia

N.-S. Sofian-Seng
Department of Food Science, Faculty of Science and Technology, Universiti Kebangsaan Malaysia, UKM, 43600 Bangi, Selangor, Malaysia
e-mail: soffalina@ukm.edu.my

H. L. Ong et al. (eds.), *Proceedings of the 3rd International Conference on Biomass Utilization and Sustainable Energy; ICoBiomasSE 2023; 4–5 September; Kuala Lumpur, Malaysia*, Green Energy and Technology,
https://doi.org/10.1007/978-981-99-9164-8_12

particle size of 200 mesh, a sample-to-solvent ratio of 2:50 (g/mL), and a sample size of 2 g yielded the best results for extracting antioxidants and phytochemical compounds from young and matured leaves. The matured leaves were found to contain higher TPC and TFC values (11.05 ± 1.10 mg GAE/g and 46.98 ± 0.03 mg QE/g, respectively) compared to young leaves (10.30 ± 0.03 mg GAE/g and 39.34 ± 0.05 mg QE/g, respectively). However, DPPH activity was found to be higher in young leaves compared to matured leaves (75.78 ± 0.48% and 70.52 ± 0.83%, respectively). It is concluded that both young and matured Harumanis leaves are a good source of phytochemicals and antioxidants.

Keywords Harumanis mangoes · Phytochemical compounds · Antioxidant activity · Mango leaves

1 Introduction

Mango, or *Mangifera indica*, is a fruit that contains a high concentration of phytochemical compounds [1]. The phytochemical compounds of mango are mainly phenolic acids, and they can be obtained from various parts of the plant such as fruit, kernel (stone), leaves, and bark. Numerous other phytochemical compounds, including mangiferin, gallic acids, gallotannins, quercetin, isoquercetin, ellagic acid, flavonoids, ascorbic acid, carotenoids, tocopherols, among others are also found in the leaves of the plant [2]. Phytochemicals, sometimes referred to as secondary metabolites, are naturally occurring bioactive molecules. They serve to protect plant cells from pollution, stress, drought, exposure to UV light, and attacks by pathogens [3].

Mango leaves contain phytochemicals that are known to have antioxidant, antidiabetic, antibacterial, immunomodulatory, antipyretic, anti-inflammatory, and analgesic properties [4–6]. The antioxidant activity in mango leaves is due to the presence of phenols and flavonoids. There are several varieties of mangoes grown in Malaysia, but the Harumanis mango is one of the most well-known mango varieties grown in the country. The Harumanis mango is only grown in Perlis, a small state located in northern Malaysia, and it is in high demand in the commercial market [7].

Phytochemical and antioxidant compounds can be extracted using a variety of extraction techniques. Traditional extraction methods generate large amounts of solvent waste, causing many environmental and health problems. By extracting antioxidants using green extraction methods such as microwave-assisted extraction (MAE), less solvent is needed, and less waste is produced during extraction as a result [8].

In this study, MAE is chosen as the extraction method to use due to its advantages, including low solvent consumption, minimal operation time, high recovery yield, high selectivity, and low sample manipulation [9]. This study evaluates the phytochemicals content and antioxidant activity of matured and young Harumanis mango leaves.

2 Materials and Methods

2.1 Chemicals and Materials

2,2-diphenyl-1-1picrylhydrazy (DPPH) and ethanol were purchased from Fisher Scientific Limited. Folin–Ciocalteu, sodium carbonate, sodium nitrate, and aluminum chloride were purchased from HmbG Chemicals while gallic acid and quercetin were purchased from Sigma Aldrich (Malaysia). All chemicals used for the experiment were of analytical grade. Harumanis pruned leaves were obtained from Harumanis Sungai Batu Pahat Plantations at Perlis, Malaysia.

2.2 Sample Preparation

The leaves were washed thoroughly to remove dirt and other impurities and then dried at 55 °C overnight in a drying oven (Thermo-Line SOV140B, China). The dried leaves were then ground using a coffee grinder (Saachi Coffee Grinder, China) and sieved into five different particle sizes: 200, 100, 60, 30, and < 30 mesh (B.S.S. standard measurement). The sieved samples were kept in the freezer (Midea R600a, China) at − 20 °C until further use.

2.3 Microwave-Assisted Extraction System

A modified microwave oven technique was used to extract the phytochemicals and antioxidants from Harumanis leaves. The oven (Sharp R357EK (China) uses a digital control system to adjust the irradiation period (from 1 s to 99 min) and microwave power (from 10 to 900W). The microwave oven was adapted to condense the vapors produced in the sample during the extraction process. Water was used as the solvent for the extraction process and was added to the ground Harumanis leaves in a round-bottom flask before irradiation. After irradiation, the sample solution containing the extracted phytochemicals and antioxidants was cooled promptly in a cooled water bath, filtered, and stored in the freezer (Midea R600a, China) until further use.

2.4 The Optimization of MAE Parameters Using One-Factor-At-A-Time (OFAT) Approach

A one-factor-at-a-time (OFAT) approach was used to optimize the MAE parameters for extracting phytochemicals and antioxidants from mango leaves. Particle size (200, 100, 60, 30, and < 30 mesh), sample-to-solvent ratio (2:50, 2:100, 2:150, 2:200, and

2:250 g/mL), and sample size (0.5, 1.0, 1.5, 2.0, 2.5, and 3.0 g) were the parameters investigated. These parameters were studied one at a time, and the optimum parameter found in each study was used in subsequent studies. After the extraction process, the liquid extract was cooled in an ice bath and filtered. The filtered extract was stored at − 20 °C in a freezer (Midea R600a, China) before analysis.

The Effect of Particle Size. The effect of particle size (200, 100, 60, 30, and 30 mesh) on phytochemical content and antioxidant property of the filtered extract was studied using 2 g of sample, 50 mL of water, irradiation power of 900 W, and extraction time of 3 min.

The Effect of Sample-to-Solvent Ratio. Based on the results, a particle size of 200 mesh was selected as the optimum particle size to use. The effect of sample-to-solvent ratio (2:50, 2:100, 2:150, 2:200, and 2:250 g/mL) on phytochemical content and antioxidant property of the filtered extract was studied using 2 g of sample, irradiation power of 900 W, and extraction time of 3 min.

The Effects of Sample Size. A particle size of 200 mesh and the sample-to-solvent ratio of 2:50 g/mL were selected based on the previous results. The effect of sample sizes (0.5, 1.0, 1.5, 2.0, 2.5, and 3.0 g) on phytochemical content and antioxidant property of the filtered extract was studied using irradiation power of 900 W and extraction time of 3 min.

2.5 Phytochemical Analysis

Total Phenolic Content. The total phenolic content (TPC) of the samples was determined using the Folin–Ciocalteu method [10]. Briefly, 0.1 mL of plant extract was added into 8 mL of distilled water followed by 0.2 mL of the Folin–Ciocalteu phenol reagent. The mixture was then incubated for 3 min. Afterward, 1 mL of a saturated solution of sodium carbonate (Na_2CO_3) (20%) was added to the mixture. The sample mixture was then incubated for another 30 min in the dark at room temperature for the color to develop. The absorbance value of the sample mixture was then measured at 765 nm using a UV–Vis spectrophotometer (Thermo Spectronic Genesys 20, USA). The total phenolic content in the samples is expressed as mg of gallic acid equivalent (GAE) per gram of dry sample (mg GAE/g).

Total Flavonoid Content. The flavonoid content of the samples was determined using the colorimetric method [11]. About 0.5 mL of the sample extract was mixed with 2 mL of distilled water and 0.15 mL of 50% sodium nitrate ($NaNO_3$). The mixture was then incubated for 5 min. Afterward, 0.15 mL of 10% aluminum chloride ($AlCl_3$) was added to the mixture. This mixture was incubated for another 15 min at room temperature. Finally, the absorbance value of the sample mixture was measured at 415 nm using a UV–Vis spectrophotometer (Thermo Spectronic Genesys 20, USA). The concentration of flavonoids in the samples was calculated

from a calibration plot and is expressed as mg quercetin equivalents per g of dried sample (mg QE/g).

2.6 Antioxidant Assay (DPPH)

The antioxidative property of the extracts was measured using a 1,1-diphenyl-2-picrylhydrazyl (DPPH) assay [12]. Briefly, 200 μL of the sample extract was added with 2.5 mL of 60 μM ethanolic DPPH. The mixture was mixed thoroughly and incubated in a dark place for 30 min. A control consisting of 200 μL of distilled water with 2.5 mL of 60 μM of ethanolic DPPH was prepared. Then, the absorbance value of the sample mixture was measured at 517 nm using a UV–Vis spectrophotometer (Thermo Spectronic Genesys 20, USA). DPPH radical scavenging activity was calculated using the equation shown as Eq. (1):

$$\text{DPPH scavenging activity}(\%) = \left(1 - \frac{\text{Absorbance of sample at 517 nm}}{\text{Absorbance of control at 517 nm}}\right) \times 100 \quad (1)$$

2.7 Statistical Analysis

Minitab (version 17; StataCorp LLC, TX, USA) and SigmaPlot (version 12.0; Systat Software Inc., San Jose, California, USA) were used to calculate the mean and standard deviation of all measurements.

3 Results and Discussion

3.1 The Effects of Particle Size

The effect of particle size on the phytochemical compounds yield and antioxidant properties of Harumanis mango leaves is shown in Fig. 1. The results show that the DPPH, TFC, and TPC are inversely proportional to sample particle size. The DPPH activity of Harumanis mango leaf extract is the highest when the particle size is the smallest (200 mesh) and they are 70.57 ± 0.61% (Fig. 1a) and 75.78 ± 0.48% (Fig. 1b) for matured and young leaves, respectively. As the particle size increases, the DPPH activity decreases. The high DPPH scavenging activity of the leaves is caused by the presence of high amounts of phenolics and flavonoids in the leaves [13].

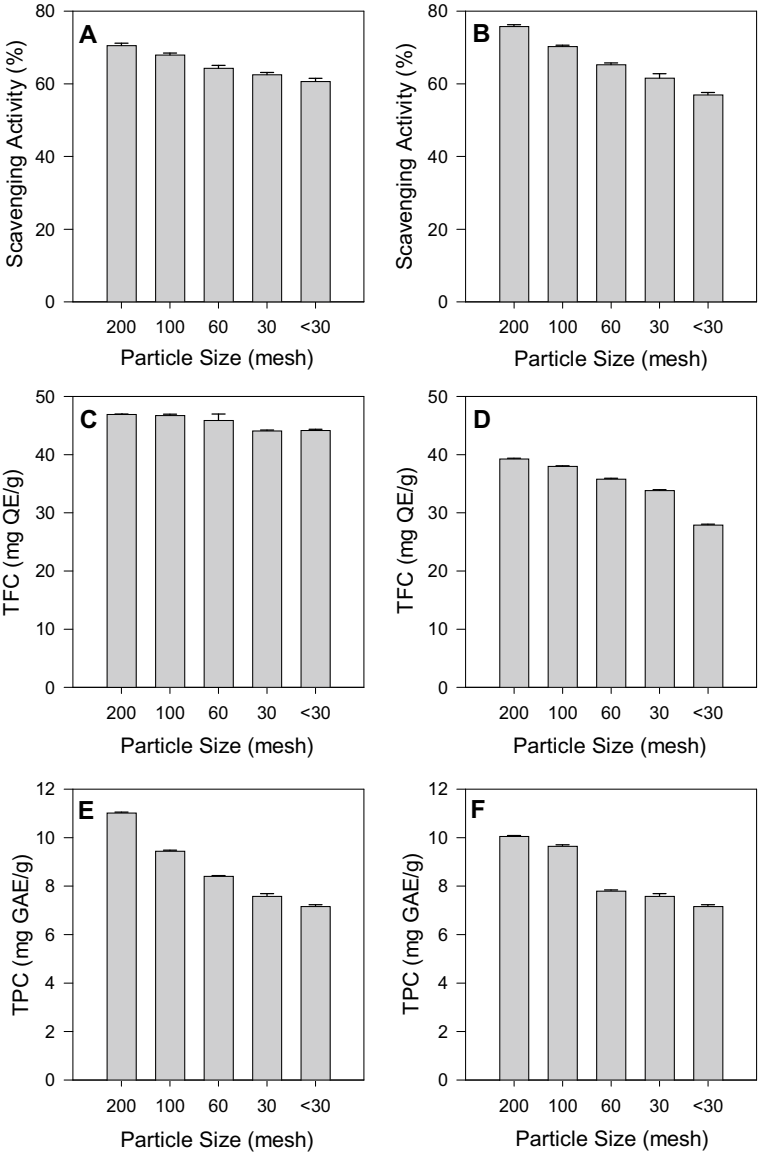

Fig. 1 The effects of particle size on the DPPH (**a** matured and **b** young leaves), TFC (**c** matured and **d** young leaves), and TPC (**e** matured and **f** young leaves)

The TFC and TPC of matured and young leaves also show a similar trend. The TFC (Fig. 1c, d) and TPC (Fig. 1e, f) of Harumanis mango leaf extracts are the highest when the particle size is the smallest and they are 46.98 ± 0.03 mg QE/g and 11.05 ± 0.002 mg GAE/g for the matured leaves; and 39.34 ± 0.05 mg QE/g and 10.08 ± 0.007 mg GAE/g for the young leaves. The matured leaves were found to have a higher phenolic and flavonoid content compared to young leaves. The maturity of the leaves plays a crucial role in influencing the photosynthesis and metabolism of the plant. A smaller particle size results in an increase in phytochemical yield due to the larger surface-to-volume ratio, which promotes greater contact between the solvent and the plant material during the extraction process [14]. The solvent will have better access to the soluble compounds within the particle. It is the most critical factor affecting the extraction efficiency of phytochemical compounds [15]. Therefore, it is better to use a small particle size to obtain the best yield of DPPH, TFC, and TPC. The particle size of 200 mesh is used in all subsequent experiments.

3.2 The Effects of Sample-To-Solvent Ratio

Figure 2 shows the effect of sample-to-solvent ratio on DPPH, TFC, and TPC values of both matured and young Harumanis mango leaves extract. The best sample-to-solvent ratio for both matured and young Harumanis mango leaves is 2:50 g/mL. The results show that the phytochemical yield and antioxidant activity are proportional to sample-to-solvent ratio. The mass transfer principle states that the higher the concentration gradient between the sample and the solvent, the stronger the driving force of mass transfer from the sample to the solvent [16]. However, when using a high sample-to-solvent ratio, the solvent becomes more rapidly saturated with phytochemicals and antioxidants, resulting in higher TFC, TPC, and antioxidant activity of the extracts [17]. A solvent volume of 50 mL is sufficient to extract the phytochemicals and antioxidants from 2 g of sample, and a larger solvent volume would only dilute the compounds of interest.

The highest DPPH activity was obtained at a sample-to-solvent ratio of 2:50 (g/mL), and it is 65.94 ± 0.87% (Fig. 2a) and 70.29 ± 0.42% (Fig. 2b) for matured and young leaves, respectively. Using matured leaves also resulted in a higher content of TFC of 44.50 ± 073 mg QE/g compared to 38.46 ± 0.38 mg QE/g for young leaves. The TPC also shows the same trend, where a greater sample-to-solvent ratio is desirable to obtain a higher concentration of phytochemicals and antioxidants. The TPC is 10.41 ± 0.03 mg GAE/g (Fig. 2e) and 10.28 ± 0.06 mg GAE/g (Fig. 2f) for matured and young leaves, respectively. Interestingly, the DPPH scavenging activity of young leaves is higher compared to that of the matured leaves. This may be explained by the excessive generation and buildup of free radicals during plant development. This process leads to a reduction in the levels of secondary metabolites and triggers the onset of senescence in the plant [18]. The sample-to-solvent ratio of 2:50 (w/v) is used in subsequent experiments.

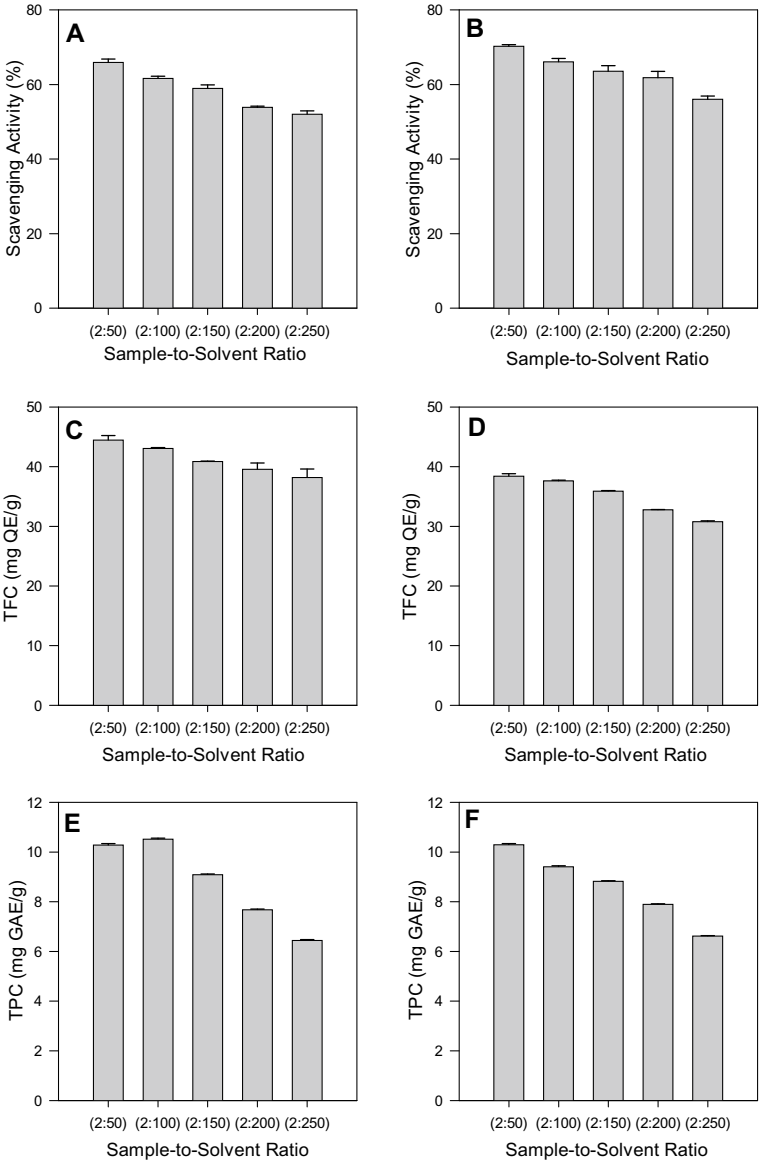

Fig. 2 The effects of sample-to-solvent ratio on the DPPH (**a** matured and **b** young leaves), TFC (**c** matured and **d** young leaves), and TPC (**e** matured and **f** young leaves)

3.3 The Effects of Sample Size

Figure 3 shows the effect of sample size on DPPH, TFC, and TPC values of Harumanis mango leaves extract. The best sample size for both leaves is 2 g. The results show that the phytochemicals compounds (TPC and TFC) and antioxidant activity (DPPH) increase with sample size, reaching a maximum at 2 g and slowly decreasing thereafter. A higher sample size simply means more material to extract the antioxidant components from [19]; however, using a sample size larger than 2 g will not increase phytochemical and antioxidant yield because the solution would already become saturated. The DPPH, TFC, and TPC contents when the sample size is 2 g are 66.30 ± 1.18%, 46.24 ± 0.02 mg QE/g, 10.99 ± 0.02 mg GAE/g, respectively, for matured leaves and 71.65 ± 0.68%, 38.30 ± 1.42 mg QE/g and 10.17 ± 0.26 mg GAE/g, respectively, for young leaves.

4 Conclusion

This study had measured the phytochemical compounds and antioxidant activities of Harumanis mango leaves extract obtained through microwave-assisted extraction (MAE). Three parameters, i.e., particle size, sample-to-solvent ratio, and sample size, have been evaluated in this study. The optimal extraction parameters to extract antioxidants from Harumanis leaves are a particle size of 200 mesh, sample-to-solvent ratio of 2:50 (g/mL), and sample size of 2 g for both matured and young leaves. These results show that Harumanis mango leaves are a promising source of natural phytochemicals and antioxidants. A significant correlation between antioxidant properties and total phenolic and flavonoid compounds were found, indicating that these compounds are a major contributor to the leaf extract's antioxidant properties. Further studies should however be conducted to understand the mechanism of extraction of phytochemical compounds and antioxidants from Harumanis mango leaves.

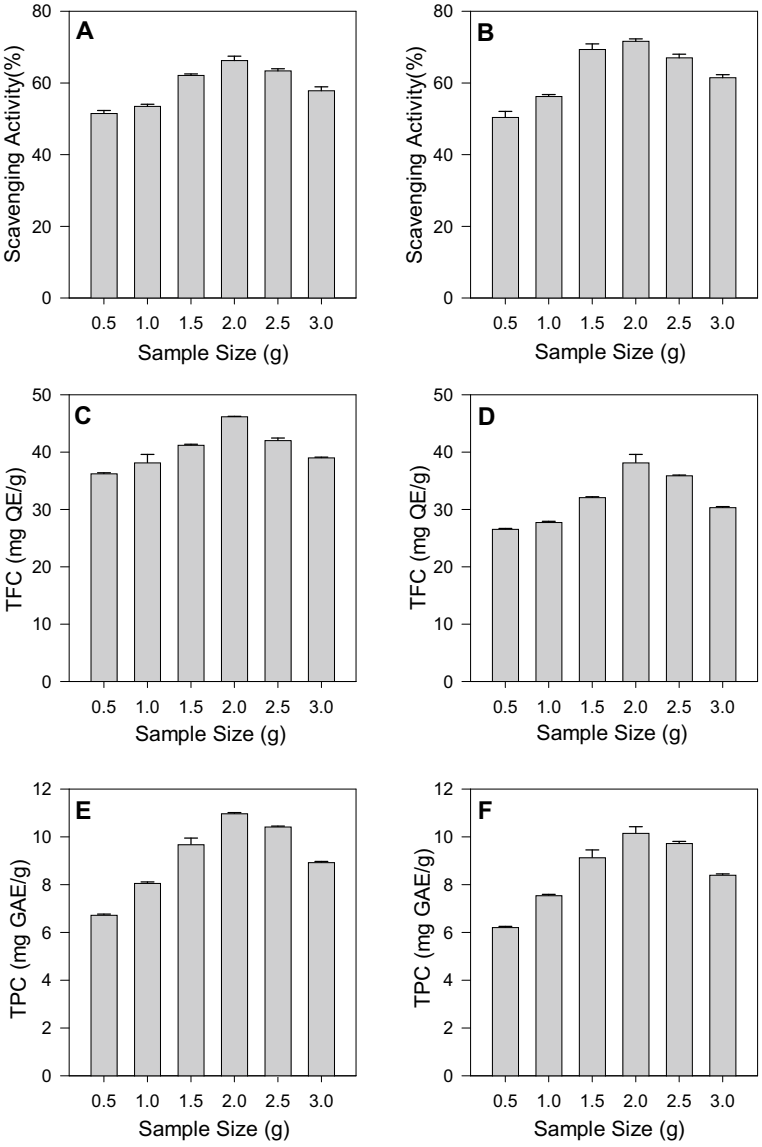

Fig. 3 The effects of sample size on the DPPH (**a** matured and **b** young leaves), TFC (**c** matured and **d** young leaves), and TPC (**e** matured and **f** young leaves)

Acknowledgements The authors would like to acknowledge the support they received from the Ministry of Higher Education Malaysia through the Fundamental Research Grant Scheme (FRGS) [grant number FRGS/1/2020/TK0/UNIMAP/03/25] and Universiti Malaysia Perlis for providing the equipment and facilities.

References

1. Shah KA, Patel MB, Patel RJ, Parmar PK (2010) *Mangifera indica* (mango). Pharmacogn Rev 4(7):42–48
2. Masibo M, He Q (2008) Major mango polyphenols and their potential significance to human health. Compr Rev Food Sci Food Saf 7(4):309–319
3. Yeshi K, Crayn D, Ritmejerytė E, Wangchuk P (2022) Plant secondary metabolites produced in response to abiotic stresses has potential application in pharmaceutical product development. Molecules 27(1):313
4. Alshammaa D (2016) Preliminary screening and phytochemical profile of *Mangifera indica* leave's extracts, cultivated in Iraq. Int J Curr Microbiol App Sci 5(9):163–173
5. Kabir Y, Shekhar HU, Sidhu JS (2017) Phytochemical compounds in functional properties of mangoes. Handb Mango Fruit Prod Postharvest Sci Process Technol Nutr 237–254
6. Pan J, Yi X, Zhang S, Cheng J, Wang Y, Liu C (2018) Industrial crops & products bioactive phenolics from mango leaves (*Mangifera indica L.*). Ind Crops Prod 111:400–406
7. Asrul MS, Abbas H, Bahagia M, Ghaffar A (2018) Morphological characterisation of harumanis mango (*Mangifera indica Linn.*) in Malaysia. Int J Environ Agric Res 4(1):45–51
8. Carpentieri S, Soltanipour F, Ferrari G, Pataro G, Donsì F (2021) Emerging green techniques for the extraction of antioxidants from agri-food by-products as promising ingredients for the food industry. Antioxidants 10:1417
9. Hamid Nour A, Ruth Oluwaseun A, Hamid Nour A, Suliman Omer M, Ahmed N (2021) Microwave-assisted extraction of bioactive compounds (review). Microwave heating—electromagnetic fields causing thermal and non-thermal effects
10. Aqilah S, Mohd Amer N, Farihan K (2020) Kinetic extraction of antioxidant and total phenolic content of *Clinachantus nutans*. IOP Confe Ser Mater Sci Eng 864(1)
11. Syazwani N, Farihan K (2018) Comparative study on the extraction methods of *Clinachanthus nutans* for total phenolic content, total flavonoid content and dpph scavenging activity. In JERE 10(1):1–8
12. Ngamsuk S, Huang TC, Hsu JL (2019) Determination of phenolic compounds, procyanidins, and antioxidant activity in processed *Coffea arabica L.* Leaves. Foods 8(9):389
13. Loganayaki N, Siddhuraju P, Manian S (2013) Antioxidant activity and free radical scavenging capacity of phenolic extracts from *Helicteres Isora L.* and *Ceiba Pentandra L.* J Food Sci Technol 50(4):687–695
14. Alexandra Pătrăuanu O, Lazăr L, Popa VI, Volf I (2019) Influence of particle size and size distribution on kinetic mechanism of spruce bark polyphenols extraction. Cellul Chem Technol 53(2):71–78
15. Prasedya ES, Frediansyah A, Martyasari NWR, Ilhami BK, Abidin AS, Padmi H, Fahrurrozi Juanssilfero AB, Widyastuti S, Sunarwidhi AL (2021) Effect of particle size on phytochemical composition and antioxidant properties of *Sargassum Cristaefolium* ethanol extract. Sci Rep 11(1):17876
16. Tan PW, Tan CP, Ho CW (2011) Antioxidant properties: effects of solid-to-solvent ratio on antioxidant compounds and capacities of Pegaga *(Centella Asiatica)*. Int Food Res J 18:557–562
17. Che Sulaiman IS, Basri M, Fard Masoumi HR, Chee WJ, Ashari SE, Ismail M (2017) Effects of temperature, time, and solvent ratio on the extraction of phenolic compounds and the anti-radical activity of *Clinacanthus Nutans Lindau* leaves by response surface methodology. Chem Central J 11(1)

18. Chen C, Mokhtar RAM, Sani MSA, Noor NQIM (2022) The effect of maturity and extraction solvents on bioactive compounds and antioxidant activity of mulberry (*Morus alba*) fruits and leaves. Molecules 27(8)
19. Alara OR, Abdurahman NH, Mudalip SKA, Olalere OA (2019) Effects of microwave-assisted extraction parameters on the recovery yield and total phenolic content of *Vernonia amygdalina* leaf extracts with different methods of drying. Jundishapur J Nat Pharm Prod 14(1):57620

Optimization of Nickel Precipitation and Leaching Process from Simulated Industrial Waste: A Study on pH, Contact Time, and Sulfuric Acid Concentration

Nurul Zufarhana Zulkurnai, Umi Fazara Md Ali, Naimah Ibrahim, Mohd Irfan Hatim Mohamed Dzahir, Nor Ashikin Ahmad, and Fathiah Mohamed Zuki

Abstract The presence of nickel in industrial waste has emerged as a significant environmental concern, predominantly attributed to the plating industry. The significant objective of this study is to optimize the precipitation and leaching method to extract valuable nickel from the waste material. The high concentration of nickel found in the waste makes it a potentially valuable resource. To explore its potential extraction, the precipitation and leaching processes were optimized using a simulated Watts bath solution which is widely employed in the industry. This study focuses on examining the influence of pH, contact time, and sulfuric acid concentration on the

N. Z. Zulkurnai · U. F. M. Ali (✉) · M. I. H. M. Dzahir · N. A. Ahmad
Faculty of Chemical Engineering & Technology, Universiti Malaysia Perlis, 02600 Arau, Perlis, Malaysia
e-mail: umifazara@unimap.edu.my

M. I. H. M. Dzahir
e-mail: irfan@unimap.edu.my

N. A. Ahmad
e-mail: ashikinahmad@unimap.edu.my

U. F. M. Ali · M. I. H. M. Dzahir
Biomass Utilization Organization, Centre of Excellence (CoEBU), Universiti Malaysia Perlis, 02600 Arau, Perlis, Malaysia

N. Ibrahim
Faculty of Civil Engineering Technology, Universiti Malaysia Perlis, 02600 Arau, Perlis, Malaysia
e-mail: naimah@unimap.edu.my

F. M. Zuki
Center for Separation Science & Technology (CSST), Department of Chemical Engineering, Faculty of Engineering, Universiti Malaya, 50603 Kuala Lumpur, Malaysia
e-mail: fathiahmz@um.edu.my

H. L. Ong et al. (eds.), *Proceedings of the 3rd International Conference on Biomass Utilization and Sustainable Energy; ICoBiomasSE 2023; 4–5 September; Kuala Lumpur, Malaysia*, Green Energy and Technology,
https://doi.org/10.1007/978-981-99-9164-8_13

extraction of nickel concentration during the precipitation and leaching processes. To develop a prediction model for the process, three models were taken into consideration: quadratic, linear, and 2F1. The quadratic model exhibited the greatest adjusted R^2 value, suggesting a superior level of fit in comparison with the linear and 2F1 models. The predicted R^2 value of 0.8169 exhibits a satisfactory level of concordance with the adjusted R^2 value of 0.9737. The recommended optimal conditions proposed by response surface methodology (RSM) consisted of a pH value of 10.56, a contact time of 16.52 h, and a sulfuric acid concentration of 1.80 M in order to achieve a nickel concentration of 28,415 mg/L.

Keywords Optimization · Precipitation · Leaching · Nickel waste · Watts bath

1 Introduction

In the realm of industrial processes, there exists a notable focus on the extraction of valuable metals from waste materials, as it holds considerable potential for generating both economic and environmental advantages [1]. Among the several metals, nickel is well recognized as a highly coveted resource due to its extensive range of applications across multiple industries. Nevertheless, the inclusion of impurities in nickel industrial waste presents a significant obstacle in terms of recovery techniques and the resulting implications for both human health and the environment.

In the context of human health, nickel presents a notable hazard due to its capacity to elicit severe disease like cancer, lung fibrosis, cardiovascular disorders, and renal problems [2]. The inadequate disposal of nickel can result in severe environmental ramifications, leading to the contamination of water and soil [3, 4]. To avert these catastrophic incidents in Malaysia, the Department of Environment Malaysia (DOE) has implemented regulations to control the discharge concentration of nickel effluent into streams by set 1.0 mg/L as a discharge limit [5]. These measures aim to safeguard both the environment and the well-being of the population by mitigating the harmful effects of nickel contamination.

Plating industry has been identified as a major contributor to the nickel contamination found in industrial waste [6]. The predominant solution employed in this industry is the Watts bath solution. The composition of Watts bath solution is a combination of nickel sulfate, nickel chloride, and boric acid. Jaroslaw et al. [7] and Laokhen et al. [8] reported that the nickel waste contains a diverse range of contaminants, such as phosphorus, boric acid, lead, copper, zinc, and aluminum [7, 8]. One of the sustainable approaches to remove the contaminant is by precipitation process [9].

As a result, the precipitation and leaching processes have garnered attention as a viable solution for recovering this valuable metal. The study done by Oustadakis et al. [10] employed magnesium oxide (MgO) as a reagent for precipitation [10]. According to his research, more refined nickel hydroxide can be acquired through precise regulation of pH levels and temperature conditions, but it has slower hydroxyl ion release compared to NaOH [10]. The study conducted by Lee [11] utilized

$Ca(OH)_2$ reagent to investigate the effects of increasing precipitation reagent on pH levels [11].

This study aims to address the gap in knowledge regarding the optimization of the nickel precipitation and leaching process from simulated Watts bath solution within the given setting. To yet, there has been a lack of study focused on optimizing the utilization of Watts bath solution. The implementation of Watts bath solution simulation provides a controlled environment for the examination and evaluation of the effectiveness of different parameters in enhancing nickel precipitation. The objective of this study is to determine the ideal circumstances for achieving the maximum concentration of nickel by methodically changing pH, contact time, and sulfuric acid concentration.

Moreover, a comprehensive mathematical model is necessary to comprehend the correlation between the process parameters and the concentration of nickel. Therefore, this study aims to evaluate various models, such as the quadratic, linear, and 2F1 models, to ensure the precipitation and leaching processes most precise and dependable depiction. The chosen model will offer a predictive framework for the estimation of nickel concentrations under varying operational situations, hence enabling the enhancement of process control and optimization.

2 Material and Method

2.1 Chemical and Material

The Watts bath solution was prepared by combining nickel sulfate ($NiSO_4$), nickel chloride ($NiCl_2$), and boric acid (H_3BO_3). Sodium hydroxide (NaOH) was utilized as the chemical for the precipitation process, and sulfuric acid (H_2SO_4) served as the leaching reagent.

2.2 Preparation of Simulated Watts Bath

A 1-L (L) beaker was filled with 1 L of distilled water. To this, 153 g of $NiSO_4$, 128 g of $NiCl_2$, and 30.9 g of H_3BO_3 were added. Beaker containing the solution was placed on a hot plate, and the temperature was adjusted to 55 °C. A magnetic stirrer was used to continuously stir the solution until all the solid compounds were completely homogenized.

2.3 Precipitation Process

The optimization process involved manipulating three key factors which is pH, contact time, and leaching reagent concentration. To achieve this, a Box–Behnken design was employed, which enabled a systematic exploration of the parameter space. The optimization of the nickel precipitation process was initiated by performing experiments at varying pH levels ranging from 8 to 13. The contact time also varied between 6 and 24 h. After each precipitation run, the obtained precipitate was carefully collected and subsequently dried in an oven at 120 °C for a period of 6 h.

2.4 Leaching Process

The dried nickel precipitate underwent the leaching process after the precipitation process. For this purpose, H_2SO_4 was employed as the leaching reagent, and its concentration was varied between 0.5 and 2.5 M. The leaching process was conducted at room temperature, and the ratio of the nickel precipitate to H_2SO_4 was maintained at 1:10. To ensure efficient dissolution of the precipitate, the mixture was subjected to agitation at 300 rpm, preventing sedimentation of the precipitate at the bottom of the beaker. The nickel concentration of each run will be determined during the optimization process by using inductively coupled plasma (ICP) machine.

2.5 Optimization Precipitation and Leaching Process

The design of experiment (DOE) methodology encompasses a set of statistical and mathematical techniques that include the fitting of polynomial equations to empirical data. In this study, a Box–Behnken design (BBD) of response surface methodology (RSM) with three levels and three factors was utilized to identify the optimal combination of precipitation and leaching process variables for the extraction of nickel from simulated Watts bath. pH, contact time, and H_2SO_4 concentration were the independent variables selected to be in this experimental design, the nickel concentration as the response for the combination of independent variables. For pH, the range varied from 8 to 13. For the contact time, the range is between 6 and 24 h. Meanwhile, for the H_2SO_4, it varied between 0.5 M and 2.5 M.

The variable levels in Table 1 are coded using the orthogonal balanced block design (BBD) method, resulting in equal spacing between the low (− 1), middle (0), and high (+ 1) levels. The inclusion of replicates at the center coordinates (0, 0, 0) allows the model to assess both the experimental error and the reproducibility of the data. The chosen experimental design comprises twelve experimental runs for combined 22 factorial designs. In addition, incomplete block designs are utilized,

Table 1 Variables and their levels for the BBD

Variable	Level		
	− 1	0	1
pH	8	10.5	13
Contact time	6	15	24
Sulfuric acid concentration	0.5	1.5	2.5

with the inclusion of five duplicated center points. This results in a total of seventeen experimental runs, as depicted in Table 1.

2.6 Analytical Method

For the analysis of nickel concentration, 10 ml of each run of leaching solution was analyzed using the inductively coupled plasma mass spectrometry (ICP-OES) machine due to its robust and precise method.

3 Results and Discussion

3.1 Precipitation and Leaching Process

The treatment process optimization, focusing on pH, contact time, and leaching reagent concentration, was carried out using a Box–Behnken design. The results of the optimization runs are presented in Table 2. To achieve the desired pH for each run, the Watts bath solution was adjusted using NaOH. The solution was continuously stirred at 300 rpm using a magnetic stirrer to ensure the respective contact time was reached.

Following the treatment process, the precipitate was filtered using filter paper, as depicted in Fig. 1a. The image reveals the successful formation and separation of nickel (II) hydroxide ($Ni(OH)_2$) precipitate from the Watts bath solution through the reaction between the Watts bath solution and sodium hydroxide (NaOH) [12]. $Ni(OH)_2$ precipitate subsequently dried in an oven for 6 h at 120 °C aiming to eliminate any excess moisture. The precipitate of $Ni(OH)_2$, which has been dried, is depicted in Fig. 1b. The physical appearance of dried $Ni(OH)_2$ precipitate is green in color in a combination of solid flaky crystal and powdery textures. The dried $Ni(OH)_2$ precipitate then underwent the leaching process, as depicted in Fig. 1c. For the leaching process, H_2SO_4 was used as the leaching reagent. During this procedure, the solid $Ni(OH)_2$ has been effectively leached, resulting in the formation of a clear green solution of $NiSO_4$ [13].

Table 2 Optimized condition for electrowinning process

Run	Parameters		
	pH	Contact time (hr)	H_2SO_4 concentration (M)
1	8	24	1.5
2	10.5	24	2.5
3	13	24	1.5
4	10.5	15	1.5
5	8	15	2.5
6	8	6	1.5
7	10.5	24	0.5
8	10.5	15	1.5
9	13	15	0.5
10	10.5	6	2.5
11	8	15	0.5
12	10.5	6	0.5
13	13	6	1.5
14	10.5	15	1.5
15	10.5	15	1.5
16	10.5	15	1.5
17	13	15	2.5

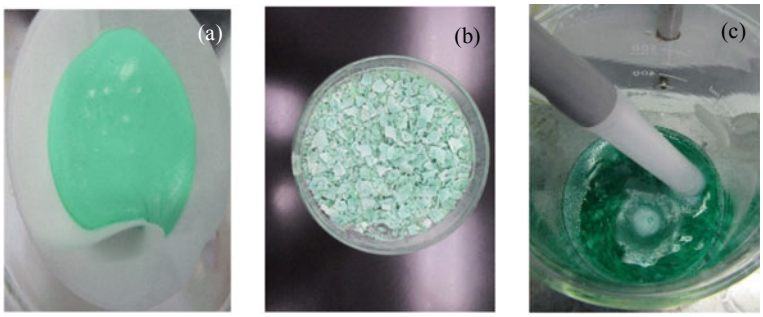

Fig. 1 Treatment process **a** filtration of precipitate, **b** dried precipitate, **c** leaching process

3.2 Optimization by Response Surface Methodology

The findings derived from the optimization of the treatment procedure, as depicted in Table 3, offer significant insights into the impact of pH, contact time, and H_2SO_4 concentration on the concentration of nickel in the treatment solution. Upon analysis of the data, significant patterns have been observed which provide confirmation of the influence that these parameters have on the process of nickel extraction.

Table 3 Result concentration of nickel for optimization process

Run	Parameters			Result
	pH	Contact time (hr)	H_2SO_4 concentration (M)	Concentration of nickel (mg/L)
1	8	24	1.5	28,986
2	10.5	24	2.5	28,385
3	13	24	1.5	28,997
4	10.5	15	1.5	27,829
5	8	15	2.5	27,275
6	8	6	1.5	24,416
7	10.5	24	0.5	28,149
8	10.5	15	1.5	27,825
9	13	15	0.5	26,627
10	10.5	6	2.5	25,140
11	8	15	0.5	26,271
12	10.5	6	0.5	21,809
13	13	6	1.5	24,648
14	10.5	15	1.5	27,906
15	10.5	15	1.5	27,839
16	10.5	15	1.5	27,853
17	13	15	2.5	26,993

First, when keeping the contact time and H_2SO_4 concentration constant, it is noticeable that pH 13 results in the largest concentration of nickel in the treatment solution, as opposed to a pH of 8. This phenomenon can be observed by doing a comparative analysis between Run 1 and Run 3, as well as Run 6 and Run 13. The results validate that elevated pH levels possess an increment capacity to produce $Ni(OH)_2$ species in the course of the precipitation process. At the high pH condition, more hydroxyl ions dissociate from the NaOH and lead to the increase of supersaturation of $Ni(OH)_2$ [14]. This finding is consistent with prior studies conducted by other researchers in 2010, thus reinforcing the importance of pH in optimizing the process of nickel extraction [15].

Similarly, when pH and contact time remain constant, the highest concentration of H_2SO_4 which in turn yields a treatment solution with the largest concentration of nickel derived from the dried precipitate. This can be observed by the comparisons made between Run 2 and Run 7, Run 5 and Run 11, and Run 9 and Run 17. The observed relationship between the concentration of H_2SO_4 and the concentration of nickel aligns with the conclusions drawn by Jin Young L. et al. in their study conducted in 2010 [15].

Furthermore, under conditions of constant pH and H_2SO_4 concentration, increasing the contact time during the precipitation process leads to an elevated concentration of nickel in the treatment solution. The observations can be made by

comparing Run 1 with Run 6, Run 2 with Run 10, Run 3 with Run 13, and Run 7 with Run 12. This finding shows that increasing the contact time increases the precipitation of hydroxide ions from NaOH and Ni^{2+} ions from the Watts bath solution, leading to the creation of $Ni(OH)_2$ [12].

Upon analysis of the optimization data, it becomes noticeable that Run 3 demonstrates the highest nickel content at 28,997 mg/L. This is closely followed by Run 1, Run 2, and Run 7, which exhibit concentrations of 28,986 mg/L, 28,385 mg/L, and 28,149 mg/L, respectively. Specifically, the four runs that exhibit the greatest nickel concentrations all possess a contact time of 24 h, suggesting that contact time has a substantial impact on the precipitation process.

The reason for Run 3 having the largest precipitation rate compared to the other four runs with the same contact time can be attributed to the fact that Run 3 was conducted at a pH of 13. This high pH level resulted in an increased concentration of hydroxyl ions, which in turn facilitated a greater precipitation of nickel from the solution [14]. The central point runs exhibit nickel concentrations ranging from 27,853 mg/L to 26,993 mg/L. The minor differences in nickel concentration among the central point runs suggest minimal errors in the optimization model.

Table 4 displays the summary data related to the fitness of the optimization model. The models were selected based on the highest-order polynomials that were not aliased, and additional terms were included if they were deemed to be statistically significant. Based on the data analysis, the quadratic model emerged as the suggested model due to its highest adjusted R^2 value compared to the linear and 2F1 models. Moreover, the quadratic model was found to be non-aliased, suggesting its suitability for the optimization process [16].

The quadratic model exhibits a strong correlation with the experimental data, as evidenced by the high adjusted R^2 value of 0.9737. This indicates a favorable match between the model and the observed data. The obtained predicted R^2 value of 0.8169, which is less than 0.2 in comparison with the adjusted R^2 value [16], provides additional evidence for the reliability of the quadratic model in its capacity to predict the nickel concentration during the optimization process.

These findings indicate that the quadratic model accurately represents the correlation between pH, contact time, and H_2SO_4 concentration, as well as their influence on the nickel concentration in the treatment solution. The model offers a significant tool for forecasting the best conditions required to attain the highest concentration of nickel.

Table 4 Fit summary data

Source	Sequential *p*-value	Lack of Fit *p*-value	Adjust R^2	Predicted R^2	
Liner	0.0001	< 0.0001	0.7440	0.6432	
2FI	0.4853	< 0.0001	0.7365	0.4806	
Quadratic	0.0002	< 0.0001	0.9737	0.8169	Suggested
Cubic	< 0.0001		0.9997		Aliased

The high adjusted R^2 value signifies that the quadratic model explains a significant proportion of the variability in the data, suggesting that the model is a valid depiction of the system under investigation. The non-aliased nature of the model further enhances its validity, by precisely capturing and assessing the impacts of the variables.

The significance and model fitness were analyzed using the analysis of variance (ANOVA). The impact of each individual variable and their interactions with one another on the response were also evaluated by this approach. Analysis of variance (ANOVA) was used to further evaluate the proposed model's dependability at a 5% significant level. Therefore, the *p*-value must be less than 0.05 in order to evaluate the model's significance [17].

The model's significance was confirmed by a model F-value of 66.77 and a *p*-value < 0.0001. The *p*-value for model *A*, *B*, and *C* are 0.7272, < 0.0001, and 0.0008, respectively (Table 5). This shows that the *B* and *C* models are significant. According to ANOVA table, the concentration of nickel is mostly affected by contact time and sulfuric acid concentration (*BC*). Similar to this, it was possible to infer that the B^2 and C^2 were important model terms for the response based on the *p*-values of the linear and quadratic terms.

Additionally, it was found that the independent variables' linear term effects on the answer were in the following order: ($B = 2313.00$) > ($C = 617.13$) > ($A = 39.63A$). This order shows contact time has the largest impact, followed by sulfuric acid concentration and pH. Equation 1 represents the final empirical model for the nickel concentration in terms of coded components.

Table 5 ANOVA (partial sum of squares—Type III) for the developed response surface model

Source	Sum of squares	df	Mean square	F-value	*p*-value	
Model	57,240,000	9	6,360,000	66.77	< 0.0001	Significant
A-pH	12,561.13	1	12,561.13	0.1319	0.7272	
B-contact time	42,800,000	1	42,800,000	449.38	< 0.0001	Significant
C-sulfuric acid concentration	3,047,000	1	3,047,000	31.99	0.0008	Significant
AB	12,210.25	1	12,210.25	0.1282	0.7309	
AC	101,800	1	101,800	1.07	0.3357	
BC	2,395,000	1	2,395,000	25.14	0.0015	Significant
A^2	29,674.12	1	29,674.12	0.3116	0.5941	
B^2	4,250,000	1	4,250,000	44.63	0.0003	Significant
C^2	4,002,000	1	4,002,000	42.02	0.0003	Significant
Residual	666,700	7	95,242.42			
Lack of fit	662,400	3	220,800	203.91	< 0.0001	Significant

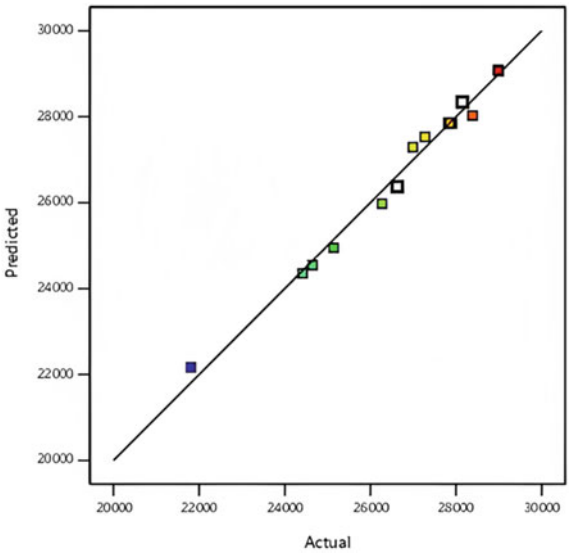

Fig. 2 Predicted versus actual value of nickel concentration (mg/L)

$$\begin{aligned}\text{Nickel Concentration} = {} & 27850.40 + 39.63A + 2313.00B \\ & + 617.31C - 55.25AB - 159.50AC - 773.75BC \\ & - 83.95A^2 - 1004.70B^2 - 974.95C^2 \end{aligned} \quad (1)$$

Figure 2 illustrates that the data points exhibit a uniform distribution and are closely matched with the linear trend. This finding suggests a strong correlation between the predicted response values and the actual observed values [18]. The close proximity of the data points to the regression line indicates that the constructed model effectively predicts the dependent variable by considering the independent variables of pH, contact time, and H_2SO_4 concentration. This alignment seen in this study demonstrates the high validity of the model for response value prediction.

Additionally, Fig. 3 shows the normal probability plot of residuals, which offers valuable insights into the distribution of the data points. The plots demonstrate that the residuals are closely aligned with the linear line, indicating a normal distribution of the data [19]. This implies that the observed data points are aligned with the assumptions of normality. A normal distribution of residuals suggests that the model is less sensitive to external noise or factors that could potentially induce deviations in the data. Therefore, the developed model is reliable for predicting the response variable.

Figures 4, 5 and 6 depict three-dimensional response surface plots that demonstrate the interaction effects of two optimization variables on the concentration of nickel. In these plots, the third variable is held constant at a zero level. These plots provide valuable insights into the impact of variation on nickel concentration during the treatment process.

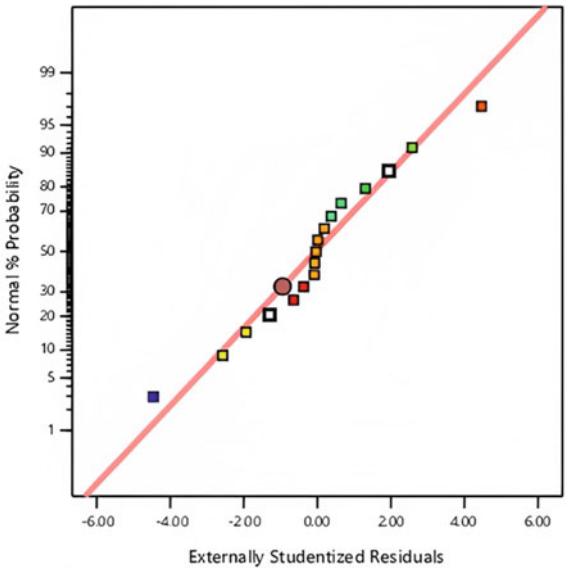

Fig. 3 Normal plot of residuals

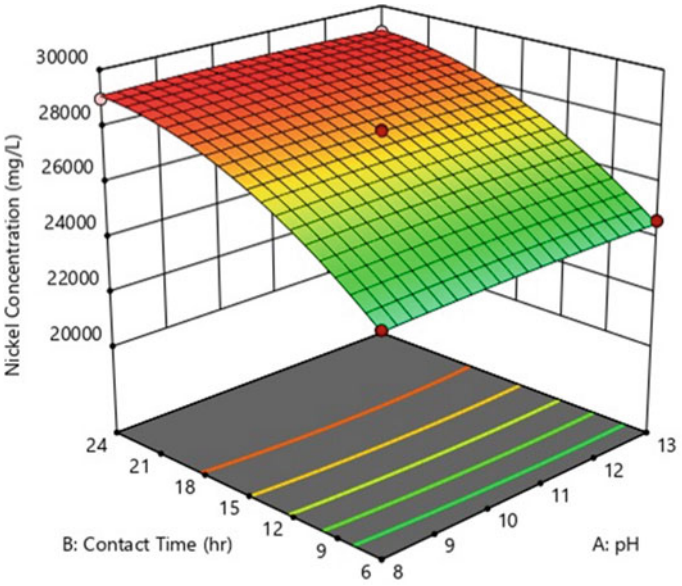

Fig. 4 Three-dimensional plot of nickel concentration with the combine effect of pH and contact time

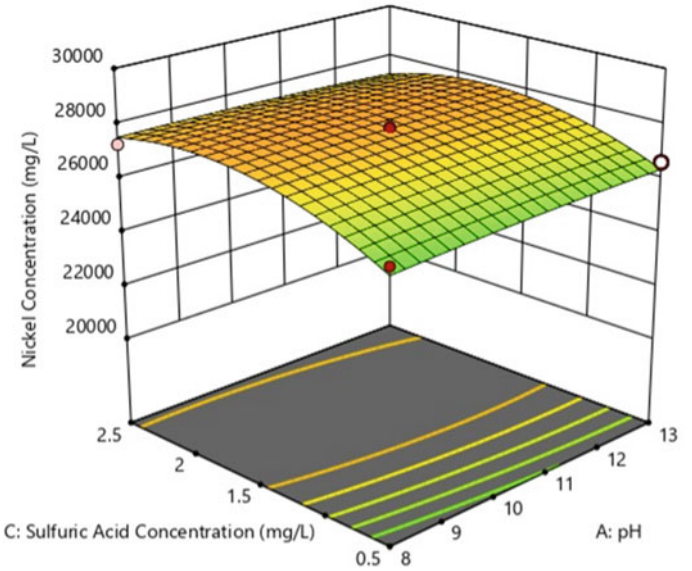

Fig. 5 Three-dimensional plot of nickel concentration with the combine effect pH and sulfuric acid concentration

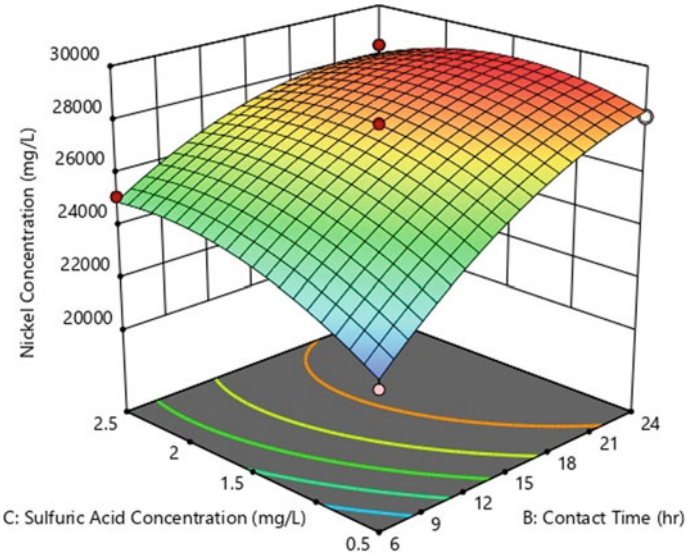

Fig. 6 Three-dimensional plot of nickel concentration with the combine effect contact time and sulfuric acid concentration

Figure 4 examines the impact of contact time and pH on the nickel concentration. The plot shows that increasing the contact time leads to higher nickel concentrations across all pH levels. This implies that a prolonged duration of contact time enhances the precipitation process, leading to higher yield extraction of nickel. The graph illustrates the significant of optimizing contact time in order to maximize the nickel concentration in the treatment solution.

In Fig. 5, it illustrates the impact of pH and sulfuric acid concentration on the nickel concentration. The data plot suggested that the optimal sulfuric acid concentration during the leaching process and pH during precipitation located near the midpoint values. This observation implies that extreme values of pH or sulfuric acid concentration may not lead to the highest nickel concentration. However, it should be noted that there exists an optimal range in which the process of nickel extraction demonstrates its highest level of effectiveness. These findings emphasize the significant of maintaining an optimum pH and sulfuric acid concentration to attain the desired nickel concentration in the treatment solution.

Figure 6 examines the impact of varying contact time and sulfuric acid concentration on the nickel concentration. The plot demonstrates that manipulating the contact time, while keeping the sulfuric acid concentration at an intermediate level, leads to elevated nickel concentrations. This suggests that a longer contact time, in combination with an optimal sulfuric acid concentration, enhances the efficiency of the leaching process and leads to an increased nickel concentration in the treatment solution. The findings of Kurama [20] and Zhanyoung et al. [21] have yielded similar outcomes [20, 21].

To evaluate the precision of the optimization results obtained through Box–Behnken design, three new batches of samples were prepared based on the suggested optimum conditions derived from the RSM software. The optimized conditions included a pH of 10.56, a contact time of 16.52 h, and an H_2SO_4 concentration of 1.80 M.

The nickel concentrations obtained from the three batches were recorded as follows: 28,405 mg/L for the first batch, 28,391 mg/L for the second batch, and 28,449 mg/L for the third batch. The overall average nickel concentration for the three replicate samples was determined to be 28,415 mg/L, as presented in Table 6.

Table 6 Experimental and predicted value of nickel concentration by using optimum preparation parameters

Replicate	Nickel concentration (mg/L)	
	Experimental	RSM predicted
1	28,405	28,270
2	28,391	
3	28,449	
Average	28,415	

By comparing the predicted nickel concentration from the RSM optimization with the experimental values obtained from the new samples, a slight difference can be observed. The predicted value from the optimization was 28,415 mg/L, which closely matches the average experimental value obtained from the three batches. This small discrepancy, with an error margin about 0.51%, suggests that the RSM optimization results are relatively accurate and reliable.

4 Conclusion

In conclusion, the optimization process of RSM by using Box–Behnken design effectively resulted in the determination of the optimal circumstances, which include a pH value of 10.56, a contact time of 16.52 h, and an H_2SO_4 concentration of 1.80 M. To validate the accuracy of these optimized results, three new sample batches were carefully run in strict accordance with the specified settings. The average concentration of nickel in these samples was determined to be 28,415 mg/L, exhibiting a minor deviation of 0.51% from the anticipated value.

Acknowledgements The authors acknowledged the financial support from University Malaysia Perlis (UniPRIMA/UniMAP/9001-00673).

References

1. Changsheng P, Ruijie J, Guangyu L, Fasheng L, Qingbao G (2014) Recovery of nickel and water from wastewater with electrochemical combination process. Sep Purif Technol 136:42–49
2. Giuseppe G, Alessia C, Graziantonio L, Maria Stefania S, Alessia Ca (2020) Review nickel: human health and environmental toxicology. Int J Environ Res Public Health 17:679
3. Ameet K, Aamna B, Ashfaque AP, Abdullaha Muhammad Saqaf J, Ali Muhammad M, Muneeba Z, Benazir L (2019) Remediation of nickel ion from wastewater by applying various techniques: a review. Acta Chemica Malaysia (ACMY) 3(1) (2019)
4. Costantino V, Enrica M, Cristiano C, Arianna DB (2022) Nickel in the environment: bioremediation techniques for soils with low or moderate contamination in European union. Environments 9:133
5. Legal Research Board, "Environmental Quality Act 1974 (Act 127), Regulations, Rules & Order," (International Law Book Services, 2018) Environmental Quality (Industrial Effluent) Regulations 2009, pp 373–436 (2018)
6. Lei Z, Jingsong W, Zhengwei X, Qingwei G, Weiming (2015) Recovery of nickel by electrolytic method from electroplating wastewater. In: 3rd International conference on material, mechanical and manufacturing engineering, pp 151–155
7. Jarosław W, Marek B, Juliusz P, Grzegorz L (2017) Nickel coatings electrodeposited from watts type baths containing quaternary ammonium sulphate salts. Int J Electrochem Sci 12:3350–3360
8. Laokhen P, Khumkoa S, Buahombura P, Piyawit W, Patcharawit T, Kareram A, Srikhang L (2019) preliminary study on recovery of nickel from electro-nickel-plating solution by eletrowinning. J Mater Sci Eng 8

9. Li L, Takahashi N, Kaneko K, Shimizu T, Takarada T (2015) A novel method for nickel recovery and phosphorus removal from spent electroless nickel plating solution. Sep Purif Technol 147:237–244
10. Oustadakis P, Agatzini LS, Tsakiridis PE (2006) Nickel and cobalt precipitation from sulphate leach liquor using MgO pulp as neutralizing agent. Miner Eng 19:1204–1211
11. Lee HY (2013) Separation and recovery of nickel from spent electroless nickel-plating solutions with hydrometallurgical process. Sep Sci Technol 48:1602–1608
12. Kunio F, Shogo Y, Masakuni M (2016) Continuous precipitation of nickel hydroxide by addition of ammonium ions. Cryst Growth Des 16:1824–1828
13. Laokhen P, Ma-Ud N, Yingnakorn T, Patcharawit T, Khumkoa S (2022) Recovery of nickel from spent electroplating solution by hydrometallurgical and electrometallurgical process. J Metals Mater Miner 32:5–100
14. Mubarok MZ, Liebarto A (2013) Precipitation of nickel hydroxide from stimulated and atmospheric-leach solution of nickel laterite ore. Procedia Earth Planet Sci 6:457–464
15. Jin Young L, Venkateswara Rao S, Nagaphani Kumar B, Dong JK, Ramachandra Reddy B (2010) Nickel recovery from spent Raneynickel catalyst through dilute sulfuric acid leaching and soda ash precipitation. J Hazardous Mater 176:1122–1125
16. Tevfik A, Mohamed Taha Osman AA (2020) Optimization and modeling of leaching parameters affecting nickel dissolution from Lateritic Ore in Eskisehir (Mihaliccik-Yunusemre) using Box-Behnken experimental design. J Environ Anal Chem 7:263
17. Shilpi D, Susmita M (2017) Box-Behnken statistical design to optimize preparation of activated carbon from Limonia acidissima shell with desirability approach. J Environ Chem Eng 5:588–600
18. Aziz ARA, Aziz SA (2018) Application of Box Behnken design to optimize the parameters for Kenaf-epoxy as noise absorber. IOP Conf Ser Mater Sci Eng 454:012001
19. Muneer MB, Chai PV, Abdelbaki B, Dina E, Abdul Wahab M, Ebrahim M (2022) Optimizing and control of effective synthesize parameters for Fe3O4 nanoparticles using response surface methodology. Chem Pap 76:6359–6370
20. Kurama H (2009) Treatment and recovery of nickel rich precipitate from plating plant waste. J Environ Eng Landscape Manage 17(4):212–218
21. Zhanyong G, Ping G, Guang S, Fachuang L (2021) Study on ultrasonically-enhanced sulfuric acid leaching of nickel from nickel-containing residue. Crystals 11:810

Adsorption of Used Cooking Oil (UCO) by Using Modified Kapok Fibre (MKF) at Different Concentrations of CaO Catalyst Through Esterification Reaction

Ain Athirah Misran and Nor Halaliza Alias

Abstract Used cooking oil (UCO) is a vegetable or animal-based oil that is generated from cooking and frying foods at room temperature. The UCO which mainly consists of fats and oils is originating from the commercial or industrial food processing operation, including the restaurants. The growing of human population has induced a large quantities of UCO. In Malaysia, the disposal of UCO from the households and restaurants into the drainage and soil has become a major problem, which has caused the blockage of drainage and sewer system due to improper disposal of practices of UCO wastewater. Therefore, a study was conducted in order to remove the oil from the UCO wastewater by using the modified kapok fibre (MKF) through the esterification reaction. In this study, the effect of calcium oxide (CaO) catalyst percentages added in the esterification was investigated. Based on the results, the adsorption capacity showed that the MKF was able to adsorb UCO up to 12.46 ± 0.5 (SE) g of oil/g with the oil removal of 27.25% by using 5 wt% CaO. As the percentages of CaO increased to 10 wt% CaO and 15 wt% CaO, both of adsorption capacity and oil removal were increased at 15.26 ± 0.6 (SE) g oil/g (33.37%) and 19.93 ± 1.3 (SE) g oil/g (43.58%), respectively. Therefore, it was found that the increasing in CaO percentages resulted in higher adsorption of UCO and percentage of oil removal. The maximum percentages of CaO was obtained by using 15 wt% CaO, where it gave the highest adsorption capacity and oil removal efficiency.

Keywords Kapok fibre · Used cooking oil · Esterification · Oil adsorption

A. A. Misran · N. H. Alias (✉)
School of Chemical Engineering, College of Engineering, Universiti Teknologi MARA, 40450 Shah Alam, Selangor, Malaysia
e-mail: norhalaliza@uitm.edu.my

H. L. Ong et al. (eds.), *Proceedings of the 3rd International Conference on Biomass Utilization and Sustainable Energy; ICoBiomasSE 2023; 4–5 September; Kuala Lumpur, Malaysia*, Green Energy and Technology,
https://doi.org/10.1007/978-981-99-9164-8_14

1 Introduction

Cooking oil has become an important material for the preparation of various food types, especially fried meals due to the transferring heat to the food as it is prepared and contributes to the flavour of the dish [3]. Basically, the cooking oils are mainly produced from edible vegetable oils such as soybean oil, corn oil, coconut oil, rapeseed oil, palm oil, and sunflower oil [13]. The primary consumers of cooking oil are mostly households, food manufacturers, and restaurants. Global household cooking oil consumption has increased steadily, with more than 200 million tons of vegetable cooking oil consumed in 2021. The vast amounts of waste cooking oil produced are the consequence of the current increase in the human population and the extent to which consumers employ frying methods in food preparations [7]. Kristiana et al. [9] have claimed that the yearly amount of used cooking oil collected from residences, restaurants, and food processing in Malaysia is between 21 and 35 kt, 16 and 22 kt and 11 and 14 kt, respectively, which indicates that the total amount of used cooking oil collected in Malaysia falls somewhere between 48 and 71 kt. As a result, the production and consumption of cooking oil has caused the increasing in the amount of waste cooking oil, which also known as used cooking oil (UCO). According to Noor [12], the increasing in the production of waste cooking oil or UCO from the household or food industrial source continues to rise in Malaysia. Improper waste management of cooking oil leads to discharge of UCO to the environment, which could affect the water drainage and plumbing system as well as to the human health.

Thus, the UCO needs to be treated properly before it is being discharged to the environment or used in other processes. Adsorption process is the most promising methods for the removal of UCO due to its effectiveness and feasibility. Mohd Jopery et al. [10], have reported that the adsorption method in removing oil spills have been considered a better way of controlling pollution by using the natural adsorbents. A simple adsorbent approach which originates from the natural organic adsorbent was widely used in removing the oil because of their greater adsorption capacities, eco-friendliness, and cost effectiveness. Natural adsorbents are not only biodegradable when it is disposed, but it is also more efficient than chemical adsorbent as they showed a greater adsorption capacity [10].

The increasing attention on the usage of kapok fibre as an oil adsorbent has become one of the alternative due to its distinct hollow structure and hydrophobic characteristics. Kapok or also known as *Ceiba pentandra* is an effective natural oil sorbent with high sorption and retention capacities, structural stability and high reusability [1]. Kapok fibre has high water repellence and high oil adsorption capability. The hydrophobic nature of kapok fibre provides an advantage over the majority of the oil spill since it can be mechanically pressed out to recover the oil and does not hold the water. However, the oil adsorption process by using natural kapok fibre is still uncertain due to the function of the empty lumen and the surface wax are still not being recognized [11]. Therefore, in order to overcome this problem, the kapok fibre is modified by using esterification reaction by varying the percentages of calcium

oxide (CaO) which added to the reaction as catalyst. The effectiveness of the amount of catalyst used was studied towards the UCO adsorption analysis.

Therefore, the modification of kapok fibre was needed so as to alter its properties and surface characteristics. This includes the removal of wax surface, functional of hollow structure of kapok fibre in retaining the oil captured and the crystallinity changed in the fibre wall matrix [16]. It was expected that the MKF would become more hydrophobic. Esterification is one of the chemical alterations method that could enhance the adsorption of oil by modifying the raw kapok fibre (RKF) into modified kapok fibre. In this reaction, an ester bond is formed by the reaction between carboxylic acid and alcohol. The catalyst, CaO, used in this reaction allows more chemical alteration on the RKF surface due to the high catalytic activity as it contains a larger number of basic sites per mass unit and has better activity when it is reused [4]. The CaO also is one of the well-researched heterogeneous catalysts as it has a higher basicity, lower solubility, lower price and easier to handle than potassium hydroxide, KOH [8].The purpose of this study is to analyse the capability of MKF to adsorb the oil from UCO wastewater. The effectiveness of the modification was investigated by studying the effect of different percentages of CaO catalyst added, namely 5, 10 and 15 wt% of the RKF mass, through the esterification reaction. In the second objective, the maximum percentage of CaO added would be identified through the esterification reaction based on the highest adsorption capacity and oil removal percentages.

2 Materials and Methodology

2.1 Materials

The RKF was provided by the School of Chemical Engineering, College of Engineering, Universiti Teknologi MARA, Shah Alam, Selangor. Then, the RKF was air dried for 24 h. Finally, the RKF was segregated and cleaned from the pods and seeds. Meanwhile, the UCO was collected from the cafeteria located in Universiti Teknologi MARA Shah Alam, Selangor. The UCO was freshly taken before the adsorption test since the UCO is easily oxidized when it is exposed to heat, light and oxygen.

2.2 Chemicals

The chemicals used in esterification reaction were stearic acid, calcium oxide and ethyl acetate. In this study, calcium oxide (CaO) was used as the catalyst to facilitate the esterification reaction.

2.3 *Esterification Reaction Setup*

The reflux condensing method has been used in the esterification process in modifying the RKF. Figure 1 illustrated the experimental setup for esterification reaction which consists of three-neck round bottomed flask, condenser, thermometer, magnetic stirrer, hot plate and a retort stand. A 1 g of RKF was weighed, and the stearic acid (SA) was measured with the ratio of 1:1 to RKF. Both of the RKF and SA were placed into a three-neck round bottomed flask. Next, the CaO catalyst of 5 wt% of RKF mass was added into the mixture. In this experiment, 100 ml of ethyl acetate was used as a solvent with the presence of magnetic stirrer (200 rpm). The duration of reflux reaction was fixed at 3 h in the oil bath (180˚C). After the reaction has completed, the obtained sample (MKF) was filtered, washed several times with 100 ml of ethanol and finally washed with 100 ml of acetone to stop the reaction in order to remove any non-structural constituents. Then, the MKF was dried in the room temperature at 30 ˚C. The esterification reaction was repeated at different concentrations of CaO, namely at 10 and 15 wt% of RKF mass, respectively.

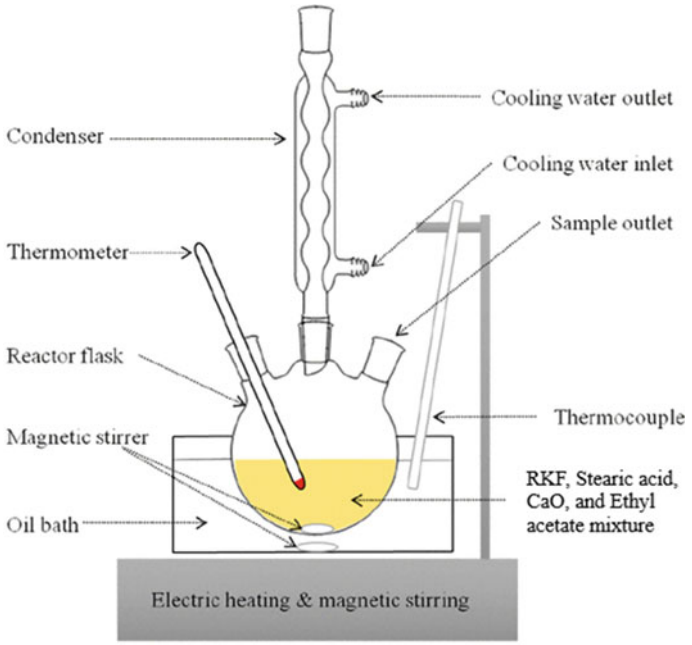

Fig. 1 Experimental setup of esterification reaction by using refluxing condensing method [17]

2.4 Preparation of UCO–Water Mixture

The MKF obtained from the esterification reaction was proceeded with the adsorption test by using UCO–water mixture. The mixture was prepared by weighing 50 g of UCO and mixed with 50 ml of tap water in a 500 ml beaker. After that, the mixture obtained was homogenized for 10 min by using magnetic stirrer (150 rpm) [2].

2.5 Adsorption Test

The adsorption test in this study was carried out by immersing the MKF in the UCO–water mixture. The weight of MKF with 5 wt% CaO of RKF mass was divided into three portions equally. Each portion was weighed to obtain the initial sorbents weight, Wi. Then, one portion of the MKF was immersed for 30 min at room temperature. After that, the mixture was drained slowly through the filter funnel and the MKF was collected. The weight of MKF after filtered was measured and recorded. The adsorption test was done in triplicates, where the average weight after filtered, W_t, was calculated. All the procedure was repeated by using 10 and 15 wt% of CaO catalyst, respectively. The filtration method was set up as shown in Fig. 2.

The oil adsorption capacity of the samples and percentage of oil removal were determined from the calculation based on Eqs. (1) and (2), respectively:

$$Q = \frac{W_t - W_i - W_w}{W_i} x100 \tag{1}$$

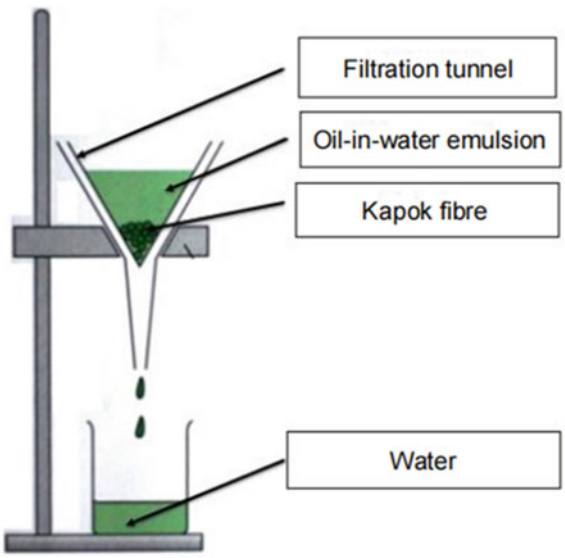

Fig. 2 Experimental setup for the filtration step [6]

where:

Q is the oil sorption capacity of the sorbents, calculated as grams of oil per gram of sample, W_t is the weight of the wet sorbent after draining (g) and W_w is the weight of the water adsorbed in the sorbent (g) [2]. Also:

$$R = \frac{W_1}{W_2} \times 100 \tag{2}$$

where:

R is the percentage of oil removal (%), W_1 is the weight of oil adsorbed by the fibre or oil adsorption capacity and W_2 is the initial weight of oil in the system (g) [14].

3 Results and Discussion

3.1 Effect of CaO Catalyst Percentages in the Adsorption of UCO by Using MKF

The effect of different percentages of CaO on the adsorption capacity of UCO by using MKF is shown in Fig. 3. Generally, the RKF is a cellulosic fibre type. The structure consists of a hydrophobic surface with a large open lumen for oil adsorption capacity and a hydroxyl group that restricts the oil adsorption as it becomes more hydrophilic [11]. Kapok fibre may be used in a variety of applications, such as in oil adsorption and oil spill clean-up [5].

The modification of RKF through the esterification reaction has improved the oil adsorption from UCO wastewater [15]. The hydrophobic waxy coating on the surface of MKF has contributed to high sorption capacity. The hydrophobic interactions and the Van der Waals forces between the oil and the waxy surface coating were important during the early stages of oil adsorption onto the kapok surface [1].

During the esterification reaction, the hydroxyl group in the RKF has been converted to ester group. The formation of an ester in the MKF after the esterification reaction is very important as it would increase the oil adsorption capacity. In this study, the oil adsorption test was conducted in order to observe the performance of MKF to adsorb oil from the UCO–water mixture. Based on Fig. 3, the higher percentage of CaO catalyst resulted in the reduction of electrostatic repulsion in modified kapok fibre and thus increased the adsorption capacity of UCO by using MKF [2]. The results showed that the amount of oil adsorption capacity of UCO by using MKF at 5, 10 and 15 wt% of RKF mass were 12.46 ± 0.5 (SE) g of oil/g, 15.26 ± 0.6 (SE) g of oil/g and 19.93 ± 1.3 (SE) g of oil/g, respectively. Based on the results, the increase in CaO catalyst percentages has increased the oil adsorption capacity.

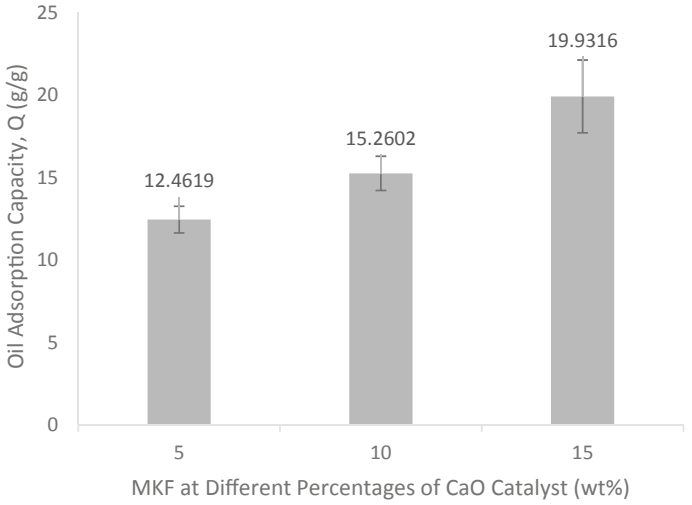

Fig. 3 Amount of UCO adsorption capacity by using MKF at different percentages of CaO catalyst

The presence of CaO catalyst allowed more chemical alteration on the RKF surface due to the high catalytic activity. According to De Souza et al. [4], the CaO has the best catalytic performance because it contains a larger number of basic sites per mass unit and has better activity when it is reused. Meanwhile, the other oxides such as BaO, SrO and MgO demonstrate a great loss in efficiency when they are used at the second time. Kawashima et al. [8], have claimed that CaO is also known as one of the well-researched heterogeneous catalysts as it has a higher basicity, lower solubility, lower price and is easier to handle than KOH.

On the other hand, Fig. 4 shows the oil removal percentages obtained from the experiments. Previous studies have shown that the percentage of oil removal is directly proportional to the percentage of CaO catalyst [2]. Based on Fig. 4, the percentages of oil removal increased rapidly with increasing of CaO concentration (wt%), which resulted in 27.25, 33.37 and 43.58% by using 5, 10 and 15 wt% of RKF mass, respectively. The results indicated that the increase in CaO catalyst percentages has also increased the percentage of oil removal.

3.2 Optimum Condition of CaO Catalyst Added into the Esterification Reaction in Producing MKF

The optimum condition for oil adsorption capacity was achieved at 19.93 ± 1.3 g of oil/g by using 15 wt% of CaO catalyst, by observing the maximum value of oil adsorption capacity and the percentage of oil removal (43.58%). Chemical modification on kapok fibre with the use of CaO as catalyst was an alternative approach

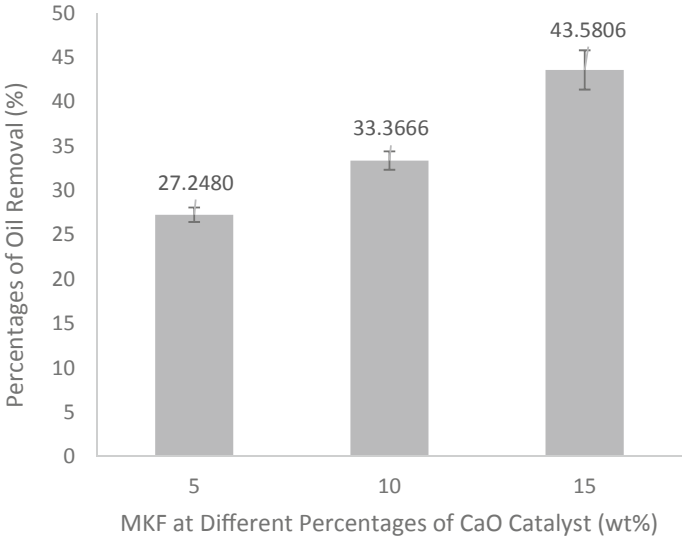

Fig. 4 Percentages of oil removal by using MKF at different percentages of CaO

to increase the oil sorption capacity. Further increment of CaO concentrations has enhanced the oil adsorption capacity of the modified kapok fibres, resulting in a higher oil adsorption capacity and oil removal efficiency.

4 Conclusion

In this study, the oil adsorption capacity and percentages of oil removal by using MKF at different percentages of calcium oxide (CaO) as catalyst through esterification reaction was investigated. The modification of RKF to MKF was able to increase the hydrophobic-oleophilic properties by replacing more O–H groups with C=O (ester) groups during the esterification reaction. The adsorption capacity shows that the MKF was able to adsorb UCO up to 12.46 ± 0.5 g of oil/g with 27.25% oil removal by using 5 wt% of CaO. However, as the concentration of CaO catalyst was increased to 10 and 15 wt%, both of oil adsorption capacity and percentages of oil removal were increased at 15.26 ± 0.6 g of oil/g (33.37%) and 19.93 ± 1.3 g of oil/g (43.58%), respectively. This can be concluded that the trend of oil adsorption capacity and percentage of oil removal were increased as the concentration of CaO catalyst increased. Meanwhile, among the concentration of CaO catalyst tested, 15 wt% of CaO catalyst showed the highest amount of UCO adsorption capacity and oil removal efficiency. This shows that the modification of RKF to produce MKF has successfully increased the oil adsorption capacity. Thus, the MKF could be one of the potential adsorbent in the removal of oil from the UCO wastewater.

5 Recommendations

Kapok fibre was an alternative to the conventional synthetic oil sorbents used for oil recovery in the absence of water due to its high oil adsorption, great reusability and outstanding biodegradability. It is recommended to increase the concentration of CaO catalyst (more than 15 wt%) in modifying the RKF to MKF in order to maximize the potential of MKF for oil adsorption from UCO wastewater.

Acknowledgements The author would like to express her gratitude to her supervisor, Madam Nor Halaliza Alias, who has provided unwavering guidance and support throughout the process of conducting this research. A special thanks to En. Faeez Sarulan, the Assistant Engineer from the Fluid Mechanics Laboratory for the guidance in conducting the experiment and finally to School of Chemical Engineering, College of Engineering, Universiti Teknologi MARA, Shah Alam for the financial support and laboratory facilities.

References

1. Abdullah MA, Rahmah AU, Man Z (2010) Physicochemical and sorption characteristics of Malaysian Ceiba pentandra (L.) Gaertn. as a natural oil sorbent. J Hazard Mater 177(1–3):683–691
2. Alias NH, Hasan SIZ (2018) Adsorption of used cooking oil (UCO) by using raw and modified kapok fibre through esterification. IOP Conf Ser Mater Sci Eng 358(1):012028
3. Daud MSM, Ngadiman NI, Suliman MS (2020) The awareness of recycling the used of cooking oil. J Crit Rev 7(8):30–32
4. De Sousa FP, Dos Reis GP, Cardoso CC, Mussel WN, Pasa VMD (2016) Performance of CaO from different sources as a catalyst precursor in soybean oil transesterification: Kinetics and leaching evaluation. J Environ Chem Eng 4(2):1970–1977
5. Futalan CM, Choi AES, Soriano HGO, Cabacungan MKB, Millare JC (2022) Modification strategies of kapok fiber composites and its application in the adsorption of heavy metal ions and dyes from aqueous solutions: a systematic review. Int J Environ Res Public Health 19(5):1–26
6. Hamidon MAB, Hussin R (2021) Superhydrophobicity of kapok fiber and its performance in oily water. Progr Eng Technol 2(1):694–701
7. Kabir I, Yacob M, Radam A (2014) Households' awareness, attitudes and practices regarding waste cooking oil recycling in Petaling, Malaysia. IOSR J Environ Sci Toxicol Food Technol 8(10):45–51
8. Kawashima A, Matsubara K, Honda K (2009) Acceleration of catalytic activity of calcium oxide for biodiesel production. Biores Technol 100(2):696–700
9. Kristiana T, Baldino C, Searle S (2022) An estimate of current collection and potential collection of used cooking oil from major Asian exporting countries. Int Council Clean Transp 13:1–21
10. Mohd Jopery NSA, Abdullah M, Kum Yoke S, Mustaffa AR (2020) The preliminary study of oil removal using lemon peel waste. Malaysian J Chem Eng Technol (MJCET) 3(1):56–61
11. Naharudin AU, Shaarani SHN, Rou LM, Hamidi NH, Ahmad N, Rasid R (2020) Kapok as an adsorbent for industrial wastewater. J Chem Eng Indus Biotechnol 5(2):48–54
12. Noor NAM (2020) A case study on cooking oil management in University cafeteria: research framework. Quantum J Eng Sci Technol 1(2):30–37
13. Singh AR, Singh SK, Jain S (2022) Effect of biodiesel on engine performance and emissions. Adv Mater Manuf Energy Eng 2:383–393

14. Sulyman M, Sienkiewicz M, Haponiuk J, Zalewski S (2018) New approaches for adsorptive removal of oil from wastewater using textile fiber as an alternative adsorbent. ACTA Sci Agr 2(6):32–37
15. Wang J, Wang A (2013) Acetylated modification of kapok fiber and application for oil absorption. Fibers Polym 14:1834–1840
16. Wang J, Zheng Y, Wang A (2012) Effect of kapok fiber treated with various solvents on oil absorbency. Ind Crops Prod 40(1):178–184
17. Zhang Q, Zhu M, Jones I, Zhang Z, Zhang D (2020) Desulfurization of spent tire pyrolysis oil and its distillate via combined catalytic oxidation using H_2O_2 with formic acid and selective adsorption over Al_2O_3. Energy Fuels 34(5):6209–6219

Effect of Process Variables on Gas Release from Free and Latex-Coated Calcium Alginate Beads

Yee-Ming Peh, Boon-Beng Lee, Farizul Hafiz Kasim, Akmal Hadi Ma'Radzi, Sakthi Balaji, Ahmad Radi Wan Yaakub, Hafizah Mohd Johar, and Mohd Asri Yusoff

Abstract Volatile compounds are emitted as gases from certain solids or liquids. These compounds are important in agricultural production as plant growth enhancers, fruit ripening agents, and pesticides. Ca-alginate beads have been used to control the release of volatile compounds. This study aims to investigate the effects of process variables on gas release (carbon dioxide gas was used as a model gas) from free and latex-coated floating calcium alginate beads. Floating beads were prepared from a sodium alginate solution containing calcium carbonate ($CaCO_3$) as a gas-forming agent. The resulting solution was then extruded into a calcium chloride ($CaCl_2$)

Y.-M. Peh · B.-B. Lee (✉) · F. H. Kasim · A. H. Ma'Radzi · A. R. W. Yaakub · H. M. Johar
Faculty of Chemical Engineering & Technology, Universiti Malaysia Perlis, 02600 Arau, Perlis, Malaysia
e-mail: bblee@unimap.edu.my

Y.-M. Peh
e-mail: pehyeeming@studentmail.unimap.edu.my

F. H. Kasim
e-mail: farizul@unimap.edu.my

A. H. Ma'Radzi
e-mail: akmalhadi@unimap.edu.my

A. R. W. Yaakub
e-mail: ahmadradi@unimap.edu.my

H. M. Johar
e-mail: hafizahjohar@unimap.edu.my

B.-B. Lee · F. H. Kasim · A. H. Ma'Radzi
Centre of Excellence for Biomass Utilization, Universiti Malaysia Perlis (UniMAP), 02600 Arau, Perlis, Malaysia

S. Balaji
Karpagam Academy of Higher Education, Coimbatore, Tamil Nadu, India

M. A. Yusoff
Koperasi Pengusaha Harumanis Y.A. Chuping Perlis Berhad, Lot 4136, Kg Baru Panggas, Jalan Kilang Gula, 02500 Kangar, Perlis, Malaysia

H. L. Ong et al. (eds.), *Proceedings of the 3rd International Conference on Biomass Utilization and Sustainable Energy; ICoBiomasSE 2023; 4–5 September; Kuala Lumpur, Malaysia*, Green Energy and Technology,
https://doi.org/10.1007/978-981-99-9164-8_15

solution and coated with latex solution. The effect of alginate concentration and extrusion tip diameter on beads size was investigated. The results indicated that increasing alginate concentrations and the extrusion tip diameter led to the formation of larger beads. Moreover, the gas (CO_2) released from free and latex-coated beads was studied. It was observed that the release rate of CO_2 from free-floating beads increased with the increased extrusion tip diameter but decreased with increasing alginate concentration. Instead, applying latex coating on floating calcium alginate beads could provide the controlled release of CO_2.

Keywords Floating calcium alginate beads · Calcium carbonate · Latex coating · CO_2 release

1 Introduction

Volatile compounds are emitted as gases from certain solids or liquids. These compounds are important in agricultural production as plant growth enhancers, fruit ripening agents, and pesticides. These compounds can release odorant, aroma, and fragrance from cosmetics, air fresheners, detergents, active ingredients for antiseptic purpose, and essential oils, which has healing properties in aromatherapy [1]. Encapsulation techniques can be used to protect them from environmental effects, thereby improving stability, controlling release rate, and providing sustained release while promoting ease of handling and extending the shelf life of compounds.

Alginate is a widely preferred polymer for controlled-release systems through encapsulation technology due to its favourable characteristics. These attributes include non-toxicity, cost-effectiveness, ease of formation, biodegradability, and biocompatibility. Alginate is a hydrophilic colloidal carbohydrate sourced from brown seaweed. Its primary structures consist of linear binary copolymers of 1–4-linked α-D-mannuronic acid (M block) and β-L-guluronic acid (G block) monomers [2, 3]. Alginate finds extensive applications in encapsulation across various fields, encompassing pharmaceuticals, animal feed, food products, biomedicine, and bioprocessing [4, 5]. It can produce a thermally stable and biocompatible hydrogel in the presence of di- or tri-cations such as calcium. Besides that, alginate beads can be easily made by dropping an alginate solution into a calcium chloride bath.

Alginate beads exhibit different stability characteristics depending on the pH conditions. They are susceptible to degradation in alkaline environments but remain stable in acidic media. Acetic acid and carbonate salts combine to form floating drug beads, which then release carbon dioxide. The gas generated permeates the alginate structure, leaving gas bubbles behind or creating pores within the beads. This gas entrapment contributes to the buoyancy of the beads, enabling them to float on the liquid surface [6, 7]. Gas-forming agents such as calcium carbonate ($CaCO_3$) and sodium bicarbonate ($NaHCO_3$) have frequently been employed for floating calcium alginate beads [6–8].

However, the low physical stability and porous structure of alginate beads lead to rapid release, low encapsulation efficiency, and easy degradation of encapsulated materials [9–12]. The application of a coating plays a crucial role in diminishing the porosity and enhancing the mechanical characteristics of calcium alginate beads. Consequently, this leads to an improvement in the overall effectiveness of encapsulation [13].

To date, the study on the effects of process variables (extrusion tip diameter and alginate concentration) on the bead diameter and gas release rate was lacking. Hence, this study is initiated to study the effects of process variables on the bead diameter and CO_2 gas release from free and latex-coated calcium alginate beads. Carbon dioxide was selected as the model gas in this study because it is simple to generate carbon dioxide by acidifying calcium carbonate, and the concentration of the CO_2 gas can be easily measured using a commercial gas detector.

2 Materials and Methods

2.1 Materials

All chemicals used for the experiment were of analytical grade. The chemicals that were used in the study are sodium alginate (Kimitsu Chemical Industries, Japan), calcium chloride (Bendosen, Norway), calcium carbonate (Local supplier, Malaysia), acetic acid (Merck, Germany), and latex solution (Bendosen, Norway).

2.2 Preparation of Solutions

Sodium alginate was dissolved in distilled water using an agitator motor, forming sodium alginate solutions at concentrations of 1.5 and 2.5% w/v. In this research, calcium carbonate was chosen as the model gas-releasing agent. Ten grams of calcium carbonate were introduced into each sodium alginate solution while maintaining continuous stirring to ensure a thorough and uniform mixture. A 1.5% w/v calcium chloride solution was also prepared by dissolving 1.5 g of calcium chloride in 100 mL of distilled water.

2.3 Preparation of Calcium Alginate Beads

The alginate beads were prepared by dropping the sodium alginate solution and calcium carbonate mixture via a syringe into a gelation bath made up of 1.5% w/v calcium chloride. Extrusion tips with different diameters (1.1 and 1.2 mm) were

used to create different-sized beads. The beads formed were kept in the gelation bath to harden for 30 min. Then, the beads were filtered, rinsed with distilled water, and dried at room temperature. This step was repeated using 2.5% w/v sodium alginate solution.

2.4 Coating of Calcium Alginate Beads

A coating solution was prepared by combining latex and distilled water at a ratio of 15 parts latex to 85 parts distilled water. The prepared Ca-alginate beads were subsequently dipped into the coating solution and dried.

2.5 Determination of Bead Diameter

The size of the free and coated beads was measured using 2D image analysis. The procedure involved spreading the beads, comprising both free (uncoated) and coated varieties, across the surface of a transparent plastic petri dish. Then, a white light source was applied at the bottom to form a contrasting background to the gel beads. Capturing images of the beads from a top-down perspective was achieved using a digital camera (Huawei, China). These captured images were subsequently imported into image analysis software (Image J, USA) to evaluate the bead diameter.

2.6 Carbon Dioxide Gas Release Studies

The release of carbon dioxide gas was studied in desiccators at room temperature. Three hundred beads were put into a universal bottle containing pH2 acetic acid and placed in desiccators. The gas release was measured using a portable gas detector (Henan Inte Electrical Equipment Co., China).

2.7 Statistical Analysis

Numerical data were presented as the mean ± standard deviation (SD) derived from multiple repetitions of the measurements.

3 Results and Discussion

3.1 Effect of Extrusion Tip Diameter on Beads Diameter

Figure 1 presents the diameters of free and latex-coated beads produced using extrusion tips of 1.1 and 1.2 mm. The results demonstrated that the diameter of the beads is significantly affected by extrusion tip diameter. As the extrusion tip diameter increased from 1.1 to 1.2 mm, the diameter of free beads increased from 2.86 to 3.01 mm and 3.08 to 3.12 mm for 1.5 and 2.5% w/v alginate concentrations, respectively. These findings are consistent with previous studies [14], which also reported an increase in bead diameter with larger extrusion tip diameters.

The increase in bead diameter with larger extrusion tip diameters can be attributed to the volume of sodium alginate-$CaCO_3$ droplets discharged from the tip. As the diameter of the extrusion tip increases, a greater volume of these droplets is released. Consequently, the resulting calcium alginate gel beads exhibit larger diameters after gelation [14].

On the other hand, the application of latex coating also leads to an increase in the diameter of the beads. For an extrusion tip diameter of 1.1 mm, the diameter of the latex-coated beads increases from 2.86 to 2.96 mm. At the same time, the diameter of the latex-coated beads increases from 3.01 to 3.10 mm for an extrusion tip diameter of 1.2 mm. These findings demonstrate that the latex coating process increases the diameter of the floating calcium alginate beads, regardless of the extrusion tip diameter used.

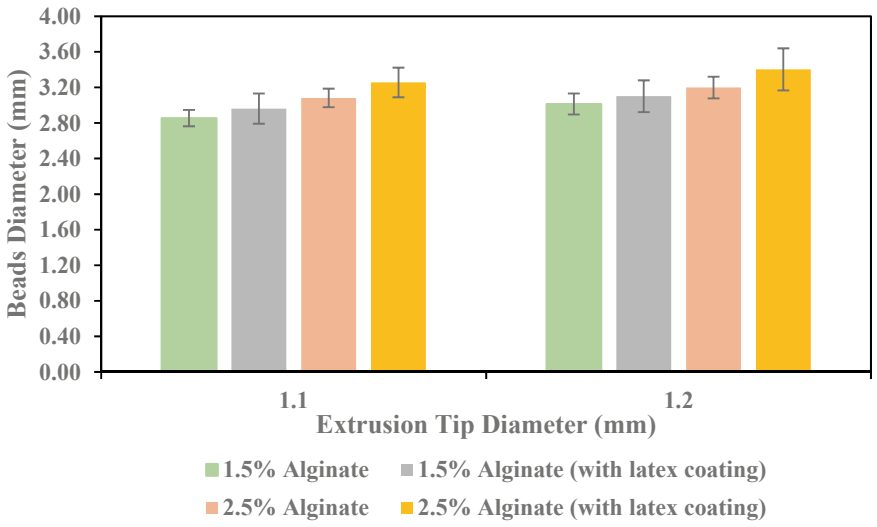

Fig. 1 Effect of extrusion tip diameter on the diameter of free and latex-coated calcium alginate beads. Data represent means ± SE ($n = 20$)

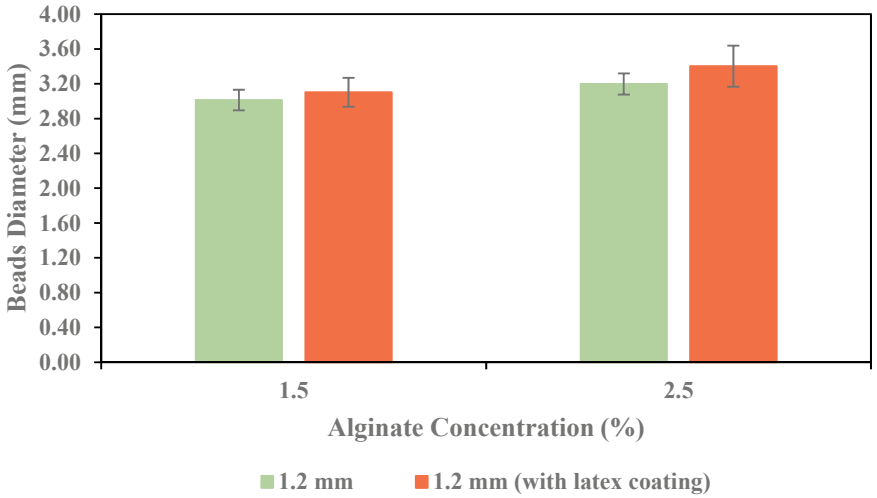

Fig. 2 Effect of alginate concentration on the diameter of free and latex-coated calcium alginate beads. Data represent means ± SE ($n = 20$)

3.2 *Effect of Alginate Concentration on Beads Diameter*

The diameter of free and latex-coated beads produced from 1.5 and 2.5% w/v alginate concentrations is shown in Fig. 2. The results indicated that the beads' diameter increases with increasing alginate concentration, as well as with the addition of latex coating. A higher alginate solution concentration produced larger beads than a lower alginate concentration. This finding is similar to previous studies, which reported that higher alginate concentrations result in the formation of larger beads compared to lower alginate concentrations [15]. Furthermore, the addition of latex coating further enhances the diameter of the beads. The latex coating process introduces an additional layer around the calcium alginate beads, increasing their size.

3.3 *Effect of Extrusion Tip Diameter on CO_2 Gas Release*

Figure 3 shows the CO_2 gas release from free and latex-coated beads using 1.1 and 1.2 mm extrusion tips. The results revealed that CO_2 release increased as the extrusion tip diameter increased. As expected, beads formulated with a larger extrusion tip diameter exhibited the highest CO_2 release rates. Interestingly, the application of latex coating on the beads resulted in a deceleration of CO_2 gas release. The latex coating forms an additional layer around the beads, which hinders the permeation of acetic acid from reacting with calcium carbonate, thereby slowing down the CO_2 release from the beads into the environment [15].

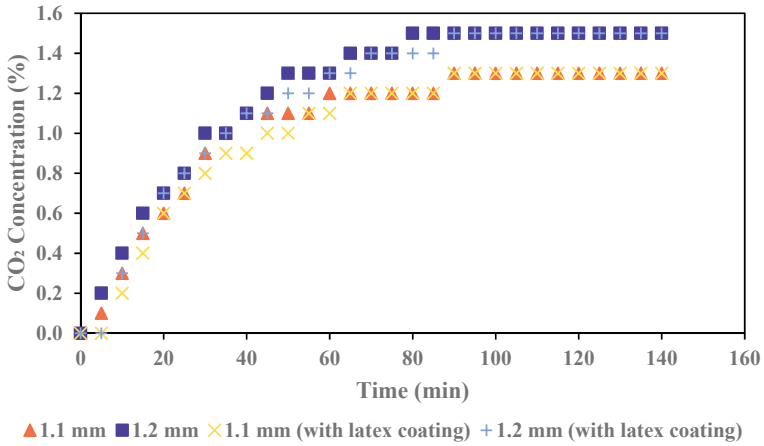

Fig. 3 Effect of extrusion tip diameter on CO_2 gas release

3.4 Effect of Alginate Concentration on CO_2 Gas Release

Figure 4 presents the CO_2 gas release from free and latex-coated beads produced from 1.5 and 2.5% w/v alginate concentrations. The results showed that the CO_2 release rate decreased with increasing alginate concentration, which can be attributed to the higher cross-link density on the bead's surface [15]. This finding aligns with previous studies, which indicated that during external gelation, the initial cross-linking of alginate chains at the bead's surface leads to a more tightly packed and less permeable structure. As a result, the diffusion of additional Ca^{2+} ions into the interior of the bead are hindered, leading to a slower release of CO_2 [16].

Furthermore, the gas release of CO_2 was decelerated after the addition of latex coating. Since the coating membrane is thick, it is difficult for the acetic acid to permeate into the beads and react with calcium carbonate. Consequently, the release of CO_2 from the beads is slowed.

4 Conclusions

This study demonstrated the effect of process variables on the bead diameter and CO_2 gas release from free and latex-coated calcium alginate beads. It was found that the bead diameter increased with increasing extrusion tip diameter and alginate concentration. Furthermore, the CO_2 release rate from the beads was found to be influenced by the extrusion tip diameter and alginate concentration. Larger extrusion tip diameters facilitated higher CO_2 release rates, while higher alginate concentrations led to a deceleration of CO_2 release. The application of latex coatings on the beads was demonstrated to slow down the release of CO_2. The latex coating formed

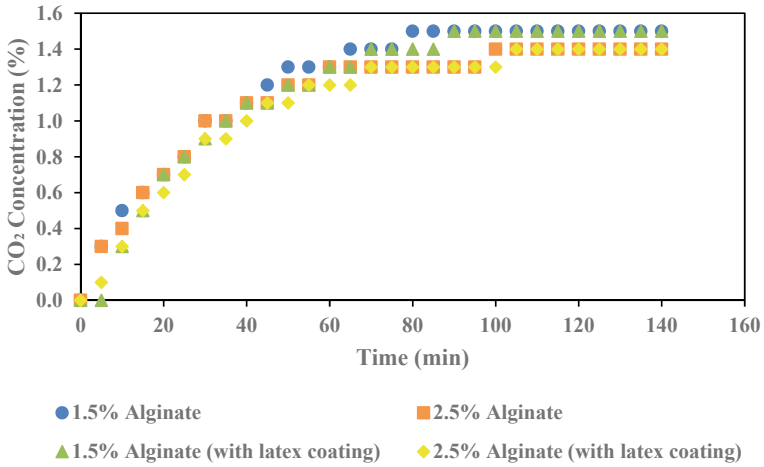

Fig. 4 Effect of alginate concentration on CO_2 gas release

an additional barrier, hindering the permeation of acetic acid and its reaction with calcium carbonate, resulting in controlled and sustained CO_2 release. These findings provide an opportunity to further investigate the application of gas-released calcium alginate beads in controlled drug delivery and active ingredient (such as fruit ripening agents, antibacterial substances, and antiseptic substances) release.

Acknowledgements The authors would like to acknowledge the support from the Fundamental Research Grant Scheme (FRGS/1/2021/TK0/UNIMAP/02/70) from the Ministry of Higher Education. The authors would also like to acknowledge the support from Universiti Malaysia Perlis.

References

1. Tholl D, Hossain O, Weinhold A, Röse USR, Wei Q (2021) Trends and applications in plant volatile sampling and analysis. Plant J 106(2):314–325
2. Properties of Alginates (2009) Alginates: biology and applications. Springer, Berlin, pp 1–53
3. Ramdhan T, Ching SH, Prakash S, Bhandari B (2020) Physical and mechanical properties of alginate based composite gels. Trends Food Sci Technol 106:150–159
4. Chan ES, Yim ZH, Phan SH, Mansa RF, Ravindra P (2010) Encapsulation of herbal aqueous extract through absorption with Ca-alginate hydrogel beads. Food Bioprod Process 88(2–3):195–201
5. Patel N, Lalwani D, Gollmer S, Injeti E, Sari Y, Nesamony J (2016) Development and evaluation of a calcium alginate based oral ceftriaxone sodium formulation. Prog Biomater 5(2):117–133
6. Choi BY, Park HJ, Hwang SJ, Park JB (2002) Preparation of alginate beads for floating drug delivery system: effects of CO_2 gas-forming agents. Int J Pharm 239(1–2):81–91
7. Sowmyasree GV, Jyoti BJ (2022) Formulation and evaluation of floating alginate beads of cefadroxil. Int J Res Eng Sci 10(11):139–150

8. Celli GB, Ghanem A, Brooks MS (2016) Development and evaluation of floating alginate microspheres for oral delivery of anthocyanins—a preliminary investigation. Food Sci Nutr 5(3):713–721
9. Hosseini SM, Hosseini H, Mohammadifar MA, German JB, Mortazavian AM, Mohammadi A, Khosravi-Darani K, Shojaee-Aliabadi S, Khaksar R (2014) Preparation and characterization of alginate and alginate-resistant starch microparticles containing nisin. Carbohydr Polym 103:573–580
10. Chan E-S, Wong S-L, Lee P-P, Lee J-S, Ti TB, Zhang Z, Poncelet D, Ravindra P, Phan S-H, Yim Z-H (2011) Effects of starch filler on the physical properties of lyophilized calcium-alginate beads and the viability of encapsulated cells. Carbohyd Polym 83(1):225–232
11. Riyajan S-A (2011) Development of neem capsule via biopolymer and natural rubber for its controlled release. In: Pesticides in the modern world—pesticides use and management, pp 233–258
12. Wang X, Gao S, Yun S, Zhang M, Peng L, Li Y, Zhou Y (2022) Microencapsulating alginate-based polymers for probiotics delivery systems and their application. Pharmaceuticals 15(5):644
13. Krasaekoopy W, Bhandari B, Deeth H (2004) The influence of coating materials on some properties of alginate beads and survivability of microencapsulated probiotic bacteria. Int Dairy J 14(8):737–743
14. Lim G-P, Lee B-B, Muhammad SA, Singh H, Ravindra P (2015) Influence of process variable and formulation composition on sphericity and diameter of ca-alginate liquid core capsule prepared by extrusion dripping method. Part Sci Technol 34(6):681–690
15. Phansroy N, Boonyod S, Mulasake O, Uttha A, Songkram C, Somboon T, Kongon J, Lersuwannapong N, Saengsuwan S, Khawdas W, Vudjung C (2023) Innovative environment-friendly liquid fertilizer bead from sodium alginate coating with IPN membrane derived from Natural rubber and Cassava starch
16. Lee P, Rogers MA (2012) Effect of calcium source and exposure-time on basic caviar spherification using sodium alginate. Int J Gastron Food Sci 1(2):96–100

Aerobic Co-composting of Spent Mushroom Medium Using Food Waste Fermented Liquid

Siti Nazrah Zailani, Adam Syahmi Zaidnuddin, Nur Fharisha Mokhtar, Enny Zulaika, Maya Shovitri, N. D. Kuswytasari, Dewi Hidayati, and Khairul Akhbar Ahmad Zabidi

Abstract Spent mushroom medium and dried sludge from bioethanol industry can be utilized into beneficial organic compost after completion the composting process. Food waste fermented liquid and commercially effective microorganisms (EM) from EMRO Sdn. Bhd. were used as the microbial inoculant for the aerobic composting. Three kg of composting pile made of spent mushroom and dried sludge are used to obtain a 23.07 C/N ratio at the initial composting process. In order to ascertain the impact of composting process in seven days, the sample from each of the composting beds for analysis of temperature, pH, moisture, and total organic matter was assessed. Food waste fermented liquid and commercial EM composts reached the thermophilic phase (40 °C) after a day of the composting process. Moisture content showed a significant result for both composting piles on day 1 due to the highest evaporation of water at the thermophilic phase. The composting process was not extended until reached stability and maturity phases; thus, the pH for both composting piles was recorded at 9, which is far from the stable compost normally at neutral pH (~7). The organic matter content of each composting pile showed gradually decreased

S. N. Zailani (✉) · A. S. Zaidnuddin · N. F. Mokhtar
Faculty of Chemical Engineering & Technology, Universiti Malaysia Perlis, 02600 Arau, Perlis, Malaysia
e-mail: sitinazrah@unimap.edu.my

E. Zulaika · M. Shovitri · N. D. Kuswytasari · D. Hidayati
Department of Biology, Institut Teknologi Sepuluh Nopember, 60111 Surabaya, Indonesia
e-mail: enny@bio.its.ac.id

M. Shovitri
e-mail: maya@bio.its.ac.id

N. D. Kuswytasari
e-mail: kuswytasari@bio.its.ac.id

K. A. A. Zabidi
Fermwaste Sdn. Bhd. Lot B3, Tingkat 1 Aras 2, Kompleks Kangar, Persiaran Jubli Emas, 01000 Kangar, Perlis, Malaysia

H. L. Ong et al. (eds.), *Proceedings of the 3rd International Conference on Biomass Utilization and Sustainable Energy; ICoBiomasSE 2023; 4–5 September; Kuala Lumpur, Malaysia*, Green Energy and Technology,
https://doi.org/10.1007/978-981-99-9164-8_16

during the composting process. The degradation rate for the composting pile using food waste fermented liquid showed slightly higher than commercial EM which was 0.0363 and 0.0232 day 1, respectively. In conclusion, food waste fermented liquid shall be used as a replacement for EM commercial as a microbial inoculant for the composting process based on the results shown in this study.

Keywords Aerobic composting · Degradation rate · Dried sludge · Food waste · And Spent mushroom medium

1 Introduction

1.1 Compost Organic Materials

Food Waste. A total of 1.3 billion tons of food were lost or wasted a year, and about one of food produced for human sustenance worldwide [1]. Due to the resource-intensive disposition of food production, food wastes and losses indirectly get a huge spectrum of negative impacts on the environment, which include erosion, habitat destruction, air and water, as well as greenhouse emissions from processes of food production, stockpiling, logistics, and waste management [2]. In Malaysia, more than 50% of the population wasted food daily [3] including solid and liquid state. Food waste was thrown in landfills or other locations along with other types of trash without any effective material or energy recovery [4]. This shows that there is an abundant amount of raw material needed to make the compost substrate. The management of food waste can be classified by 3R (reducing, reusing, and recycling) and could be promoted as food-related routine and practices [5].

Spent Mushroom Medium. The soil-like substance left over after a harvest of mushrooms is known as spent mushroom substrate. Spreading spent mushroom substrate over freshly sown grass works very well. The substance keeps the water in the soil while the seeds develop and protects against birds devouring the seeds. The high level of organic matter in the spent substrate makes it a suitable soil conditioner or soil additive [6]. The discarded compost may be utilized in organic farming to increase soil water penetration, water holding capacity, permeability, and aeration after the mushrooms have been harvested.

Dried Sludge. The fermentation process of the production of bioethanol generated sludge beneath the sewage treatment pond. Sewage sludge has potential fertilizer properties and can be used to enrich agricultural soils due to high nitrogen, phosphorus, and organic matter content [7]. The treatment of sewage sludge is becoming an important practical concern. This is a result of the dramatic rise in urban population and ongoing changes in living conditions, which have resulted in high water consumption and consequent discharge of spent water into surface watercourses. Unfortunately, the quality of the surface waters has worsened due to the organic

and inorganic load of discharged wastewater; these waters frequently became so contaminated that it had to be regarded as really "dead" ecosystems.

1.2 Microbial Inoculant

Microbial inoculants are commonly employed to manage pests, enhance the quality of the soil and crop, and ultimately improve human health [8]. Furthermore, the utilization of organic waste is important because it is a significant alternative to industrialized fertilizers in agriculture the use of organic waste as a source of nutrients, either in full or in part. This encourages the recycling of nutrients within the production system and lowers production costs [9] such as the utilization of food waste. In this study, the food waste fermented liquid and commercial effective microorganisms (EM) were used as microbial inoculants to enhance the degradation of organic matter during composting. Today's commercial EM is a liquid mixed culture made up of yeast, photosynthetic bacteria, and lactic acid bacteria.

1.3 Aerobic Composting

Aerobic composting is the breakdown of organic materials utilizing oxygen (O_2)-dependent microbes. Composting bacteria are found in the dampness surrounding organic matter and are naturally occurring. The bacteria take up oxygen from the air that diffuses into the wetness. In aerobic composting, O_2 is needed as gaseous H_2O (vapor) and CO_2 are generated. To have enough O_2 for the oxidizing organic material, aeration is needed and to evaporate excess moisture. In order to provide effective aeration of the compost feedstock, different authors have applied different rotation cycles, forced and natural aeration. Moreover, conventional composting parameters such as temperature, moisture content, pH, C/N, volatile solids, and organic matter were monitored during the process.

1.4 Composting Parameter

Temperature. Aerobic composting takes place with aerobic bacteria at thermophilic temperature (> 40 °C). The emitted heat energy from the degradation of OM by microorganism raised up the temperature and avoid the formation of pungent and harmful odor during composting. At this level of temperature, the thermophilic population of microorganisms are able to destroy the human and plant pathogen

and weed. Therefore, most of the modern composting system is operating in thermophilic temperature range (55–65 °C) [10]. A certain population of microorganism are inactivated or failed to survive at extremely high temperature.

Moisture Content. The water content act as a medium for transport of the dissolved nutrient and chemical reaction. The water molecule can be reacted with those nutrients and absorbed by the relative microorganism. However, the excess moisture (more than 65%) leads to an undesirable anaerobic condition in the composting system [10]. It is due to the leachate forming and generating the off-smelling substance and reduces the porosity of composting material. If insufficient moisture content (less than 30%) take place, it will affect the microbial activity and also decreases the ability and rate of OM degradation. The general optimum moisture content of the composting system is about 40–60%. The moisture content is also related to aeration and temperature. The movement of air will cause the diffusion of the water molecule as well as a decrease in thermal stability (temperature) of the composting system.

pH. Generally, the pH value from 6.0 to 7.5 is suitable for the growth of bacteria, while 5.5–8.0 is favorable for the growth of fungi. The pH of compost is varied depending on the surrounding temperature as well as the supply of O_2. The pH between 5.5 and 8, neutral to acidic conditions, is ideal for compost microorganisms to thrive. Organic acids are created in the first phases of degradation. The acidic environment promotes the growth of fungus and the lignin and cellulose degradation processes [11]. Thus, optimal pH between 5.5 and 8 may speed up the composting process due to the microorganism in the compost mixture which can operate or breakdown the material easily.

Organic Matter (OM). Total organic carbon (TOC) is a direct measurement for that organic and inorganic carbon contain within the soil OM. The OM of compost contained about 58% organic carbon by weight [12]. Therefore, the carbon content of each individual feedstocks may vary from this ratio. The TOC and TOM values can be calculated by using Eq. (1)

$$\mathrm{TOC} = 0.58 \times \mathrm{TOM} \tag{1}$$

where TOC is total organic carbon (%) and TOM is total organic matter (%).

1.5 First-Order Kinetic Study of Degradation Process

To demonstrate, the first-order kinetic model was used to examine the composting process, and a graph of TOM versus t was created. The graph of ln $\mathrm{TOM/TOM_0}$ versus t (day) will be displayed using the computed value rate of reaction to determine the k value. By determining the slope of a straight-line graph of ln $\mathrm{TOM/TOM_0}$ versus t (day), the value of k will be determined. The straight-line graph, which depicts the link between the first-order kinetic model and microbial inoculants, will yield a

regression value of $r^2 > 0.6$. The most popular approach to explaining the composting process is the first-order kinetic model based on the degradation of OM as given in Eq. (2).

$$r = \frac{\mathrm{d(OM)}}{\mathrm{d}t} = -k\mathrm{OM} \tag{2}$$

2 Materials and Methods

2.1 Preparation of Food Waste Fermented Liquid

Food waste (5 kg vegetable waste) was collected from the nearby wet market without isolating the type of the vegetables. The food waste was chopped to about 2–3 cm size and added to the closed container (7 days). After 7 days, the fermented liquid (leachate) was collected and removed from the solid food waste. Another new food waste (5 kg vegetable waste) was collected and mixed with the collected leachate and closed the container for another 7 days. After 7 days, the process was repeated again by removed the solid waste, collected the leachate, and measured the volume of the liquid. The dried sludge, molasses, and rice water was prepared with the similar weight of the fermented liquid and mixed into the closed container. The food waste fermented liquid was ready for the inoculation on the composting of spent mushroom medium after 14 days completion of liquid fermentation where the pH reduced below 3.5.

2.2 Preparation of Commercial Effective Microorganisms

Preparation of active EM-1 stock solution started with 1 part of EM stock that was mixed with 1 part of molasses and 20 parts of water [13]. The mixture was kept in an air-tight container and left in a gloomy area for about 7 days. The pH of the activated EM solution obtained should be below 4, where it indicates that the EM has been completely activated [14] and ready to inoculate with the compost raw materials.

2.3 Preparation of Composting Bed and Analysis of Parameter

Three kg of each composting pile is made of spent mushroom medium and dried sludge to obtain a 23.07 C/N ratio at the initial composting process. The composting

Table 1 Design experiment for types of variables

Manipulated variables	Controlled variables	Measured variables
Microbial inoculants 1. Food waste fermented liquid 2. Commercial EM	Initial C/N ratio = 23.07	Temperature
	Compost size = 3 kg	Moisture content
	Particle size = 20 mm	pH
	Composting time = 7 days	TOM

process took place in a 40 cm × 40 cm × 20 cm (length × width × height) container. To enhance the surface area per volume for microbial access to the composting medium, the SMM and DS were sieved in average size of 20 mm prior to composting. In order to hold the 3 kg of mixed heaps required to finish the composting process, two compost containers with holes were made. To prevent the leachates produced during the composting cycle from gathering at the bottom of the compost bed, the filter layer was constructed at the bottom of the container. Following the creation of the compost container, food waste fermented liquid and commercial EM were added to the compost medium. In order to ascertain the impact of composting process in seven days, the sample from each of the composting beds for analysis of temperature, pH, moisture, and total organic matter was assessed. The variables were studied as given in Table 1.

3 Results and Discussion

3.1 Analysis of Compost Raw Materials

To ascertain the precise composition of each raw material as shown in Fig. 1 utilized prior to the composting process, the raw materials must be characterized. The chemical characterizations of raw materials (spent mushroom medium and dried sludge) were given in Table 2.

(a) (b)

Fig. 1 **a** Spent mushroom medium after being isolated and **b** bio-ethanol sludge after drying process

Table 2 Composition of compost raw materials

Parameter	Spent mushroom medium	Dried sludge
pH	9.30 ± 0.17	7.80 ± 0.31
Moisture content (%)	78.64 ± 0.64	16.92 ± 1.21
TOC (%)	33.24 ± 0.87	34.62 ± 0.59
TOM (%)	57.31 ± 1.68	59.69 ± 1.00
TKN (%)	1.04 ± 0.02	2.05 ± 0.03
C/N ratio	32.08 ± 0.63	16.89 ± 0.10

3.2 Analysis of Composting Process

Temperature. The stability of the composting process is mostly determined by temperature. Temperature helps to distinguish between different stages of the composting process and to show how effectively microbial activity is performing at each stage. Figure 2 illustrates the temperature profile of the compost for about 7 days of composting with various microbial inoculants, including commercial effective microorganism and food waste fermented liquid. Both composting beds reached the thermophilic phase temperature on day 1; the temperatures then tended to drop abruptly after day 2 and then gradually decline throughout the composting process. By day seven, the temperature in every composting bed had stabilized. Due to inadequate insulation in the composting beds, the temperature in both of the beds quickly drops after the first day and day four of composting.

Moisture Content. The moisture content value obtained in this study is shown in Fig. 3. The range of moisture content in this study was within 44.3–53.4%. Based on previous research, the range of an ideal moisture content that must be possessed by compost medium was within 40–60% [15]. While in other study, it stated that the optimum moisture content to ensure the condition in an active phase is within range of 45–50% [16].

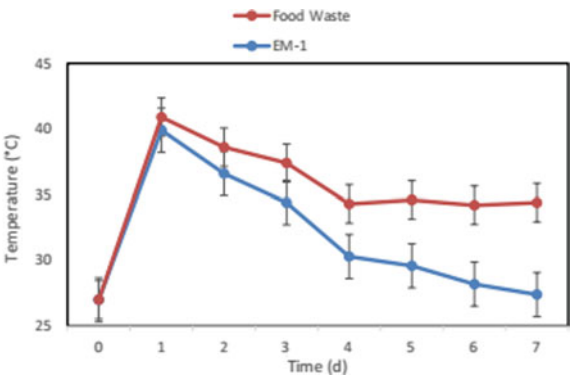

Fig. 2 Temperature profile of composting beds

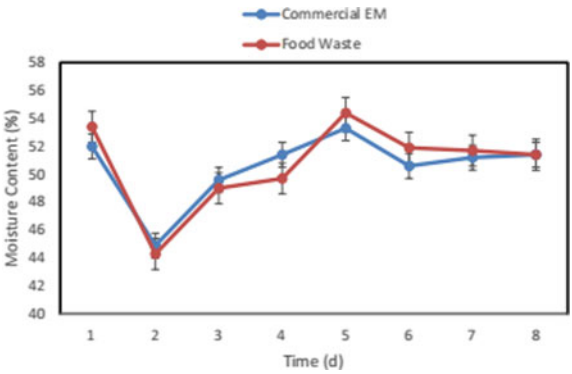

Fig. 3 Moisture content of composting beds

The temperature distribution of the compost medium affects moisture content. The rise in compost temperature is the primary cause of moisture content loss [17], as higher temperature leads the robust evaporation water (higher water lost) as shown at day 2 with about 43.3%. Regarding the commercial EM, the moisture content was at its peak on day 5 and its lowest on day 2, which were 53.3 and 44.9%, respectively. The maximum moisture content was on day 5 for food waste EM, which was 54.4%.

pH. The pH of the composting beds was one of the factors used in this study to assess the quality of the compost. Although it may vary depending on the kind of compost's raw materials, compost with a pH that is close to neutral is preferred. Figure 4 shows the pH profile of both composting beds during composting. At the start of the composting process, the initial pH for composting beds revealed a substantial difference. This is due to the fact that the kind of material and microbial inoculant present in composting beds affect pH for certain beds [18].

TOM. During the composting process, the TOM of each of the compost system were analyzed by using furnace and recorded along the composting. Then, the degradation of TOC was calculated and plotted the graph. A graph of TOC degradation versus

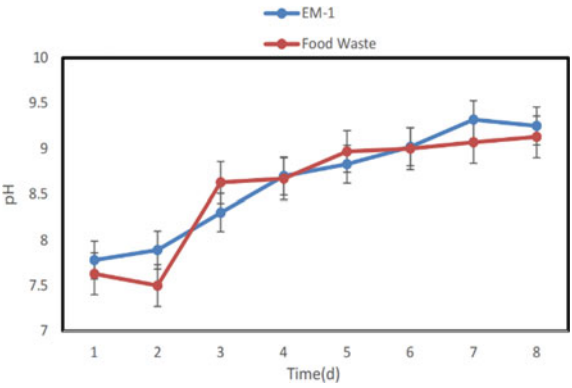

Fig. 4 pH profile

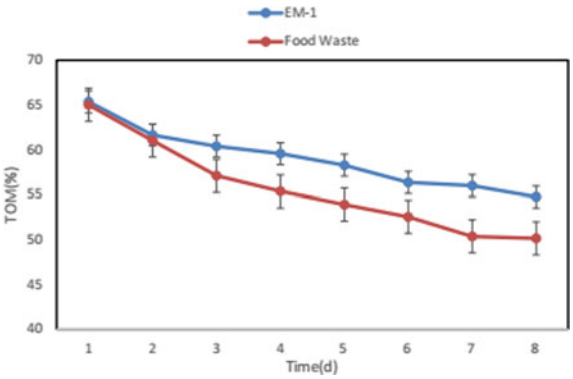

Fig. 5 TOM of composting beds

time of composting with different type of microbial inoculants was shown in Fig. 5. Even though the temperature of the composting beds has entered the mesophilic range after day 1 as shown in Fig. 2, the breakdown of TOM is still happening at a slower rate than when the temperature is in the thermophilic range. The TOM degradation process in composting continues until the TOM is completely destroyed [19].

3.3 Analysis of Kinetic Study

The first-order kinetics were used to describe the hydrolysis of insoluble organic matter, followed by formation of biomass. The graph of $\ln TOM/TOM_0$ versus time (d) of compost with various microbial inoculants is shown in Fig. 6. The degradation of TOM follows the first-order kinetic model, as the straight lines of the graph appeared with $r^2 > 0.6$. The k value was compared for both food waste and EM commercial composting as given in Table 3.

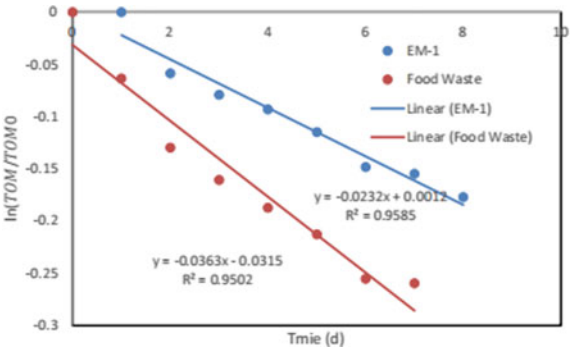

Fig. 6 In TOM/TOM_0 versus time (d) of the composting bed

Table 3 Parameter of the first-order kinetic composting

Microbial inoculant	r^2	Rate constant, k
Commercial EM	0.9585	0.0232
Food waste fermented liquid	0.9502	0.0363

According to Table 3, commercial effective microorganism and compost beds containing food waste microbial inoculant had the greatest reaction rate constants, k, at 0.0363 and 0.0232, respectively. The steeper slope results in a greater response k, as seen in Fig. 6. The sharpest slope between the two composting beds concluded that the composting beds with the food waste microbial inoculant had the optimum response rate constant.

4 Conclusion

The organic matter content of each composting pile showed gradually decreased during the composting process. The degradation rate for the composting pile using food waste fermented liquid showed slightly higher than commercial EM which was 0.0363 and 0.0232 day 1, respectively. In conclusion, food waste fermented liquid shall be used as a replacement for EM commercial as a microbial inoculant for the composting process based on the results shown in this study.

Acknowledgements The authors acknowledge research grants from Universiti Malaysia Perlis with ITS Matching Grant 9001-00717. We would like to extend our appreciation to the Center of Biomass and Utilization and Faculty of Chemical Engineering and Technology for the facilities and spaces.

References

1. Gustavsson J, Cederberg C, Sonesson U (2011) Global food losses and food waste. Save Food at Interpack Düsseldorf 29
2. Mourad M (2016) Recycling, recovering and preventing "food waste": competing solutions for food systems sustainability in The United States and France. J Clean Prod 126:461–477
3. Phooi CL, Azman EA, Ismail R (2022) Role of organic manure bokashi improving plant growth and nutrition: a review. Sarhad J Agr 38(4):1478–1484
4. Ouda OKMR, Nizami SA, Rehan AS, Al-Waked MR, Korres NE (2016) Waste to energy potential: a case study of Saudi Arabia. Renew Sustain Energy Rev 61:328–340
5. Attiq S, Danish Habib M, Kaur P, Junaid Shahid Hasni M, Dhir A (2021) Drivers of food waste reduction behaviour in the household context. Food Q Prefer 94
6. Li H, Yoshida S, Mitani N, Egusa M, Takagi M, Izawa H, Matsumoto T, Kaminaka H, Ifuku S (2022) Disease resistance and growth promotion activities of chitin/cellulose nanofiber from spent mushroom substrate to plant. Carbohyd Polym 284:119233

7. Iticescu C, Georgescu LP, Murariu G, Circiumaru A, Timofti M (2018) The characteristics of sewage sludge used on agricultural lands. In: AIP conference proceedings
8. Alori ET, Babalola OO (2018) Microbial inoculants for improving crop quality and human health in Africa. Front Microbiol 19(9):2213
9. Sutarti S, Muttaqin Z, Setyawan A (2019) Utilization of organic and inorganic waste diversification to improve families income in Panggung Jati Taktakan Serang. In: Proceedings of the 1st workshop multimedia education, learning, assessment and its implementation in game and gamification, Medan Indonesia
10. Garg A, Tothill IE (2009) A review of solid waste composting process—the UK perspective. In: Martin-Gil J (ed) Compost II. Dynamic soil, dynamic plant 3 (Special Issue 1), pp 57–63
11. Sundberg C, Yu D, Franke-Whittle I, Kauppi S, Smårs S, Insam H, Romantschuk M, Jönsson H (2013) Effects of pH and microbial composition on odour in food waste composting. Waste Manage 33(1):204–211
12. Yang Y, Awasthi MK, Bao H, Bie J, Lei S, Lv J (2020) Exploring the microbial mechanisms of organic matter transformation during pig manure composting amended with bean dregs and biochar. Biores Technol 313:123647
13. Lee CT (2016) Physico-chemical and biological changes during co-composting of model kitchen waste, rice bran and dried leaves with different microbial inoculants. Malaysian J Anal Sci 20(6):1447–1457
14. Pushpa TB, Sekaran V, Basha SJ, Jegan J (2016) Investigation on preparation, characterization and application of effective microorganisms (EM) based composts-an ecofriendly solution. Nat Environ Pollut Technol Int Q Sci J 15:153–158
15. Azeddin EB, Abdelilah IH (2023) Physico-chemical characterization of decomposing banana, pomegranate and mandarin peels in water and soil for a sustainable valorization. Ind Crops Prod 193:116207
16. Moncks PCS, Corrêa ÉK, Guidoni L, Moncks RB, Corrêa LB, Lucia T, Jr, Araujo RM, Yamin AC, Marques FS (2022) Moisture content monitoring in industrial-scale composting systems using low-cost sensor-based machine learning techniques. Bioresource Technol 359
17. Madejón E, Jesús Díaz M, López R, Cabrera F (2002) New approaches to establish optimum moisture content for compostable materials. Biores Technol 85(1):73–78
18. Mathew J, Ameen A, Ahmad J, Raza S (2016) Effect of pH and moisture content on composting of municipal solid waste. Int J Sci Res Publ 6(5):35
19. Sullivan DM, Bary AI, Miller RO, Brewer LJ (2018) Interpreting compost analyses. In: Oregon State University extension service

Physicochemical Properties of Industrial Wood Waste-Derived Cellulose Nanofibrils

Ming Hui Hing, Mohd Hanif Mohd Pisal, Nur Atirah Afifah Sezali, Hui Lin Ong, and Ruey-An Doong

Abstract Wood is an important raw material, especially for construction and industrial scale activities which have resulted in a large amount of wood waste (WW). The accumulation of industrial WW has led to serious environmental issues; hence, the utilization of the industrial WW is being studied by researchers due to the rich content of cellulose. This study investigated the physicochemical properties of cellulose nanofibrils (CNFs) derived from industrial WW. The preparation of the CNFs involves the pretreatment of WW with an alkaline deep eutectic solvent (DES) and bleaching with peracetic acid, followed by 2,2,6,6-tetramethylpiperidine-1-oxyl (TEMPO)-mediated oxidation and mechanical post-treatment. Interestingly, the yield of the CNFs produced was 52%, which is half of the raw material used. Furthermore, the morphology of the WW-derived CNFs was analyzed from scanning electron microscopy (SEM) and transmission electron microscopy (TEM). The WW-derived CNFs showed a uniform size with a width of around 20–100 nm and a length of several micrometers. Moreover, the production of WW-derived CNFs was further verified by Fourier transform infrared spectroscopy (FTIR) for the surface functional groups, X-ray diffraction (XRD) for the crystallography, and thermal gravimetry analysis (TGA) for thermal stability. The results obtained from these

M. H. Hing · M. H. M. Pisal (✉) · N. A. A. Sezali · H. L. Ong
Faculty of Chemical Engineering & Technology, Universiti Malaysia Perlis (UniMAP), 02600 Arau, Perlis, Malaysia
e-mail: hanifpisal@unimap.edu.my

H. L. Ong
e-mail: hlong@unimap.edu.my

M. H. M. Pisal · H. L. Ong
Centre of Excellence for Biomass Utilization, Universiti Malaysia Perlis (UniMAP), 02600 Arau, Perlis, Malaysia

N. A. A. Sezali · R.-A. Doong
Institute of Analytical and Environmental Sciences, National Tsing Hua University, 101, Sec. 2, Kuang-Fu Road, Hsinchu 300044, Taiwan, R.O.C.
e-mail: radoong@mx.nthu.edu.my

H. L. Ong et al. (eds.), *Proceedings of the 3rd International Conference on Biomass Utilization and Sustainable Energy; ICoBiomasSE 2023; 4–5 September; Kuala Lumpur, Malaysia*, Green Energy and Technology,
https://doi.org/10.1007/978-981-99-9164-8_17

characterization methods have proved the successful transformation of the industrial WW into a high-potential nanomaterial, which is the CNFs that can be used for further applications in paper making, composites, packaging, textiles, biomedicine, energy storage, and electronics.

Keywords Biomass · Industrial wood waste · Cellulose nanofibrils · Deep eutectic solvent · TEMPO oxidation

1 Introduction

The alarming accumulation of industrial wood waste (WW) on an unimaginable level is a result of the continuous expansion of industrial activities worldwide. A remarkable amount of 1 billion tons of WW accumulates each year, leading to serious environmental-related issues [1]. Unfortunately, only a small proportion of 15% from the WW is being recycled, leaving the rest of the waste to compost in landfills. Interestingly, WW contains a large amount of cellulose with outstanding mechanical properties which make the WW one of the valuable sources of cellulose. As a type of softwood, WW comprises about 46–48% cellulose, 27–28% lignin, and 20–23% hemicellulose [2]. In general, cellulose is a biopolymer that can be derived into nanomaterials such as cellulose nanofibrils (CNFs) for a wider range of applications such as in biomedical, composite reinforcement, packaging films, and barrier materials. Due to the increasing need for novel and sustainable materials, CNFs derived from wastes or renewable sources have received a great interest for industrial applications as a mechanically strong nanomaterial. To date, 2,2,6,6-tetramethylpiperidine-1-oxyl (TEMPO)-mediated oxidation of cellulose is the only method that has been emphasized to modify the structure of cellulose into becoming CNFs [3]. It is essential to select a suitable reagent in producing CNFs to ensure the properties of the CNFs suit the application of interest.

This research work investigated the physicochemical properties of CNFs derived from WW. There was a series of processes starting from pretreatment of WW with an alkaline deep eutectic solvent (DES) followed by bleaching process to significantly remove lignin and hemicellulose, leaving a rich content of cellulose. Then, the process continued with TEMPO oxidation of cellulose followed by mechanical disintegration as a post-treatment to obtain CNFs. The TEMPO-mediated oxidation has introduced carboxylate groups to the structure of the cellulose, improving its dispersibility in water [4]. The yield percentage at different stages of process was determined, and the physicochemical properties of the WW-derived CNFs were also investigated. Overall, this research work significantly highlights the potential of CNFs derived from wastes or renewable sources for a variety of industries including papermaking, composites, packaging, textiles, biomedicine, and even energy storage devices [5].

2 Experimental

2.1 Materials and Chemicals

The industrial wood waste (WW) used in this work was collected from T.H. Mineral Water Industries (M) Sdn. Bhd., Kaki Bukit, Perlis, Malaysia. Materials such as glycerol ($C_3H_8O_3$, anhydrous, $MW = 92.10$ g mol^{-1}, 99.9%), acetic acid ($C_2H_4O_2$, $MW = 60.05$ g mol^{-1}), hydrochloric acid (HCl, $MW = 36.46$ g mol^{-1}, 36.5–38.0%), and paraffin oil ($\rho = 0.85$ gcm^{-3}) were purchased from Fisher Scientific. Additionally, 2,2,6,6-tetramethylpiperidine-1-oxyl (TEMPO) ($C_9H_{18}NO$, $MW = 156.25$ g mol^{-1}), potassium carbonate (K_2CO_3, $MW = 138.20$ g mol^{-1}), sodium bromide (NaBr, $MW = 102.89$ g mol^{-1}, 98%), and sodium hypochlorite (NaOCl, $MW = 74.44$ g mol^{-1}, 6–14%) were acquired from Sigma-Aldrich. The bleaching agent, hydrogen peroxide (H_2O_2, $MW = 34.01$ g mol^{-1}, 30%), was purchased from Riedel–de Haen while other reagents were used as received, without further purification. For the preparation of all solutions, bi-distilled deionized (DI) (18.2 MΩ-cm) water was used, unless otherwise mentioned.

2.2 Extraction of Cellulose from the Industrial Wood Waste (WW)

The collected WW was washed with warm water, dried, and ground into fine powders (~ 104 μm). About 25 g of WW was pretreated with 100 g alkaline DES in a paraffin oil bath at 140 °C for 100 min. The DES was prepared prior to the pretreatment by mixing glycerol and K_2CO_3 at a molar ratio of 1:7 at 80 °C for 2 h, according to the procedures stated by Lim et al. [6]. Cellulose pulp obtained was filtered and washed several times with DI water until the pH of the filtrate became neutral. Next, the cellulose pulp was bleached with a peracetic acid according to the method described in [7]. The bleaching process was performed at 65 °C for 2 h followed by filtering and washing with DI water for several times until a pH of close to 7 was obtained. The extracted cellulose was freeze-dried for 48 h.

2.3 Preparation of Industrial Wood Waste-Derived Cellulose Nanofibrils (CNFs)

The TEMPO-mediated oxidation of cellulose was performed according to the method described in [7]. A suspension of WW-derived cellulose in DI water (1 g/mL) was mixed with 0.032 g TEMPO and 0.32 g NaBr. Then, the oxidation reaction was started by adding NaOCl solution at 5 mmol per g of cellulose. An appropriate

amount of NaOH solution was added to maintain the pH of the suspension at pH 10 for 10 min, and it was left to react for 75 min. The suspension was then neutralized by the addition of 0.5 M HCl solution. The resulting suspension was centrifuged at 10,000 rpm for 20 min and dialyzed against DI water for 24 h to remove salts and unwanted small molecules. The WW-derived CNFs were then obtained after mechanically disintegrating the oxidized pulp using an Ultra Turrax homogenizer (IKA Homogenizer model T25 digital S22) at 12,000 rpm for 2 h. The WW-derived CNFs were then filtered using a vacuum filter and a 0.2 μm membrane filter before being freeze-dried for 36 h.

2.4 Characterization of Cellulose Nanofibrils (CNFs)

The yield, *Y (%)* of the extracted cellulose and cellulose nanofibrils (CNFs) from wood waste (WW) was calculated according to Eq. (1). The calculation was done in triplicate for better accuracy of the results.

$$\text{Yield, } Y(\%) = \frac{\text{Dry weight of product (g)}}{\text{Dry weight of WW (g)}} \times 100\% \tag{1}$$

The morphology of the WW, cellulose, and CNFs was characterized using a scanning electron microscope (SEM, JEOL JSM-6700 F OXFORD INCA ENERGY 400) operated at 20 kV and 20 mA, while the morphology of CNFs was further examined by a high-resolution transmission electron microscope (HRTEM, JEOL 2010) operated at 200 kV. The Fourier transform infrared (FTIR, Perkin-Elmer Spectrum 400 Series) spectroscopy was conducted on the WW, cellulose, and CNFs at a resolution of 4 cm^{-1} and a scanning range of 750–4000 cm^{-1}. The specimens were prepared into a pellet by grinding with KBr prior to the FTIR analysis. The crystallography of the specimens was characterized by X-ray diffraction (XRD, Bruker Advance D8) with Ni-filtered Cu Kα radiation ($\lambda = 1.5406$ Å) at $2\theta = 10°$–$50°$. From the XRD analysis, the crystallinity index (CrI) of WW, cellulose, and CNFs was calculated using Eq. (2) where I_{002} is the intensity of the crystalline region and I_{am} is the intensity of the amorphous region [8].

$$\text{crystallinity Index, CrI}(\%) = \frac{I_{002} - I_{am}}{I_{am}} \times 100\% \tag{2}$$

2.5 Thermal Analysis

The thermal stability of the WW, cellulose, and CNFs was determined by thermal gravimetry analyzer with a Mettler Toledo DSC/TGA 3+ Stare system at a heating rate of 10 °C min^{-1} from 30 to 800 °C.

3 Results and Discussion

3.1 Percentage of Yield of Industrial Wood Waste (WW)-Derived Cellulose and Cellulose Nanofibrils (CNFs)

Wood waste (WW)-derived cellulose was obtained after the pretreatment of WW with the alkaline DES and further bleaching with peracetic acid solution. The cellulose was then used for the TEMPO oxidation process, producing the WW-derived CNFs. The yield, *Y (%),* for the cellulose (after pretreatment and bleaching process) and CNFs corresponds to the weight of WW used in this work is given in Table 1. From the initial treatment of WW with the alkaline DES, about 31% of the weight was reduced, indicating the significant removal of lignin and hemicellulose from the WW by the alkaline DES. Generally, DES is a solvent consisting of a hydrogen bond donor (HBD) and a hydrogen bond acceptor (HBA), which can be tuned according to the purpose of interest [9]. The alkaline DES was able to effectively dissolve and separate lignin and hemicellulose, leaving better accessibility of cellulose for further treatment processes [6]. The resulting cellulose pulp ($69 \pm 2.2\%$) is consistent with the other reported values as mentioned by Zhang et al. [10] in which the yield obtained from pre-treating poplar wood chips with lactic acid-choline chloride DES at different temperatures was in a range of 53–70%.

The bleaching process with peracetic acid solution has resulted in a decrement in the yield of 9% for the cellulose as the peracetic acid further removed the residual lignin, leaving the white-colored cellulose. This is agreed with the result reported by Zhao et al., in which a yield of ~ 54% was obtained after bleaching sugarcane bagasse with a peracetic acid solution prepared by mixing acetic acid and hydrogen peroxide at a volume ratio of 2:1 [11]. In the case of the WW-derived CNFs, the yield shows that WW is rich in cellulose content as the value obtained is 52% using

Table 1 Yield of industrial wood waste (WW)-derived cellulose pulp, cellulose, and cellulose nanofibrils (CNFs) correspond to the original weight of WW used

Specimens	Cellulose after pretreatment	Cellulose after bleaching	Cellulose nanofibrils (CNFs)
Yield, *Y (%)*	69 ± 2.2	60 ± 1.6	52 ± 0.9

TEMPO oxidation aided by mechanical post-treatment, which is more than those from non-wood sources [12], proving the efficient production of the WW-derived CNFs.

3.2 Characterization and Thermal Analysis of Industrial Wood Waste-Derived Cellulose and Cellulose Nanofibrils (CNFs)

3.2.1 Scanning Electron Microscopy (SEM) and Transmission Electron Microscopy (TEM)

The morphology of the WW, cellulose, and CNFs is presented in Fig. 1. Initially, the WW presented rough and irregular structures (Fig. 1a), but as the WW was pretreated using the alkaline DES and bleaching with peracetic acid, the structure turned into large-sized fibers with a diameter of 10–20 μm (Fig. 1b), indicating an efficient removal of hemicellulose and lignin [13]. The removal of lignin and hemicellulose alone does not help in the preparation of CNFs; therefore, the TEMPO oxidation aided by mechanical post-treatment were performed to break down the cell wall of the cellulose fibers and release the fundamental building blocks of the fibers [14]. The nanofibrillar structure of the WW-derived CNFs is clearly shown in the TEM image in Fig. 1d in which the nanofibrils were disintegrated uniformly with a width size of around 20–100 nm and several micrometers in length. Besides, the CNFs produced from this work are comparable with the CNFs produced by other reported results. Islam et al. [7] reported the homogenous fibrils structure from the rice straw-derived cellulose with a diameter size of 5–10 μm. The cellulose was then defibrillated into CNFs with a width of 10 nm, while in another research which was conducted by He et al. [15] also presented CNFs with slightly similar size of 500–2000 nm in length. On top of the smooth and cylindrical structure of the nanofibers, the continuous network of nanofibrils from the CNFs are clearly shown in Fig. 1c, d.

3.2.2 Fourier Transform Infrared Spectroscopy (FTIR)

Further characterization was done by FTIR to determine the surface functional groups available for the specimens. The FTIR spectra of all specimens are presented in Fig. 2 while the associated major peaks of the specimens based on the FTIR spectra were labeled accordingly. There is a broad peak at 3276 cm^{-1} associated with the intermolecular stretching vibration of hydroxyl (O–H) groups for the WW and another appearance of peak at 2900 cm^{-1} which is related to the stretching of C-H bonds of cellulose in the WW [16]. For the WW, there are visible peaks observed at 1651, 1543, and 1249 cm^{-1} which corresponded to C=O from lignin, C=C stretching of acetic and uronic ester group present from lignin, and out of plane C–O stretching due

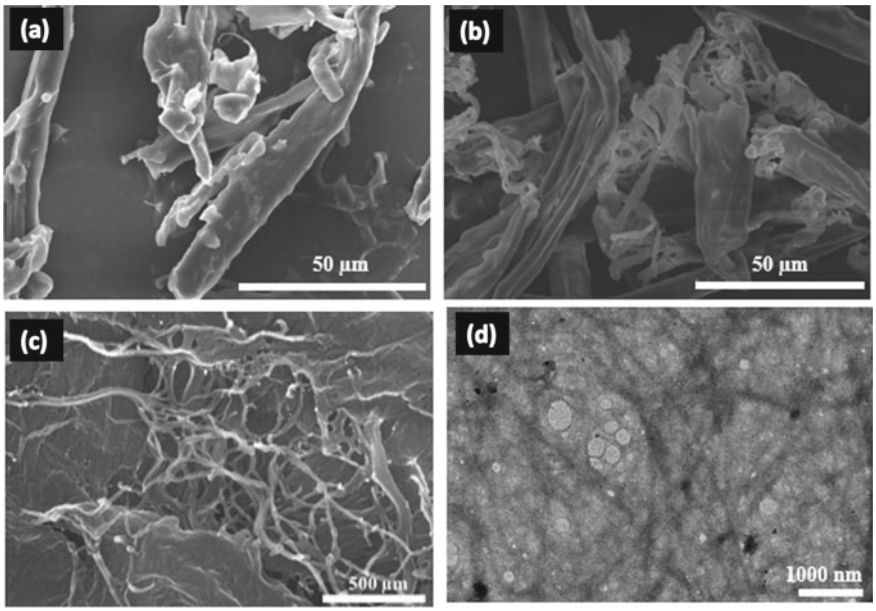

Fig. 1 SEM images of **a** industrial wood waste (WW), **b** cellulose (after pretreatment and bleaching), **c** cellulose nanofibrils (CNFs), and **d** a TEM image of the CNFs

to the presence of xylene and syringyl ring in lignin and hemicellulose, respectively [17–19]. The intensity of these peaks was significantly reduced as the WW underwent a series of treatment and processes to be converted into cellulose and CNFs. Also, the FTIR spectrum of cellulose shows that all peaks associated with lignin and hemicellulose were reduced, indicating the successful removal of lignin and hemicellulose. The removal of lignin and hemicellulose will leave O–H groups on the surface of cellulose to be exposed to the carboxylate groups during the TEMPO oxidation process [19]. The peak related to the intermolecular stretching of O–H groups within 3700–3000 cm^{-1} is still visible for cellulose but significantly reduced in CNFs. The reduction of this peak for CNFs can be explained by the insertion of carboxyl groups, replacing the O–H groups as the result of TEMPO oxidation although the peak related to carboxyl group around 1650 cm^{-1} is not obviously observed [19, 20]. It can be concluded that the cellulose was successfully converted into CNFs as the spectrum of CNFs retained all the peaks related to the backbone of cellulose at 899 and 595 cm^{-1}.

3.2.3 X-Ray Diffraction (XRD)

The XRD patterns for the WW, cellulose, and CNFs are presented in Fig. 3 together with the corresponding values of crystallinity index (CrI*)*. Generally, the three major

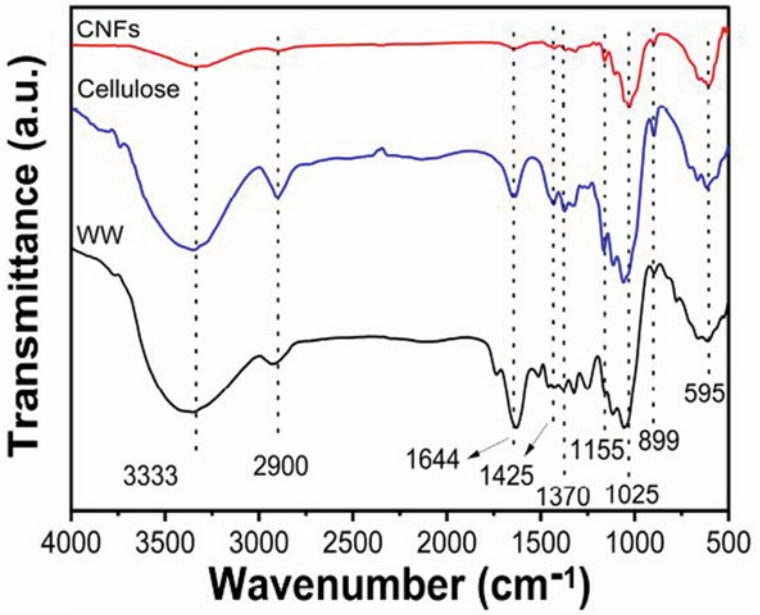

Fig. 2 FTIR spectra of the industrial wood waste (WW), cellulose, and cellulose nanofibrils (CNFs)

peaks corresponding to cellulose crystallography are observed around $2\theta = 16°$, 22°, and 34° for the three specimens, in which the peaks corresponded to the (110), (200), and (004) crystalline planes of cellulose, respectively [21]. The peak at (200) plane confirmed the polymorphic crystalline form of cellulose I as there is only one peak observed. Compared to the WW, the intensity of this peak for cellulose and CNFs increased, hence, explained the efficient removal of lignin and hemicellulose from the WW [7]. These results agree with the findings from FTIR discussed previously. As the intensity of the peak related to (200) plane increased, the values of CrI increased as well. This can be observed from Fig. 3 where the value of CrI (71.44%) for CNFs is the highest compared to cellulose and WW with broader peaks. The reason for the rise in the crystallinity of the CNFs can be attributed to the less orderly rearrangement of cellulose molecules after a series of chemical treatments [22]. Besides, the dissolution of amorphous compounds such as lignin and hemicellulose during the treatments with the alkaline DES and bleaching with peracetic acid also contributed to the increment in the crystallinity of the cellulose and CNFs.

3.2.4 Thermal Analysis

Other than the morphology and structural characterization, the thermal property of the WW, cellulose, and CNFs was also determined at a temperature range of 30–800 °C and presented in Fig. 4, showing that all the specimens experienced three

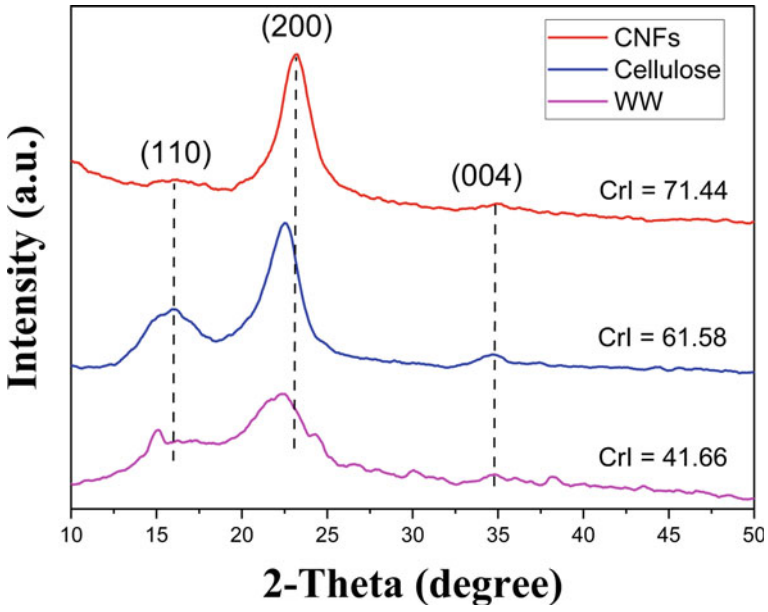

Fig. 3 XRD patterns for the industrial wood waste (WW), cellulose, and cellulose nanofibrils (CNFs)

stages of thermal decomposition. In the early stage, WW, cellulose, and CNFs, were hydrophilic in nature due to the presence of large number of O–H groups. This led to a slight weight loss of 7–11% between the temperatures of 40 and 105 °C, which might be attributed to the evaporation of the weakly attached water molecules [23]. The second stage of thermal degradation for WW took place between the temperature of 270 and 360 °C. The several shoulder peaks on the DTG curve of WW suggest that more than one process was involved in the degradation of cellulosic components such as cellulose, hemicellulose, and pectin [15]. Additionally, at the temperature of 360–700 °C, the breakdown of non-cellulosic components like lignin occurred, reducing the weight of WW. After the calcination process at 800 °C, around 10 wt% of the WW was still retained.

Due to the elimination of amorphous components during the alkaline pretreatment and bleaching, cellulose presented a considerably higher thermal stability than WW. Most of the weight loss happened between 300 and 350 °C, and after that, minimal weight loss observed until the temperature reached 800 °C. Primary weight loss for CNFs occurred at 210–350 °C due to the presence of sodium anhydroglucuronate units on the surface of the TEMPO-oxidized CNFs. The DTG curves show that the maximum degradation temperature (T_{max}) was 326 °C for WW, 321 °C for CNFs, and 354 °C for cellulose. In comparison with cellulose and CNFs, the WW has a lower thermal stability and a higher concentration of hemicellulose, lignin, and pectin. When CNFs is decarboxylated, the carboxyl groups on its surface undergo a direct transition from the solid to gas phases, resulting in a lower breakdown

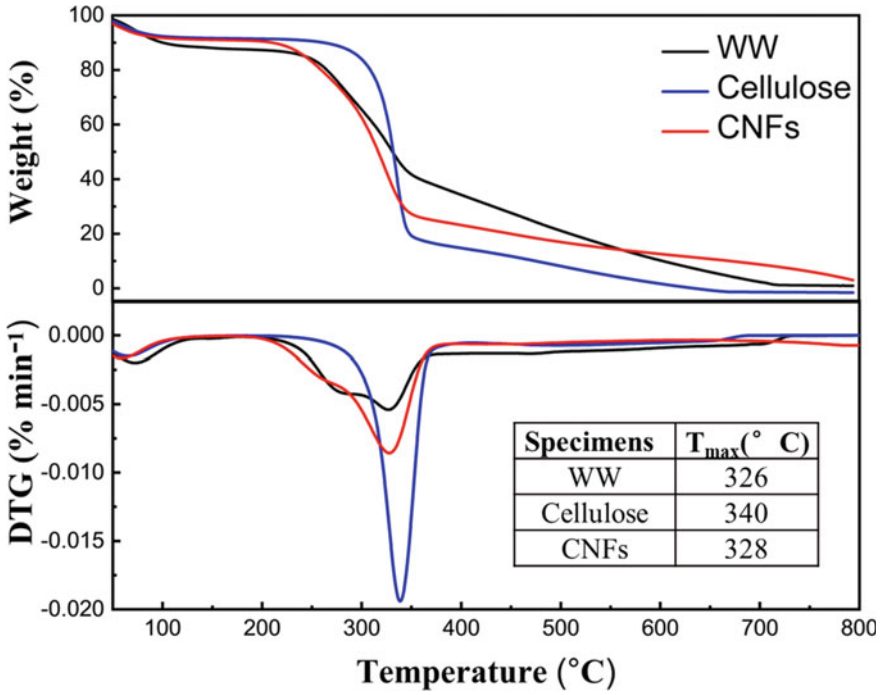

Fig. 4 TGA and DTG curves of the industrial wood waste (WW), cellulose, and cellulose nanofibrils (CNFs)

temperature (T_{max}) than with cellulose. Additionally, the small-sized fiber dimension of CNFs is more susceptible to thermal degradation, leading to a lower degradation temperature [7].

4 Conclusion

This research highlighted the utilization of industrial wood waste (WW) into a highly potential nanomaterial, namely cellulose nanofibrils (CNFs). The WW-derived CNFs were prepared by a series of processes starting from pretreatment of WW with an alkaline deep eutectic solvent (DES), bleaching with peracetic acid, TEMPO oxidation process, and mechanical post-treatment. The production of CNFs resulted in a high yield of 52%, making it considerable for further development in scale-up and industrial applications. The morphology, surface functional groups, crystallography, and thermal behavior of CNFs derived from the WW were determined. The CNFs produced showed a uniform fibril structure with a width of about 20–100 nm and a length of several micrometers. The findings from the FTIR and XRD showed that

the removal of lignin and hemicellulose was effective, leading to successful transformation of CNFs by TEMPO oxidation process. The effective removal of lignin and hemicellulose also increased the crystallinity of CNFs. However, CNFs presented slightly lower thermal stability as compared to cellulose and WW. The findings from this work are to discover the potential of CNFs produced from renewable sources such as industrial wood waste for further development as a sustainable and green material.

Acknowledgements The authors would like to acknowledge the financial support given by the Ministry of Higher Education Malaysia through the Fundamental Research Grant Scheme (FRGS) under Grant Number FRGS/1/2023/TK09/UNIMAP/02/4, the Centre of Excellence for Biomass Utilization (CoEBU), Universiti Malaysia Perlis (UniMAP).

References

1. Messerle VE, Mosse AL, Ustimenko AB, Slavinskaya NA, Sitdikov ZZ (2020) Recycling of organic waste in a plasma reactor. J Eng Phys Thermophys 93(4):987–997
2. Trache D, Tarchoun AF, Derradji M, Hamidon TS, Masruchin N, Brosse N, Hussin MH (2020) Nanocellulose: from fundamentals to advanced applications. Front Chem 8:392
3. Yang X, Reid MS, Olsen P, Berglund LA (2019) Eco-friendly cellulose nanofibrils designed by nature: effects from preserving native state. ACS Nano 14(1):724–735
4. Isogai A, Saito T, Fukuzumi H (2011) TEMPO-oxidized cellulose nanofibers. Nanoscale 3(1):71–85
5. Teng CP, Tan MY, Toh JPW, Lim QF, Wang X, Ponsford D, Lin EMJ, Thitsartarn W, Tee SY (2023) Advances in cellulose-based composites for energy applications. Materials 16(10):3856
6. Lim WL, Gunny AAN, Kasim FH, AlNashef IM, Arbain D (2019) Alkaline deep eutectic solvent: A novel green solvent for lignocellulose pulping. Cellulose 26:4085–4098
7. Islam MA, Ong HL, Halim KAA, Ganganboina AB, Doong RA (2021) Biomass–derived cellulose nanofibrils membrane from rice straw as sustainable separator for high performance supercapacitor. Ind Crops Prod 170:113694
8. Segal LGJMA, Creely JJ, Martin AE Jr, Conrad CM (1959) An empirical method for estimating the degree of crystallinity of native cellulose using the X-ray diffractometer. Textile Res J 29(10):786–794
9. Zdanowicz M, Wilpiszewska K, Spychaj T (2018) Deep eutectic solvents for polysaccharides processing. a review. Carbohydr Polym 200:361–380
10. Zhang L, Chu J, Gou S, Chen Y, Fan Y, Wang Z (2021) Direct fractionation of wood chips by deep eutectic solvent facilitated pulping technology and application for enzyme hydrolysis. Ind Crops Prod 171:113927
11. Zhao X, van der Heide E, Zhang T, Liu D (2011) Single-stage pulping of sugarcane bagasse with peracetic acid. J Wood Chem Technol 31(1):1–25
12. Kaffashsaie E, Yousefi H, Nishino T, Matsumoto T, Mashkour M, Madhoushi M, Kawaguchi H (2021) Direct conversion of raw wood to TEMPO-oxidized cellulose nanofibers. Carbohydr Polym 262:117938
13. Astruc J, Nagalakshmaiah M, Laroche G, Grandbois M, Elkoun S, Robert M (2017) Isolation of cellulose-II nanospheres from flax stems and their physical and morphological properties. Carbohydr Polym 178:352–359
14. Boufi S, Chaker A (2016) Easy production of cellulose nanofibrils from corn stalk by a conventional high speed blender. Ind Crops Prod 93:39–47

15. He M, Yang G, Chen J, Ji X, Wang Q (2018) Production and characterization of cellulose nanofibrils from different chemical and mechanical pulps. J Wood Chem Technol 38:1–10
16. Kalita E, Nath BK, Deb P, Agan F, Islam MR, Saikia K (2015) High quality fluorescent cellulose nanofibers from endemic rice husk: Isolation and characterization. Carbohydr Polym 122:308–313
17. Moosavinejad SM, Madhoushi M, Vakili M, Rasouli D (2019) Evaluation of degradation in chemical compounds of wood in historical buildings using FT-IR and FT-Raman vibrational spectroscopy. Maderas. Ciencia y tecnología 21(3):381–392
18. Ozgenç O, Durmaz S, Boyaci IH, Eksi-Kocak H (2017) Determination of chemical changes in heat-treated wood using ATR-FTIR and FT Raman spectrometry. Spectrochimica Acta Part A: Mol Biomol Spectro 171:395–400
19. Pucetaite M (2012) Archaeological wood from the Swedish warship Vasa studied by infrared microscopy
20. Lan X, Ma Z, Szojka AR, Kunze M, Mulet-Sierra A, Vyhlidal MJ, Boluk Y, Adesida AB (2021) TEMPO-oxidized cellulose nanofiber-alginate hydrogel as a bioink for human meniscus tissue engineering. Front Bioeng Biotechnol 9:766399
21. Jiang F, Hsieh YL (2013) Chemically and mechanically isolated nanocellulose and their self-assembled structures. Carbohydr Polym 95(1):32–40
22. Kumar S, Prasad L, Bijlwan PP, Yadav A (2022) Thermogravimetric analysis of lignocellulosic leaf-based fiber-reinforced thermosets polymer composites: an overview. Biomass Convers Biorefin 1–26
23. Camargos CH, Poggi G, Chelazzi D, Baglioni P, Rezende CA (2022) Strategies to mitigate the synergistic effects of moist-heat aging on TEMPO-oxidized nanocellulose. Polym Degradation Stab 200:109943
24. Qua EH, Hornsby PR, Sharma HSS, Lyons G (2011) Preparation and characterization of cellulose nanofibers. J Mater Sci 46:6029–6045
25. Huang Y, Meng F, Liu R, Yu Y, Yu W (2019) Morphology and supramolecular structural characterization of cellulose isolated from heat-treated moso bamboo. Cellulose 26:7067–7078

Bioenergy Integration

A Review on Recent Optimal Sizing Methodologies and Evaluation Indicators for Hybrid Renewable Energy System

Mazwin Mazlan, Shahril Irwan Sulaiman, and Hedzlin Zainuddin

Abstract Electricity demand in islands and remote areas is generally supplied by diesel generators or other fossil fuels because they are far from the utility grid. Nevertheless, the research trends nowadays are to reduce the reliance on fossil fuels by working on renewable energy. Renewable energy sources provide numerous benefits to rural and remote areas, including sustainability, environmental tolerance, low pollution, and economic advantages. However, the majority of renewable energy sources are uncontrolled and unpredictable. To address these drawbacks, hybrid systems involving the use of multiple types of renewable energy resources and/or traditional energy resources and/or storage systems have been developed. However, sizing for hybrid renewable energy can be difficult due to a number of factors, such as the sizing of system components and the integration of each component to optimize system performance. As a result, the primary purpose of this work is to conduct a review of the most recent configuration of HRES, techniques to addressing optimization issues, and evaluation indicators of hybrid renewable energy system (HRES).

Keywords Hybrid renewable energy system (HRES) · Sizing methodology · Software tool · Artificial methods · Evaluation indicator

M. Mazlan (✉)
Universiti Malaysia Perlis, 02600 Arau, Perlis, Malaysia
e-mail: mazwin@unimap.edu.my

S. I. Sulaiman · H. Zainuddin
Universiti Teknologi MARA, 40450 Shah Alam, Selangor Darul Ehsan, Malaysia
e-mail: hedzl506@uitm.edu.my

H. L. Ong et al. (eds.), *Proceedings of the 3rd International Conference on Biomass Utilization and Sustainable Energy; ICoBiomasSE 2023; 4–5 September; Kuala Lumpur, Malaysia*, Green Energy and Technology,
https://doi.org/10.1007/978-981-99-9164-8_18

1 Introduction

Renewable energy sources have become a popular option for generating electricity due to the increasing demand for lowering carbon dioxide emissions and the depletion of fossil fuel reserves [1]. The utilization of renewable energy is significantly important for the world because global energy sources are no longer sufficient to meet the energy demand.

The most common renewable energy sources (RES) in residential applications are wind and solar due to the maturity of the accompanying energy conversion technologies, affordability, and government backing through incentive schemes [2]. However, due to the intermittent nature of solar irradiance and wind speed, the power output of these RES fluctuates widely and is therefore incapable of meeting residential energy demands on their own.

To address these drawbacks, HRES involving the use of multiple types of renewable energy resources and/or integration with conventional energy resources and/or storage systems have been developed [3].

2 Hybrid Renewable Energy System (HRES) Configuration

Combining two or more renewable energy sources to produce electricity or other forms of energy is an HRES [4]. These may include solar, wind, hydroelectric, geothermal, biomass, and other sources of renewable energy. The purpose of integrating these sources is to produce a more reliable and efficient energy system capable of meeting the energy requirements of a specific application or system. The essential components of HRES are depicted in Fig. 1, where the system can be configured differently depending on the application and available resources. Meanwhile, in order to construct a dependable and cost-effective hybrid renewable energy system, the size of each component must be determined [5].

3 Sizing Optimization Methods of HRES

3.1 Sizing HRES Using Software Tools

Various assessment software tools for sizing system components of HRES are reviewed in [4, 6]. Among the available software tools are HOMER (hybrid optimization model for electric renewable), HYBRIDS2, iHOGA (hybrid optimization by genetic algorithm), HYBRIDS, and TRNSYS. However, HOMER is the most popular software for sizing HRES. The strengths and weaknesses of each software tool have been reported by [7, 8], and Table 1 presents a list of widely considered software tools for the design of HRES.

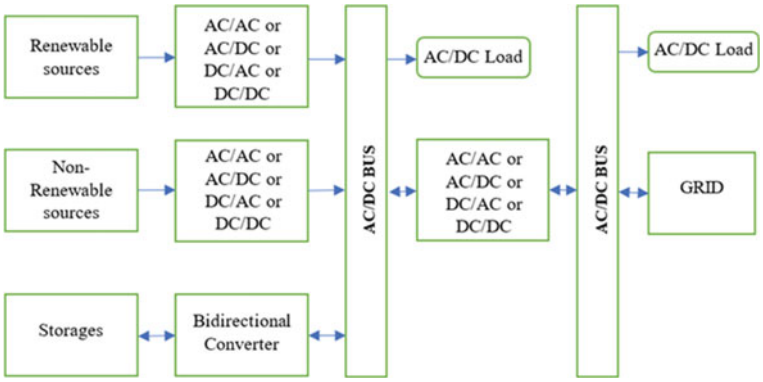

Fig. 1 Basic components of HRES

Table 1 Sizing HRES using software methods

No.	Software tools	System configuration	Objective of study	References
1	HOMER	PV/wind/battery/diesel	Techno-economic analyses	[9]
		PV/wind/battery/diesel	Techno-economic and environmental	[10]
		PV/battery/biogas generator	Techno-economic and environmental	[11]
2	HYBRIDS2	PV/wind/fuel cell/ electrolyzer/hydrogen	Techno-analysis	[12]
3	iHOGA	PV/wind compared battery/diesel	Techno-economic analyses	[13]
4	TRNSYS	PV/wind	Techno-economic and environmental	[14]

3.2 Sizing HRES Using Traditional Method

The traditional approach is defined by its utilization of mathematical calculations in order to achieve the optimal solution. Due to their limited space optimization, researchers rarely employ these techniques [15]. However, as shown in Table 2, there are a variety of traditional techniques [16, 17].

3.3 Sizing HRES Using Artificial Intelligent (AI) Methods

Artificial intelligence (AI) is becoming more popular in renewable energy research to solve optimization and design challenges. These are not limited to determining local

Table 2 Sizing HRES using traditional methods

No.	Method	System configuration	Objective of study	References
1	Analytical	PV/wind	Economic analysis	[18]
2	Iterative	PV/wind/battery	Techno-analysis	[19, 20]
		PV/battery	Techno-analysis	[21]
3	Probabilistic	PV/wind/battery/biomass	Techno-analysis	[22–24]
4	Graphical	PV/wind	Techno-analysis	[25]
5	Linear Programming	PV/wind	Economic analysis	[26]
		PV/wind	Techno-economic analyses	[27]

Table 3 Sizing HRES using artificial methods

No.	Method	System configuration	Objective of study	References
1	Particle swarm optimization (PSO)	PV/fuel cell/battery	Techno-analysis	[28]
		PV/wind/battery/ diesel	Economic analysis	[29]
2	Genetic algorithm (GA)	PV/wind/battery	Techno-analysis	[30]
3	Artificial bee swarm optimization (ABSO)	PV/wind/fuel cell	Techno-analysis	[31]
4	Simulated annealing (SA)	PV/wind/battery	Economic analysis	[32]
5	Cuckoo search (CS)	PV/wind	Techno-economic and environmental	[33]
6	Ant colony optimization (ACO)	PV/wind/battery	Techno-economic analyses	[34]
7	Flower pollination (FPA)	PV/wind/fuel cell/ hydrogen	Techno-analysis	[35]

optimal configuration but also global optimum system configuration with relative computing ease when compared with traditional approaches [16, 17]. Some of AI techniques are listed in Table 3.

3.4 Sizing HRES Using Hybrid Methods

A hybrid algorithm is any algorithm that combines more than two algorithms in order to overcome the limitations of a single algorithm. Table 4 shows the combination of two algorithms.

Table 4 Sizing HRES using hybrid methods

No.	Method	System configuration	Objective of study	References
1	Hybrid big bang–big crunch (HBB–BC)	PV/wind/ battery	Economic analysis	[36]
2	GA-PSO	PV/wind/ battery	Economic analysis	[37]
3	Fuzzy-PSO	PV/wind/ battery	Techno-economic	[38]
4	PSO-DE	PV/wind/ battery/diesel	Techno-socio-economic-environmental	[39]
5	PSO and gravitational search (PSOGSA)	PV/wind/ battery/diesel	Techno-economic	[40]

4 Evaluation Criteria for HRES

Kahraman et al. revealed that one of the major efforts required for designing HRES for a certain region is the determination of assessment criteria for hybrid renewable energy systems [41]. Topcu and Ulengin [42] analyzed potential energy options based on their environmental, physical, economic, political, and other uncontrollable factors, while Ribeiro et al. [43] created a multi-criteria decision analysis (MCDA) instrument that allows ranking of various scenarios based on their performance on 13 criteria spanning economic, job market, quality of life of local populations, technical, and environmental concerns for the Portuguese case. Figure 2 depicts the various evaluation criteria and factors involved in the design of HRES. Several of these evaluation criteria are broadly explained using mathematical formulation. Previous review in [16, 43, 44] described a variety of parameters that can be considered when sizing a HRES. Table 5 shows the parameters for the determination of feasibility and reliability, which assists the system designer in designing an effective system design for the application or system.

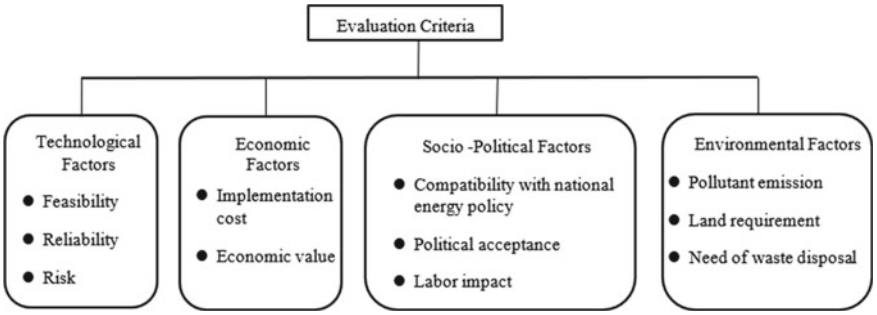

Fig. 2 Evaluation criteria and factors for designing HRES

Table 5 Parameters for evaluation criteria for HRES

No.	Parameter	Formula	References
Technological factors			
1	Loss of power supply probability (LPSP)	$\text{LPSP} = \frac{\sum_{t=1}^{n} E_{\text{deficit}}}{\sum_{t=1}^{n} E_{\text{load demand}}}$	[45] [31] [46]
2	Loss of load probability (LLP/LOLP)	$\text{LLP} = \frac{\sum_{t=1}^{n} \text{shortage}(t)}{\sum_{t=1}^{n} D(t)}$ where shortage: Unmet load during time period $D(t)$: Electricity demand	[45] [46]
3	Loss of load risk (LOLR)	$\text{LOLR} = 1 - p$ or $\text{LOLR} = q$ where p: Cumulative probability of meteorological status which corresponds to electrical energy generation q: Probability of failure	[47] [45]
Economic factors			
1	Total annual cost (TAC)	$\text{TAC} = \text{C}_{\text{anual capital}} + \text{C}_{\text{annual maintenance}} + \text{C}_{\text{replacement}}$ Change the initial capital cost into the annual capital cost by using the capital recovery factor (CRF) $\text{CRF} = [r(1+r)^d]/[(1+r(1+r)^d - 1]$ where r: Interest rate d: Number of years in system life span	[31] [46]
2	Annualized cost of system (ACS)	ACS is the total cost of annual capital, replacement, and maintenance	[46]
3	Cost of energy (COE)	COE is the proportion of ACS to TAEP (total annual energy production $\text{TAEP} = \sum_{i=1}^{365} E_g(i)$ $\text{COE} = \frac{\sum_{i=1}^{n} \text{ACS}_i}{\sum_{i=1}^{n} \text{TAEP}}$ where $E_g(i)$: Total daily energy generated	[45]

(continued)

Table 5 (continued)

No.	Parameter	Formula	References
4	Life cycle cost (LCC)	$LCC = C + OM_{NPV} + R_{NPV} - S_{NPV}$ where C: Capital costs OM_{NPV}: Net present value (NPV) of operation and maintenance costs R_{NPV}: NPV of replacement costs S_{NPV}: NPV of salvage value	[45]
5	Levelized cost of energy (LCOE)	$LCOE = \frac{TAC}{E_{Tot}}$ where $E_{Tot:}$ Total annual energy generated	[46]
6	Net present value (NPV)	$NPV = \sum NPV_{income} + \sum NPV_{end} - C_{investment} - \sum NPV_{OM} - \sum NPV_{r}$ where NPV_{income}: Present discounted values of incomes from electricity sales to grid NPV_{end}: Present discounted values of income from the residual amount of the system components at the end lifetime of the system. $C_{investment}$: Initial total investment cost NPV_{OM}: Discounted values of the future operation and maintenance costs during the lifetime of the system NPV_{r}: Discounted values of the future replacement costs to replace components while the lifetime of the system	[6]
Socio-political factors			
1	Job creation (JC)	$JC = J_{PV} \times P_{PV} + JC_{wind} \times P_{wind}$ $+JC_{diesel} \times E_{diesel} + JC_{batt} \times E_{batt} + JC_{hydro} \times P_{hydro}$ where JC_{PV}: Number of jobs per MWp of the PV generator (job/MW) P_{PV}: Peak power of the PV generator (MWp). JC_{wind}: Number of jobs per MW of wind turbines (job/MW) P_{wind}: Maximum power of the group of wind turbines (MW) JC_{diesel}: Number of jobs created by the diesel (job/GWh/yr) E_{diesel}: Annual energy supplied by the diesel (GWh/yr) JC_{batt}: Number of jobs created per MWh of nominal capacity of storage in the battery bank (job/MWh) E_{batt}: Nominal capacity of the battery bank (MWh) For the jobs created by the hydropower station, we consider the parameter JChydro (job/MW), which is the number of jobs created per MW of installed capacity of hydropower stations. $P_{hydro:}$ installed capacity of hydropower stations (MW)	[48, 49]

(continued)

Table 5 (continued)

No.	Parameter	Formula	References
2	Human development index (HDI)	HDI is a measure of a country's economic and social development level which considers the life expectancy at birth, years of education, per capita national income, etc. [50] $\text{HDI} = 0.0978$ $\text{In}\left(\text{E}_{\text{L\_annual\_per\_capita}}\right) - 0.0319$ where $\text{E}_{\text{L\_annual\_per\_capita}}$: Annual electricity consumption per capita (kWh/year/person)	[49]
3	Social acceptance	Owing to the negative social impacts of HRES such as land use, visual impact, acoustic noise, and electromagnetic interference, should be considered when building a hybrid energy system	[46]
Environmental factors			
1	CO_2 emission	The CO_2 emission of a generator at time t is Related to its fuel consumption by: $\text{E}_{\text{CO}_2}(t) = \text{SE}_{(\text{CO}_2)}(\text{kg/l}) \times F(t)(\text{l/h})$ where $\text{SE}_{(\text{CO}_2)}$: Specific emission of carbon dioxide per liter of fuel and it is given as 2.7 kg/l	[51]
2	Embodied energy (EE)	EE is the non-renewable energy utilized by all processes involved in the production of a hybrid system, from the acquisition of raw materials to its final assembly $\text{EE} = \text{E}_{\text{PV}} + \text{E}_{\text{WT}} + \text{E}_{\text{Batt}} + \text{E}_{\text{Pump}} + \text{E}_{\text{Tank}} + \text{E}_{\text{RO}}$ where E_{PV}: Embodied energy of photovoltaic panels E_{WT}: Embodied energy of wind turbine. E_{Batt} is the embodied energy of the battery $\text{E}_{\text{Pump:}}$ Embodied energy of motor pumps combined to the EE of the converters E_{Tank}: Embodied energy of tanks E_{RO}: Embodied energy of the reverse osmosis membrane	[52]

5 Conclusion

Hybrid renewable energy system (HRES)-based power generation has been recognized as a feasible and cost-effective power generation option in off-grid applications due to advancements in power converters and renewable energy technologies that improve system efficiency. In this study, an attempt has been made to review relevant aspects of the hybrid renewable energy system for off-grid applications, recent developments in sizing optimization methodologies, a critical comparison of the configuration of HRES, techniques for addressing optimization issues, and evaluation indicators of HRES. In addition, an evaluation of HRES including their assessment parameters in terms of economic, reliability, environmental, and social aspects is also presented. Optimization of HRES is mostly reached using artificial methods or commercial software, and HOMER is the most commercial software used in optimization. However, in recent years, a lot of hybrid optimization methods have been developed to optimize HRES. Other than that, it is necessary to use many

methods in each study to reach the optimum results in sizing, control, and energy management. The comparison between many methods ensures the best performance of the system and realizes the objective aims of the study. For further work, it is necessary to use many control methods in HRES, where parameters that should be controlled are stability (voltage and frequency of the system), protection (observation of power flow), and power balance (optimal load distribution). The management methods used in HRES may also be reviewed in detail in future.

References

1. Dolatabadi A, Mohammadi-Ivatloo B (2018) Stochastic risk-constrained optimal sizing for hybrid power system of merchant marine vessels. IEEE Trans Industr Inf 14(12):5509–5517
2. Roy P, He J, Zhao T, Singh YV (2022) Recent advances of wind-solar hybrid renewable energy systems for power generation: a review. IEEE Open J Ind Electronics Soc 3:81–104
3. Bakhtiari H, Naghizadeh RA (2018) Multi-criteria optimal sizing of hybrid renewable energy systems including wind, photovoltaic, battery, and hydrogen storage with ϵ-constraint method. IET Renew Power Gener 12(8):883–892
4. Zhou Y (2022) Advances of machine learning in multi-energy district communities–mechanisms, applications and perspectives. Energy and AI 10
5. Nafeh A (2011) Optimal economical sizing of A PV-wind hybrid energy system using genetic algorithm. Int J Green Energy 8(1):25–43
6. Lian J, Zhang Y, Ma C, Yang Y, Chaima E (2019) A review on recent sizing methodologies of hybrid renewable energy systems. Energy Convers Manage 199
7. Ammari C, Belatrache D, Touhami B, Makhloufi S (2022) Sizing, optimization, control and energy management of hybrid renewable energy system—a review. Energy Built Environ 3(4):399–411
8. Erdinc O (2012) Optimum design of hybrid renewable energy systems: overview of different approaches. Renew Sustain Energy Rev 16(3):1412–1425
9. Ibrahim MM, Mostafa NH, Osman AH, Hesham A (2020) Performance analysis of a stand-alone hybrid energy system for desalination unit in Egypt. Energy Convers Manage 215
10. Kotb KM, Elkadeem MR, Elmorshedy MF, Dán A (2020) Coordinated power management and optimized techno-enviro-economic design of an autonomous hybrid renewable microgrid: a case study in Egypt. Energy Convers Manage 221
11. Das BK (2021) Techno-economic and environmental assessment of a hybrid renewable energy system using multi-objective genetic algorithm: a case study for remote Island in Bangladesh. Energy Convers Manage 230
12. Mills A, Al-Hallaj S (2004) Simulation of hydrogen-based hybrid systems using Hybrid2. Int J Hydrogen Energy 29(10):991–999
13. Fatih-Güven A, Mahmoud-Samy M (2022) Performance analysis of autonomous green energy system based on multi and hybrid metaheuristic optimization approaches. Energy Convers Manage 269
14. Anoune K, Laknizi A, Bouya M, Astito A, Ben Abdellah A (2018) Sizing a PV-Wind based hybrid system using deterministic approach. Energy Convers Manage 169:137–148
15. Mishra S, Saini G, Saha S, Chauhan A, Kumar A, Maity S (2022) A survey on multi-criterion decision parameters, integration layout, storage technologies, sizing methodologies and control strategies for integrated renewable energy system. Sustain Energy Technol Assessments 52
16. Sinha S, Chandel SS (2015) Review of recent trends in optimization techniques for solar photovoltaic-wind based hybrid energy systems. Renew Sustain Energy Rev 50:755–769
17. Abaye AE (2018) System analysis and optimization of photovoltaic—wind hybrid system: review. Int Res J Eng Technol (IRJET) 5(1):197–220

18. Madhlopa A, Sparks D, Keen S, Moorlach M, Krog P, Dlamini T (2015) Optimization of a PV—wind hybrid system under limited water resources. Renew Sustain Energy Rev 47:324–331
19. Ashok S (2007) Optimised model for community-based hybrid energy system. Renew Energy 32(7):1155–1164
20. Abdul Aziz NI, Sulaiman SI, Shaari S, Musirin I, Sopian K (2017) Optimal sizing of stand-alone photovoltaic system by minimizing the loss of power supply probability. Sol Energy 150:220–228
21. Abdul Aziz NI, Sulaiman SI, Shaari S, Musirin I (2015) An iterative algorithm for sizing stand-alone photovoltaic system. Appl Mech Mater 785:601–605
22. Liu WH, Sharifah Rafidah WA, Haslenda H, Jeng SL, Nor Erniza MR (2016) Sizing of hybrid power system with varying current type using numerical probabilistic approach. Appl Energy 184:1364–1373
23. Bagul AD, Salameh ZM (1996) Sizing of a stand-alone hybrid wind-photovoltaic system using a three-event probability density approximation. Sol Energy 56(4):323–335
24. Tina G, Gagliano S, Raiti S (2006) Hybrid solar/wind power system probabilistic modelling for long-term performance assessment. Sol Energy 80(5):578–588
25. Tomas M (1996) Sizing of hybrid photovoltaic-wind energy systems. Sol Energy 57(4):277–281
26. Chedid R, Rahman S (1997) Unit sizing and control of hybrid wind-solar power systems. IEEE Trans Energy Convers 12(1):79–85
27. Nogueira CEC, Vidotto ML, Niedzialkoski RK, De Souza SNM, Chaves LI, Edwiges T, Santos DBD, Werncke I (2014) Sizing and simulation of a photovoltaic-wind energy system using batteries, applied for a small rural property located in the south of Brazil. Renew Sustain Energy Rev 29:151–157
28. Bigdeli N (2015) Optimal management of hybrid power system: a PV/fuel cell/battery comparison of optimal hybrid approaches. Renew Sustain Energy Rev 42:377–393
29. Amer M, Namaane A, Sirdi NKM (2013) Optimization of hybrid renewable energy systems (HRES) using PSO for cost reduction. Energy Procedia 42:318–327
30. Javadi MR, Mazlumi K, Jalilvand A (2011) Application of GA, PSO and ABC in optimal design of a stand-alone hybrid system for North-West of Iran. In: ELECO 2011 7th international CLECO 2011—7th international conference on electrical and electronics engineering, Bursa, Turkey
31. Maleki A, Askarzadeh A (2014) Artificial bee swarm optimization for optimum sizing of a stand-alone PV/WT/FC hybrid system considering LPSP concept. Sol Energy 107:227–235
32. Ekren O, Ekren BY (2010) Size optimization of a PV/wind hybrid energy conversion system with battery storage using simulated annealing. Appl Energy 87(2):592–598
33. Nadjemi O, Nacer T, Hamidat A, Salhi H (2017) Optimal hybrid PV/wind energy system sizing: application of cuckoo search algorithm for Algerian dairy farms. Renew Sustain Energy Rev 70:1352–1365
34. Alireza A (2014) Application of ant colony optimization (ACO) for designing a hybrid system. Int J Eng Appl Sci (IJEAS) 6(2):52–63
35. Hadidian Moghaddam MJ, Kalam A, Nowdeh SA, Ahmadi A, Babanezhad M, Saha S (2019) Optimal sizing and energy management of stand-alone hybrid photovoltaic/wind system based on hydrogen storage considering LOEE and LOLE reliability indices using flower pollination algorithm. Renew Energy 135:1412–1434
36. Ahmadi S, Abdi S (2016) Application of the Hybrid Big Bang-Big Crunch algorithm for optimal sizing of a stand-alone hybrid PV/wind/battery system. Sol Energy 134:366–374
37. Ghorbani N, Kasaeian A, Toopshekan A, Bahrami L, Maghami A (2018) Optimizing a hybrid wind-PV-battery system using GA-PSO and MOPSO for reducing cost and increasing reliability. Energy 154:581–591
38. Nemouchi W, AmraneY, Nemouchi H (2022) Optimal sizing design of stand- alone hybrid system using a fuzzy PSO. In: Lecture notes in networks and systems, vol 361. LNNS, Tipasa, Algeria, pp 100–110

39. Singh P, Pandit M, Srivastava L (2022) Techno-socio-economic-environmental estimation of hybrid renewable energy system using two-phase swarm-evolutionary algorithm. Sustainable Energy Technol Assessments 53
40. Castro RCC (2019) Hybrid particle swarm optimization and gravitational search algorithm for optimal sizing of hybrid renewable energy systems. In: Asia-Pacific power and energy engineering conference, APPEEC, Macao, China
41. Kahraman C, Kaya I, Cebi S (2009) A comparative analysis for multiattribute selection among renewable energy alternatives using fuzzy axiomatic design and fuzzy analytic hierarchy process. Energy 34(10):1603–1616
42. Topcu YI, Ulengin F (2004) Energy for the future: energy for future: an integrated decision aid for the case of Turkey. Energy 29(1):137–154
43. Ribeiro F, Ferreira P, Araújo M (2013) Evaluating future scenarios for the power generation sector using a Multi-Criteria Decision Analysis (MCDA) tool: the Portuguese case. Energy 52:126–136
44. Bhandari B, Lee KT, Lee GY, Cho YM, Ahn SH (2015) Optimization of hybrid renewable energy power systems: a review. Int J Precis Eng Manuf Green Technol 2(1):99–112
45. Khan FA, Pal N, Saeed SH (2018) Review of solar photovoltaic and wind hybrid energy systems for sizing strategies optimization techniques and cost analysis methodologies. Renew Sustain Energy Rev 92:937–947
46. Khatib T, Ibrahim IA, Mohamed A (2016) A review on sizing methodologies of photovoltaic array and storage battery in a standalone photovoltaic system. Energy Convers Manage 120:430–448
47. Sawle Y, Gupta SC, Bohre AK (2016) PV-wind hybrid system: a review with case study. Cogent Eng 3(1)
48. Chauhan A, Saini RP (2016) Techno-economic feasibility study on integrated renewable energy system for an isolated community of India. Renew Sustain Energy Rev 59:388–405
49. Dufo-López IR, Cristóbal-Monreal IR, Yusta JM (2016) Optimisation of PV-wind-diesel-battery stand-alone systems to minimise cost and maximise human development index and job creation. Renew Energy 94:280–293
50. Al-falahi MDA, Jayasinghe SDG, Enshaei H (2017) A review on recent size optimization methodologies for standalone solar and wind hybrid renewable energy system. Energy Convers Manage 143:252–274
51. Ogunjuyigbe ASO, Ayodele TR, Akinola OA (2016) Optimal allocation and sizing of PV/Wind/Split-diesel/Battery hybrid energy system for minimizing life cycle cost, carbon emission and dump energy of remote residential building. Appl Energy 171:153–171
52. Affi S, Cherif H, Belhadj J (2021) Smart system management and techno-environmental optimal sizing of a desalination plant powered by renewables with energy storage. Int J Energy Res 45(5):7501–7520